UNIVERSITY OF SOUTHAMPTON

Physics-Based Aeroacoustic Modelling of Bluff-Bodies

by

Edward Peers

Thesis for the degree of Doctor of Philosophy

in the
Faculty of Engineering, Science and Mathematics
School of Engineering Sciences

June 2009

UNIVERSITY OF SOUTHAMPTON

ABSTRACT

FACULTY OF ENGINEERING, SCIENCE AND MATHEMATICS
SCHOOL OF ENGINEERING SCIENCES

Ph.D

Physics-Based Aeroacoustic Modelling of Bluff-Bodies

by Edward Peers

In this work physics-based modelling of bluff-body noise was performed with application to landing gear noise prediction. The landing gear is a primary contributor to airframe noise during approach. Noise is primarily generated from the unsteady pressures resulting from the turbulent flow around various components. The research was initiated in response to the need for an improved understanding of landing gear component noise characteristics and to assist in the development of landing gear noise prediction tools. A computational approach was adopted so that the noise generating physics of the problem could be captured. Governing laws were solved numerically to predict the noise source characteristics and the resulting acoustic far-field. Three-dimensional compressible Navier-Stokes simulations were performed to solve the unsteady turbulent near-field flow and the acoustic analogy was used to predict the resulting far-field acoustic pressure. The flow solver included a high-order computational aeroacoustics code adopting large-eddy simulation, whilst a Ffowcs Williams and Hawkings solver was used for the acoustic prediction. Circular cylinders in various configurations were selected to represent basic landing gear struts and results were used to form a modelling database. Initially, cylinders at various Reynolds numbers were investigated in cross-flow to determine the noise characteristics of a simple model strut. The work was extended to investigate the effect of strut alignment to the flow by simulating cylinders in yaw. The effect of yaw was shown to modify the peak level and frequency of far-field noise spectra. Component interaction effects were then investigated by simulating cylinders in tandem arrangements. The resulting aerodynamic and far-field noise characteristics were shown to be complex and extremely sensitive to the separation distance between the cylinders. Finally, a prediction model was developed and validated by comparing predictions against theory and measurements of the noise radiated by a simple two-wheel landing gear model. The results demonstrated the capability of the model to accurately predict correct spectral and directivity characteristics.

Contents

List of Figures

List of Tables

Acknowledgements

There are many individuals that I would like to thank for providing me with support during my period of study. Foremost, I would like to thank my supervisor, Professor Xin Zhang, for his guidance, encouragement and inspiration, and to whom I owe the opportunity of completing this PhD. I would also like to thank Dr. Stephen Chow and Dr. Malcolm Smith for their support and advice throughout the project.

I would like to thank my friends in the department at Southampton: Andy and Dave for their company on the golf course, and all those who I have had the pleasure of sharing an office with.

My family have been invaluable to me and have supported me throughout my life and study. I would like to thank my parents for their encouragement and financial support, and also my sister Lucy.

Last, but not least, I would like to thank my wife, Beth, who has been a tremendous support throughout and has kept me going through thick and thin...

Nomenclature

All units are in SI

Alphanumeric

b_i	Heat transport vector
c	Sound speed
c_p	Specific heat at constant pressure
c_v	Specific heat at constant volume
d	Length scale in S-A model
e	Specific stagnation energy per unit volume
f	Frequency; also, damping function
k	Turbulent kinetic energy
k_c	Thermal conductivity
l	Length scale
p	Static pressure
q	Heat flux vector
t	Time
u, v, w	Velocity components in the x, y, and z directions
x, y, z	Cartesian coordinate system
t_{adv}	Advanced time
u_τ	Friction velocity
p'	Acoustic pressure
y^+	Non-dimensional wall distance
$\tilde{d}$	Modified length scale in DES model
$\hat{n}$	Unit normal vector
$\overline{p'^2}$	Mean-square acoustic pressure
$\mathbf{q}$	Primitive variables
C	Constant
E	Spectral energy
F	Function
G	Free-space Green function
$H(f)$	The Heavyside function
I	Acoustic intensity
J	Jacobian of transformation
M	Mach number
Q	Monopole term
R	Observer radius
Re	Reynolds number
S	Separation distance between tandem cylinder centers
St	Strouhal number, fD/U_∞

T	Temperature
U, V, W	Contravarient velocities
C_D	Drag coefficient
C_L	Lift coefficient
C_p	Pressure coefficient
C_{DES}	Constant in DES model
C_{bp}	Base pressure coefficient
E_w	Empirical wheel spectrum
F_i	Dipole term in Equation 2.7
G_ν	Production term in S-A model
I_t	Turbulence intensity
L_c	Correlation length
L_z	Simulated span
M_c	Component local Mach number
P_{ij}	Compressive stress tensor
R	Specific gas constant
R_∞, R_i	Riemann invariants
Re_t	Turbulent Reynolds number
St_m	Modified Strouhal number
T_{ij}	The Lighthill stress tensor
V_n	Velocity normal component
V_t	Velocity parallel component
Y_ν	Destruction term in S-A model
S_{ij}	Mean strain rate
C_L'	Lift coefficient RMS
$\mathbf{E}$, $\mathbf{F}$, $\mathbf{G}$	Flux derivative vectors
$\mathbf{P}$	Characteristic transformation matrix
$\mathbf{Q}$	Solution vector
$\mathbf{S}$	Spectrum matrix
$\mathbf{S_c}$	Characteristic source term
$\mathbf{S}_v$	Source term containing the viscous flux derivatives

Abbreviations

2-D	Two-dimensional
3-D	Three-dimensional
CAA	Computational Aeroacoustics
CAD	Computer Aided Design
CFD	Computational Fluid Dynamics
CFL	Courant-Friedrichs-Levy
CPU	Central Processing Unit
dB	Decibel
dB(A)	"A" weighted decibel level
DES	Detached-Eddy Simulation
DNS	Direct Numerical Simulation
EPNL	Effective Perceived Noise Level
ESDU	Engineering Sciences Data Unit
GUI	Graphical User Interface
LBM	Lattice Boltzmann Method
LES	Large-Eddy Simulation
LG	Landing Gear

LS	Laminar separation
OASPL	Overall Sound Pressure Level
PIV	Particle Image Velocimetry
PSD	Power spectral density
RAIN	Reduction of Airframe and Installation Noise
RANS	Reynolds Averaged Navier-Stokes
RMS	Root Mean Square
S-A	Spalart and Almaras
SPL	Sound Pressure Level
SQL	Structured Query Language
SST	Shear Stress Transport
TS	Turbulent separation
URANS	Unsteady Reynolds Averaged Navier-Stokes

Greek

α	Angle of incidence
β_{bz}	Bufferzone exponential damping coefficient
Δt	Physical time step
Δt^*	Non-dimensional time step
$\Delta x, \Delta y, \Delta z$	Cell dimensions in x, y, and z directions
Δ	Max cell dimension ($\max(\Delta x, \Delta y, \Delta z)$)
δ_f	Dirac delta function
δ_{ij}	Kronecker delta function
ϵ	Dissipation term in SA model
γ	Ratio of specific heats
Λ	Yaw angle
μ	Viscosity
μ_t	Turbulent viscosity
∇	Gradient operator
ν	Kinematic viscosity
ν_t	Eddy viscosity
Ω_s	Component dimension factor
ϕ	Polar angle
ρ	Density
$\rho^{'}$	Density perturbation
τ	Shear stress tensor
θ	Azimuth angle
θ_{sep}	Separation angle measured from front stagnation point
$\tilde{\nu}$	Modified turbulent eddy viscosity
ς	Damping coefficient
ξ, η, ζ	Generalised coordinate directions

Subscripts

$()_0$	Quantity at rest
$()_\infty$	Freestream quantity
$()_c$	Component value
$()_n$	Normal velocity
$()_z$	Computational quantity
$()_{\text{exp}}$	Experimental value
$()_{\max}$	Maximum value

$()_{\min}$	Minimum value
$()_{\text{ref}}$	Reference value
$()_{\text{s}}$	Strut parameter
$()_{\text{wall}}$	Wall quantity
$()_{\text{w}}$	Wheel parameter
$()_{bz}$	Bufferzone variable

Chapter 1

Introduction

1.1 Outline

In this introductory chapter the research background and motivation are outlined and the PhD objectives are stated. Finally an outline of the thesis structure is given.

1.2 Background and Motivation

The study of the noise radiated by civil aircraft landing gear has received a great deal of attention in recent years from researchers and engineers in the civil aerospace industry. This has been fuelled by plans to introduce more stringent legislation to monitor the noise levels produced by civil aircraft upon take-off and landing [1].

Although during the take-off phase the majority of noise produced by an aircraft is radiated by its engines, in the approach and landing phases airframe noise can dominate the total noise [5]. The landing gear has been identified as a major contributor to the overall airframe noise due to the highly separated and unsteady turbulent flow it induces [9, 30]. Therefore the attenuation of landing gear noise is extremely valuable in terms of reducing the overall aircraft landing noise.

In recent years the study of landing gear noise has become gradually more intense. Both full-scale and model landing gears have been tested in wind tunnel and fly-over environments [9, 14, 39, 59, 76]. This has led to the identification and ranking of landing gear noise sources. Although the basic noise mechanisms are understood well by classical theory [11, 49], work is required to investigate the impact of various geometrical parameters on the far-field noise characteristics. The basic noise is a result of the fluctuating forces and turbulent wakes produced by the unsteady flow around the various components. These components vary in size and shape from wheels to pipes leading to noise spanning

at least three decades in frequency. Therefore the landing gear generates noise that has broadband spectral characteristics [9, 14, 59, 76]. Due to the close proximity between components, the resulting flow field interaction can be extremely complex leading to complex noise mechanisms [14, 39, 48, 68].

Large civil aircraft may have several multiple-wheel landing gear bogies which are inherently noisy due to a design that is driven by structural considerations. In order that the next generation of low-noise gear can be developed, low-noise must become a design driver. Currently, the assessment of the noise characteristics of landing gear designs and low-noise treatments can only be achieved satisfactorily through experiments, which tend to be both expensive and time-consuming [9, 15, 16]. The development of reliable noise prediction tools is crucial to aid the design process of low-noise landing gears. With such tools design iterations of new landing gear and noise reduction treatments could be performed with noise control as a major driver.

A successful prediction tool must achieve high accuracy and must be convenient; however the complexity of the landing gear geometry hampers the ability to predict the noise. Therefore semi-empirical prediction methods have been adopted to date [25, 32, 71] to help simplify the problem. Semi-empirical prediction schemes avoid a detailed breakdown of both the landing gear geometry and the description of the noise characteristics. Therefore, their use as design tools is limited since the effect of many geometrical parameters cannot be predicted. Alternatively, in a physics-based approach governing laws are solved and each noise source is modelled explicitly with an increased amount of detail in the prediction. Such an approach could be extremely useful to aid the design process of new landing gear and is an extension of component noise modelling investigations.

1.3 Research Objectives

The primary objective of this Ph.D project was to develop a physics-based aeroacoustic model for the prediction of landing gear noise. The process involved investigating the noise generating mechanisms of basic landing gear components in various configurations. It was intended that the model could be used as an engineering tool to assess the noise produced by a landing gear or to assess the effectiveness of noise reduction treatments.

Due to the complex nature of the problem, the aim of this research was to provide a solid framework for a new model and demonstrate its capability to predict the noise radiated by a simple landing gear. A validation case was selected for this purpose [39], which consisted of noise measurements of a scale model two-wheel nose landing gear. Although lacking features of modern operational landing gear, the model consisted of simple struts in various configurations and was therefore deemed suitable to validate the current work.

1.4 Thesis Outline

The thesis is organised as follows: first an extensive literature review is provided in Chapter 2. This includes a review of relevant research up to the present time. The literature review is followed by a description of the new prediction approach in Chapter 3, and the computational methodology in Chapter 4. Next the component modelling results are presented in Chapters 5, 6 and 7. Chapter 8 then focuses on a high-order computation of tandem cylinder interaction. This is followed by validation of the new prediction model in Chapter 9. Finally, conclusions are drawn and suggested future work is outlined in Chapter 10.

Chapter 2

Literature Review

2.1 Overview

In this chapter a comprehensive review of literature relevant to the current research is presented. This incorporates a large range of subjects including bluff-body and landing gear aeroacoustic research. Various landing gear noise prediction methods are critically reviewed along with numerical methods and studies pertinent to the current research.

2.2 Introduction

Early airframe noise experiments were performed in the early 1970's [4,5,29,39] and these indicated that landing gear noise can be a significant contributor to the overall airframe noise. Landing gear noise research dates back to the early scale model experiments of Heller and Dobrzynski in 1977 [39]. Little research was performed during the 1980's until the 1990's, when airframe noise research was rejuvenated. Such research included full-scale testing of landing gears [14] which resulted in more reliable results compared to those obtained for low-fidelity scale models. In the early 21st century, computation began to play a large role in the prediction of aerodynamic noise. In this chapter, landing gear noise research along with other relevant research is summarised.

This chapter is organised as follows: First bluff-body noise studies are reviewed in Section 2.3 followed by experimental landing gear noise research in Section 2.4. Various landing gear noise prediction models are reviewed in Section 2.5.2. The second half of the chapter focuses on numerical studies starting with issues and methods in Section 2.6, followed by bluff-body and landing gear computational aeroacoustics in Sections 2.7 and 2.8.

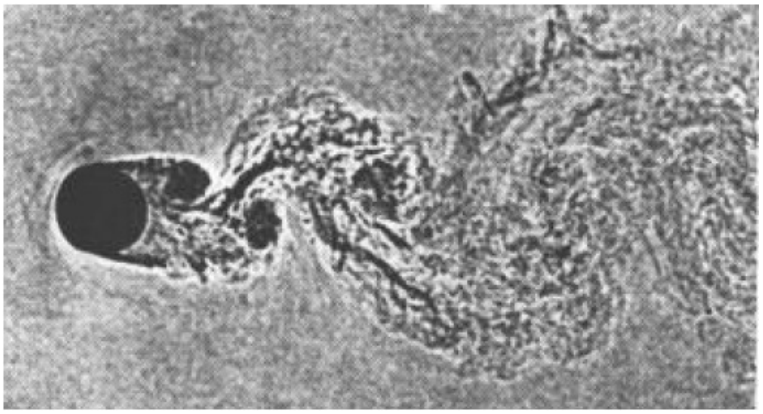

FIGURE 2.1: Shadowgraph visualisation of the turbulent wake and vortex structure of the flow around a circular cylinder, Van Dyke [19].

2.3 Bluff-Body Flows

A typical landing gear can be described as a collection of non-streamlined (bluff) bodies of different shape, size, and alignment. Therefore an understanding of bluff-body noise is extremely valuable to a fundamental investigation of landing gear noise sources. The flows around all bluff-bodies have similarities. Such flows are characterised by large regions of flow separation leading to high drag and significant flow unsteadiness. This unsteadiness is manifested as fluctuating pressure on the surface of the body and in the resulting wake. This unsteadiness is visualised in the shadowgraph obtained by Van Dyke [19] shown in Figure 2.1. Often the fluctuations may be periodic, leading to an Aeolian tone at the vortex shedding frequency [82].

Schewe [64] reviewed experiments carried out over a wide range of Reynolds numbers for various bluff-body sections. In all cases the force coefficients and Strouhal numbers were significantly affected by Reynolds number. Schewe also concluded that flows around 2-D bodies are highly three-dimensional beyond very low Reynolds numbers.

The nature of the separated flow region is largely dictated by the location of transition and boundary layer separation on the body surface. These factors are extremely sensitive to the body shape and size, orientation, Reynolds number, the viscosity of the fluid, and the freestream turbulence intensity. This makes bluff body aeroacoustics a particularly challenging subject.

2.3.1 Circular Cylinder Noise

Many landing gear struts and components such as the main leg, wheels, axles and piping, are circular in cross-section. The flow around a circular cylinder has been the topic of extensive research for a number of years. However, it remains perhaps the most

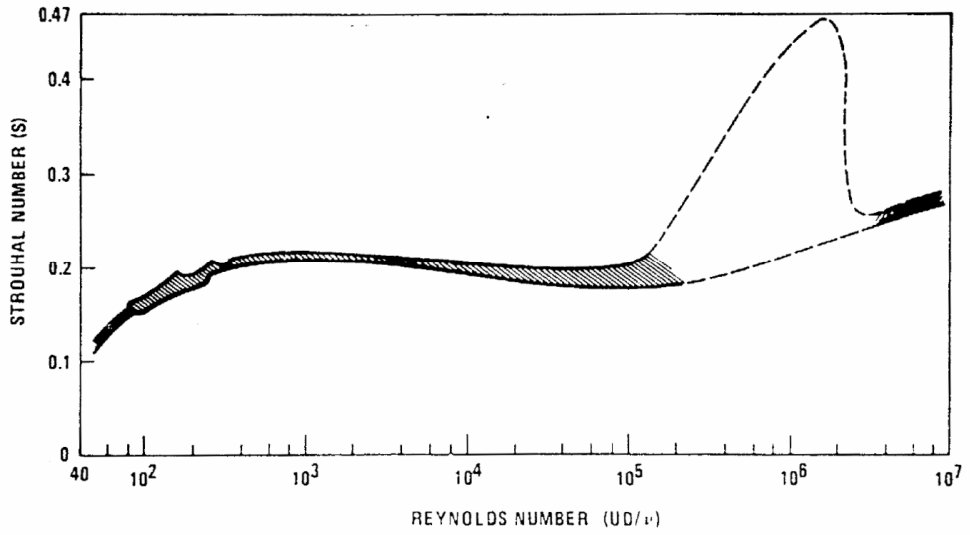

FIGURE 2.2: Relationship between Reynolds number and the Strouhal number of the circular cylinder vortex shedding frequency, Blevins [3].

challenging of bluff body cross sections to study due to the sensitivity of the flow field to relatively small changes to the incoming flow characteristics.

Amongst the most comprehensive collection of circular cylinder data is that published by Zdravkovich [82] who provided a summary of research. Zdravkovich defined a number of *flow regimes* delimited by the Reynolds number defined according to the location of transition. The transition from laminar to turbulent flow has four distinct phases, namely subcritical, critical, supercritical, and postcritical. In subcritical regimes, the boundary layer remains laminar resulting in laminar separation (LS). The regime is characterised by regular vortex shedding at a Strouhal number of around 0.2 for Reynolds numbers between 200 and 10^5. The Strouhal number is defined as:

$$St = \frac{fD}{U_\infty}, \tag{2.1}$$

where f is the shedding frequency, D is the cylinder diameter and U_∞ is the freestream velocity [82]. At Reynolds numbers beyond 10^5 up to 4 million, the boundary layer becomes turbulent before the separation point, leading to turbulent separation (TS) regimes, i.e. the critical, supercritical, and postcritcal regimes. These are challenging regimes to investigate both experimentally and numerically due to the sensitivity of the transition location. The boundary layer turbulence delays separation from about $\theta_{\text{sep}} = 90$ deg up to $\theta_{\text{sep}} = 115$ deg measured clockwise from the front stagnation point, and this marks the onset of the drag crisis. The drag crisis reflects the disparity between the LS and TS regimes where delayed separation leads to a narrowing of the wake and either a significant rise in the Strouhal number or a loss of periodic vortex shedding altogether [82]. Additionally, the magnitude of the oscillating lift and drag forces on

the cylinder are significantly reduced. In terms of sound generation, the tone generated by periodic shedding may be lost and replaced by a broadened spectrum with a weaker spectral peak. Due to the sensitivity of the transition mechanism to variations in the freestream turbulence level or surface roughness, experiments performed at this range of Reynolds number show wide variability [65]. Figure 2.2 illustrates the relationship between Re and St and the variability that arises beyond $Re = 10^5$ [3].

The postcritical regime, which occurs above a Reynolds number of roughly 4 million, is characterised by fully turbulent boundary layers. Periodic vortex shedding is re-established at higher Strouhal numbers between $St = 0.26$ and $St = 0.3$ accompanied by an increase in the RMS force coefficients [82]. In this regime, the strong relationship between Re and St, amoung other parameters, is re-established.

The Reynolds number range at which each change in flow regime occurs is extremely sensitive to disturbances such as freestream turbulence, surface roughness, oscillation, and free ends [82]. The Re ranges specified by Zdravkovich are based upon ideal flow conditions. Therefore, if the flow is disturbed in some way, then characteristics of higher Reynolds number regimes may be experienced at a much lower Re. If the boundary is "tripped", for example, then higher Re regimes may be simulated at a much lower Reynolds number. A number of these disturbances and geometrical features apply to landing gear components, forcing boundary layer turbulence. Therefore the supercritical and postcritical regimes are of more interest to the understanding of landing gear component flows.

It is well-known that the basic characteristic of cylinder noise is an Aeolian tone corresponding to the Strouhal number of the shedding frequency and a dipole directivity field. Stowell and Deming [77] were the first to measure the directivity of the noise radiated by circular rods and demonstrated that the sound field has a dipole character with peaks normal to the freestream flow direction and cylinder axis. Curle [11] found that whenever there is a fluctuating force between a fluid and a solid boundary, a dipole radiation field may result. Curle's dimensional analysis also showed that theoretically the sound intensity scales with the sixth-power of the velocity. This was confirmed experimentally by Schlinker *et al.* [65] in their experiments of vortex noise from cylinders in subcritical regimes. Schlinker *et al.* also took measurements at higher Reynolds numbers and found that when the shedding mechanism broke down in the critical regime the resulting spectrum became more broadband. The characteristics of the Aeolian tone produced by a circular cylinder in a high Reynolds number flow were investigated experimentally by Fujita and Suzuki [28] at $Re = 2.5 \times 10^5 - 2 \times 10^6$. They found that the Strouhal number of the Aeolian tone jumped from 0.2 to 0.45 between $Re = 3 \times 10^5 - 7.5 \times 10^5$, then returned to 0.2 at higher Re. The peak sound pressure level (SPL) appeared to reduce beyond $Re = 3 \times 10^5$ up to $Re = 4 \times 10^5$ before it once again increased with the mean velocity.

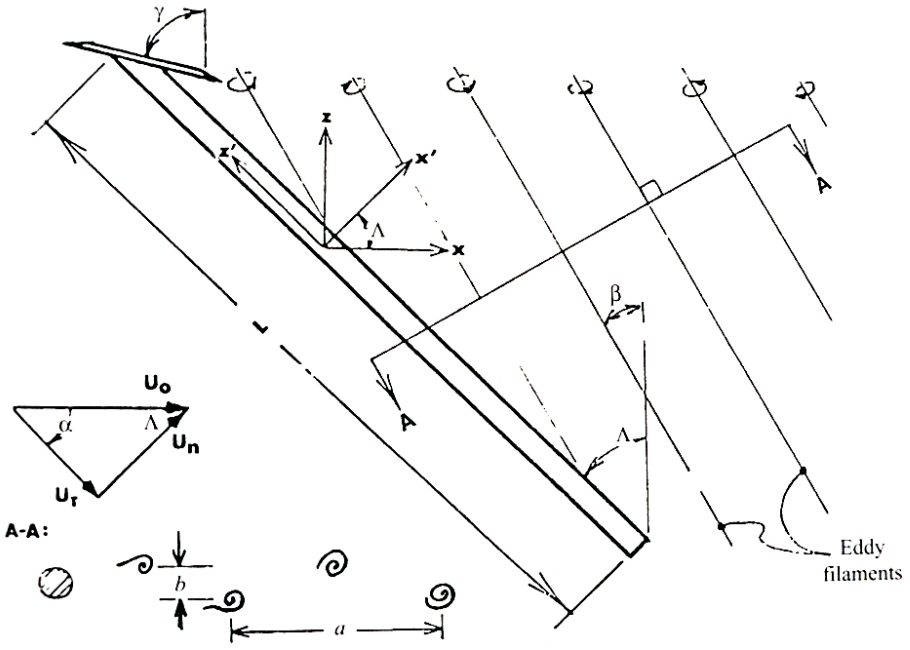

FIGURE 2.3: Definition of yawed cylinder geometry and nomenclature, Ramberg [58].

Florence and Brooks [42] performed acoustic measurements on single rods to study the effect of Reynolds number, surface roughness, and freestream turbulence on the radiated noise. The Reynolds number of the experiments ranged between $Re = 3.8 \times 10^3$ and $Re = 10^5$. Directivity measurements for the high freestream turbulence level, $6.5\% \leq Ti \leq 8.5\%$, cases were found to be in good agreement with the dipole assumption. High freestream turbulence was shown to broaden the spectral shape and reduce the peak SPL.

The nature of the wake and shedding clearly has a strong impact on the acoustic far-field and the correct prediction of the near-field flow is crucial to capture the correct far-field acoustic characteristics. It is possible that circular cylinders could be used to model landing gear struts, but care must be taken to ensure the correct conditions are modelled to represent realistic flow fields.

2.3.2 Cylinders in Yaw

The yaw angle, Λ, is defined as the angle between the cylinder axis and the normal to the freestream velocity as sketched in Figure 2.3. In this respect most landing gear struts are yawed to the incoming flow as their orientation is driven by structural and mechanical considerations. The yaw angle has the following relationship with the angle of incidence, α [83]:

$$\Lambda + \alpha = 90 \text{ deg.} \tag{2.2}$$

When a circular cylinder is yawed, its cross-section becomes elliptical in the $x = 0$ plane and the freestream velocity has two components: one normal, V_n, and one parallel to the cylinder axis, V_t. Figure 2.3 defines the yawed cylinder geometry and associated nomenclature. As well as a reduced normal velocity, the effectively less bluff cross-section in the direction of the freestream vector impacts the nature of the resulting wake and vortex shedding [83].

Experiments have shown that yawed cylinder flows are heavily influenced by the cylinder ends and by the cylinder aspect ratio [83]. These parameters disrupt the spanwise flow near the extrema of the cylinder span, and experiments have also shown that the vortex structures in the near wake of a cylinder in yaw initially align parallel to the cylinder axis when observed far from the cylinder ends. Measurements have suggested that the forces acting on the cylinder surface and the vortex shedding frequency are approximately the same as for a cylinder in cross-flow if only the normal component of the freestream velocity is used. This became known as the "Independence Principle" [83]. However, early attempts to model the effect of yaw by replacing the freestream velocity by the normal velocity V_n were only partially successful as the theory tended to break down for large yaw angles and near the cylinder ends [83].

There is very limited published work on the aerodynamic noise generated by yawed cylinders. Choi and Hong [8] performed an experimental study of yawed cylinders and found that, as the yaw angle increased and V_n decreased, the unsteady lift fluctuation along the cylinder span reduced, leading to a lower sound pressure level. Haramoto *et al.* [33] performed experiments at Reynolds numbers of 1×10^4 and 2×10^4 with the aim of investigating the effect of yaw angles ranging from $\Lambda = 0$ to $\Lambda = 50$ deg on the far-field noise. They found that the peak SPL reduced with increasing yaw. The shedding frequency also reduced with increasing yaw angle at the rate predicted using the Independence Principle. There is however a lack of research that has focused on the effect of yaw angle on the radiated noise at higher Reynolds numbers. Therefore further investigation is required to determine if the same trends apply to turbulent separation cases that could be used to model landing gear struts.

2.3.3 Cylinders in Tandem

Interaction mechanisms are a major complication to the understanding of landing gear component noise. The close proximity between components results in interacting flow fields and also acoustic shielding and scattering effects. For instance, wheel gap noise has been identified as an important noise source [47], and interaction mechanisms between struts have also been frequently identified [14,39,47]. The tandem cylinder arrangement is representative of several component interactions on a real landing gear and is perhaps the most fundamental geometry that can be used to model and understand the physical mechanisms involved in component interaction noise.

S/D	**Regime Notes**
$1.0 - 1.3$	Non-reattachment of free shear layers separated from upstream cylinder on downstream cylinder. Vortex street behind downstream cylinder is formed by the free shear layers from upstream cylinder.
$1.1 - 3.3$	Free shear layers from upstream cylinder may reattach alternatively, permanently or intermittently onto the downstream cylinder. No shedding in gap region.
$3.0 - 4.0$	Intermittent shedding behind upstream cylinder.
$3.8 - 6.0$	Pairing of eddies from the upstream and downstream cylinders. Synchronisation of the two vortex streets in phase and frequency.
> 5.0	Uncoupled vortex shedding behind both cylinders.

TABLE 2.1: Summary of tandem cylinder regimes.

Zdravkovich's review on cylinders also included cylinders arranged in tandem. He divided the tandem cylinder configuration into approximate regimes categorised by the separation distance S/D [83], where S is the separation between cylinder centres, and D is the cylinder diameter. The regimes are summarised in Table 2.1. Each regime specifies the nature of the wake behind each cylinder and the way in which they interact. At the smallest separation distances, the free shear layers which separate from the upstream cylinder do not reattach onto the downstream cylinder, but rather enclose it. As S/D is increased, the flow becomes unpredictable as the wake-body-wake interactions intensify and the cylinders tend to have different shedding frequencies. At very large separation distances, the flow around the upstream cylinder closely resembles that of a single cylinder. There is an overlap in the specified S/D ranges due to Reynolds number effects, indicating that the location of transition also plays an equally important role in tandem cylinder flows.

Lin *et al.* [50] performed experiments using PIV techniques in an attempt to characterise the flow features of two cylinders in tandem by controlling the separation distance. The value of Re based on the cylinder diameter was 1×10^5. They found that in the gap region between the cylinders, small-scale concentrations of vorticity formed in the separated shear layers which buffeted the surface of the downstream cylinder. This influenced the eventual shedding of large-scale vortices. The flow structure aft of the downstream cylinder was seen to be substantially altered relative to the single cylinder case. A critical separation distance was observed where no vortices were formed in the gap region, and this distance was shown to be a function of the Reynolds number.

Experiments were performed by Jenkins *et al.* [43] to characterise the unsteady flow structures around tandem cylinders with a separation of $S/D = 1.435$ and $S/D = 3.7$ at $Re = 1.66 \times 10^5$. The boundary layer on the upstream cylinder was tripped to simulate

a higher Reynolds number flow regime. It was observed in the $S/D = 1.435$ case the cylinders together behaved much like a single bluff body, since no vortices were shed from the upstream cylinder and the shear layer enclosed the gap region. In the $S/D = 3.7$ configuration, vortices were shed from the upstream cylinder in the gap region. These vortices were shown to interact with the front surface of the downstream cylinder, leading to higher pressure fluctuations on its surface. The span-wise correlation lengths in the wake region of the tandem configurations were measured to be less than that of a single cylinder at the same Reynolds number.

The noise generated by tandem cylinders was also investigated experimentally by Hutcheson and Brooks [42]. Several configurations were investigated such as in line cylinders with equal and non-equal diameters at a range of separation distances. For equal diameter cylinders, shifts in the Strouhal number and peak SPL were observed relative to a single cylinder at separation distances between $S/D = 1$ and $S/D = 4.5$. At $S/D = 1$, the spectra displayed a large tone at a frequency much higher than that of a single cylinder, and at $S/D = 2$ and $S/D = 3$ the tone was lower in frequency than that of a single cylinder. Finally, for $S/D = 4.5$ a large tone was produced at a frequency similar to that of a single cylinder. Another important result was that the variation of St with Re was approximately constant, indicating that Reynolds effects were negligible for this configuration.

2.4 Experimental Landing Gear Noise Studies

2.4.1 Airframe Noise Studies

Blumenthal *et al.* [5] of Boeing reviewed aircraft environmental problems in the early 1970's, of which the main focus was engine noise. However, due to the introduction of quieter engines they noted "a new consideration or problem appears to be emerging for future aircraft designers". This was airframe noise. The Boeing Company conducted early tests of airframe noise on Boeing 727 and 747 aircraft and it was demonstrated that the aircraft noise levels asymptotically approached a limit as engine noise was reduced. The asymptote itself represented non-engine noise, or airframe noise. It was demonstrated that the flaps and landing gear could contribute as much as 10-12 dB to the effective perceived noise level (EPNL) of the aircraft on approach.

Gibson investigated non-engine aerodynamic noise of a large aircraft [29]. It was found that both the landing gear and the flaps generated significant low-frequency noise. The effect of the landing gear and wheel wells were shown to be significant and responsible for the largest noise increase between the "clean" and "dirty" configurations. The total effect of the dirty configuration was an increase of roughly 4 dB to the overall sound pressure level (OASPL) at an altitude of 27.7m and a velocity of 102.5m/s. Grosche

et al. [30] conducted wind tunnel tests of a 1/10th scale Airbus A340 to identify noise sources using a highly directional microphone array. Again the landing gear along with the slats and flaps in their extended position were identified as the major noise sources.

Chow *et al.* [9] presented a summary of the comprehensive airframe noise work conducted for the RAIN project. Landing gear and high lift devices were identified as the dominant airframe noise sources. Their studies showed that landing gear noise dominated high-lift device noise for larger, wide-body aircraft, whereas for medium size aircraft the noise from the high lift devices dominated. Noise interaction effects between the flaps and the landing gear were also identified.

The identification of landing gear noise as an important noise source led to research efforts to investigate landing gear component noise in more detail.

2.4.2 Landing Gear Component Noise Studies

Heller and Dobryznski [39] performed early landing gear experiments in the 1970's to determine the noise radiation from landing-gear/wheel-well configurations of large commercial aircraft. The wheels and doors were found to contribute very little to the overall noise, with the dominant sources being the smaller features such as the struts and braces. In the case of the four-wheel gear, the interaction between the wake produced by the forward set of wheels and the rearward set of wheels was also identified as a dominant noise source. The characteristic discrete tones produced by the empty wheel-well were found to be severely damped out when the landing gear was installed. Such interaction between components was shown to be significant, suggesting that noise sources do not act independently. The data was used to acceptably predict the noise spectrum of full scale landing gear from two aircraft, but for a third aircraft the spectrum was severely over-predicted. The experimenters comment that this was due to the lack of fine detail in the scale models that probably constituted rather important sound sources in the medium to high frequency range.

Such scaling of models was identified as a fundamental problem in other studies. Tests conducted on a 4.7% scale DC-10 model by Hayes *et al.* [37] showed that as a result of the severe scaling and lack of model detail the landing gear was found to make little contribution to the overall broadband spectrum, contradicting full-scale test data. Stoker [76] compared the aeroacoustic measurements of a Boeing 777 in flight against results from previous scale model tests. Analysis of phased array data revealed that the apparent major noise sources were dependent on the scale of the model. There is clearly some doubt toward the dependability of scale model tests.

Ravetta *et al.* [59] tested a high fidelity model of a 26% scale Boeing 777 main landing gear. A phased array was used to identify and rank the noise sources. It was found that the back brace, rear truck, rear rock-guard sub-assemblies, torque link, front cable

harness, and wheel hubs were the main contributors to the low frequency noise. At medium frequencies, the major noise sources were found to be the strut-wind tunnel interface, the brakes and axles, and the hydraulic cylinder. While at high frequencies, the strongest sources were the brakes and axles, the rear lock link, and the main strut cables sub-assembly. The high level of detail in the model enabled a far more thorough analysis of the noise sources compared to the early scale model tests.

The first tests on a full-scale landing gear were performed by Dobryznski *et al.* [14] in the German-Dutch Wind Tunnel. Various configurations were tested to identify the noise contribution of various components to the overall spectrum. An operational, fully dressed gear was progressively covered with fairings to achieve low noise configurations. It was noted that the local flow velocities at the position of the landing gear may be less than the flight speed. Previous studies had revealed that for the not dissimilar A319 aircraft at a typical angle of attack of $\alpha = 5$ deg the local Mach number was only 78% of the flight speed. Subsequently, it was emphasised that for the purpose of comparing with flyover data, or developing a noise prediction scheme, the true relation between flight speed and local airspeed should be understood.

The aerodynamic noise signature of the landing gear was found to be broadband in nature with constant levels up to several kHz, and not predominantly low frequency as earlier studies lead to believe [29]. The sound energy was shown to increase with the sixth-power of the flow velocity, except for the noise radiated into the forward arc, which was more related to the seventh-power of the flow velocity. It was shown that the polar radiation directivity was almost omni-directional at low Strouhal numbers, but had weak maxima in the forward and rearward arc at higher Strouhal numbers. It was thought that noise was also produced by the interaction of turbulent wake flows with the downstream gear components. This was supported by the increased omni-directivity at intermediate Strouhal numbers of the low noise configuration compared to the operational configuration.

The sound distribution of a four-wheel bogie with brakes exposed showed that noise from tyre-wake-tyre interaction effects, although present, were much lower than the noise radiating from other local noise sources. However, the tyre-wake-tyre interaction effects were shown to be enhanced when the brake fairings were applied, which is likely to be a result of the increased local flow velocity due to the volume displacement of the fairing.

The EPNL of the landing gear was calculated so that operational and low noise configurations could be compared. The results showed that, for a twin-wheel gear potential noise reduction was in the region of 8 EPNL dB, and 3 EPNL dB for the four-wheel bogie. This difference was partly attributed to be due to the tyre-wake-tyre interaction effects of four-wheeled bogies, which if eliminated could lead to a further 3 EPNL dB reduction.

More recently, Airbus performed tests on a full scale A340 nose and main gear, including a 6-wheel mock-up configuration [15]. Some basic noise reduction concepts were tested and their effectiveness identified. The tests revealed that the flow excited cavity resonances in tube-type pins in various joints linking the gear components, particularly in the cavity of the pin linking the brakes and the brake rods. The tones were more pronounced at low flow velocities and were nearly undetectable at 78 m/s and highly dependent on the inflow velocity, turbulence level and direction of the inflow. The directivity of all gears was practically omni-directional for the range of Strouhal numbers with only very weak maxima in the forward and rearward arcs, consistently with the previous tests [14].

To accompany the full scale A340 and A320 landing gear wind tunnel tests, full flight tests of an A340 were completed [9, 16]. It was found that, for this aircraft, the landing gear noise dominated the noise produced by the high-lift devices and that the landing gear noise radiated predominantly in the forward and rearward arcs. The broadband noise signature of the landing gear was shown to increase with the sixth-power of velocity, indicating a predominant dipole-type source.

Lazos [47] conducted particle image velocimetry (PIV) experiments on a four-wheeled Boeing 757 model to examine the mean flow features with emphasis in the gap between the forward and aft wheels. The PIV results highlighted a vortex that persisted in the gap which was thought to cause noise by scrubbing turbulent eddies against the wheel surface. Another type of landing gear interaction noise was investigated by Dobrzynski *et al.* [17] who studied the effect of the arrangement between the main landing gear and the centre landing gear of larger wide-body aircraft, such as the Airbus A340. In contrast to what was expected, the interaction between the turbulent wake from the upstream centre landing gear and the main landing gear did not cause excessive interaction noise, independent of the gear arrangement. This was likely due to the large and off-centre separation of the gear which is likely to have minimised any wake-gear interaction.

This section has reviewed important landing gear experimental research, and local landing gear noise sources have been identified that would need to be considered in a prediction approach. There have been several attempts to predict landing gear noise using semi-empirical and statistical-based approaches. These are reviewed in the next section.

2.5 Landing Gear Noise Prediction

2.5.1 Airframe Noise Prediction

Possible methods for the prediction of airframe noise were considered in the early 1970's [35,60]. Hardin *et al.* [35] discussed two possible approaches for the prediction of airframe noise. The first was to consider the aircraft as a whole, employing empirical relations

derived from experimental data for prediction. The second method was to consider the components of the aircraft separately to obtain an understanding of their individual noise generation characteristics, then to sum their contributions. These methods were also discussed by Revell [60].

Fink published work outlining a noise component method for airframe noise [25, 26]. Fink used scaling laws to predict the component noise of the clean wing, horizontal tail, vertical tail, landing gear, leading edge slats and flaps, and trailing edge flaps. Fink's assumption was that these components do not interact, but that the sum of the individual components defined the total airframe noise. For the landing gear component, Fink's model consisted of simply fitting empirical equations to the previous two-wheel and four-wheel data of Heller and Dobrzynski [39]. Fink's model was frequently used to compare predictions with flight test data and consistently led to poor noise predictions, particularly in directivity [31, 66]. Fink's model was later modified by ESDU [41] who made changes to the directivity and spectral functions based on more recent data.

Fink also studied noise interaction effects between the major components for a landing configured aircraft [27]. The study revealed that such effects were small and within the accuracy of the noise prediction of the separate components. However, some interactions significantly redistributed the local noise source strengths by changing the flow velocities and turbulence levels. It was shown that in some cases interaction effects were favourable, leading to a reduction in the noise source strength.

Hardin [34] outlined methods for the prediction of airframe noise and argued that, for an aircraft in its approach regime, one must consider the components as a system and not in isolation. Block also showed that there are significant interaction effects between the landing gear and the trailing edge flaps [4]. Hardin suggested that the development of airframe noise prediction schemes should be approached by considering a landing configured aircraft in its entirety. In the case of the landing gear noise prediction, for example, the local flow velocities, and not the freestream velocity should be considered. The local velocities will differ from the freestream velocity due to the installation effect of the wing and flow deflection from the fuselage.

It is clear that interaction effects between the various airframe components are important. Such effects will determine the oncoming flow parameters to the landing gear, such as the velocity profile and the turbulence level. For the landing gear, interactions between the individual components can be extremely influential on the radiated noise and these must be considered in a successful prediction scheme.

2.5.2 Landing Gear Component Noise Prediction

The comprehensive array of landing gear noise test data obtained for Airbus aircraft [14] was used by Smith and Chow [71] to develop a landing gear noise prediction model. It

was thought that landing gear noise mechanisms were too complex to be handled by the then state of computational power, so that the most practical way to predict landing gear noise was to develop a semi-empirical prediction scheme.

The basis of the model was to use a number of empirical constants to fit standard source characteristics to particular components. Using the numerous landing gear configurations studied by Heller and Dobrzynski [39], it was possible to identify the contributions of four fundamental sources corresponding to the fairings and struts, wheels, dressings, and the tyre-wake interaction. Scaling laws were adopted to normalise the noise data so that it could be used for noise source modelling.

The scaling laws for each component group were based upon the basic scaling law for the acoustic intensity of acoustically compact sources derived by Curle [11]. This scaling law was used as a basis to derive expressions for the mean square far-field pressure consisting of a non-dimensional and empirical spectrum function, and a directivity function. The characteristic shape of each spectrum produced by the component groups was a simple "haystack", with a peak centred at the expected vortex shedding frequency of the component. The breadth of the haystack was one of the parameters fitted in the model. However, the spectrum is not a function of the observer angle and the model does not account for whether the component is in clean or turbulent flow, its cross-section, or flow inclination. Assumptions were made so that the wind tunnel data could be used to model real flight conditions. The prediction method was used to predict flyover data reasonably well with the exception of a discrepancy in directivity that was shown between the wind tunnel and the flyover data.

The initial model was later improved and validation results were published [72]. The model was used to predict the noise of various low-noise configurations of a full scale A340 model and results were compared against wind tunnel data [15]. The model predicted the low noise configuration of the A340 nose gear to yield a reduction of -3.1 dB(A) compared to the measured value of -2.4 dB(A). The model also showed reasonable agreement when used to predict the noise reduction of intermediate builds. Some adjustments were made to account for the effects the add-on fairings made to the flow field, such as increased local velocities. Similar results were found for the main four-wheel landing gear.

Boeing presented work on landing gear noise research based on scaled and full-scale landing gear models [32, 66]. Guo and Yamamoto [32] developed an empirical landing gear prediction model based upon systematic testing and data analysis of full scale Boeing 737 landing gear. The analysis resulted in grouping the landing gear components according to the characteristics of their noise using data of progressively dressed landing gears in a similar fashion to Smith and Chow [71]. The component groups were identified as the wheels, the main struts, and the small details; each contributing to different parts of the frequency domain.

The analysis indicated that low and medium frequency noise scaled with the sixth-power of the Mach number, but that high frequency noise scale with the seventh power. The latter result was thought to be typical of noise generated by turbulent flows, and not by unsteady forces on the surfaces of the components. This was explained by the fact that high frequency noise sources are not generally compact. Analysis of phased microphone array data supported this result, since high frequency noise sources were shown to be associated with the wake where there are no gear components.

For each of the frequency domains, empirical formulae were derived for the sound pressure as a function of the flow conditions, gear geometry, and microphone locations. For the low and medium frequencies, parameters such as the number of struts and wheels were variables in the formulae. Due to the arbitrary nature of the small details, a complexity factor was introduced to represent the aggregate effect of all the small features. This complexity factor was related to gross aircraft parameters such as maximum take-off weight, as it was assumed that larger aircraft have more complex landing gears. Comparison against Fink's model [25] revealed that the models agreed fairly well at low frequencies, but Fink's model showed a faster roll-off at higher frequencies leading to a significant noise under-prediction.

Details of another empirical model were published in the form of an updated sub-component airframe noise prediction method [66]. The major part of this work was an empirical landing gear noise prediction scheme based upon experiments of full-scale Boeing 737 landing gears [66] in the Boeing Low Speed Aeroacoustic Facility (BLSAF).

Analysis of free-field microphone and phased array data showed that the gear noise could be separated into four major noise components, namely the low frequency, medium frequency, high frequency, and tyre noise components. Local flow velocities under the wing were obtained using panel code applied to a B737-400 in approach configuration, and the local flow Mach number in this study was assumed to be 83% of freestream velocity.

The prediction scheme was compared with selected runs of B737 data. The comparisons showed strong agreement between prediction and measured data at high frequencies, but some disagreement at the mid and low frequencies. The discrepancy was assumed to be caused by a poor collapse of spectra for the tyre and mid frequency components. Comparisons made with Fink's code [25] indicated that Fink's model tended to predict a faster roll-off at high frequencies, leading to under-prediction. The lack of full-scale noise data meant that these empirical noise models developed by Boeing could not be tested satisfactorily.

The experimental studies performed by Dobrzynski *et al.* [15], showed that a reliable landing gear noise prediction scheme should account for the contribution of individual components. The empirical models reviewed here all involve a rather coarse component breakdown and many assumptions in an attempt to simplify the complex geometry. Due

to the empirical nature of these models, a detailed physical understanding of the noise source mechanisms cannot be obtained and their use is somewhat limited to geometrically similar landing gears. The limitations of these highly empirical models could be overcome by introducing an increased level of physics into the prediction and incorporate an improved level of detail in the modelling and description of the noise source characteristics.

Guo [31] developed an outline for a statistical model of landing gear noise prediction. The basis of the model was a decomposition of the landing gear into three spectral components, in a similar fashion to the empirical models [32,66]. Guo derived asymptotic results for each of the frequency domains, leading to explicit analytical equations for the far-field noise.

The very low frequency noise was thought to be associated with the very large components and therefore it was suggested a numerical simulation of a simplified gear could be a feasible means of prediction. For low frequencies, it was proposed that the noise could be calculated by integrating the pressures on the component surfaces, and it was suggested that numerical simulations were again feasible, but this time on a component basis. High frequency noise was assumed to be generated by components with small length scales. Due to the rapid phase variations of the sources, it was suggested that they tend to cancel each other out so that only sources with a phase variation of zero contribute to the far-field noise. Therefore, it was thought that surface pressures are needed at only a few locations on the gear, which could be derived empirically or numerically.

This decomposition resulted in simple analytical expressions that are trivial to solve. However, these expressions require statistical data of the surface pressure fluctuations, which are difficult to obtain. However, the model outlined a sensible step forward by incorporating more flow physics into landing gear noise predictions.

Lopes *et al.* [56] presented progress on the development of a landing gear prediction model using an acoustic "toolkit". Ambitious plans were outlined to develop a model that could predict the noise generated by complex landing gears by dividing the gear into a number of elements or objects, each of which is described by a simple acoustic model. Each acoustic element in the toolbox has three attributes; an upstream environment, a downstream environment, and the element geometry. The upstream and downstream environments included local flow velocity, incoming turbulence level, and incident acoustic field, which accounts for shielding and scattering/diffraction effects. In this way components are allowed to interact.

However, in the published work it was assumed that all components of the landing gear could be represented by a very simple empirical spectrum. Additionally, and interaction effects were ignored and turbulence levels and local velocities were not specified. The wheels were represented rather crudely by a cylindrical ring broken up into a number of

circular cylinder segments. Some initial predictions were made, but due to the state of the model, these showed a large deficiency and only served the purpose of identifying the shortcomings of the model. However, the model methodology is a sensible suggestion towards an improved modelling approach.

There appears to be a need for a new generation of landing gear noise prediction models that incorporates more physics in to the noise prediction, negating the need to rely upon empirical constants. This will help to increase the fidelity of predictions so that the prediction model can be used as a design tool. Current semi-empirical models rely upon calibration of experimental results and are likely not to be applicable to new landing gear designs and configurations. There also appears to be a lack of detail in predictions and an often poor breakdown of noise sources.

2.6 Numerical Aeroacoustics

2.6.1 Issues and Methods

The aim of computational aeroacoustics (CAA) is to predict aerodynamically generated noise and its propagation and characteristics using numerical methods. The governing equations, to be solved numerically, are the Navier-Stokes equations. These are derived from the equations of conservation of mass, momentum, and energy.

Computational fluid dynamics (CFD) has been successfully applied to many aeronautical applications in recent years. However, an aeroacoustic problem is not easily solved directly using existing CFD codes to solve the unsteady Navier-Stokes equations from the noise source up to a far-field observer location, due to the limits in computational power.

Tam [78] stated that "one must recognise that the nature, characteristics, and objectives of aeroacoustics problems are distinctly different from those commonly encountered in aerodynamics". Aeroacoustic problems by definition are dependent on time, whereas many aerodynamic problems are time-independent, and this introduces the first major difference between the two disciplines of CFD and CAA. Combined with the fact that high frequency noise associated with short wavelengths and length scales is of importance to aircraft noise, the discipline of aeroacoustics introduces unique computational issues.

The noise from landing gear is broadband across a large frequency range. High-frequency noise is generally caused by small details on the landing gear and is non-trivial. Tam [78] suggested that typically a minimum of six to eight grid points per wavelength is required for proper resolution. Therefore, the spatial resolution of the grid is determined by the smallest wavelength or highest frequency to be resolved. This leads to a large number of grid points to obtain correctly resolved waves.

The large disparity between the freestream flow velocity and the RMS velocity fluctuation presents a big challenge to direct numerical simulation. Numerical procedures are required to have a very high accuracy to limit numerical noise. Roe [62] stated that "there is a fear among investigators that the acoustic solutions may be hopelessly corrupted by computational noise".

Tam also recognised the disparity between length scales as a problem [78]. This makes the spatial resolution of a direct numerical simulation (DNS) very important. Excessive CPU time is a result of the computational time step dictated by the finest mesh. In aerodynamic problems, it is the near-field around the body of interest that is important. In aeroacoustic problems, it is the directivity and spectrum of the radiated sound at the far-field that is important. Therefore the spatial resolutions requirements are very high throughout the domain. The distance to the far-field is normally very long and this requires the numerical scheme to be free of excessive numerical dispersion, dissipation, and anisotropy. This becomes very difficult to achieve when the number of mesh points per wavelength is severely limited by the available computational power. Alternative approaches are required to make numerical aeroacoustics more feasible.

2.6.2 Acoustic Analogies

Acoustic analogies essentially decouple the propagation of sound waves from their generation. This is because of the fundamental assumption of a one-way coupling between flow and sound, that is that the sound is generated by flow inhomogeneities but the flow itself is not influenced by the acoustic field. Methods based on the acoustic analogy pioneered by Lighthill [49] and extended by others [11, 24] require only near-field flow information, providing a cost-effective alternative to solving the acoustic waves up to the far-field. Details of the near-field flow can be obtained computationally using traditional CFD techniques and this information can then be used to carry out acoustic analysis to predict the propagation of sound.

In 1952, Lighthill [49] published a pioneering paper establishing the theory of sound generated aerodynamically. Lighthill's theory was based upon the rearrangement of the Navier-Stokes equations showing how the source of aerodynamic noise could be obtained from exact time-accurate calculations or experiment. The result was a wave equation including a source term. Lighthill's inhomogeneous wave equation is:

$$\left[\frac{\partial^2}{\partial t^2} - c_0^2 \nabla^2\right] \rho' = \frac{\partial^2 T_{ij}}{\partial x_i \partial x_j}. \tag{2.3}$$

The left-hand side of Equation 2.3 is the linear wave equation and the right-hand side represents a quadrupole distribution. T_{ij} is the Lighthill stress tensor

$$T_{ij} = \rho u_i u_j + P_{ij} - c_0^2 \rho' \delta_{ij}, \tag{2.4}$$

where P_{ij} is the compressive stress tensor

$$P_{ij} = p\delta_{ij} - \mu \left\{ \frac{\partial u_i}{\partial x_j} + \frac{\partial u_j}{\partial x_i} - \frac{2}{3} \left(\frac{\partial u_k}{\partial x_k} \right) \delta_{ij} \right\}. \tag{2.5}$$

Lighthill's general theory was later extended by Curle in 1955 [11] to incorporate the influence of solid boundaries upon the sound field. The results indicated that in addition to reflecting and diffracting any sound which may already be present, the solid boundaries introduce a resultant dipole field across their surface. The far-field sound pressure generated by this additional mechanism is related to the fluctuating force acting on the surface and its intensity depends upon a characteristic velocity over the surface to approximately the sixth-power. The Lighthill-Curle inhomogeneous wave equation is

$$\left[\frac{\partial^2}{\partial t^2} - c_0^2 \nabla^2 \right] \rho' = \frac{\partial^2 T_{ij}}{\partial x_i \partial x_j} - \frac{\partial}{\partial x_i} \left[P_{ij} \delta(f) \frac{\partial f}{\partial x_i} \right]. \tag{2.6}$$

where f is the geometric function of the closed-surface solid boundary.

The work of both Lighthill and Curle was extended in 1969 by Ffowcs Williams and Hawkings (FW-H) [24] to include arbitrary convective motion of the source. The FW-H formulation embodies the most general form of the acoustic analogy, and is an exact rearrangement of the Navier-Stokes equations that yields the acoustic signal at a far-field observer location if the details of the source in the near field are known. It allows to take not only impermeable walls, but also permeable interior surfaces as integration surfaces, even if the surface lies in the non-linear region - unlike the Kirchhoff method [57]. It is not only restricted to stationary surfaces, but is also applicable to moving surfaces as well. The FW-H formulation has also been found to be both analytically and numerically superior to Kirchhoff's integral formulation [6] over a range of applications. The FW-H equation can be written in differential form as:

$$\begin{aligned} \left(\frac{\partial^2}{\partial t^2} - c_0^2 \frac{\partial^2}{\partial x_i \partial x_j} \right) \left(H(f_s)\rho' \right) &= \frac{\partial^2}{\partial x_i \partial x_j} \left(T_{ij} H(f_s) \right) \\ &- \frac{\partial}{\partial x_i} \left(F_i \delta(f_s) \right) + \frac{\partial}{\partial t} \left(Q \delta(f_s) \right), \end{aligned} \tag{2.7}$$

where

$$F_i = \left(P_{ij} + \rho u_i \left(u_j - v_j \right) \right) \frac{\partial f_s}{\partial x_j},$$
$$Q = \left(\rho_0 v_i + \rho \left(u_i - v_i \right) \right) \frac{\partial f_s}{\partial x_i}.$$

The contribution of the Lighthill stress tensor, T_{ij}, to the right-hand side of equation 2.7 is known as the quadrupole term. This is followed by the dipole term F_i, involving an unsteady force, and Q represents a monopole-type term. The function f_s defines the integration surface moving at speed v_j and is a function of time so that it always surrounds a moving source region of interest. The FW-H equation is typically solved using a Green function technique. Lockard [51] provided a comparison between FW-H solvers for airframe noise applications.

The quadrupole term is often dropped from the FW-H equation since for low Mach number flows the contribution to the sound field from the dipoles should be greater than that for the quadruples for which, $I \propto [Mc]^5$, whereas for the surface dipoles $I \propto [Mc]^3$. Formulation 1A of Farrassat [22] is one such example.

Acoustic analogies are far less computationally expensive than resolving directly the acoustic wave propagation to the far-field. It is for this reason that all previous numerical landing gear noise prediction studies make use of the acoustic analogy in the form of the FW-H equation [53, 73].

2.6.3 Turbulence Modelling

Due to the high-Reynolds numbers associated with landing gear components, direct numerical simulation (DNS) of all turbulent scales was considered far too impractical as the cost required to resolve the entire range of scales is proportional to Re_t^3, where Re_t is the turbulent Reynolds number. There are two alternative methods that can be adopted to predict the effect of turbulence on the mean flow at lower computational cost: Reynolds-averaging (or ensemble-averaging) and filtering. However, both approaches introduce additional terms in the governing equations that need to be modelled in order to close the full set of equations.

The additional terms in the Reynolds-averaged Navier Stokes (RANS) equations are the so-called Reynolds stresses. The most common method of modelling the Reynolds stresses uses the Boussinesq hypothesis which relates the Reynolds stresses to the mean velocity gradient and the turbulent viscosity, μ_t. Turbulence models that use the Boussinesq hypothesis are termed RANS turbulence models. From a computational standpoint the use of RANS models is cheap, but since all turbulent scales are modelled some error is introduced into the solution.

The Large-Eddy Simulation (LES) approach reduces the modelling error associated with RANS methods by explicitly solving the larger turbulent eddies using a time-dependent simulation of the "filtered" Navier-Stokes equations. Usually, the filter removes eddies that are smaller than the grid size and these are modelled using a sub-grid model. However, LES requires a fine grid, especially in the near wall region, so that the turbulent eddies can be simulated accurately in both time and space, and as a result, LES is still impractical for high Reynolds number flows.

Detached-Eddy Simulation (DES) is a LES/RANS coupling approach and offers a practical alternative to LES. The method combines a RANS turbulence model with a filtered version of the same model to create two separate regions inside the flow domain. The RANS model models the full spectrum of turbulence in the near-wall region, whilst away from the wall, the pure LES model is recovered to resolve the larger turbulent scales. The result is that the grid resolution can be relieved in the near-wall RANS region making DES more cost efficient than LES.

2.7 Numerical Bluff-Body Aeroacoustics

2.7.1 Circular Cylinders

The first step toward the accurate prediction of cylinder noise using numerical tools is the near-field prediction of the noise source. Cox [10] investigated the vortex shedding noise for cylinders at subcritical and supercritical Reynolds numbers. He first used 2-D unsteady RANS (URANS) simulations of the flow field. The near-field results were used to predict the far-field acoustic pressure by solving the FW-H equation. The acoustic results were compared with the experiment of Revell at $Re = 9 \times 10^4$ [60] and showed an over-prediction of the shedding frequency and the peak and overall sound pressure levels. Cox concluded that 2-D simulations led to an over prediction of both noise amplitude and frequency due to high three-dimensionality of the real flow. Three-dimensional results showed much better agreement with experiment, which used periodic boundary conditions at the cylinder ends to model a infinite span.

Travin *et al.* [79] used DES to simulate the flow over cylinders at a range Reynolds numbers between 5×10^4 and 3×10^6. Both laminar and turbulent separation cases where simulated. Turbulent separation was forced so that the numerical results could be compared to experimental results at very high Reynolds numbers. To achieve turbulent separation in the computations, the turbulent viscosity, μ_t, was defined a number of times higher than the molecular viscosity, μ. The TS cases were found to be relatively insensitive to the Reynolds number. Agreement for drag, shedding frequency, pressure, and skin friction was reasonable, and there was a definite improvement over RANS modelling results. Similar results were found by Vatsa and Singer [80] who set μ_t at

5 times the molecular viscosity to achieve turbulent separation at critical Reynolds numbers.

Seo *et al.* [67] predicted the noise for long-span bodies using results from short span computations. The spanwise correlation of the vortex shedding can often be greater than the span used in a CFD simulation, especially for turbulent flow at low Mach numbers, making the prediction of long-span cylinders challenging. They used results from an LES simulation coupled with an FW-H solver and a new method of compensating for a short simulation span and obtained good agreement with experiment.

2.7.2 Yawed Cylinders

Alongside their experimental effort, Haramoto *et al.* [33] performed computations of inclined cylinders at yaw angles of $\Lambda = 0$ deg and $\Lambda = 20$ deg at Reynolds numbers of 1×10^4 and 2×10^4. Their results showed mixed agreement with the trends expected from the literature [82] and their experiments. In one case, the peak SPL was higher for the yawed cylinder compared to the cylinder in cross-flow. It was concluded that the spanwise grid resolution and long spanwise correlation length expected for the low Reynolds number flow was responsible for this discordance with the established trend.

2.7.3 Tandem Cylinders

One advantage of investigating tandem cylinders numerically is the ability to assess the self-noise of each cylinder and any additional noise by specifying multiple FW-H integration surfaces. In this way, the directivity and spectra for each cylinder can be identified and predicted separately.

Khorrami *et al.* [44] performed 2-D simulations of tandem cylinders using URANS turbulence modelling. Numerical results were compared with the results of a parallel experimental effort [43] for $S/D = 1.435$ and $S/D = 3.7$. It was found that for the $S/D = 1.435$ case the computations were unable to sustain the initial flow unsteadiness, which lead to damping of the fluctuations over time. The predicted shedding frequency for the $S/D = 3.7$ case was close to the experimental value, however the turbulence modelling was incapable of capturing the full wake dynamics observed in the experimental PIV snapshots. This work was extended to 3-D computations using a zonal approach where the flow field was assumed to be quasi-laminar, except for a narrow strip surrounding the cylinder surfaces [45]. The results highlighted the sensitivity of the solution to the turbulence model and the grid resolution. The results for the larger separation cases were in better agreement with experiment than at shorter separation distances.

Further work was completed focusing on the $S/D = 3.7$ case and this time including far-field acoustic predictions using FW-H solvers [55]. The agreement with experiment was

generally quite good. It was found that the downstream cylinder dominated the far-field acoustic spectrum due to the larger pressure fluctuations on the cylinder surface. The unsteady pressure fluctuation on the downstream cylinder was some 10-15 dB higher than that on the upstream cylinder. The calculated directivity pattern was similar to that of a single cylinder with the primary noise radiation direction slightly downstream. The influence of FW-H integration surface location was made by comparing results using on-body surfaces to off-body surfaces up to several cylinder diameters away. Only minor differences were seen between results, indicating that the surface pressure fluctuations dominated the noise production process.

2.8 Numerical Landing Gear Aeroacoustics

2.8.1 Simulation of Landing Gear Flow Fields

Only in recent years the available computational resources and performance has allowed CFD to be applied to full landing gear geometries [38, 48, 54]. However, due to computational constraints, landing gear geometries must usually be heavily simplified.

CFD of a simplified landing gear was presented by Hedges *et al.* [38]. Calculations were performed using DES and URANS methods, and a comparison was made against the experimental results of Lazos [47]. A structured grid consisting of roughly 2.5 million points was generated around a highly simplified B757 main landing gear. The simulations predicted the pressure over the surface of the wheels with good agreement with experiment. The same could be said for the gross flow features and surface pressures. However, the comparison of drag was poor, especially for the aft wheel. Although the predicted flow fields of URANS and DES results were similar, DES performed consistently better. Due to the lack of unsteady experimental data, the accuracy of the prediction could not be properly evaluated.

Results of URANS simulations of a landing gear flow field using the $k-\omega$ turbulence model of Menter was presented by Li *et al.* [48]. The model geometry in this case was more realistic and included several finer details such as yokes, pins, and part of the door. A structured grid was utilised consisting of 13.3 million grid points. The results show that the presence of the diagonal struts and the door significantly influenced the flow field. Vortex shedding at a frequency of approximately 800 Hz occurred off the right rear wheel on the side of the diagonal strut, but not on the other rear wheel, indicating strong interaction mechanisms between components. Vortex shedding at about 600 Hz also occurred from the downstream strut, and streamwise vortices originated from the top and bottom upstream corners of the door. Pressure fluctuations with a frequency of about 24 kHz were found behind the mid portion of the main leg and flow separation occurred at the leading edge of the door, which never reattached. The flow oscillated

strongly over the right front wheel only. The asymmetry of the solution inferred strong interactions between the various parts of the gear assembly.

2.8.2 Landing Gear Aeroacoustic Prediction

Souliez *et al.* [73] performed computations of aerodynamic noise from a landing gear in a uniform flow using the FW-H equation. The FW-H equation was solved using surface integrals over both the landing gear surface and a permeable surface away from the landing gear. Computational unstructured grids were constructed for two four-wheeled landing gear models with and without diagonal struts. The results for the porous FW-H surface predictions showed better agreement with experiment, whereas the solid FW-H surface missed by more than 50% some of the pressure fluctuations. Thus it was suggested that quadrupole effects may represent a significant contribution to the overall near-field sound level. It was shown that the diagonal struts significantly increased the sound intensity in the streamwise direction, and interfered with the vortex shedding from the gear leg.

An aeroacoustic analysis of a simplified Boeing 757 gear was performed by Lockard *et al.* [53] based upon the URANS simulations provided by Li *et al.* [48]. The medium resolution structured grid consisted of 1.8 million grid points. The simulations showed surface pressure distributions suggesting highly non-linear and interactive near-field flow dynamics. High frequency sources could not be captured by the coarse grid. The gear boxes and connectors were shown to be primarily responsible for the broadband component of the noise, and also a variety of tones. The wheels were identified as the primary noise radiators, with hub caps bearing no significance. The main leg was responsible for two loud tones and their harmonics. The region around the door and main leg led to complicated flow physics and a more detailed simulation would have been required to better understand the mechanisms involved.

The work by Lockard *et al.* [53] was extended by implementing a denser grid of 13 million grid points over the same simplified geometry including a comparison between turbulence models [54]. URANS employing the SST $k-\omega$ turbulence model was compared against DES. The DES calculations were more consistent with the anticipated physics. In all cases the DES predictions exhibited much higher levels of flow detail for the sub-components. Analysis of the directivity predicted by the two models showed large differences. The DES model showed a larger variation in directivity and predicted the strongest radiation behind the gear, and to the sides, especially behind the door, with a minimum directly below the gear. Porous surface predictions which enclosed the gear predicted considerably higher noise levels than the predictions obtained from the solid integration surfaces. This was thought to be due to errors caused by vortices passing through the permeable surfaces. The differences between the models suggest that further validation was needed. The work showed that numerical noise predictions

of a landing gear are possible, but are too computationally expensive even for simplified geometries.

The state-of-the-art suggests that there is much to improve before a numerical prediction of complex landing gear configurations is possible. Numerical methods are still too computationally expensive, limiting the fidelity of the models and leading to excessively long computation times. Such simplified geometries do not represent operational landing gears and so their analysis can be misleading. Therefore, a component-based approach may be more suitable for numerical landing gear noise prediction.

Chapter 3

Modelling Methodology

3.1 Outline

In this chapter, the methodology of the new physics-based prediction scheme is presented. A component-based approach was adopted to simplify the complexity of a typical landing gear. In this way the landing gear geometry can be decomposed and modelled using a set of representative components. The noise radiated by the components can then be predicted by solving the governing equations of fluid motion using a numerical method. The total noise is calculated from the aggregate of the individual source contributions with consideration of interaction mechanisms between components.

3.2 Physics-Based Approach

It was important that the prediction scheme incorporated as much of the noise generating physics and geometrical complexity of the landing gear into the noise prediction as possible. Hence a "physics-based" approach was required rather than a statistical or empirical-based approach [25, 32, 71]. This ensured that the model was sensitive to the geometrical parameters and flow variables and that the predictions are not limited by the constraints of experimental techniques and databases. Therefore the effect of small changes, or "deltas", to the geometry or the local environment could be predicted. The aim was that the new prediction model would provide high-fidelity predictions based upon a good understanding of the noise generating mechanisms and noise characteristics of the individual components, leading to low-noise design guidelines.

3.2.1 Computational Approach

It has been shown that the noise generating physics of landing gear noise sources can be captured numerically by solving the governing equations of fluid dynamics using computational techniques [53, 54, 73]. A computational approach has many advantages over empirical approaches that rely on experimental databases that are limited by practical constraints, such as the wind tunnel environment and the available measurement techniques. For example, it is extremely difficult to obtain a full three-dimensional directivity information for a particular geometry.

The first step to obtaining a prediction is to predict the unsteady turbulent near-field around the body, from then to calculate how the near-field perturbations are radiated into the far-field and perceived as noise to the observer. Chapter 2 indicated that the use of conventional CFD coupled with the solution of the FW-H equation is a method that has been successfully used to predict the far-field acoustic pressure, given initial flow conditions and a geometry [10, 55, 67]. This is known as a "two-step" approach, since the prediction of the near-field acoustic source and of the far-field acoustic pressure are separate. Once a solution for the far-field acoustic pressure is obtained in the form of a time-history at discrete observer locations, it can be processed to yield the acoustic spectra and directivity information, which describe the characteristics of the far-field noise. Full details of the computational methodology are provided in Chapter 4.

3.2.2 Component-Based Approach

The literature review indicated that full-blown high-fidelity landing gear computations will not be achievable for some time [38, 48, 54, 73]. The alternative to performing full landing gear simulations is to employ a component-based approach. In this approach the detailed landing gear geometry is decomposed into individual components so that numerical prediction becomes feasible. Complex components may be broken down in several stages and modelled by multiple components if required. The various landing gear struts are described in Figure 3.1, which serves to illustrate how the landing gear can be decomposed.

In this component-based approach, the total landing gear noise is calculated as the aggregate of the individual sources. However, strong interaction effects often exist between components. These interactions can have a large impact on the noise generating mechanisms [14, 39, 48, 68]. These interactions usually take the form of body-wake-body interference and of acoustic scattering and shielding. Therefore the component-based method must incorporate interaction effects rather than assume a collection of non-interacting bodies.

The total landing gear noise must be calculated outside of the non-linear near-field region, so that the super-position principle can be applied to the acoustic waves. The

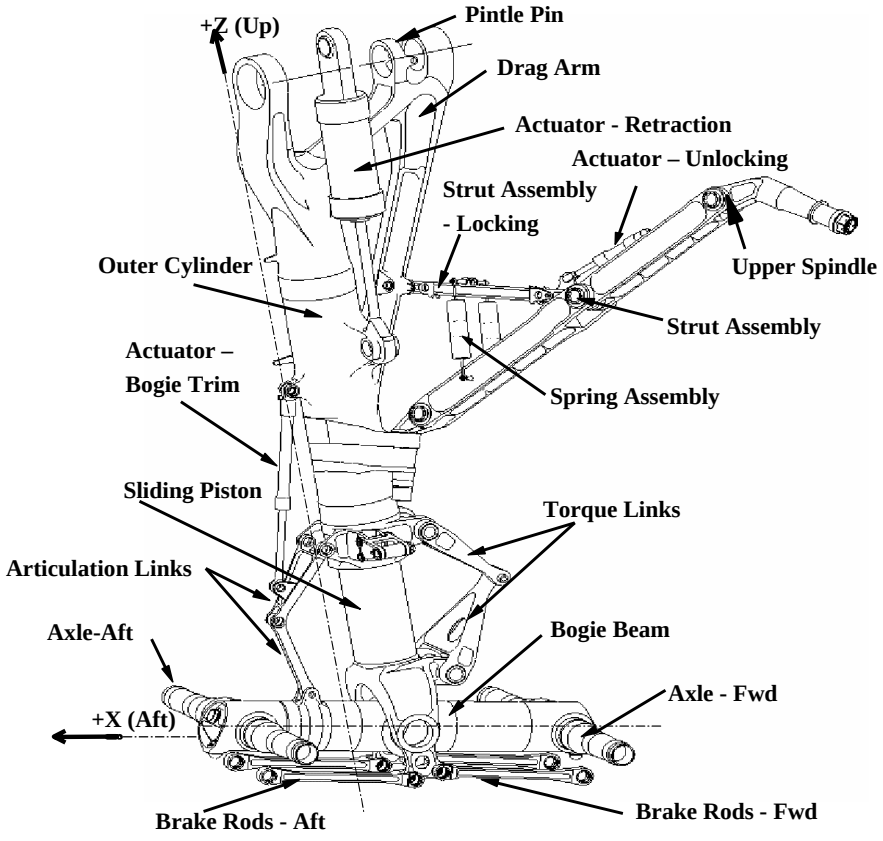

FIGURE 3.1: Description of a typical main landing gear in the absence of wheels and dressings (courtesy of Airbus).

superposition principle states that, for a linear homogeneous system, any linear combination of solutions to the system is also a solution to the same system:

$$\text{IF } 0 = F(x_1) = F(x_2) = \cdots, \quad \text{THEN } F\left(\sum_{i=1}^{n} \alpha_i x_i\right) = 0. \tag{3.1}$$

Thus the total noise is deduced by aggregating the contributions of the predicted mean-square far-field acoustic pressure, $\overline{p'^2}$, for each individual component at each discrete observer location. The mean-square far-field acoustic pressure for the total geometry can then be expressed as

$$\overline{p'^2}_{\text{total}} = \sum_{j=1}^{n_s} \left[\overline{p_j'^2}\right]_{\text{s}} + \sum_{j=1}^{n_w} \left[\overline{p_j'^2}\right]_{\text{w}} + \sum_{j=1}^{n_o} \left[\overline{p_j'^2}\right]_{\text{o}} + \Pi \tag{3.2}$$

where

n = number of components

$[]_{\text{s}}$ = contribution from strut components

FIGURE 3.2: Operational Airbus A340 main landing gear.

$[]_w$ = contribution from wheels
$[]_o$ = contribution from other components; e.g. doors, fittings
Π = contribution from acoustic interaction effects

The component groups in Equation 3.2 should accommodate any external component that is exposed to the flow field. The term Π includes a complex array of acoustic interaction effects such as scattering, shielding, and refraction of the acoustic waves radiating from the various sources, which should be included for accuracy. Aerodynamic interaction effects are of equal importance as they play a major role in determining the far-field noise characteristics. Simulations to obtain $\overline{p_j'^2}$ for each component should include consideration of any aerodynamic interactions. In this work, an effort is made to consider the aerodynamic interaction between struts in a tandem arrangement.

3.2.3 Representative Geometries

The complexity of the landing gear geometry and the geometrical disparity between components is clearly illustrated in Figures 3.2 and 3.1. It is infeasible to explicitly model each component. Instead the landing gear geometry can be described using a limited number of components that are representative of the real components. These

can be grouped together into similar groups such as "circular struts", "H-beam sections", "wheels", and so on to form a modelling database. Therefore some simplification or generalisation of the landing gear components is required to form a set of generic, representative components that can be used to model the real landing gear. The integrity of the real landing gear geometry is maintained by ensuring that potentially important features are not neglected when investigating the model components. The level of detail in the representative components is largely controlled by the computational cost required to perform the numerical simulation.

3.2.4 Scaling Laws

The result of Curle's theoretical work on the influence of solid boundaries upon aerodynamic sound [11] was that in the far-field, defined where

$$x \gg \lambda \qquad \text{and} \qquad x \gg l$$

where x is the source-observer distance, λ is a typical wavelength of the source, and l is the typical dimension of the solid body, the derived dipole term takes the form:

$$\rho - \rho_0 = -\frac{1}{4\pi c_0^3}\frac{x_i}{x^2}\frac{\partial}{\partial t}\int_S P_i\left(\mathbf{y}, t - \frac{r}{c_0}\right)\mathrm{d}S(\mathbf{y}). \tag{3.3}$$

In Equation 3.3, P_i is the force per unit area exerted on the fluid by the solid boundaries defined by the surface S at position $\mathbf{y}$ in the x_i direction at the retarded time t. If $l \ll c_0/\omega$, where ω is a typical sound frequency, then the ratio r/c_0 of the retarded time may be neglected leading to

$$\rho'(x,t) = \rho - \rho_0 = \frac{1}{4\pi c_0^3}\frac{x_i}{x^2}\frac{\partial}{\partial t}F_i(t), \tag{3.4}$$

where $F_i(t) = \int_S P_i \mathrm{d}S(\mathbf{y})$ is the total resultant force exerted upon the fluid by the solid boundaries. Since ω will generally be in the order of U_0/l, where U_0 is the freestream velocity, it follows that this last simplification should be possible if

$$l \ll \frac{c_0}{\omega} \approx \frac{c_0 l}{U_0}, \quad \text{i.e. if} \quad \frac{U_0}{c_0} = M \ll 1$$

Therefore, for low Mach number flows, the surface noise is that generated by a single dipole representing the fluctuating forces exerted by the fluid on the solid body.

Lighthill has shown that the intensity of the quadroupole sources, I_Q, in similar flows is given by

$$I_Q \approx \rho_0 U_0^8 c_0^{-5} l^2 x^{-2} f(R). \tag{3.5}$$

In a similar fashion, the sound generated by the dipole can be estimated by $F_i(t) = \int_S P_i \mathrm{d}S(\mathbf{y})$ is of order $\rho_0 U_0^2 l^2 g(R)$, therefore

$$\rho - \rho_0 \approx \rho_0 U_0^3 c_0^{-3} l x^{-1} g(R).$$

Finally, the dipole sound intensity

$$\begin{aligned} I_D &= c_0^3 \rho_0^{-1} (\rho - \rho_0)^2 \\ &= \rho_0 U_0^6 c_0^{-3} l^2 x^{-2} g(R). \end{aligned} \tag{3.6}$$

To summarise this result, dimensional analysis of the Lighthill-Curle [11] equation shows that the sound generated in the far-field by the surface dipoles from a body immersed in the flow should be given by the general form:

$$I_D \propto \frac{\rho_0 U_0^6 l^2}{c_0^3 x^2}, \tag{3.7}$$

where

I	= acoustic intensity
U_0	= characteristic velocity of the flow
l	= characteristic length of the body
c_0	= local sound speed of the fluid at rest
ρ_0	= density of the fluid at rest
x	= the distance from the source

Typical landing gear components are essentially bluff-bodies and since the landing gear is only deployed at low Mach numbers (i.e. $M \ll 1$) the dipole sources due to the unsteady forces on the component surfaces tend to dominate the far-field noise characteristics [9, 14, 39, 59, 76]. This is reasonable since from Equations 3.5 and 3.6

$$\frac{I_Q}{I_D} \propto \left(\frac{U_0}{c_0}\right)^2,$$

indicating that at low Mach numbers the contribution to the sound field from the dipoles should be greater than that of the quadrupoles. Therefore, the acoustic scaling law of Curle [11], defined by Equation 3.7, was adopted in the prediction model so that the computed far-field sound pressure could be further scaled if necessary.

The dipole scaling law was manipulated to derive an expression for the mean-square far-field acoustic pressure for a bluff-body. The time-averaged acoustic intensity $\bar{I}$ of a

periodic wave is related to the mean-square far-field pressure, $\overline{p'^2}$, by

$$\bar{I} \equiv \frac{\overline{p'^2}}{\rho_0 c_0}. \tag{3.8}$$

Combining Equations 3.7 and 3.8 and defining the far-field pressure as a function of the Strouhal number, and the observer location in terms of a polar angle, θ, and an azimuth angle, ϕ, the final dimensionally correct scaling law for bluff-body landing gear components can be expressed as:

$$\overline{p'^2(St_m, \theta_c, \phi_c, M_\infty, \theta_o, R_o)} = \frac{(\rho_0 c_0^2)^2 M_c^6 \Omega \mathbf{S}(St_m, \theta_c, \phi_c)}{(1 - M_\infty \cos\theta_o)^4 R_o^2}. \tag{3.9}$$

In Equation 3.9 M_c and M_∞ are the local component and flight Mach numbers respectively, R_o is the observer distance, and ρ_0 and c_0 represent the local atmospheric conditions. Two polar coordinate reference frames are defined for the prediction model. The first is component-based, corresponding to the local reference frame of each component, and the second is a moving reference frame, corresponding to the flight direction, which is used for the final prediction. These are described by Figures 3.3 and 3.4 accordingly. The length-scale term in Equation 3.7 is replaced by the component dimension factor, Ω, which for a typical strut as a dipole source is

$$\Omega = L_c^2, \tag{3.10}$$

where L_c is the length of the component. The term $(1 - M_\infty \cos\theta_o)^{-4}$ is the convective amplification factor for a dipole noise source, where θ_o is the polar angle in the flyover plane measured from the flight direction, and St_m is a modified Strouhal number that includes the Doppler factor $(1 - M_\infty \cos\theta_o)$.

The key term in Equation 3.9 is the "physical" spectrum matrix $\mathbf{S}(St_m, \theta_c, \phi_c)$, which allows the far-field pressure spectrum to be described as a function of frequency and observer location. The spectrum matrix is obtained from numerical simulations of the particular component, which contains discrete spectra for the observer as a function of the modified Strouhal number, St_m, and the observer polar and azimuth angles, θ_c and ϕ_c, with respect to the component axis. Essentially the term $\mathbf{S}$ includes the directivity information so that a unique spectrum can be determined by Equation 3.9 for an arbitrary observer location. This is a crucial development on existing models where a semi-empirical directivity function is used to scale a simple non-unique noise spectrum function that is independent of the observer location [25, 32, 71]. Moreover, semi-empirical methods are usually only applicable to observers in the flyover plane as they are developed using experimental databases, limited to a small range of microphone locations.

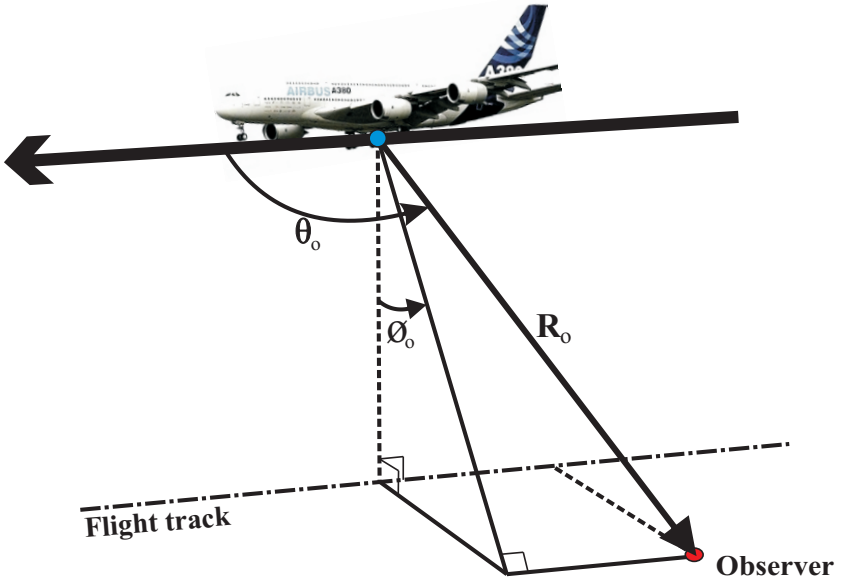

FIGURE 3.3: Definition of the prediction model coordinate system ($0 \leq \theta_o \leq \pi$, $0 \leq \phi_o \leq 2\pi$).

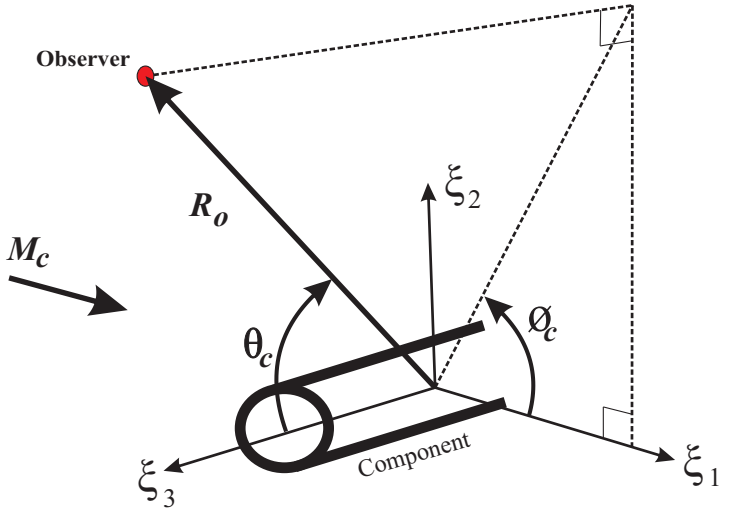

FIGURE 3.4: Definition of the component-based coordinate system ($0 \leq \theta_c \leq \pi$, $-\pi \leq \phi_c \leq \pi$).

Parameter	**Description**
c_0	Ambient sound speed of fluid at rest
D_w	Wheel diameter
L_c	Component characteristic length
M_c	Component local Mach number
M_w	Wheel local Mach number
M_∞	Aircraft Mach number
N_1	Number of wheels positioned laterally
N_2	Number of wheels positioned longitudinally
R_o	Distance to the observer
St	Strouhal number based on the reference velocity & length scale
St_c	Strouhal number based on the component velocity and L_c
St_m	Modified Strouhal number, $(1 - M_\infty \cos\theta_o)St_c$
St_w	Strouhal number based on the wheel velocity and diameter
$\mathbf{S}$	Normalised component spectrum matrix
W	Wheel width
χ	Bogie angle to the flow
θ_c	Polar angle relative to the strut z-axis, $0 \leq \theta_c \leq \pi$
θ_o	Polar angle in the flight direction, $0 \leq \theta_o \leq \pi$
ϕ_c	Azimuth angle relative to the component x-axis, $-\pi \leq \phi_c \leq \pi$
ϕ_o	Azimuth angle lateral to the flight trajectory $0 \leq \phi_o \leq 2\pi$
ρ_0	Ambient density of fluid at rest
Ω	Component dimension factor
$(1 - M_\infty \cos\theta_o)^{-4}$	Convective amplification factor for dipole source

TABLE 3.1: Definition and description of prediction scheme input parameters.

Computational wheel noise modelling was not performed in this research. Instead the semi-empirical model developed by Smith and Chow [71] was used to provide the prediction for wheel noise. For the wheel noise prediction, the physical-based spectrum $\mathbf{S}$ in Equation 3.9 is replaced by the empirical spectrum $E_w(St_w)$ and the component dimension parameter for the wheels is given by:

$$\Omega_w = N_1 W D_w (1 + (N_2)\sin\chi), \tag{3.11}$$

where N_1 is the number of wheels positioned laterally with width W and diameter D_w, N_2 is the number of wheels positioned longitudinally, and χ is bogie angle to the flow. The empirical spectrum is in the form of a smooth broad hump, more details of which are outlined in References [71, 72]. Note that the spectrum is only a function of the Strouhal number, and the wheel noise is assumed to be omni-directional.

The full scaling law used for wheel noise is given by:

$$\overline{p'^2(St_w, M_\infty, \theta_o, R_o)} = \frac{(\rho_0 c_0^2)^2 M_w^6 \Omega_w E_w(St_w)}{(1 - M_\infty \cos\theta_o)^4 R_o^2}, \tag{3.12}$$

The full aircraft prediction is given by Equation 3.2 after the rotation of the component local coordinates (θ_c, ϕ_c) to the aircraft coordinates (θ_o, ϕ_o) and dimensionalisation of the components Strouhal number to frequency. For the struts and wheels described thus far this can be expressed as:

$$\overline{p'^2}_{\text{total}} = \frac{(\rho_0 c_0^2)^2}{(1 - M_\infty \cos\theta_o)^4 R_o^2} \left(\sum_{j=1}^{n_s} M_{c_j} \Omega_j \mathbf{S}_j(f, \theta_o, \phi_o) + M_w^6 \Omega_w E_w(f) \right) \tag{3.13}$$

where the component spectrum matrices have been rotated so that they are aligned with the aircraft coordinate system.

The complete listing of the variables in Equation 3.13 is tabulated in Table 3.1. The validation of the scaling law described by Equation 3.9 applied to the computational results is provided in Chapter 9.

3.3 Modelling Database

The modelling database contains far-field acoustic spectra defined by the function **S**. The spectra are normalised by Equation 3.9 using the simulation parameters. The scope of this PhD was to investigate some fundamental component groups that could be used to model the components of a simple landing gear geometry.

Figures 3.1 and 3.2 of the A340 main landing gear indicate that many struts are circular in cross-section. A selection of circular struts were identified by inspecting a CAD model and are listed in Table 3.2. The CAD model was used to determine the strut diameters so that estimated Reynolds numbers (based upon a Mach number of 0.2) could be calculated. This information is reported in Table 3.2. The typical alignment of the struts to the freestream is also listed.

As well as being aligned at various angles, the struts are often positioned to encourage body-wake-body interactions. Based upon this simple analysis three modelling components were identified. Each component is based upon the circular cylinder cross-section. The modelling components are introduced in the following sections.

3.3.1 Circular Struts

The noise produced by an isolated single cylinder in cross-flow (aligned with the spanwise axis perpendicular to the freestream vector) provided the basic model through which to investigate strut noise. The Reynolds numbers listed in Table 3.2 correspond to critical and postrcritical Reynolds numbers. In real landing gear flows, it is expected that each component would encounter a non-ideal inflow as a result of the disturbed flow

Component	**Diameter (m)**	***Re***	**Alignment**
Axles	1.52×10^{-1}	7.16×10^{5}	Horizontal
Brake rods	6.53×10^{-2}	3.08×10^{5}	Horizontal
Sidestay cylinder	3.15×10^{-2}	1.49×10^{5}	Yawed
Lower Side Stay	1.70×10^{-1}	7.99×10^{5}	Yawed
Main Leg	3.83×10^{-1}	1.81×10^{6}	Vertical
Retraction Actuator	7.98×10^{-2}	3.77×10^{5}	Yawed
Sliding Piston	3.41×10^{-1}	1.61×10^{6}	Vertical

TABLE 3.2: Table of landing gear struts of circular cross-section, reporting diameter, approximate Reynolds number, and general alignment, based on a full-scale Airbus A340 main landing gear.

field originating from upstream of the landing gear components, or installation effects. Moreover, landing gear parts are not typically smooth, uniform cylinders, but often have a combination of surface roughness, small dressings, and geometrical features that will lead to turbulent boundary layer separation. It is therefore realistic that the flow around even the smallest components will correspond to high-Reynolds number regimes, i.e. the critical and postcritical regimes. Therefore, the investigation of circular cylinders in cross-flow should be performed at high-Reynolds numbers and the numerical method should ensure that high-Reynolds number regimes are modelled. Details and results for cylinders in cross-flow are presented in Chapter 5.

3.3.2 Arbitrarily Aligned Struts

Chapter 2 indicated that strut alignment to the freestream will impact the far-field acoustic characteristics. It was therefore important that strut inclination to the local velocity vector was a parameter considered in the new prediction model. This was investigated by performing calculations at various yaw angles ranging from $\Lambda = 0$ deg (cross-flow) to $\Lambda = 45$ deg. This covered the range of inclination that is expected for struts in a typical landing gear configuration. Modelling details and results are presented in Chapter 6.

3.3.3 Component Interactions

Chapter 2 also indicated that tandem cylinder flows are a useful geometry in which to investigate interaction mechanisms [43,44,55]. The flow regimes defined by Zdravkovich [82] were used to select a range of separation distances that represented various interaction mechanisms so that the effect of the proximity between components on the flow and noise could be modelled. The investigations were limited to two equal diameter cylinders in cross-flow with a range of separation distances between two and five cylinder diameters. The numerical results are presented in Chapter 7.

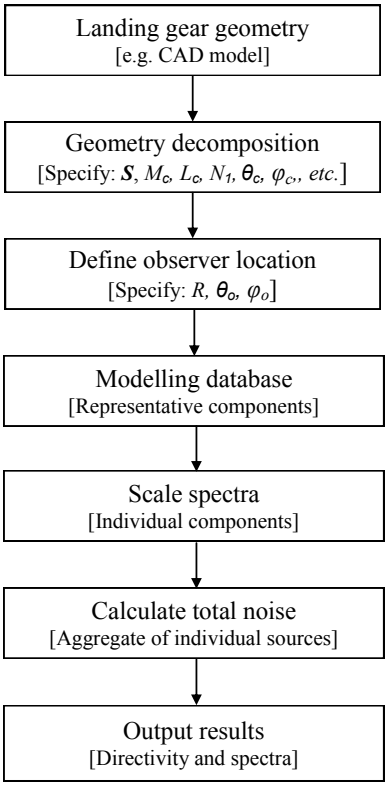

FIGURE 3.5: Flow diagram of the aeroacoustic landing gear prediction scheme.

3.4 Design Tool

3.4.1 Modelling Process

In this section the modelling process is described starting with a CAD model through to the output of the far-field acoustic prediction. Figure 3.5 illustrates each fundamental stage of the prediction routine.

The procedure is described by the following steps:

Step 1 - Geometry information. Geometry information is obtained from a detailed CAD model. The model should contain enough information so that component dimensions and location/alignment can be determined.

Step 2 - Model decomposition. The landing gear structure is decomposed into its constituent components and suitable representative components are selected from the modelling database to model each individual component.

Step 3 - Observer location. Observer locations are defined relative to each component with respect to the coordinate system defined in Figure 3.4.

Step 4 - Database. The modelling code acquires the appropriate normalised spectra from the modelling database.

Step 5 - Scale spectra. The spectra are scaled according to the parameters determined in steps 2 and 3.

Step 6 - Compute total noise. The overall noise is calculated. This takes the form of a composite and total spectrum, and the OASPL directivity.

Step 7 - Design iterations. Design parameterisation may be performed to compare various configurations by repeating the process.

3.4.2 Modelling Code

MATLAB code was developed to automate the prediction procedure wherever possible. This code was designed to read the input parameters defined by the engineer and then perform the mathematical manipulation and database acquisition tasks. The main functions of the code are to scale the normalised spectra, perform the rotation of the component coordinates to the aircraft coordinates, and calculate the overall noise levels.

3.4.3 Remote Database

Databases were developed that contain the normalised spectral information for the modelling components. These consist of both local and remote Structured Query Language (SQL) databases hosted at Southampton University, which allows remote users to access the latest modelling results.

3.4.4 Graphical User Interface

A graphical user interface (GUI) was developed to enhance the users' interaction with the main code. The GUI was programmed using the C# language which communicates with the MATLAB code via the .NET framework. The requirement of the host machine is a WINDOWS operating system with .NET Framework installed. The GUI consists of a simple interface in which all of the input parameters including the geometrical information can be entered by the user.

3.5 Summary

An outline of the new physics-based prediction model has been presented. The aim of the model was to include as much of the geometric complexity as possible, but to model

each complex component by a representative component available within a modelling database. The new model employs a numerical approach to solve the governing equations of fluid flow and acoustic propagation so that the physics of the landing gear noise sources can be captured. Each component in the database contains acoustic spectra and directivity information. Acoustic scaling laws were adopted so that the various dimensions and flow velocities for each strut can be accounted for, without the need to perform additional simulations. The total noise is calculated as the aggregate of the individual component noise.

Various programming languages were utilised to automate the prediction process and package it as an engineering tool. A GUI was designed to allow input variables to be defined easily, a central code was programmed using MATLAB to perform the mathematical tasks, and a remote database was developed to store the modelling data.

Chapter 4

Numerical Method

4.1 Outline

In this chapter the numerical method is outlined that was used to predict the far-field acoustic characteristics. This was achieved by using a low-order Navier-Stokes flow solver and a high-order CAA solver to provide the turbulent near-field flow prediction. The far-field acoustic prediction was computed using an acoustic solver based on the FW-H equation. Details are provided for the governing equations, turbulence modelling, grid generation, boundary conditions, and solution strategy.

4.2 Two-Step Approach

The computational procedure is divided into two sections. Firstly, the governing laws of fluid dynamics were solved numerically around various geometries on a computational grid. The integral solutions of the Navier-Stokes equations are discretised and solved numerically at each grid point in the domain. This provided the detailed time-dependent flow information in the vicinity of the noise source. This flow information was sampled along FW-H integration surfaces that surrounded the source. The next step was to solve the FW-H equation, to yield the acoustic information at the far-field using the CFD results as input. This hybrid method is known as a "two-step" approach, and is illustrated in Figure 4.1. The advantage of the two-step approach is that the small acoustic perturbations do not need to be resolved up to the far-field, therefore alleviating the computational cost. Once the far-field numerical result had been obtained, Curle's dipole scaling law in Equation 3.7 was employed by the prediction model to predict the acoustic pressure at other observer locations. The details of each stage of the method are outlined in the forthcoming sections.

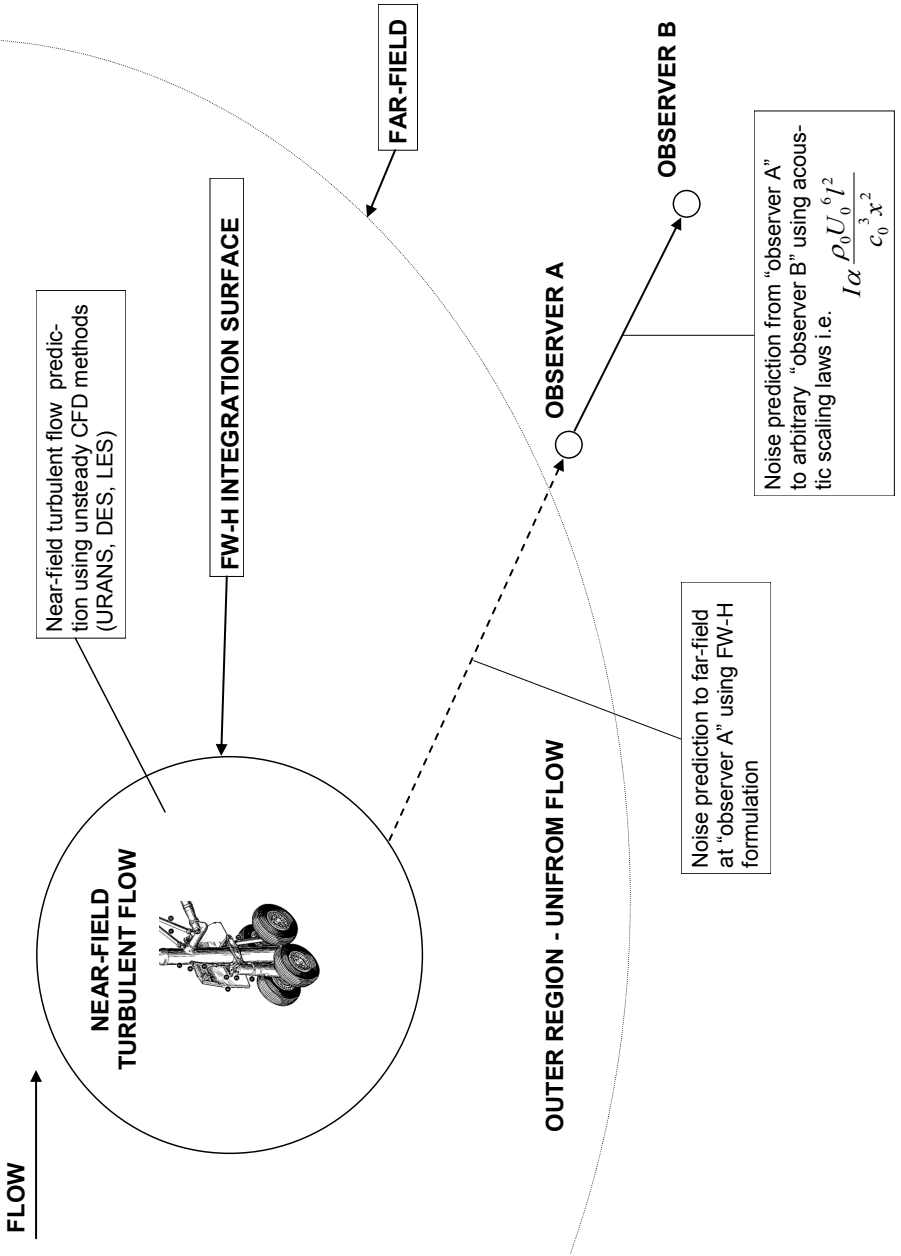

FIGURE 4.1: Description of the adopted "two-step" computational approach.

4.3 Low-Order Flow Solver

The flow solver used to obtain the CFD results in Chapters 5-7 was a cell-centred finite volume CFD code. In this section the governing equations, computational setup, turbulence modelling, and boundary conditions are summarised.

4.3.1 Governing Equations

The equations solved were the unsteady, compressible Navier-Stokes equations. They establish that changes in density, momentum and specific internal energy in infinitesimal volumes of fluid are the sum of dissipative viscous forces, changes in pressure, gravity, additional forces acting inside the fluid and of the work and heat transfer to the fluid.

In Favre-averaging, a dependent variable Φ is decomposed into a mean part $\tilde{\Phi}$ and fluctuating part Φ', so that

$$\Phi = \tilde{\Phi} + \Phi', \tag{4.1}$$

where $\tilde{\Phi}$ is a density weighted average variable

$$\tilde{\Phi} = \frac{\overline{\rho\Phi}}{\bar{\rho}}. \tag{4.2}$$

Decomposing each of the flow variables in the same way yields the Favre-averaged Navier-Stokes equations for variable density flows:

$$\frac{\partial \bar{\rho}}{\partial t} + \frac{\partial}{\partial x_i}(\bar{\rho}\tilde{u}_i) = 0, \tag{4.3}$$

$$\frac{\partial}{\partial t}(\bar{\rho}\tilde{u}_i) + \frac{\partial}{\partial x_j}(\bar{\rho}\tilde{u}_i\tilde{u}_j) = -\frac{\partial \bar{p}}{\partial x_i} + \frac{\partial}{\partial x_j}\left(-\overline{\rho u_i' u_j'} + \bar{\tau}_{ij}\right), \tag{4.4}$$

$$\begin{aligned}\frac{\partial \bar{\rho}\tilde{E}}{\partial t} + \frac{\partial}{\partial t}\left[\left(\bar{\rho}\tilde{E} + \bar{p}\right)\tilde{u}_j\right] &= -\frac{\partial}{\partial x_j}\left(\bar{q}_j + \overline{\rho u_j' e'}\right) + \frac{\partial}{\partial x_j}\left(\tilde{u}_i(\bar{\tau}_{ij} - \overline{\rho u_i' u_j'})\right) \\ &+ \frac{\partial}{\partial x_j}\left(\overline{\tau_{ij} u_i'} - \frac{1}{2}\overline{\rho u_j' u_i' u_i'}\right).\end{aligned} \tag{4.5}$$

where the Favre-averaged total energy is given by

$$\bar{\rho}\tilde{E} = \bar{\rho}(\tilde{e} + \frac{1}{2}\tilde{u}_i\tilde{u}_i) + \frac{1}{2}\overline{\rho u_i' u_i'}, \tag{4.6}$$

where $\tilde{e}$ is the Favre-averaged specific energy. The additional terms, $\overline{\rho u_i' u_j'}$ and $\overline{\rho u_i' e'}$, are the Reynolds stress tensor and the turbulent heat flux respectively. These terms represent the effects of turbulence and must be modelled to solve the RANS equations. The Boussinesq assumption was employed to relate the Reynolds stresses to the mean

velocity gradients. This results in the viscous stress tensor

$$\bar{\tau}_{ij} = (\mu + \mu_t)\left[\left(\frac{\partial \bar{u}_j}{\partial x_i} + \frac{\partial \bar{u}_i}{\partial x_j}\right) - \frac{2}{3}\frac{\partial \bar{u}_k}{\partial x_k}\delta_{ij}\right], \tag{4.7}$$

and the heat flux vector

$$\bar{q}_j = -\left(\frac{\mu}{Pr} + \frac{\mu_t}{Pr_t}\right) c_p \frac{\partial \bar{T}}{\partial x_j}, \tag{4.8}$$

where μ_t is the turbulent viscosity, T is the temperature, and Pr_t is the turbulent Prandtl number. The third term on the right hand side of Equation 4.6 represents the molecular diffusion and turbulent transport of the turbulent kinetic energy. These terms were ignored based on order of magnitude arguments [81]. Additionally, viscous terms involving fluctuating quantities in the stress tensor and contributions of turbulent fluctuations to the total energy in Equation 4.5, were ignored.

4.3.2 Solver Details

In the finite-volume approach, the governing equations are integrated over a control-volume defined by the computational grid. This yields discrete equations that conserve each quantity and that can be solved numerically. The solver used a pressure-velocity correction approach to enforce mass conservation and to obtain the pressure field. The SIMPLE algorithm was used for this purpose. The discretisation scheme used for pressure, density, and energy was second-order upwind. For the momentum and turbulent viscosity calculations, a second-order central differencing scheme was chosen. For time-stepping, an implicit second-order time marching scheme with dual time stepping was adopted.

The code was run in a parallel environment on a Linux cluster allowing multi-processor jobs to be submitted. In parallel operation the grids were efficiently divided into a number of partitions using an auto-partitioning algorithm in order to efficiently distribute the grid among the allocated computational nodes. In a typical run, the solver used 16 processors each equipped with 1GB of RAM, for approximately 1500 CPU hours.

4.3.3 Turbulence Model

Detached-eddy simulation has been shown to be a useful approach to model bluff body flows [79] and was the chosen method adopted to model the turbulent field. The DES model used was coupled with the Spalart-Almaras RANS model [75]. The Spalart-Almaras (S-A) model uses only one additional transport equation to compute the quantity, $\tilde{\nu}$, which is a modified form of the turbulent kinematic viscosity. The turbulent

viscosity, μ_t, is related to the modified turbulent viscosity by

$$\mu_t = \rho\tilde{\nu} f_{v1}, \tag{4.9}$$

where f_{v1} is a viscous damping function. The transport equation for $\tilde{\nu}$ is:

$$\frac{\partial}{\partial t}(\rho\tilde{\nu}) + \frac{\partial}{\partial x_j}(\rho\tilde{\nu}u_j) = G_\nu + \frac{1}{\sigma_{\tilde{\nu}}}\left[\frac{\partial}{\partial x_j}\left\{(\mu+\rho\tilde{\nu})\frac{\partial\tilde{\nu}}{\partial x_j}\right\} + C_{b2}\rho\left(\frac{\partial\tilde{\nu}}{\partial x_j}\right)^2\right] - Y_\nu + S_{\tilde{\nu}}. \tag{4.10}$$

Appendix B outlines the various functions and constants used in the S-A model including those in Equations 4.9 and 4.10.

In the standard S-A model, the production term is proportional to the magnitude of the vorticity, however, a vorticity/strain relationship was used [12] so that the effect of the mean strain on the turbulence production is considered.

The standard S-A model uses the distance to the closest wall as the definition of the length scale d, which is critical in determining the rate of production and destruction of the turbulent kinematic viscosity. The DES model proposed by Shur *et al.* [69] uses a new length scale $\tilde{d}$ defined as

$$\tilde{d} = \min(d, C_{\text{DES}}\Delta), \tag{4.11}$$

where C_{DES} is an empirical constant with a value of 0.65, and Δ is the grid spacing based on the largest grid dimension in the x, y, or z directions for a particular cell. When the distance to the nearest wall is smaller than $C_{\text{DES}}\Delta$, the model behaves as a RANS model, and when d is larger than $C_{\text{DES}}\Delta$, then DES is in pure LES mode. Therefore the transition between RANS and LES can be controlled by either adjusting $C_{\text{DES}}\Delta$, or by locally refining the grid.

4.3.4 Boundary Conditions

The boundary conditions used in the simulations were a no-slip wall boundary condition specified on the cylinder surface, a pressure far-field boundary condition along the outer domain, and a periodic condition along the $z-$plane (spanwise) boundaries.

No-Slip Wall The no-slip wall condition ensures that the velocity relative to the wall is zero by satisfying

$$\underline{\mathrm{u}} = 0 \tag{4.12}$$

at at the wall. The near-wall mesh was sufficiently fine in the wall normal direction so that $\Delta y u_\tau/\nu \approx 1$. This ensured that the extreme velocity gradient in the resulting

boundary layer was adequately resolved. The modified turbulent viscosity $\tilde{\nu}$ and the normal pressure gradient were also set to zero at the walls.

Pressure Far-Field The pressure far-field boundary condition modelled a freestream condition at infinity by maintaining a specific value for the far-field static pressure, the freestream Mach number, the flow direction, and the turbulence parameters. It was a non-reflecting boundary condition, therefore suitable for aeroacoustic calculations, based on Riemann invariants for a one-dimensional flow normal to the boundary. The Riemann invariants (characteristic variables) corresponding to incoming and outgoing waves in subsonic flow are given by:

$$R_\infty = v_{n_\infty} - \frac{2c_\infty}{\gamma - 1}, \tag{4.13}$$

$$R_i = v_{n_i} + \frac{2c_i}{\gamma - 1}, \tag{4.14}$$

where v_n is the magnitude of the velocity normal to the boundary, γ is the ratio of specific heats for an ideal gas, and the subscript i refers to the conditions within the cell adjacent to the boundary face. Adding and subtracting the invariants in Equations 4.13 and 4.14 yields the following expressions:

$$v_n = \frac{1}{2}(R_i + R_\infty), \tag{4.15}$$

$$c = \frac{\gamma - 1}{4}(R_i - R_\infty), \tag{4.16}$$

where v_n and c become the values of the normal velocity and sound speed applied on the boundary respectively. At outflow boundaries, the tangential velocity components and entropy were extrapolated from the interior, and combined with v_n and c the density, velocity, temperature, and pressure along the boundary were calculated. The the non-reflecting boundary condition the characteristics of the waves propagating into the domain are set to zero. The typical domain extent to the far-field boundary was typically 25-30 cylinder diameters to ensure the boundary was far away from the disturbed near-field region.

Spanwise Periodic Boundary Condition The periodic boundary condition was defined on the two outer span-wise planes, z_1 and z_2, and was used to model an infinite span. The condition treated the flow at z_1 as though the opposing periodic plane z_2 is a direct neighbour to the cells adjacent to z_1. In this manner the flow through the periodic boundary adjacent to a fluid cell was calculated from the flow conditions at the cell adjacent to the opposite periodic plane. Therefore, the simulated span, L_z, should be equal or greater than the expected spanwise correlation length L_C which can

be obtained from experiment or from the literature. The span modelled in the present computations was restricted to $L_C = 2D$ due to computational cost. Experiments show that for supercritical circular cylinder flows $L_C \approx 2D$ [82], and therefore a simulated span of $L_z = 2$ was chosen. Computational studies [79] have also concluded that a simulated span of $L_z = 2D$ is adequate for circular cylinders at supercritical Reynolds numbers.

4.3.5 Grid Generation

Generating suitable grids so that the discretised Navier-Stokes equations could be solved was the first step in the solution process. Grid quality is largely responsible for the integrity and accuracy of a solution. A good quality grid enables the transient flow variables to be adequately resolved and will minimise numerical error. The grids were designed with consideration for the geometry and the expected aerodynamic flow field, the solver type, the boundary conditions, the FW-H integration surface position, the turbulence modelling, and the computational efficiency.

Curvilinear structured multi-block grids were generated around the cylinder geometries. For single cylinders, "O" domains were constructed extending 30 cylinder diameters from the body, whereas rectangular domains were constructed for the tandem cylinder geometries. The spanwise grid dimension was two cylinder diameters with up to 50 grid points along the span in the $z-$plane.

The effectiveness of modelling the turbulence using DES is extremely dependent on the quality of the numerical grid. The grid determines the length of the turbulent scales that can be modelled or resolved which is largely controlled by $\Delta = \max(\Delta x, \Delta y, \Delta z)$, therefore it was important to develop spatial discretisation design in all directions to achieve maximum efficiency. A high resolution was used where high levels of turbulence were expected.

The grid resolution was finest in the boundary layers and close to regions of disturbed flow, including the body near-field and the turbulent wake. The non-dimensional wall distance y^+ for a wall bounded flow is defined as:

$$y^+ \equiv \frac{u_\tau y}{\nu}, \tag{4.17}$$

where u_τ is the friction velocity and y is the height of the nearest cell to the wall. Maintaining a value of $y^+ \approx 1$ for the first few cells adjacent to the wall ensured that the grid was able to resolve the laminar sublayer [74]. Away from the body and the turbulent wake, the grid resolution was much coarser so that the computational cost could be reduced as far as possible. The total number of grid points in the single cylinder grids was 2.1 million, reaching 3.2 million cells in the tandem cylinder grids.

More computational mesh details specific to each test case are provided in the results chapters.

4.3.6 Convergence Criterion

The computational time step was chosen so that the shedding periods from the cylinders were properly resolved. Typically the non-dimensional time step Δt^* for the simulations was 0.02 where:

$$\Delta t^* = \frac{\Delta t U_\infty}{D}. \tag{4.18}$$

For most calculations, the cylinder diameter D was 0.0311 m yielding a physical time-step of 9×10^{-6} s. This corresponded to a sampling frequency of 111 kHz. According to the Nyquist criterion this meant that the highest resolved frequency was 55.5 kHz. For a cylinder shedding at a Strouhal number of $St = 0.2$ at $M = 0.2$ the shedding frequency would be approximately 443 Hz, and the shedding period approximately 2.25×10^{-3} s. Therefore each shedding cycle was resolved in approximately 250 time steps.

The implicit dual time-stepping method was employed with 25 sub-iterations to ensure convergence. Convergence was determined by monitoring global variables such as the lift and drag coefficients, and the time step residuals (mass imbalance in each cell).

4.4 High-Order CAA Solver

Southampton University's Computational Aeroacoustics (SotonCAA[1]) code was used to solve the Navier-Stokes equations in generalised coordinates using high-order numerical schemes. These schemes are up to sixth-order accurate in space, and fourth-order accurate in time. The code employs multi-block structured grids and can be used for parallel computing. The code possesses excellent wave propagation characteristics, with marginal dispersion, dissipation, and anisotropy errors, making it suitable for solving aeroacoustic problems.

4.4.1 Governing Equations

The governing equations solved by SotonCAA are the compressible three-dimensional Navier-Stokes equations in curvilinear coordinates. In absence of body forces and external heat addition, these equations may be written as

[1]The SotonCAA code is a high-order CFD code developed at the University of Southampton, optimised for aeroacoustic applications.

$$\frac{\partial \hat{\mathbf{Q}}}{\partial t} + \frac{\partial \hat{\mathbf{E}}}{\partial \xi} + \frac{\partial \hat{\mathbf{F}}}{\partial \eta} + \frac{\partial \hat{\mathbf{G}}}{\partial \zeta} = \frac{M_\infty}{Re_L}\left[\frac{\partial \hat{\mathbf{E}}_v}{\partial \xi} + \frac{\partial \hat{\mathbf{F}}_v}{\partial \eta} + \frac{\partial \hat{\mathbf{G}}_v}{\partial \zeta}\right], \tag{4.19}$$

where $\hat{\mathbf{Q}}$ is the solution vector of conserved variables

$$\hat{\mathbf{Q}} = (1/J)\left[\rho,\ \rho u,\ \rho v, \rho w,\ \rho E\right]^T \tag{4.20}$$

J is the Jacobian of transformation

$$J = \left|\frac{\partial(\xi,\eta,\zeta)}{\partial(x,y,z)}\right|. \tag{4.21}$$

The inviscid fluxes, $\hat{\mathbf{E}}$, $\hat{\mathbf{F}}$, $\hat{\mathbf{G}}$, and viscous fluxes, $\hat{\mathbf{E}}_v$, $\hat{\mathbf{F}}_v$, $\hat{\mathbf{G}}_v$, are given by

$$\hat{\mathbf{E}} = \frac{1}{J}\begin{bmatrix} \rho U \\ \rho u U + \xi_x p \\ \rho v U + \xi_y p \\ \rho w U + \xi_z p \\ (\rho E + p)U \end{bmatrix}, \quad \hat{\mathbf{E}}_v = \frac{1}{J}\begin{bmatrix} 0 \\ \xi_x\tau_{xx} + \xi_y\tau_{xy} + \xi_z\tau_{xz} \\ \xi_x\tau_{xy} + \xi_y\tau_{yy} + \xi_z\tau_{yz} \\ \xi_x\tau_{xz} + \xi_y\tau_{yz} + \xi_z\tau_{zz} \\ \xi_x b_x + \xi_y b_y + \xi_z b_z \end{bmatrix} \tag{4.22}$$

$$\hat{\mathbf{F}} = \frac{1}{J}\begin{bmatrix} \rho V \\ \rho u V + \eta_x p \\ \rho v V + \eta_y p \\ \rho w V + \eta_z p \\ (\rho E + p)V \end{bmatrix}, \quad \hat{\mathbf{F}}_v = \frac{1}{J}\begin{bmatrix} 0 \\ \eta_x\tau_{xx} + \eta_y\tau_{xy} + \eta_z\tau_{xz} \\ \eta_x\tau_{xy} + \eta_y\tau_{yy} + \eta_z\tau_{yz} \\ \eta_x\tau_{xz} + \eta_y\tau_{yz} + \eta_z\tau_{zz} \\ \eta_x b_x + \eta_y b_y + \eta_z b_z \end{bmatrix} \tag{4.23}$$

$$\hat{\mathbf{G}} = \frac{1}{J}\begin{bmatrix} \rho W \\ \rho u W + \zeta_x p \\ \rho v W + \zeta_y p \\ \rho w W + \zeta_z p \\ (\rho E + p)W \end{bmatrix}, \quad \hat{\mathbf{G}}_v = \frac{1}{J}\begin{bmatrix} 0 \\ \zeta_x\tau_{xx} + \zeta_y\tau_{xy} + \zeta_z\tau_{xz} \\ \zeta_x\tau_{xy} + \zeta_y\tau_{yy} + \zeta_z\tau_{yz} \\ \zeta_x\tau_{xz} + \zeta_y\tau_{zy} + \zeta_z\tau_{zz} \\ \zeta_x b_x + \zeta_y b_y + \zeta_z b_z \end{bmatrix} \tag{4.24}$$

where ρ, u, v, w, p and E are the fluid density, Cartesian velocity components, static pressure, and specific total energy, respectively. The specific total energy is defined as

$$E = e + \frac{1}{2}(u^2 + v^2 + w^2) \tag{4.25}$$

where e is the specific internal energy density. The pressure is related to the other thermodynamic variables by the equation of state for an idea gas

$$p = (\gamma - 1)\rho + \left(E - \frac{1}{2}(u^2 + v^2 + w^2)\right), \tag{4.26}$$

where $\gamma = c_p/c_v$ is the ratio of specific heat coefficients under constant pressure and constant volume. The contravarient velocities, U, V, and W, are defined by

$$\begin{aligned} U &= \xi_x u + \xi_y v + \xi_z w, \\ V &= \eta_x u + \eta_y v + \eta_z w, \\ W &= \zeta_x u + \zeta_y v + \zeta_z w. \end{aligned} \tag{4.27}$$

The viscous stress terms τ_{ij} are related to the Cartesian velocity components by the equation

$$\tau_{ij} = \mu \left[\left(\frac{\partial u_j}{\partial x_i} + \frac{\partial u_i}{\partial x_j} \right) - \frac{2}{3} \frac{\partial u_k}{\partial x_k} \delta_{ij} \right] \tag{4.28}$$

where μ is the molecular viscosity and δ_{ij} is the Kronecker delta. The terms b_j are defined as follows

$$b_j = u_i \tau_{ij} + \frac{1}{(\gamma - 1)} \frac{\mu}{Pr} \frac{\partial c^2}{\partial x_j} \tag{4.29}$$

where c is the local sound speed.

The governing equations are non-dimensionalised by reference length L^*, freestream values of density ρ^*_∞, sound speed c^*_∞, and viscosity μ^*_∞, where superscript $()^*$ denotes a reference quantity. On this basis the characteristic parameters of Mach number M_∞, Reynolds number Re_L, and Prandtl number Pr, have the following definitions

$$M_\infty = \frac{|\mathbf{u}^*_\infty|}{c^*_\infty}, \quad Re_L = \frac{\rho^* |\mathbf{u}^*_\infty| L^*}{\mu^*_\infty}, \quad Pr = \frac{c^*_p \mu^*_\infty}{k^*_c} \tag{4.30}$$

where $\mathbf{u}^*_\infty$ is the freestream velocity vector, c^*_p is the specific heat coefficient at constant pressure and k^*_c is the thermal conductivity coefficient.

4.4.2 Spatial Discretization

The solver uses a finite-difference approach to discretize the governing equations motivated by the natural extension to high-order accuracy. For any scalar quantity φ, the first spatial derivative $(\partial\varphi/\partial\xi)_i$ at any point i is computed in the transformed plane by solving:

$$\frac{1}{2} D^F_i = \frac{1}{2\beta_F \Delta\eta} [b_F(\varphi_{i+1} - \varphi_i) + d_F(\varphi_{i-1} - \varphi_i) + e_F(\varphi_{i-2} - \varphi_i)] - \frac{\alpha_F}{2\beta_F} D^F_{i+1}, \tag{4.31}$$

$$\frac{1}{2} D^B_i = \frac{1}{2\beta_F \Delta\eta} [b_F(\varphi_i - \varphi_{i-1}) + d_F(\varphi_i - \varphi_{i+1}) + e_F(\varphi_i - \varphi_{i+2})] - \frac{\gamma_B}{2\beta_B} D^B_{i-1}, \tag{4.32}$$

$$D_i = \frac{1}{2}(D^F_i + D^B_i), \tag{4.33}$$

where D_i is the desired approximation of the spatial derivative obtained by adding the forward and backward estimates of the spatial derivative, D_i^F and D_i^B. The coefficients b_f, d_f, and e_f determine the spatial properties of the algorithm. In this work, the sixth-order prefactored compact scheme of Hixon [40] was employed for high-accuracy spatial discretisation.

At each time-stepping stage, the derivatives of the inviscid flux terms were calculated by first forming the fluxes at each grid point and subsequently differentiating each component using the equations above. For the computation of the viscous terms, the primitive variables were first differentiated to form the components of the stress tensor and the heat flux vector at each grid point. The viscous flux derivatives were then computed by a second application of the same scheme.

4.4.3 Filtering Scheme

Prefactored compact schemes can be susceptible to the growth of high-frequency modes originating from grid non-uniformity, boundary conditions, and non-linear flow features. Therefore a high-order filtering scheme was employed to dampen high frequency modes in the numerical prediction. The scheme adopted was an explicit filtering scheme given by

$$\hat{\varphi}_i = \sum_{j=-m}^{j=m} \alpha_j \varphi_{i+j}, \tag{4.34}$$

where $\hat{\varphi}$ is the filtered version of the variable φ, α_j are the filtering coefficients, and $2m$ is the order of the filter. The coefficients used ensure the spectral characteristics of the filter closely match those of the spatial compact discretization, therefore preserving the spatial accuracy. A seven point stencil, 6th-order was used in the LES simulations. Central differencing stencils were adopted for the interior points whereas a biased stencil was adopted at points approaching the boundary, which gradually reduced the order of the filter to third-order at the boundary point. The filter was applied sequentially in each coordinate direction to the conserved variables at the end of each time-stepping cycle.

4.4.4 Temporal Integration

A second-order implicit scheme was chosen for the temporal integration. This was chosen in preference to a 4th-order Runge-Kutta scheme due to its comparatively higher CFL limit. The implicit scheme allowed a Courant number of typically $\Delta t c_\infty / \Delta x = 8$ to be adopted in the simulations, substantially reducing simulation time.

To achieve second-order accuracy, a pseudo-time τ is introduced to Equation 4.19 so that the original governing Equations 4.19 can be written as:

$$\frac{\partial \hat{\mathbf{Q}}}{\partial \tau} + \frac{\partial \hat{\mathbf{Q}}}{\partial t} + \frac{\partial \hat{\mathbf{E}}}{\partial \xi} + \frac{\partial \hat{\mathbf{F}}}{\partial \eta} + \frac{\partial \hat{\mathbf{G}}}{\partial \zeta} = \frac{M_\infty}{Re_L}\left[\frac{\partial \hat{\mathbf{E}}_v}{\partial \xi} + \frac{\partial \hat{\mathbf{F}}_v}{\partial \eta} + \frac{\partial \hat{\mathbf{G}}_v}{\partial \zeta}\right], \tag{4.35}$$

The scheme uses an implicit lower-upper approximate factorization algorithm employing Newton-like subiterations [61]. Between three and five subiterations has been shown to be suitable [61], and in the current simulation a Courant number of $\Delta t c_\infty/\Delta x = 8$ with $\Delta t = 0.00375 c_\infty/D$ and 5 sub-iterations per time-step were employed.

4.4.5 Turbulence Model

For the high-order solver, large-eddy simulation was adopted to model the turbulence. In LES the large scale turbulent eddies are solved explicitly whereas the small scale components are modelled by a so-called subgrid scale model. A filter is used to decompose an arbitrary variable φ into large and subgrid components such that

$$\bar{\varphi} = \int_\vartheta \aleph \varphi d\vartheta, \tag{4.36}$$

where $\aleph$ is the grid filtering function and the integration is performed across the entire domain. The variable φ can then be written as:

$$\varphi = \bar{\varphi} + \varphi_{\mathrm{sg}}, \tag{4.37}$$

where $\bar{\varphi}$ is the large scale component to be explicitly computed and φ_{sg} is the subgrid component to be modelled by the subgrid scale model. The Favre-averaged variable is defined by

$$\tilde{\varphi} = \frac{\overline{\rho\varphi}}{\bar{\rho}}. \tag{4.38}$$

With this formulation the vector of conserved variables $\hat{\boldsymbol{Q}}$ in Equation 4.20 can be written as

$$\hat{\mathbf{Q}} = (1/J)\left[\bar{\rho},\, \bar{\rho}\tilde{u},\, \bar{\rho}\tilde{v}, \bar{\rho}\tilde{w},\, \bar{\rho}\tilde{E}\right]^T, \tag{4.39}$$

whereas the flux vectors in Equations 4.22-4.24 can be rewritten as

$$\hat{\mathbf{E}} = \frac{1}{J}\begin{bmatrix} \bar{\rho}\tilde{U} \\ \bar{\rho}\tilde{u}\tilde{U} + \xi_x\bar{p} \\ \bar{\rho}\tilde{v}\tilde{U} + \xi_y\bar{p} \\ \bar{\rho}\tilde{w}\tilde{U} + \xi_z\bar{p} \\ \bar{\rho}\tilde{E}\tilde{U} + \xi_{x_i}\tilde{u}_i\bar{p} \end{bmatrix}, \quad \hat{\mathbf{E}}_v = \frac{1}{J}\begin{bmatrix} 0 \\ \xi_{x_i}(\tilde{\tau}_{i1} + \tau^s_{i1}) \\ \xi_{x_i}(\tilde{\tau}_{i2} + \tau^s_{i2}) \\ \xi_{x_i}(\tilde{\tau}_{i3} + \tau^s_{i3}) \\ \xi_{x_i}[\tilde{u}_j(\tilde{\tau}_{ij} + \tau^s_{ij}) - \tilde{q}_i - \ell^s_i] \end{bmatrix} \tag{4.40}$$

$$\hat{\mathbf{F}} = \frac{1}{J}\begin{bmatrix} \bar{\rho}\tilde{V} \\ \bar{\rho}\tilde{u}\tilde{V} + \eta_x\bar{p} \\ \bar{\rho}\tilde{v}\tilde{V} + \eta_y\bar{p} \\ \bar{\rho}\tilde{w}\tilde{V} + \eta_z\bar{p} \\ \bar{\rho}\tilde{E}\tilde{V} + \eta_{x_i}\tilde{u}_i\bar{p} \end{bmatrix}, \quad \hat{\mathbf{F}}_v = \frac{1}{J}\begin{bmatrix} 0 \\ \eta_{x_i}(\tilde{\tau}_{i1} + \tau^s_{i1}) \\ \eta_{x_i}(\tilde{\tau}_{i2} + \tau^s_{i2}) \\ \eta_{x_i}(\tilde{\tau}_{i3} + \tau^s_{i3}) \\ \eta_{x_i}[\tilde{u}_j(\tilde{\tau}_{ij} + \tau^s_{ij}) - \tilde{q}_i - \ell^s_i] \end{bmatrix} \tag{4.41}$$

$$\hat{\mathbf{G}} = \frac{1}{J}\begin{bmatrix} \bar{\rho}\tilde{W} \\ \bar{\rho}\tilde{u}\tilde{W} + \zeta_x\bar{p} \\ \bar{\rho}\tilde{v}\tilde{W} + \zeta_y\bar{p} \\ \bar{\rho}\tilde{w}\tilde{W} + \zeta_z\bar{p} \\ \bar{\rho}\tilde{E}\tilde{W} + \zeta_{x_i}\tilde{u}_i\bar{p} \end{bmatrix}, \quad \hat{\mathbf{G}}_v = \frac{1}{J}\begin{bmatrix} 0 \\ \zeta_{x_i}(\tilde{\tau}_{i1} + \tau^s_{i1}) \\ \zeta_{x_i}(\tilde{\tau}_{i2} + \tau^s_{i2}) \\ \zeta_{x_i}(\tilde{\tau}_{i3} + \tau^s_{i3}) \\ \zeta_{x_i}[\tilde{u}_j(\tilde{\tau}_{ij} + \tau^s_{ij}) - \tilde{q}_i - \ell^s_i] \end{bmatrix}. \tag{4.42}$$

With this formulation the stress tensor and the heat flux vector are given by

$$\tilde{\tau}_{ij} = \tilde{\mu}\left[\left(\frac{\partial\tilde{u}_j}{\partial x_i} + \frac{\partial\tilde{u}_i}{\partial x_j}\right) - \frac{2}{3}\frac{\partial\tilde{u}_k}{\partial x_k}\delta_{ij}\right], \tag{4.43}$$

$$\tilde{q}_i = \frac{1}{(\gamma-1)}\frac{\tilde{\mu}}{Pr}\frac{\partial\tilde{T}}{\partial x_i}, \tag{4.44}$$

where $\tilde{T}$ is the temperature. The additional terms in the filtered Navier-Stokes equations, τ^s_{ij} and ℓ^s_i, are the subgrid-stress and heat flux vectors

$$\tau^s_{ij} = -\frac{Re_L}{M_\infty}\bar{\rho}\left(\widetilde{u_i u_j} - \tilde{u}_i\tilde{u}_j\right), \tag{4.45}$$

$$\ell^s_i = \frac{Re_L}{M_\infty}\bar{\rho}\left(\widetilde{u_i T} - \tilde{u}_i\tilde{T}\right). \tag{4.46}$$

In SotonCAA the Smagorinsky subgrid-stress (SGS) model [70] was employed to obtain the subgrid terms. The compressible version of the model is given by

$$\tau^s_{ij} - \frac{1}{3}\tau^s_{kk}\delta_{ij} = -2\mu_t\left(\tilde{\phi}_{ij} - \frac{1}{3}\tilde{\phi}_{kk}\delta_{ij}\right), \tag{4.47}$$

where

$$\tilde{\phi}_{ij} = \frac{1}{2}\left(\frac{\partial\tilde{u}_i}{\partial x_j} + \frac{\partial\tilde{u}_j}{\partial x_i}\right), \tag{4.48}$$

and

$$\mu_t = \frac{Re_L}{M_\infty}C_{\text{sgs}}\Delta^2\bar{\rho}\tilde{\phi}_M, \tag{4.49}$$

where $\tilde{\phi}_M$ is the magnitude of the rate-of-strain tensor which is defined by

$$\tilde{\phi}_M = (2\tilde{\phi}_{ij}\tilde{\phi}_{ij})^{1/2}, \tag{4.50}$$

and the eddy viscosity length scale Δ is given by

$$\Delta = \left(\frac{1}{J}\right)^{1/3}. \tag{4.51}$$

The constant turbulent Prandtl number assumption is used to calculate the subgrid scale heat flux vector:

$$\ell_i^s = -\left(\frac{\mu_t}{Pr_t}\right)\frac{\partial \tilde{T}}{\partial x_i}. \tag{4.52}$$

In the model, C_{sgs} is the eddy-viscosity model constant which was set to 0.008464 and the isotropic part of the stress tensor, $\frac{1}{3}\tau_{kk}$, was neglected for the low Mach number calculation.

4.4.6 Boundary Conditions

Wall Boundary Condition No-slip boundary conditions were employed along the cylinder walls which is imposed by setting the three velocity components u, v, w to zero as in Equation 4.12. The pressure on the wall was determined from linear extrapolation from the nearest adjacent mesh points and the wall temperature was set to ensure that the adiabatic condition is satisfied.

Buffer Zone Boundary Condition Along the external boundaries, an explicit buffer zone method was adopted [20]. In the buffer zone method the computational domain is extended to create a buffer zone where the solution vector is explicitly damped after each time step toward a target value $\mathbf{Q}_{target}$ using

$$\mathbf{Q}^{n+1} = \acute{\mathbf{Q}}^{n+1} - \varsigma(\acute{\mathbf{Q}}^{n+1} - \mathbf{Q}_{target}), \tag{4.53}$$

where $\acute{\mathbf{Q}}^{n+1}$ is the solution vector after each time step and ς is the damping coefficient that varies smoothly according to the function

$$\varsigma(X_{bs}) = \varsigma_{max}\left(1 + \frac{x_{bz} - L_{bz}}{L_{bz}}\right)^{\beta_{bz}}, \tag{4.54}$$

where L_{bz} is the width of the buffer zone, x_{bz} is the distance measured from the inner boundary of the buffer zone and ς_{max} and β_{bz} are coefficients which determine the shape of the damping function.

4.4.7 Characteristic Interface Condition

Grid singularity due to grid skew is a major problem for high-order finite differencing stencils. Grid singularity occurs where two or more grid lines meet at different angles

leading to singular points. At these singular points the grid metrics are inaccurate and can lead to high instability in computations with curvilinear grids. Skewed grid lines are often unavoidable for even simple geometries and can severely limit the usefulness of high-order accurate CFD code. Figure 4.2 illustrates the errors that arise at locations of high skew.

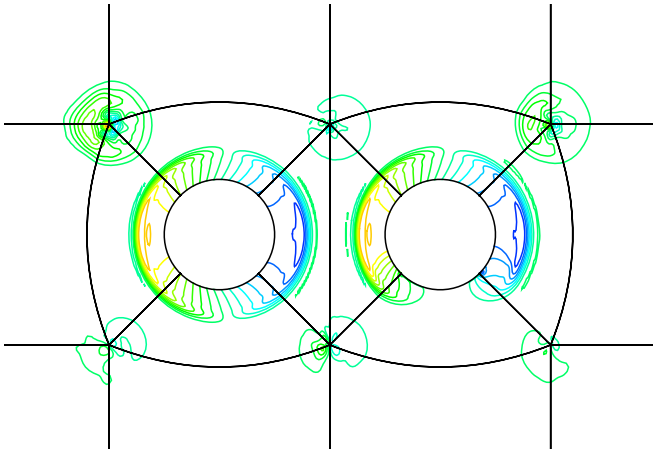

FIGURE 4.2: Pressure contour discontinuities resulting from a tandem cylinder computation on a grid with high skew and adopting central differencing across block boundaries.

A solution to this problem was proposed by Kim and Lee [46], using the characteristic form of the governing equations. In this approach, the computational domain is decomposed so that the inter-block boundaries coincide with the singular grid lines. Biased stencils for the numerical scheme are used so that the differencing stencils do not cross the interface, thereby avoiding discontinuity at each singular point, whereas central differencing is maintained within the block interiors. Interface conditions are then imposed at the block interfaces for communication between the blocks.

In the following, the characteristic interface conditions are derived and the implementation procedure is explained. For clarity, equations are derived relative to the ξ direction; however, the general case has been implemented in SotonCAA so that any block orientation can be used.

Equation 4.19 can be written in characteristic form in the direction normal to the interface, where ξ is a constant value:

$$\frac{\partial \mathbf{R}}{\partial t} + \bar{\lambda}\frac{\partial \mathbf{R}}{\partial \xi} = \mathbf{S}_C \tag{4.55}$$

where the terms in Equation 4.55 are defined as

$$\delta\mathbf{R} = \bar{\mathbf{P}}^{-\mathbf{1}}\delta\mathbf{Q}, \qquad \lambda\frac{\partial \mathbf{R}}{\partial \xi} = \bar{\mathbf{P}}^{-\mathbf{1}}\left(\xi_x\frac{\partial \mathbf{E}}{\partial \xi} + \xi_y\frac{\partial \mathbf{F}}{\partial \xi} + \xi_z\frac{\partial \mathbf{G}}{\partial \xi}\right), \tag{4.56}$$

and $\mathbf{S_c}$ consists of the source terms in Equations 4.19:

$$\mathbf{S}_C = J\bar{\mathbf{P}}^{-1}\left\{\hat{\mathbf{S}}_v - \left[\mathbf{E}\frac{\partial}{\partial\xi}\left(\frac{\xi_x}{J}\right) + \mathbf{F}\frac{\partial}{\partial\xi}\left(\frac{\xi_y}{J}\right) + \mathbf{G}\frac{\partial}{\partial\xi}\left(\frac{\xi_z}{J}\right) + \frac{\partial\hat{\mathbf{F}}}{\partial\eta} + \frac{\partial\hat{\mathbf{G}}}{\partial\zeta}\right]\right\} \tag{4.57}$$

where $\bar{\mathbf{P}}^{-1}$ is a transformation matrix which is defined in Appendix B, and $\hat{\mathbf{S}}_v$ is a source term that consists of the viscous flux derivatives on the right hand side of Equation 4.19. The terms **E**, **F**, and **G**, are the inviscid flux vectors in Cartesian coordinates. The characteristic differential variables and the corresponding convection speeds are represented as

$$\delta\mathbf{R} = \begin{bmatrix} \delta\rho - \frac{\delta p}{c^2} \\ \delta\tilde{W} \\ \delta\tilde{V} \\ \frac{\delta p}{\rho c} + \delta\tilde{U} \\ \frac{\delta p}{\rho c} - \delta\tilde{U} \end{bmatrix}, \qquad \bar{\lambda}(diag) = \begin{bmatrix} U \\ U \\ U \\ U + c\sqrt{\xi_x^2 + \xi_y^2 + \xi_z^2} \\ U - c\sqrt{\xi_x^2 + \xi_y^2 + \xi_z^2} \end{bmatrix} \tag{4.58}$$

where the tilde indicates a quantity normalised by $|\nabla\xi|$, c is the speed of sound and, U, V and W are the contravarient velocities. The contravarient velocity and its differential are given by

$$U = \xi_x u + \xi_y v + \xi_z w, \qquad \delta\tilde{U} = \tilde{\xi}_x\delta u + \tilde{\xi}_y\delta v + \tilde{\xi}_z\delta w \tag{4.59}$$

whereas the velocity differentials in parallel to the ξ direction are given as

$$\delta\tilde{V} = -\tilde{\xi}_x\delta v + \tilde{\xi}_y\delta u, \qquad \delta\tilde{W} = \tilde{\xi}_x\delta w - \tilde{\xi}_z\delta u. \tag{4.60}$$

The characteristic waves can be easily classified as outgoing or incoming by the sign of their convection speeds, and so waves passing between the block interfaces can be compensated for in each block.

The Interface Condition Interface conditions are used to communicate the incoming and outgoing characteristic waves between adjacent blocks in a strict manner. The aim is to match the primitive variables on the left and right side of the interface, and this should be satisfied regardless of time. This can be expressed as

$$(\rho^L, \mathbf{v}^L, p^L) = (\rho^R, \mathbf{v}^R, p^R), \qquad \partial_t(\rho^L, \mathbf{v}^L, p^L) = \partial_t(\rho^R, \mathbf{v}^R, p^R). \tag{4.61}$$

In terms of the characteristic variables, this is expressed as

$$\frac{\partial\mathbf{R}^L}{\partial t} = \frac{\partial\mathbf{R}^R}{\partial t}. \tag{4.62}$$

If the convection term in Equation 4.55 is given as

$$\mathbf{L} = \bar{\lambda}\frac{\partial\mathbf{R}}{\partial\xi}, \tag{4.63}$$

then Equation 4.62 can be represented as

$$\mathbf{L}^L - \mathbf{S}_C^L = \mathbf{L}^R - \mathbf{S}_C^R, \tag{4.64}$$

where $\mathbf{L}$ is given by

$$\mathbf{L} = J\bar{\mathbf{P}}^{-1}\left\{\frac{\partial \mathbf{E}}{\partial \xi} - \left[\mathbf{E}\frac{\partial}{\partial \xi}\left(\frac{\xi_x}{J}\right) + \mathbf{F}\frac{\partial}{\partial \xi}\left(\frac{\xi_y}{J}\right) + \mathbf{G}\frac{\partial}{\partial \xi}\left(\frac{\xi_z}{J}\right)\right]\right\}. \tag{4.65}$$

Equation 4.64 represents the interface conditions in terms of spatial derivatives and is used to communicate physical information through the interface. Either the left or right convection term should be corrected by the other one based on the sign of the convection speeds. Thus, the interface conditions can be summarised as follows:

$$L_m^L = L_m^R - S_{Cm}^R + S_{Cm}^L \quad \text{if} \quad \lambda_m^L/|\lambda_m^L| = \lambda_m^R/|\lambda_m^R| \leq 0, \tag{4.66}$$

$$L_m^R = L_m^L - S_{Cm}^L + S_{Cm}^R \quad \text{if} \quad \lambda_m^L/|\lambda_m^L| = \lambda_m^R/|\lambda_m^R| \geq 0, \tag{4.67}$$

where the subscript m represents the components of a vector $m = 1, ..., 5$.

Implementation Procedure These characteristic interface conditions have been implemented into SotonCAA as suggested by Kim and Lee [46]. The procedure to be completed for each stage of the time-marching steps is described as follows:

1. The flux derivatives in Equation 4.19 are first evaluated for each block using a biased stencil so that the blocks remain isolated. The normal flux derivative on the interface is then to be corrected, for example $\partial\hat{\mathbf{E}}/\partial\xi$. In this explanation the ξ direction is used, however the code has been generalised to accommodate any block-to-block orientation.

2. The initial guess of the characteristic convection term $\mathbf{L}$ is then calculated for the left and right blocks using Equation 4.65.

3. The new corrected characteristic convection term for each block is then calculated using the interface conditions and is represented by $\mathbf{L}^*$

4. The normal-flux derivative term is then recalculated by the corrected characteristic convection term using the following identity:

$$\left(\frac{\partial \hat{\mathbf{E}}}{\partial \xi}\right)^* = \frac{1}{J}\bar{\mathbf{P}}\mathbf{L}^* + \left[\mathbf{E}\frac{\partial}{\partial \xi}\left(\frac{\xi_x}{J}\right) + \mathbf{F}\frac{\partial}{\partial \xi}\left(\frac{\xi_y}{J}\right) + \mathbf{G}\frac{\partial}{\partial \xi}\left(\frac{\xi_z}{J}\right)\right]$$

   where $\bar{\mathbf{P}}$ is the inverse matrix of $\bar{\mathbf{P}}^{-1}$ and is given in Appendix B. This new corrected term is then returned to Equation 4.19 to be integrated in time.

5. Finally, the primitive variables on the interface are refined by averaging the left and right-hand values so that $(\rho^L, \mathbf{v}^L, p^L)^* = (\rho^R, \mathbf{v}^R, p^R)^*$

These boundary conditions have been implemented into SotonCAA to enable the code to solve the flow around the tandem cylinder geometries where grid skew was unavoidable. The procedure outlined by Kim and Lee [46] was extended for the general case where the block coordinate systems are arbitrary. The boundary conditions have been implemented for turbulent Navier-Stokes computations and were parallelised for multi-processor tasks. Full details of the implementation are provided in Appendix B and validation cases are included in Appendix A.

4.5 Acoustic Solver

4.5.1 Ffowcs Williams and Hawkings Equation

The Ffowcs Williams and Hawkings (FW-H) equation [24] is an inhomogeneous wave equation derived from the exact rearrangement of the Navier-Stokes and the continuity equations. The FW-H equation is defined by Equation 2.7, but can be expressed in terms of the far-field acoustic pressure, $p' = p - p_0$, as:

$$\begin{aligned} \frac{1}{c_0^2}\frac{\partial^2 p'}{\partial t^2} - \nabla^2 p' &= \frac{\partial^2}{\partial x_i \partial x_j} T_{ij} H(f) \\ &- \frac{\partial}{\partial x_i}\left[P_{ij} n_j + \rho u_i (u_n - v_n)\right] \delta(f) \\ &+ \frac{\partial}{\partial t}\left[\rho_0 v_n + \rho(u_n - v_n)\right] \delta(f), \end{aligned} \tag{4.68}$$

where

u_i = fluid velocity component in x_i direction
u_n = fluid velocity component normal to the surface $f = 0$
v_i = surface velocity component in the x_i direction
v_n = surface velocity component normal to the surface
$\delta(f)$ = Dirac delta function
$H(f)$ = Heaviside function
n_j = outwards unit normal vector to the surface $f = 0$

The function f describes the surface S and is defined to be positive everywhere outside the surface S and negative in the interior of S, which facilitates the use of generalised function theory and the free-space Green function in the solution of Equation 4.68. T_{ij} and P_{ij} are the Lighthill and compressive stress tensors defined by Equations 2.4 and 2.5 respectively.

Equation 4.68 represents the FW-H equation in differential form. The solution of Equation 4.68 consists of surface and volume integrals. The retarded time formulation of the FW-H equation involves the calculation of acoustic signals by summing all the signals received by an observer at the same time t. Depending on the location and the velocity of both source and observer, these signals are emitted at different times and travel over a different distance to reach the observer at the same time t. Hence, the retarded time formulation can be regarded as the signal analysed from the point of view of the observer. The retarded time, τ, is defined as follows:

$$\tau = t - \frac{r}{c_0}, \tag{4.69}$$

where r is the distance to the observer. The solution of Equation 4.68 is obtained using the free-space Green function which is given by:

$$G(\mathbf{x}, \mathbf{y}, t, \tau) = \frac{\delta(g)}{4\pi r}, \tag{4.70}$$

where

$$g = \tau - t + \frac{|\mathbf{x} - \mathbf{y}|}{c_0}, \quad r = |\mathbf{x} - \mathbf{y}|. \tag{4.71}$$

The solution as listed in Reference [23] is:

$$p'(x,t) = p'_Q(x,t) + p'_L(x,t) \tag{4.72}$$

The term $p'_T(x,t)$ is known as the thickness noise and $p'_L(x,t)$ the loading noise, given by

$$\begin{aligned} 4\pi p'_T(x,t) &= \int_S \left[\frac{\rho_0 \left(\dot{U}_n + U_{\dot{n}} \right)}{r(1-M_r)^2} \right]_{\text{ret}} dS \\ &+ \int_S \left[\frac{\rho_0 U_n \left\{ r\dot{M}_r + c(M_r - M^2) \right\}}{r^2(1-M_r)^3} \right]_{\text{ret}} dS \end{aligned} \tag{4.73}$$

$$\begin{aligned} 4\pi p'_L(x,t) &= \int_S \left[\frac{\dot{L}_r}{cr(1-M_r)^2} \right]_{\text{ret}} dS \\ &+ \int_S \left[\frac{L_r - L_M}{r^2(1-M_r)^2} \right]_{\text{ret}} dS \\ &+ \int_S \left[\frac{L_r \left\{ r\dot{M}_r + c(M_r - M^2) \right\}}{cr(1-M_r)^3} \right]_{\text{ret}} dS. \end{aligned} \tag{4.74}$$

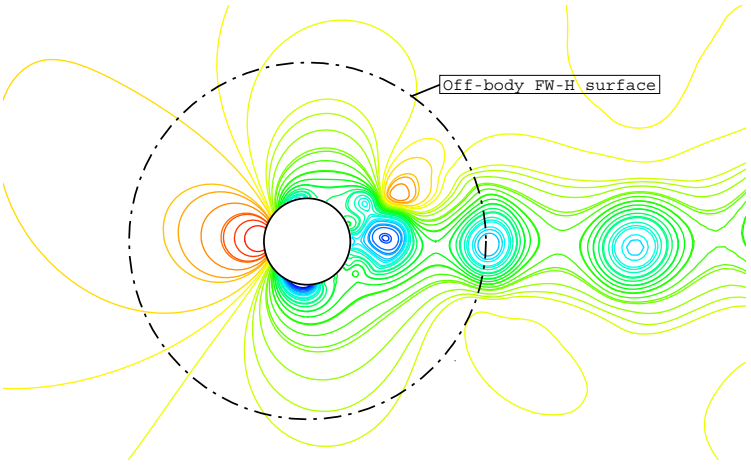

FIGURE 4.3: Example of off-body permeable FW-H integration surface for single cylinder simulations.

where

$$U_i = v_i + \frac{\rho}{\rho_0}(u_i - v_i), \tag{4.75}$$

$$L_i = P_{ij}\hat{n}_j + \rho u_i(u_n - v_n). \tag{4.76}$$

Definitions of the equation variables can be found in Reference [23]. The complete solution contains both volume and surface integrals. The surface integrals represent the contribution from monopole and dipole acoustic sources and partially by quadrupole sources, whereas the volume integrals represent the contribution from the quadrupole sources only. According to Lighthill's [49] quadrupole theory $I \propto [Mc]^5$, while for Curle's [11] dipole theory $I \propto [Mc]^3$. Therefore, at low Mach numbers the contribution of the volume integrals becomes small compared to that of the surface integrals, and the volume integrals are often dropped for low-subsonic flows. The retarded time solution, with the volume quadrupole term neglected, is often known as formulation 1A of Farassat [22], and this was employed by the FW-H solver.

It is not required that the integration surface $f = 0$ coincides with body surfaces or walls, and therefore the formulation allows for "off-body" permeable surfaces to be placed in the flow field. However, the grid resolution in the interior of the surface f should be fine enough to resolve the unsteady flow structures within it. Care was taken during the development of the computational grids to ensure this, and FW-H surface comparisons were made to verify the grid resolution inside the permeable surface.

Once the unsteady solution had become fully developed in such a way that the flow field statistics had become stationary (such as $\overline{C_D}$) the storage of the unsteady quantities on the surfaces was initiated and continued until a satisfactory time history had been gathered. Once this had been achieved, the FW-H formulation was solved for the defined array of far-field observers. For surfaces that were defined along a solid body only the

unsteady pressure was required by the FW-H solver, whereas for permeable surfaces the density and velocity components were also required.

4.5.2 Integration Surface Placement

Multiple on-body and off-body surfaces were defined in each simulation. Figure 4.3 illustrates an example location of the surfaces for the single cylinder cases. The radius of the permeable surfaces was typically two cylinder diameters. The passage of vortices through permeable integration surfaces has been identified as a potential cause of error in some applications and Lockard proposed a suitable correction [52]. In a 2-D URANS circular cylinder test case the differences between on-body and off-body surfaces was small and this difference was successfully corrected. However, the correction was not successful when applied to the 3-D detached-eddy simulation of flow around a circular cylinder. Therefore care was taken to examine any differences between on-body and off-body FW-H predictions. An integration surface sensitivity study for 2-D turbulent circular cylinder flow is included in Appendix A.

4.5.3 Far-Field Observers

For each simulation a spherical surface of far-field observers was defined at a radius of $R = 100$ cylinder diameters with a resolution of $\pi/18$ for the azimuth and polar angles, θ and ϕ respectively, where $(0 \leq \theta \leq 2\pi)$ and $(0 \leq \phi \leq \pi)$. The solution to the FW-H equation yielded a time history of the far-field acoustic pressure p' at each specified observer. The time histories were then post-processed to yield the acoustic spectral and directivity characteristics of the source.

4.6 Summary

In this section the important details and a description of the computational method were provided. The adopted "two-step" approach employed both a low-order Navier-Stokes CFD solver and a high-order CAA solver to compute the turbulent near-field, and an acoustic solver to solve the FW-H equation to yield the far-field acoustic prediction. Detached-eddy simulation and large-eddy Simulation were employed to model the turbulence and structured curvilinear grids are generated over the cylinder bodies. Characteristic boundary conditions were implemented into the CAA finite difference solver to accommodate skewed grids. A spherical arrangement of far-field observers was defined to capture the three-dimensional spectral and directivity characteristics of the noise source. Post-processing of the predicted far-field acoustic pressure history provided the acoustic spectrum and directivity results.

Chapter 5

Circular Cylinders in Cross-Flow

5.1 Outline

In this chapter the noise radiated by a single circular cylinder in cross-flow is investigated. The purpose of this work was to determine the characteristics of basic strut noise. Three-dimensional detached-eddy simulation provided the near-field turbulent flow field, whilst the FW-H equation was solved to predict the far-field acoustic pressure. For DES, the low-order solver was used.

5.2 Computational Setup

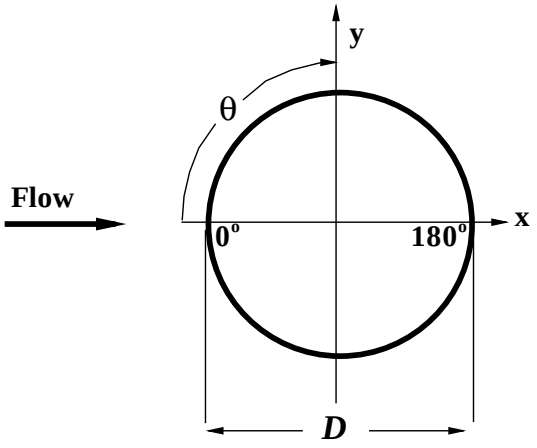

FIGURE 5.1: Definition of single cylinder geometry and nomenclature.

The single cylinder geometry and nomenclature used in this chapter are defined in Figure 5.1. In this 2-D illustration, the $z-$axis corresponds to the spanwise direction and is

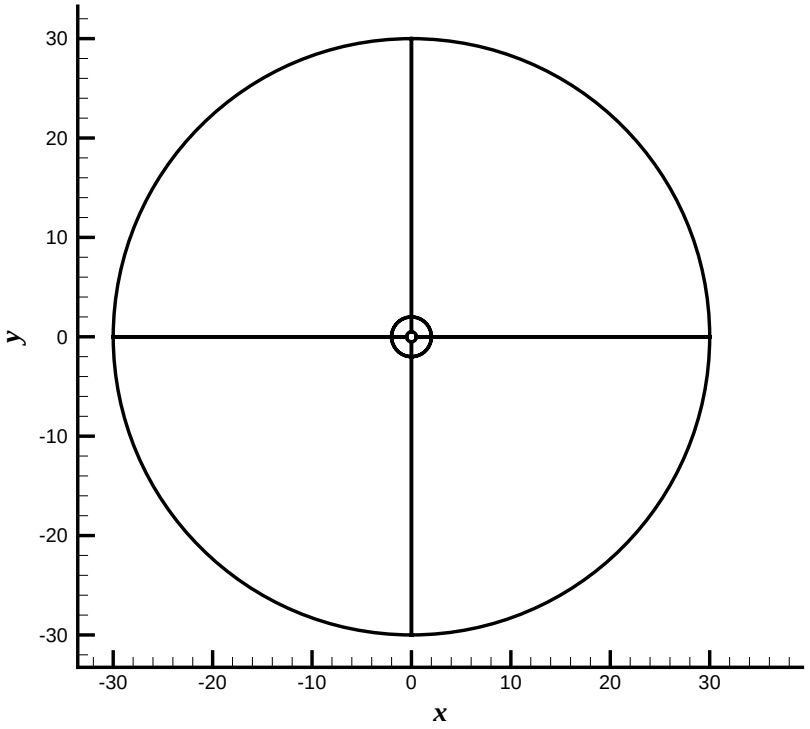

(a) Block structure

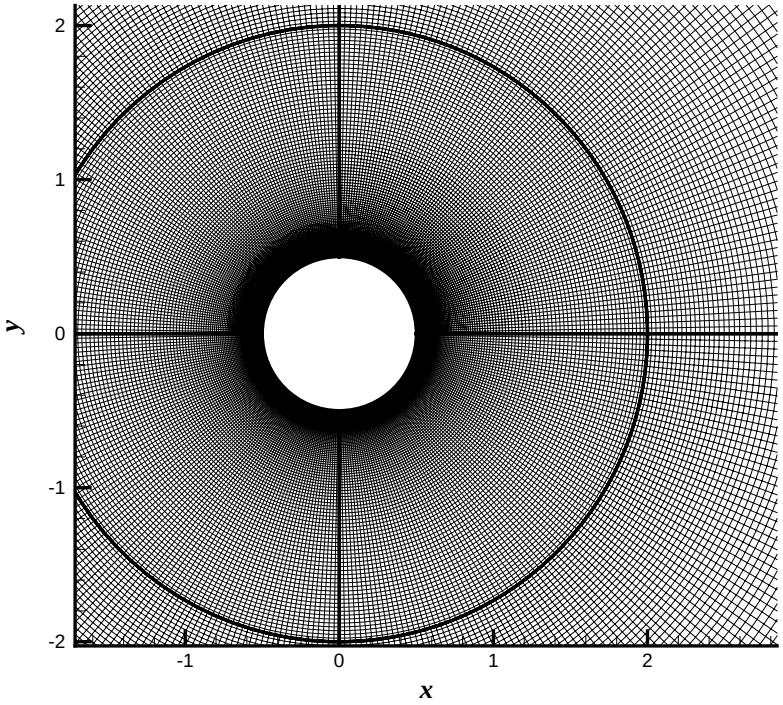

(b) Near-field grid

FIGURE 5.2: Non-dimensional single circular cylinder grid: (a) block structure and far-field domain, (b) near-field grid.

Parameter	**Symbol**	**Value**
Freestream Mach number	M	0.2
Cylinder diameter	D	0.020-0.2204 m
Turbulent viscosity ratio	$\frac{\mu_t}{\mu}$	10
Non-dimensional time step	Δt^*	0.02
Reynolds number	Re	$9 \times 10^4 - 10^6$

TABLE 5.1: Simulation parameters for single cylinder cross-flow simulations.

directed out of the page. Three-dimensional grids were generated suitably for detached-eddy simulation. The computational domain extends $30D$ outwards from the cylinder axis in the (x, y) plane, as shown in Figure 5.2(a). The span used in the computations was limited to two cylinder diameters and periodic boundary conditions were employed to simulate an infinite span. Experimental efforts [82] have measured the spanwise correlation length to be $L_C < 2D$ for supercritical flows and computational studies [79] have shown a span of $2D$ to be adequate to resolve the spanwise flow. Grids were generated with 20, 30, 40, and 50 spanwise grid-points to ensure proper resolution of the spanwise flow, and so that a grid dependence study could be performed. The grids featured circumferential clustering in the wake region where high resolution was required to resolve the unsteady flow structures. The value of y^+ for the first cells adjacent to the cylinder surface in each grid was $y^+ \approx 1$ to ensure proper resolution of the boundary layers. The grids were refined accordingly for each Reynolds number simulation.

The range of Reynolds numbers investigated was between $Re = 9 \times 10^4$ and $Re = 10^6$. This was achieved by maintaining a constant Mach number of $M = 0.2$ and varying the diameter of the cylinder between $D = 0.020$m and $D = 0.2204$ m. The simulation parameters are listed in Table 5.1. The range of Reynolds numbers correspond to subcritical, critical and supercritical cylinder flow regimes [82]. However, turbulent separation (TS) regimes (supercritical) were simulated in all simulations by setting the freestream turbulent viscosity level high enough relative to the molecular viscosity, following the strategy used by Travin *et al.* [79].

Both on-body and off-body permeable FW-H integration surfaces were defined in the computational domain. The non-dimensional time step in each computation was $\Delta t = 0.02D/U_\infty$ yielding approximately 250 time steps per shedding cycle for a Strouhal number of 0.2. The solutions were run for approximately 8000 time steps until a quasi-steady solution was reached before the sampling of flow variables on the FW-H integration surfaces. The computations were then run for another ≈ 10000 time steps to sample the unsteady flow statistics in the domain and along the integration surfaces. This yielded a total solution time of approximately 350 non-dimensional times which was sufficient to obtain a representative sample of 70 shedding cycles.

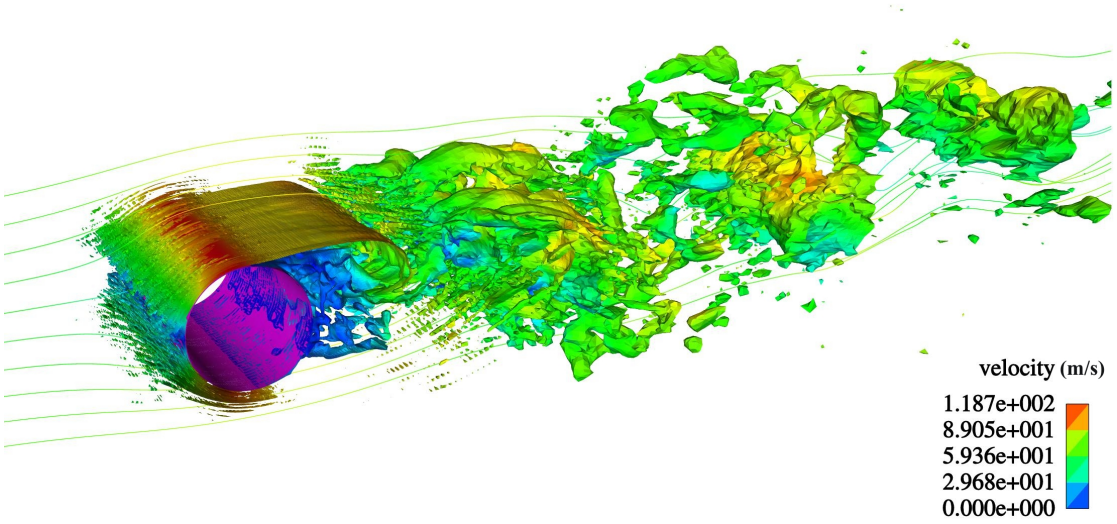

FIGURE 5.3: 3-D DES single cylinder flow visualisation of cc140k:TS2 simulation: iso-surface of instantaneous vorticity contours coloured by velocity magnitude in m/s.

5.3 Aerodynamic Results

Reported in Table 5.3 are the single cylinder results, indicating the predicted lift coefficient RMS, $\overline{C_L'}$; mean drag coefficient, $\overline{C_D}$; Strouhal number of the primary vortex shedding frequency, St; separation angle, θ_{sep}; minimum pressure coefficient, $-\overline{C_{p_{\text{min}}}}$; back pressure coefficient (the $\overline{C_p}$ at 180 degrees), $\overline{C_{bp}}$; and the peak SPL at an observer located at $R = 100D$, $\theta = 90$ deg, perpendicular to the cylinder axis; where the overline represents a time-averaged quantity. A summary of experimental results in [82] for supercritical flows is provided for comparison.

The comparison between results and experiment show that all simulations exhibit features associated with supercritical flows. The predicted low mean drag coefficient is consistent with the drag crisis which is a feature of TS flows due to the larger separation angles (i.e. $\theta_{\text{sep}} > 90$ deg) [82]. Separation occurred between $\theta_{\text{sep}} = 93.4$ deg at $Re = 9 \times 10^4$ up to $\theta_{\text{sep}} = 108$ deg at $Re = 1 \times 10^6$, leading to narrower wakes at higher Reynolds numbers. This was consistent with the measured mean drag coefficient which was between $\overline{C_D} = 0.683 - 0.484$; decreasing with increasing Reynolds number, reflected also by the rise in the base pressure coefficient $\overline{C_{bp}}$. In each case, vortex shedding at Strouhal numbers between $St = 0.27 - 0.311$ was predicted which is consistent with values found in experiment (see Figure 2.2). The shedding frequency increased with Re due to the delay of separation. The shedding frequencies were determined from the power spectral density of the lift coefficient shown in Figure 5.5 for the cc90k:TS2 case. The predicted $\overline{C_L'}$ ranged between 0.078 and 0.146 giving an indication of the strength of the surface pressure perturbations associated with the lift dipole.

Case	Re	Grid	$\overline{C_L'}$	$\overline{C_D}$	St	θ_{sep} (deg)	$-\overline{C_{p_{\min}}}$	$-\overline{C_{bp}}$	SPL †
cc90k:TS	9.0×10^4	340,230,30	0.112	0.683	0.277	93.4	1.85	0.757	75.4 dB
cc140k:TS1	1.4×10^5	340,230,20	0.146	0.636	0.285	100.0	2.00	0.743	-
cc140k:TS2	1.4×10^5	340,230,30	0.077	0.614	0.297	97.4	1.96	0.723	77.16 dB
cc140k:TS3	1.4×10^5	340,230,40	0.076	0.602	0.290	97.0	1.92	0.685	-
cc140k:TS4	1.4×10^5	340,230,50	0.075	0.597	0.298	97.0	1.91	0.676	-
cc300k:TS	3.0×10^5	340,230,30	0.090	0.555	0.315	102.6	2.06	0.661	78.5 dB
cc1m:TS	1.0×10^6	340,230,30	0.078	0.484	0.331	108.0	2.07	0.545	83.5 dB
Exp. [82]	$\approx 5 \times 10^6$	-	0.05-0.13	0.5-0.8	0.2-0.45	110.0	-	0.5-0.9	-

† Peak SPL at observer radius $R = 10$ m, $\theta = 90$ deg, span $L = 1$ m.

TABLE 5.2: Results summary of 3-D DES single cylinder in cross-flow simulations.

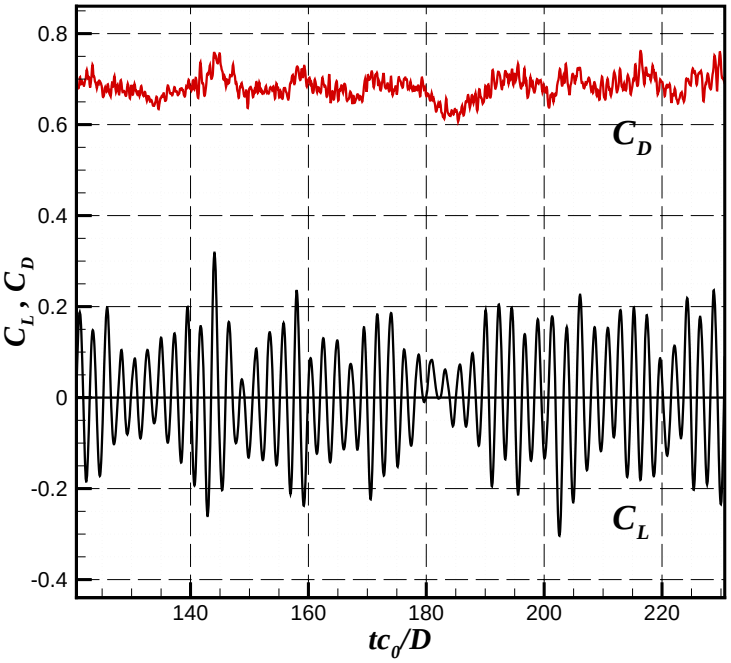

FIGURE 5.4: Sample of the C_L and C_D history prediction for 3-D DES single cylinder, $Re = 1.4 \times 10^5$, 30 mesh points along the cylinder span.

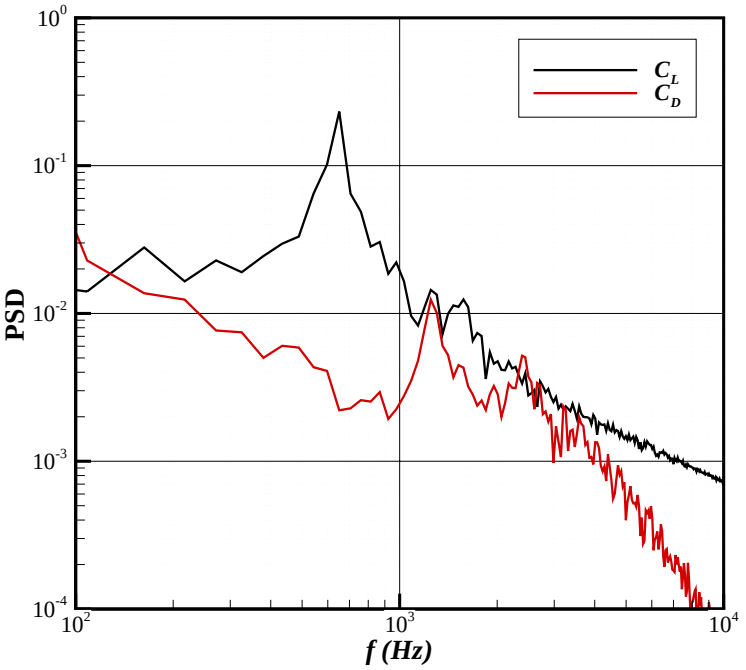

FIGURE 5.5: Power spectral density of surface force coefficients predicted for 3-D DES single cylinder, $Re = 1.4 \times 10^5$, 30 mesh points along the cylinder span.

Figure 5.3 shows the instantaneous iso-surface of vorticity coloured by velocity magnitude and the velocity streamlines predicted for the cc140k:TS2 case. This illustrates the highly three-dimensional non-linear flow field and also the resolution characteristics of the grid. Fairly weak and irregular vortex shedding was predicted behind the cylinders, which is a characteristic of the supercritical regime [82]. The shedding characteristics are strongly correlated with the body force histories shown in Figure 5.4, and the unsteady statistics reported in Table 5.3.

Figure 5.6(a) compares the predicted pressure coefficient along the upper cylinder surface to experimental results. The difference surface pressure distributions measured by Roshko, Cantwell, and Fage show the sensitivity of the circular cylinder flow to both Reynolds number and the transition location. The data from Cantwell and Coles [7] at Re=1.1×10^5 refers to subcritical flow and exhibits a C_p profile with a higher $\overline{C_{p_{\min}}}$ and lower $\overline{C_{bp}}$ due to early laminar separation. The experimental data from Roshiko [63] and Fage [21] was performed at supercritical and postcritical Reynolds numbers and are thus more comparable to the current supercritical simulations. In the surface pressure distribution of supercritical cylinders, the location of $\overline{C_{p_{\min}}}$ moves toward the cylinder rear and the suction increases as the extent of the favourable pressure gradient region increases. Also, the value of θ_{sep} moves downstream (which occurs along the pressure recovery curve) and the pressure recovery ($\overline{C_{bp}} - \overline{C_{p_{\min}}}$) increases. The rise in base pressure results in a lower mean drag. The measured and predicted results for the base pressure coefficient $\overline{C_{bp}}$, $\overline{C_{p_{\min}}}$, and the adverse pressure recovery compare favourably.

The aerodynamic quantities of particular interest to the far-field acoustics are the RMS lift and drag coefficients, and the Strouhal number. These provide an indication of the pressure fluctuation magnitude on the cylinder surface and an estimate of the peak frequency in the far-field acoustic pressure spectrum. Figure 5.4 shows a sample of the lift and drag coefficient histories. The plot shows large variations in C_L and C_D which are indicative of strong modulations in the vortex shedding. The magnitude of the fluctuating drag is much lower than that of the fluctuating lift and operates at approximately twice the shedding frequency. The power spectral density (PSD) of C_L and C_D is presented in Figure 5.5 that indicates the frequency content of the signals. The PSD is obtained from the discrete Fourier Transform of the time series over the computational time $200 \leq tD/U_\infty \leq 350$, sampled at $\Delta tD/U_\infty = 0.02$ using a Hamming window. The lift coefficient exhibits a large peak at $f = 659$ Hz which is the vortex shedding frequency and a secondary peak at roughly twice the shedding frequency representing the first harmonic. The magnitude of the drag content is much lower with a broad peak at approximately twice the shedding frequency.

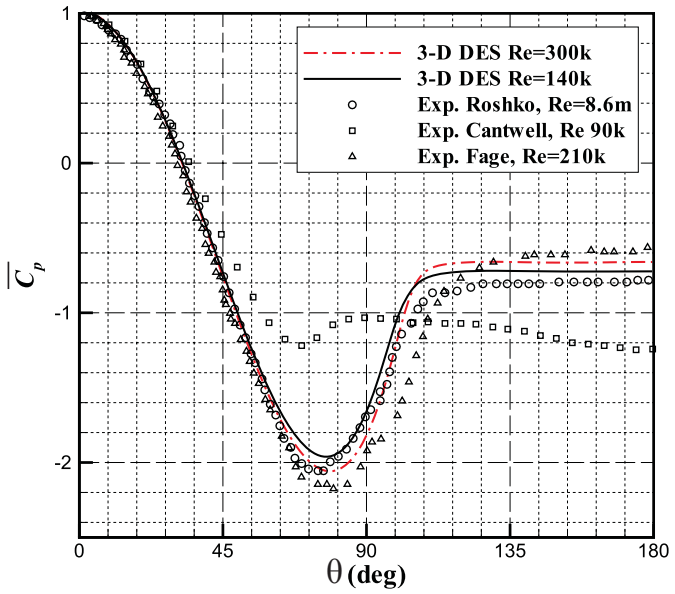

(a) $\overline{C_p}$.

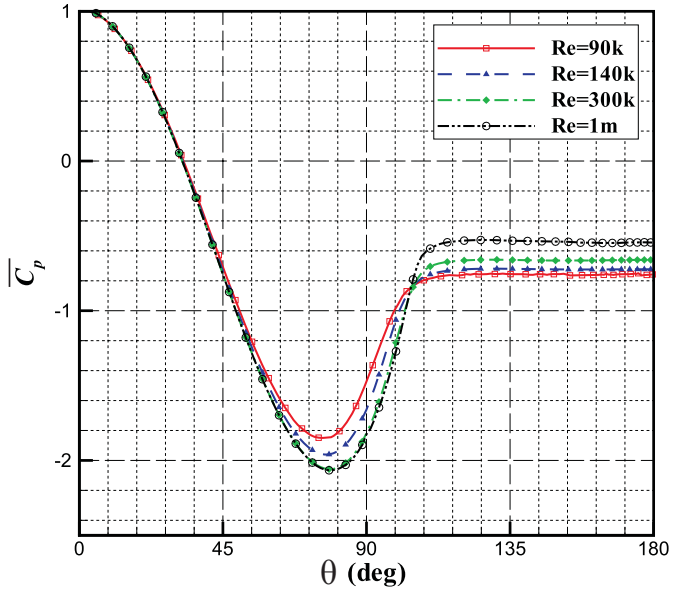

(b) $\overline{C_p}$ at different Re.

FIGURE 5.6: Mean surface pressure coefficient prediction: (a) comparison with experiments [7, 21, 63], (b) $\overline{C_p}$ at different Re.

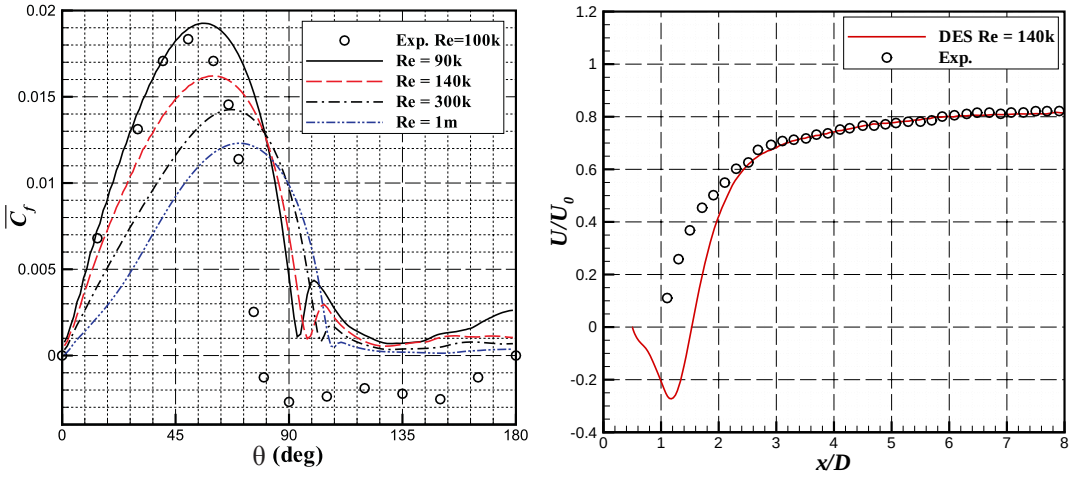

(a) Skin friction coefficient.

(b) Centerline velocity.

FIGURE 5.7: Single cylinder results: (a) skin friction coefficient prediction and comparison with experiment [2], (b) time-averaged streamwise velocity along centreline and comparison with experiment [7].

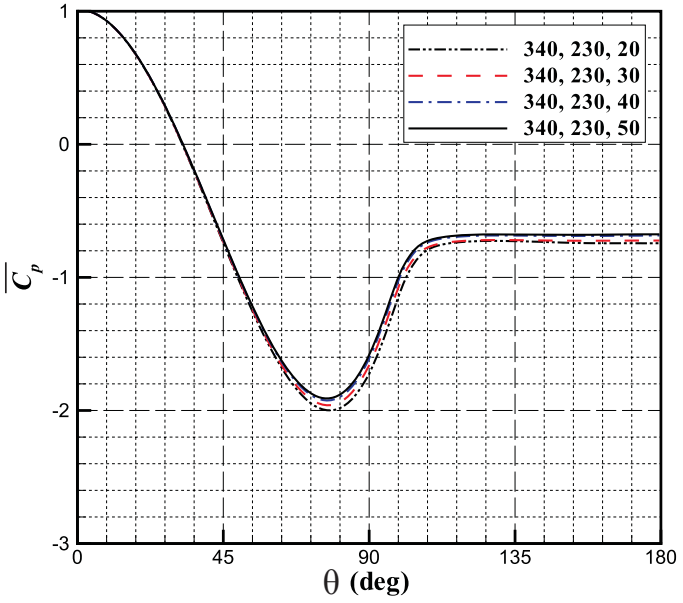

FIGURE 5.8: Surface pressure coefficient distribution at different spanwise grid densities.

5.3.1 Reynolds Number Effects

The results generally show a correlation between the flow statistics and Reynolds number, although no large variation was seen between the various parameters, except for $\overline{C'_L}$. This was expected since the location of transition, which normally dictates the flow regime, was controlled in the numerical simulations by setting the free-stream eddy-viscosity. This is in agreement with Travin *et al.* [79] who also found their TS DES cases to be relatively insensitive to Reynolds number.

Figure 5.6(b) compares the $\overline{C_p}$ distributions predicted at the different Reynolds numbers. The results are consistent with the anticipated physics and strongly reflect the supercritical flow regime. The value of $\overline{C_{p_{\min}}}$ is shown to become lower at higher Re, indicating higher suction as separation is delayed and the favourable pressure gradient region becomes larger. Figure 5.6(b) also shows a longer pressure recovery region at higher Re, leading to an increase in the base pressure and thus a lower drag coefficient.

Figure 5.7(a) shows the time- and span-averaged skin friction coefficient variation with Reynolds number and comparison with experiment [2]. The experimental result at $Re = 1 \times 10^5$ exhibits a lower separation angle and only one positive $C_{f_{\max}}$, indicating laminar separation. The characteristics of the numerical $\overline{C_f}$ curves are typical of the supercritical regime. The second $\overline{C_{f_{\max}}}$ is caused by a recirculation region begins at the first $\overline{C_{f_{\min}}}$. Separation occurs after the second $\overline{C_{f_{\max}}}$ when $\overline{C_f}$ becomes zero, however since the separation angle varies along the span, the time- and span-averaged $\overline{C_f}$ does not appear to cross zero in this figure. The effect of Reynolds number on the results can be clearly seen by the reduction of the first and second $\overline{C_{f_{\max}}}$, and an increase in θ_{sep} with increasing Re.

Figure 5.7(b) compares the mean centreline $x-$velocity where $x/D = 0$ corresponds to the cylinder centre. The agreement with experiment [7] at the same Reynolds number is fairly good, however the simulation over predicted the length of the recirculation bubble in the cylinder wake. The results converge well from a position two cylinder diameters downstream.

5.3.2 Spanwise Grid Density Dependence

Table 5.3 presents results for cylinder simulations performed at $Re = 1.4 \times 10^5$ with a varying grid density in the $z-$direction along the cylinder span. The purpose was to ensure that the default density of 30 grid points was indeed sufficient to capture the important flow structures. The results for $\overline{C'_L}$, $\overline{C_D}$, St, and θ_{sep} show that the results obtained using 30, 40, and 50 grid points compare favourably and tend toward the 50 grid point solution. The results for 20 spanwise grid points show poor agreement with the other predictions, indicating an insufficient spanwise resolution. The prediction of

the cylinder surface pressure coefficient distribution at different spanwise grid density is shown by Figure 5.8 as partial assessment of grid independence. Figure 5.8 indicates a relative insensitivity of $\overline{C_p}$ on the spanwise grid density. The prediction of the base pressure coefficient, $\overline{C_{bp}}$, is within a couple of percent. Therefore, a spanwise resolution of 30 grid points was used in subsequent simulations.

5.4 Acoustic Results

In this section, the acoustic predictions are presented and discussed. Figure 5.9 shows the instantaneous pressure perturbation in the non-linear near-field region. Large perturbations are clearly induced on the cylinder surface and in the unsteady wake. Weaker perturbations were resolved, which can be seen to radiate into the far-field.

The FW-H prediction of the far-field acoustic pressure was obtained at an observer radius of $R = 100D$ using a cylindrical surface that coincides with the cylinder surface. The FW-H surface is open at the ends of the cylinder and is $2D$ in span. Figure 5.10 presents a short sample of the predicted far-field acoustic pressure at observers located at $\theta = 90$ deg and $\theta = 180$ deg corresponding to locations directly above and behind the cylinder respectively. At $\theta = 90$ deg the observer is directly affected by the lift dipole acting perpendicularly to the freestream exhibiting larger perturbations with a period equal to that of the vortex shedding. At $\theta = 180$ deg the observer is affected by pressure fluctuations due to the drag force perturbations on the cylinder which are much lower in magnitude and approximately twice the frequency due to the coupling of the vortices from the upper and lower surfaces.

5.4.1 Spectral Characteristics

The Fast Fourier transform (FFT) of the acoustic pressure history was taken to yield the spectral characteristics of the signals. Each FFT was performed over a number of blocks. Each block contained a time record of $20.5D/U_\infty$, sampled at $0.02D/U_\infty$. This gives a Nyquist frequency of $f = 25U_\infty/D$ and a narrowband spectral resolution of $f = 0.025U_\infty/D$. Each block was windowed using a Hamming window. Selected spectra for the cc140k:TS2 case calculated from the on-body FW-H surface are presented in Figure 5.11. In Figure 5.11(a) the spectra at a range of observer locations close to 90 degrees are plotted. Each spectrum features a dominant peak corresponding to the shedding frequency and a smaller broadened peak at the frequency of the first harmonic. The highest level of approximately 76.5 dB is predicted at $\theta = 90$ deg, with a level of 74 dB predicted at the $\theta = 50$ deg observer, and 73 dB at the $\theta = 130$ deg observer. The small difference between $\theta = 50$ deg and $\theta = 130$ deg can be explained by convective amplification effects. Figure 5.11(b) presents the spectra at observers parallel to the

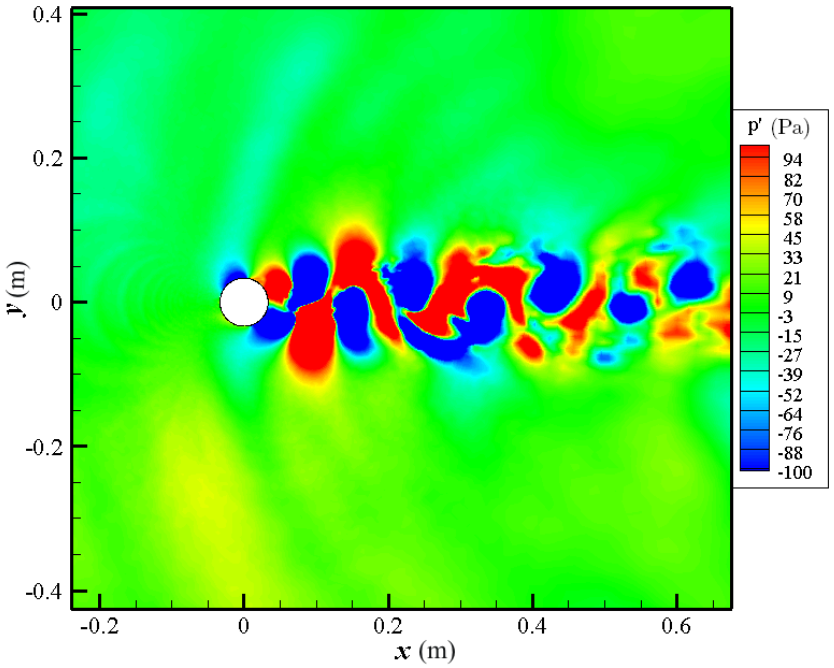

FIGURE 5.9: 3-D DES single cylinder flow visualisation of instantaneous pressure perturbation, $p' = p - p_\infty$ (Pa).

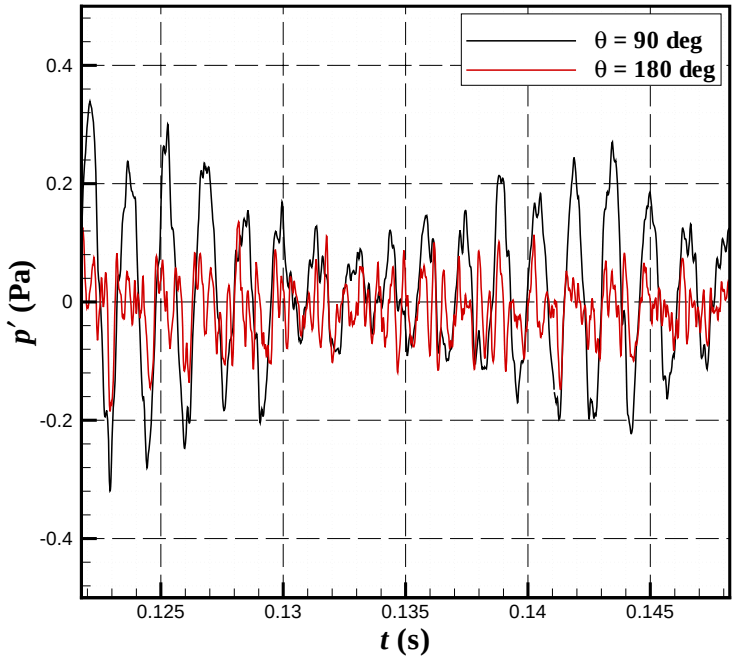

FIGURE 5.10: Far-field acoustic pressure prediction, p', for observers located at $\theta = 90$ deg and $\theta = 180$ deg.

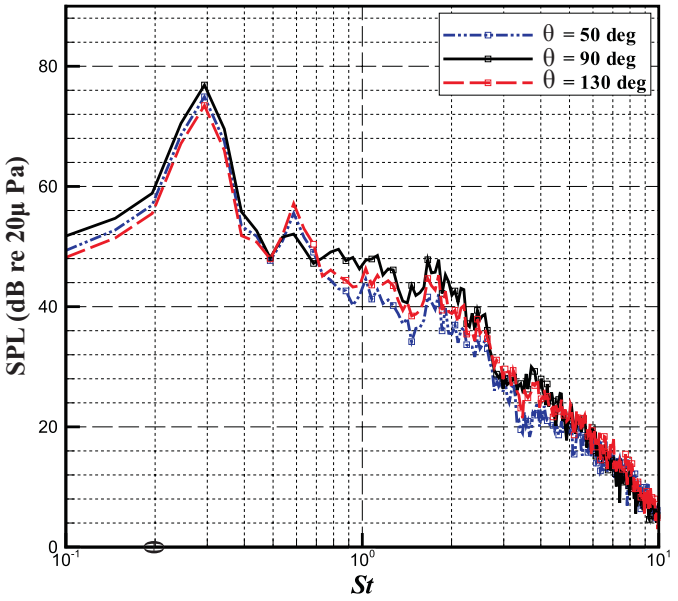

(a)

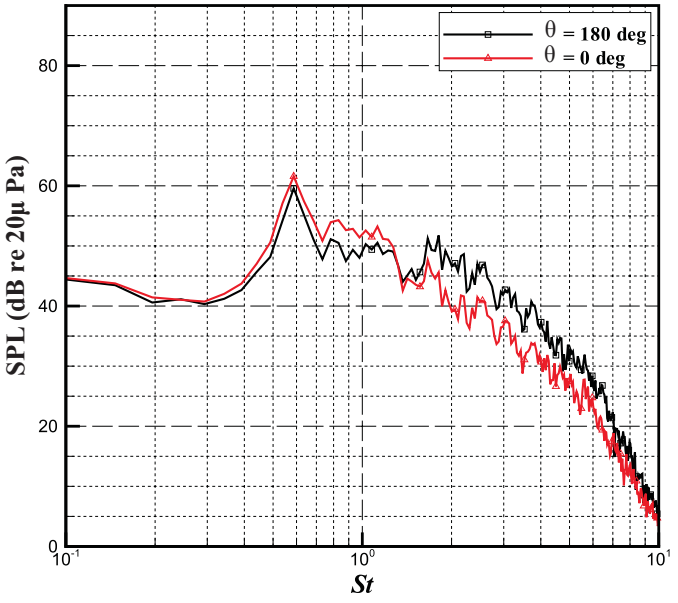

(b)

FIGURE 5.11: Far-field acoustic prediction for a single cylinder: (a) comparison between acoustic pressure for observers $\theta = 50, 90, 130$ deg, (b) $\theta = 0, 180$ deg. $R = 100D$

freestream vector where the component of the fluctuating forces parallel to the freestream dominate. The resultant spectra are broader consisting of a weaker peak of ≈60 dB due to the pressure fluctuations associated with the unsteady drag forces. The slight differences between spectra corresponding to upstream and downstream observers can be explained by convective amplification effects and the unsteady pressure on the rear of the cylinder due to the separated region.

The spectral characteristics are clearly dependent on observer location, indicating the need for a spectral function in the prediction model that is a function of radiation angle. Observers that are in the radiation path of the fluctuating lift forces experience higher levels of acoustic pressure with a dominant low frequency tone associated to the fluctuations in the lift coefficient, whereas those that are in the path of the drag forces exhibit a lower sound pressure level and a broader spectrum with a weaker tone at twice the vortex shedding frequency.

Influence of FW-H Integration Surface Predictions of the far-field acoustic pressure were obtained on two FW-H surfaces. The off-body permeable surface was circular with a radius of $2D$ centred at $x = y = 0$. The on-body integration surface was only capable of capturing acoustic perturbations on the cylinder surface, whereas the off-body surface was capable of capturing any source within its interior. Both time step size and the grid determine the resolution characteristics of both surfaces. In Figure 5.12(a) the result for an observer located at $\theta = 90$ degrees is presented. The predictions from the two FW-H integration surfaces show a strong collapse at the shedding frequency, although the permeable surface prediction of the first harmonic is considerably higher. Since the second harmonic corresponds to the frequency that vortices pass through the integration surface, this additional noise is likely to be due error caused by the passage of vortices through the permeable surface [52]. The permeable surface also predicts higher levels beyond a Strouhal number of $St = 2$ corresponding to $f \geq 4400$ Hz. A similar result is obtained for the observer located at $\theta = 180$ shown in Figure 5.12(b).

Without inclusion of the volume integral in the FW-H solution, it is not possible to determine whether the difference is due to additional noise sources or error due to vortices passing through the wake [55]. However, Lockard has shown a strong agreement between on-surface and several permeable surface predictions for bluff body flows at $M = 0.2$, concluding that permeable integration surfaces are not necessary [55]. It is expected at the low incompressible Mach number associated with an aircraft approach that the effect of volume sources will be negligible and the use of on-body integration surfaces is sufficient to capture the far-field noise characteristics. Therefore the additional noise captured by the permeable surface is presumed to be due to error and only the on-surface predictions are considered in the remainder of this chapter.

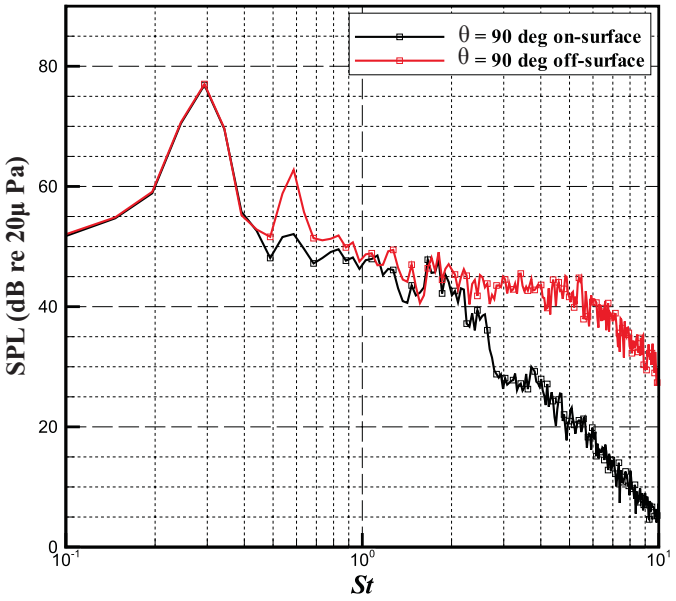

(a) $\theta = 90$ deg

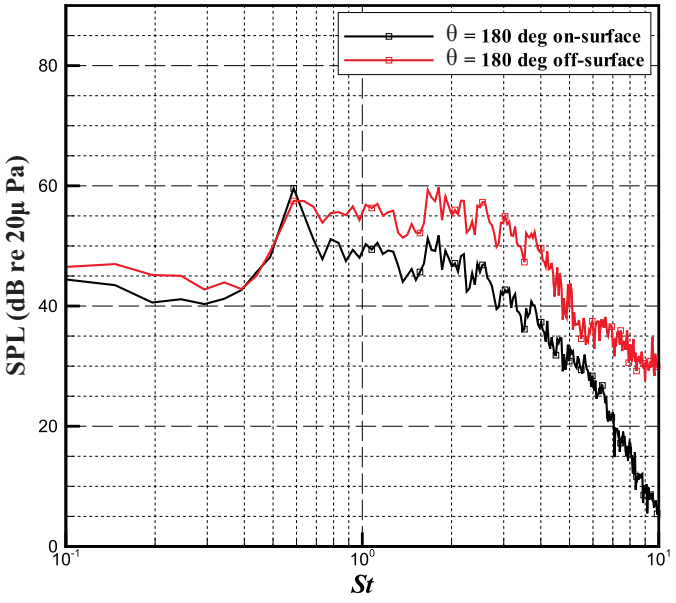

(b) $\theta = 0$ deg

FIGURE 5.12: FW-H integration surface prediction comparison for a single cylinder in cross-flow, $Re = 1.4 \times 10^5$: (a) $\theta = 90$ deg, (b) $\theta = 180$ deg. $R = 100D$

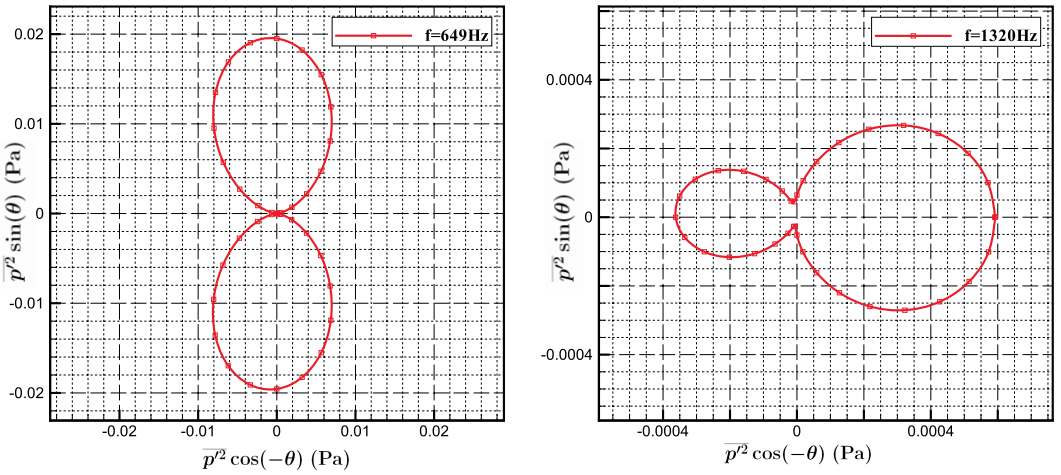

(a) Lift dipole.

(b) Drag dipole.

FIGURE 5.13: Directivity of sound pressure at: (a) vortex shedding frequency, $f = 649$ Hz, (b) fundamental drag fluctuation frequency, $f = 1320$ Hz.

5.4.2 Directivity Characteristics

Directivity plots were produced to obtain a representation of the overall acoustic field. These were generated by integrating the predicted sound pressure level over the range of resolved frequencies according to Equations D.5 and D.6. In Figure 5.14(a) the directivity of the OASPL is plotted to show the 2-D directivity characteristics in the $x-y$ plane where the flow is from left to right. A distinct dipole directivity pattern was predicted which is aligned perpendicular to both the freestream and the cylinder axis. This figure shows the maximum ΔOASPL to be approximately 10 dB across the range of θ, indicating strong directivity effects. The dipole exhibits a slight radiation bias into the forward arc due to convective amplification effects, but is almost symmetrical along $y = 0$.

To compare the contribution of the lift and drag pressure forces on the cylinder surface to the far-field noise, the directivity of $\overline{p'^2}$ at the frequency of the fluctuating lift and drag forces was extracted from the far-field spectra. The result it plotted in Figure 5.13. At $f = 649$ Hz, corresponding to the shedding frequency in the $Re = 1.4 \times 10^5$ simulation, the dipole pattern of Figure 5.13(a) resembles the integrated pressure directivity patterns in Figure 5.14(b) indicating the dominance of the lift dipole. At $f = 1320$ Hz, corresponding to the fluctuating drag, the dipole is aligned parallel to the flow with a higher radiation directivity downstream, corresponding to the unsteadiness in the separated region at the rear of the cylinder. The magnitude of the drag dipole is less than that of the lift dipole, indicating the dominance of the lift dipole to the overall sound pressure level.

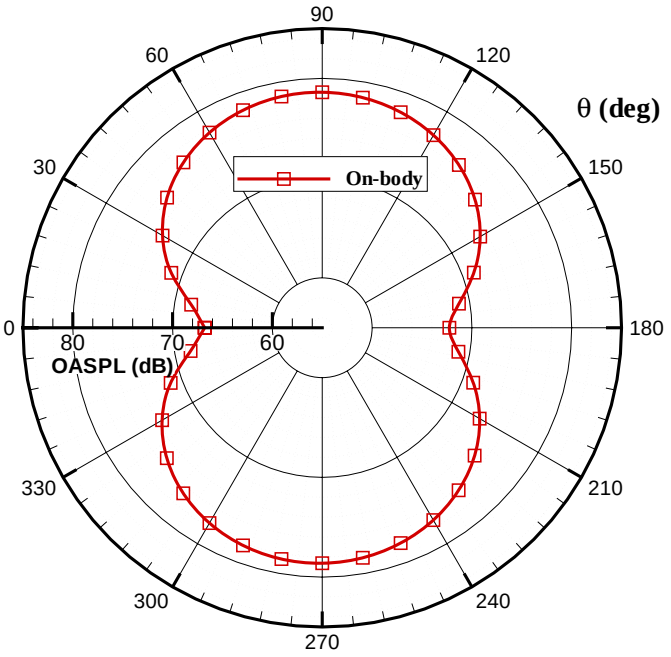

(a) OASPL directivty.

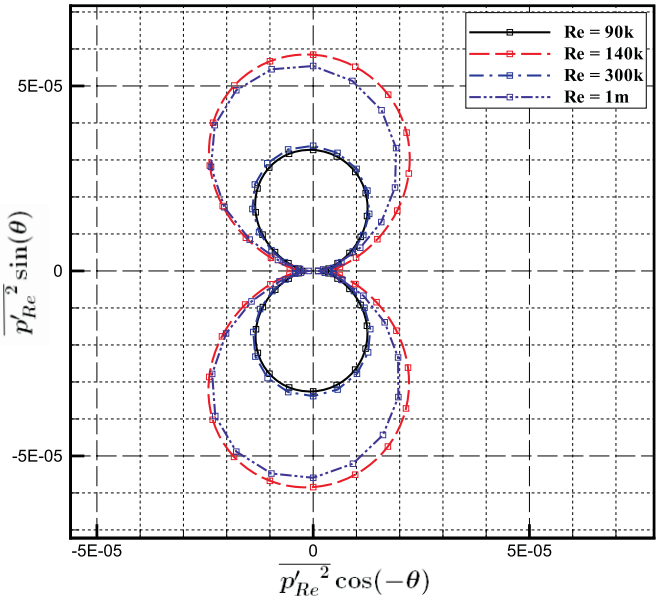

(b) *Re* comparison.

FIGURE 5.14: Far-field directivity prediction for a single circular cylinder: (a) OASPL prediction for $Re = 1.4\times10^5$, (b) Reynolds number comparison, $Re = 1.4\times10^5$-1×10^6, of normalised far-field sound pressure, $\overline{p'_{Re}{}^2}$.

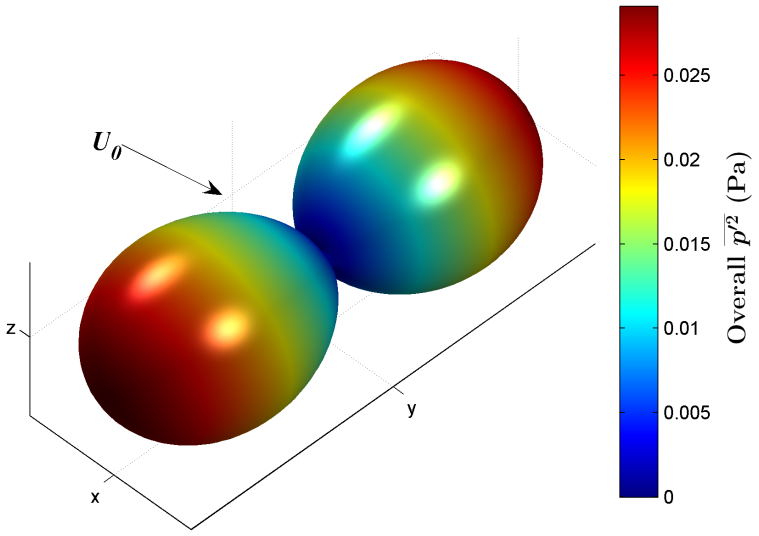

(a) Overall sound pressure.

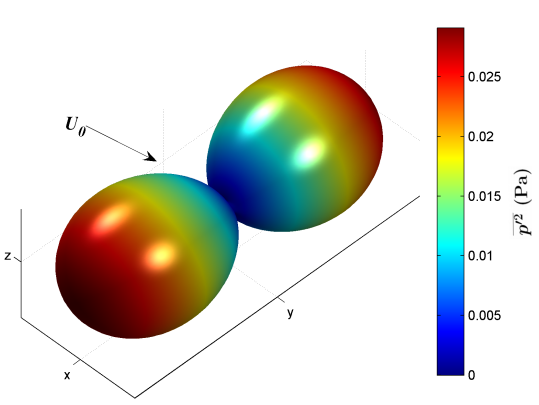

(b) Lift dipole contribution, $f = 649$ Hz.

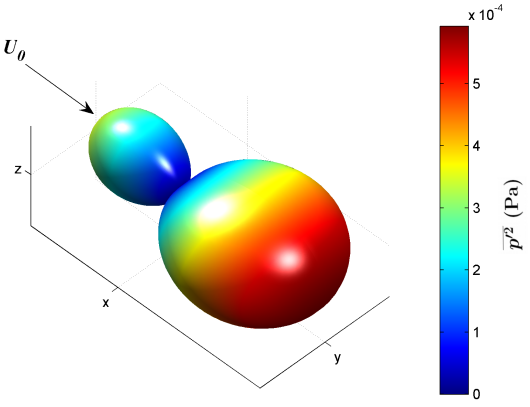

(c) Drag dipole contribution, $f = 1320$ Hz.

FIGURE 5.15: Three-dimensional mean-square pressure, $\overline{p'^2}$, directivity prediction for single cylinder: (a) overall sound pressure, (b) lift dipole at $f = 649$ Hz, (c) drag dipole at $f = 1320$ Hz.

The three-dimensional directivity field was also computed and is presented in Figure 5.15. In the 3-D surface plots the cylinder axis is parallel to the $z-$axis and centred along the line $x = y = 0$. Figure 5.15(a) shows the total directivity of the overall mean-square pressure, $\overline{p'^2}$, integrated over the resolved frequency range. It is clear that the direction of maximum radiation is perpendicular to the cylinder axis and the freestream vector, whereas the minimum occurs along the cylinder axis at $x = y = 0$. The contribution from the lift dipole dominates the shape of the surface. The depression at $x = y = 0$ is caused by the coincident minimum of both dipoles. Figures 5.15(b) and 5.15(c) show the directivity of the peak sound pressure at the frequencies corresponding to the lift and drag fluctuations indicating the influence of the respective dipoles.

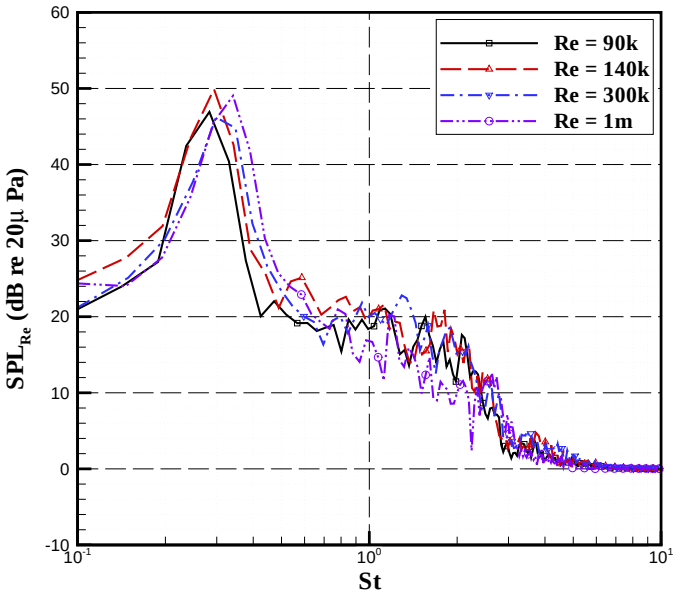

(a) $\theta = 90$ deg.

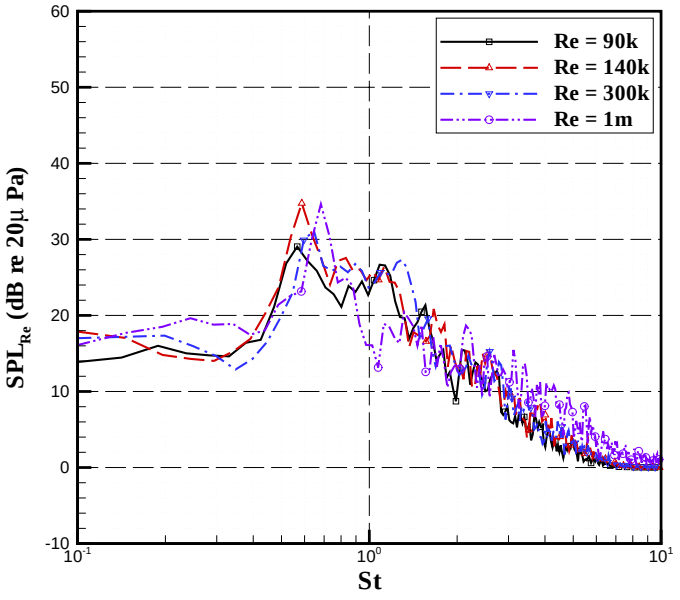

(b) $\theta = 180$ deg.

FIGURE 5.16: Collapse of non-dimensional acoustic spectra for a single cylinder at various Reynolds numbers: (a) $\theta = 90$ deg, (b) $\theta = 180$ deg.

5.4.3 Reynolds Number Effects

In Figure 5.14(b) the predictions of mean square far-field pressure are presented, where $\overline{p'_{Re}{}^2}$ indicates normalisation by $\rho U_\infty^6 L_s^2/c_\infty^3 R^2$ to eliminate Reynolds number effects. Figure 5.14(b) shows that there is no marked difference between the characteristics of the dipole directivity pattern at difference Reynolds numbers, however there is an difference in the strength of the dipole type far-field radiation, which appears to be uncorrelated to the Reynolds number. The SPL_{Re} spectra are shown in Figure 5.16, where the mean square far-field pressure has been normalised by $\rho U_\infty^6 L_s^2/c_\infty^3 R^2$. In Figure 5.16(a) the increase in shedding frequency and a slight decrease in the peak level with increasing Reynolds number is clear. However, the differences are small with the difference in peak level being $\Delta\mathrm{SPL}_{\mathrm{peak}} = 2$ dB. There is no other significant change in the spectral characteristics, and there is a fairly strong collapse between other parts of the spectra except for the $Re = 1 \times 10^6$ simulation due to a lower sampling frequency leading to an earlier cut-off of the resolved frequencies

5.5 Summary

In this chapter, the basic noise generating mechanisms of a circular cylinder have been investigated. Three-dimensional detached-eddy simulation was used to provide the near-field turbulent solution. The results showed that supercritical flow was successfully simulated and good agreement with experiment was made in most cases. The aerodynamic results showed subtle Reynolds number effects, since the supercritical flow regime was simulated in all cases. The far-field noise predictions were made by solving the FW-H equation and full 3-D predictions of the acoustic pressure was achieved. The expected dipole radiation pattern associated with circular cylinder noise was predicted. Also a strong relationship between observer location and the spectral characteristics was clearly demonstrated, asserting the need for these effects to be included in the prediction model. The Reynolds number effects on the spectral and directivity characteristics were shown to be fairly negligible. The simulations have provided a database that can be used to model basic strut noise and also a reference on which yawed and tandem cylinders can be investigated.

Chapter 6

Circular Cylinders in Yaw

6.1 Outline

In this chapter the modelling of basic circular strut noise is extended to investigate the characteristics of arbitrarily aligned struts. This was achieved by modelling cylinders in yawed flow. The purpose was to assess the effect of yaw angle on the far-field acoustic spectra and directivity characteristics, so that the correct physics could be captured in the prediction model. The simulations were performed using the low-order flow solver with DES at a Reynolds number of 1.4×10^5, and supercritical flow was simulated.

6.2 Computational Setup

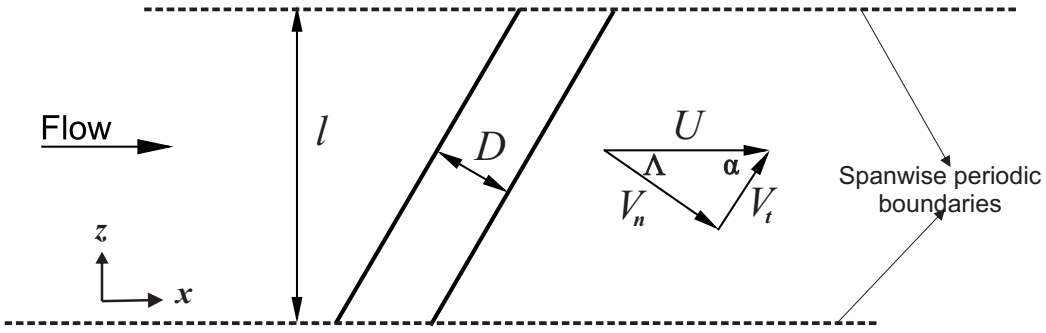

FIGURE 6.1: Definition of geometry and nomenclature used in yawed cylinder simulations.

The yawed cylinder geometry and nomenclature are defined in Figure 6.1. In this figure, the $x-$direction is defined parallel to the freestream vector and the $z-$direction perpendicular to it. The angle θ is measured clockwise from the front stagnation point parallel to the $x - y$ plane. The range of yaw angles investigated was $\Lambda = 0 - 45$ deg in 15 deg

Parameter	**Symbol**	**Value**
Yaw angle	Λ	0-45 deg
Freestream Mach number	M	0.2
Cylinder diameter	D	0.0311 m
Turbulent viscosity ratio	$\frac{\mu_t}{\mu}$	10
Non-dimensional time step	Δt^*	0.02
Reynolds number	Re	1.4×10^5

TABLE 6.1: Simulation parameters used in the yawed cylinder simulations.

increments. Two-dimensional grid sections were developed with elliptical cross-sections. To generate the grids, a cylinder diameter of $y_D = 0.0311$ m was maintained in the $y-$direction whilst the $x-$dimension was determined by $x_D = \frac{y_D}{\cos\Lambda}$. The grids were then extruded by $2D$ along a vector corresponding to the yaw angle. This meant that the normal span $2D\cos\Lambda$ in the $z-$direction was reduced with increasing yaw angle, and thus the normal spanwise grid spacing Δz was also reduced. The grid construction followed the same guidelines as those used to develop the grids for cross-flow cylinders. The cylinder span was resolved by 30 equally spaced grid points and the total grid dimension was (340,230,30) resulting in 2.35 million grid points in total. The computational parameters such as time step, and number of sub-iterations, remained consistent with those reported in Chapter 5. Table 6.1 reports a selection of the simulation parameters.

The computations were performed at $Re = 1.4 \times 10^5$ by adopting the same approach described in Chapter 5 to model the supercritical flow regime. Although $Re = 1.4 \times 10^5$ is fairly low for full-size landing gear components, the results reported in Chapter 5 indicated that Reynolds number effects were fairly small for forced TS flows, and that the characteristics of the supercritical regime were successfully captured at all the simulated Reynolds numbers. The $\Lambda = 0$ deg case corresponds to the cross-flow cc140k:TS2 result reported in Chapter 5 and was used as the reference case on which to determine the effect of yaw.

6.3 Aerodynamic Results

Reported in Table 6.2 is a selection of results for the yawed cylinder cases. Parameters denoted by subscript "n" indicate normalisation with the normal velocity, V_n. Quantities include the predicted lift coefficient RMS, $\overline{C_L'}$; mean drag coefficient, $\overline{C_D}$; Strouhal number, St; separation angle, θ_{sep}; back pressure coefficient, $\overline{C_{bp}}_n$; and the peak SPL at an observer located at $R = 100D$ and $\theta = 90$ deg, perpendicular to the cylinder axis. The relationship between a selection of these parameters and Λ is plotted in Figure 6.3.

Λ	Re_n	$\overline{C'_L}$	$\overline{C'_{Ln}}$	$\overline{C_D}$	$\overline{C_{Dn}}$	St	St_n	θ_{sep} (deg)	$-\overline{C_{bp_n}}$	SPL†
0°	140k	0.077	0.077	0.614	0.614	0.297	0.297	97.4	0.723	75.3 dB
15°	135k	0.067	0.072	0.537	0.576	0.287	0.297	102.7	0.682	71.6 dB
30°	121k	0.066	0.088	0.390	0.520	0.253	0.292	104.5	0.687	69.6 dB
45°	99k	0.034	0.068	0.213	0.426	0.212	0.299	107.2	0.674	65.2 dB

† Peak SPL at observer radius $R = 10$ m, span $L = 1$ m, $\theta = 90$ deg.

TABLE 6.2: Results summary of 3-D DES of yawed cylinders at $Re = 1.4 \times 10^5$, $\Lambda = 0 - 45$ deg.

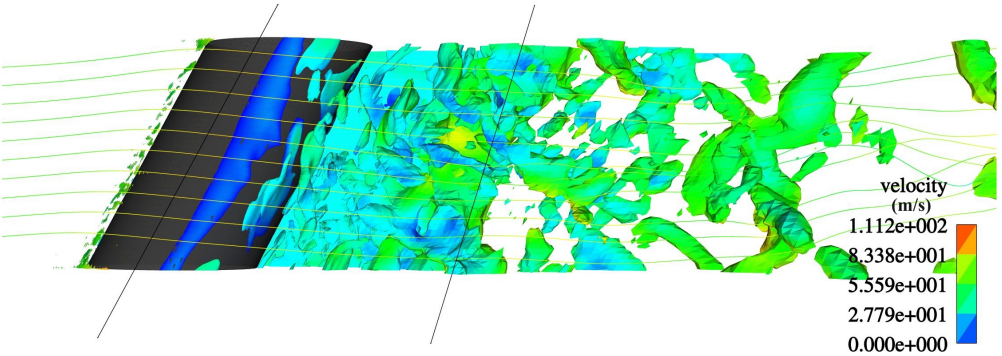

(a) $\Lambda = 30$ deg.

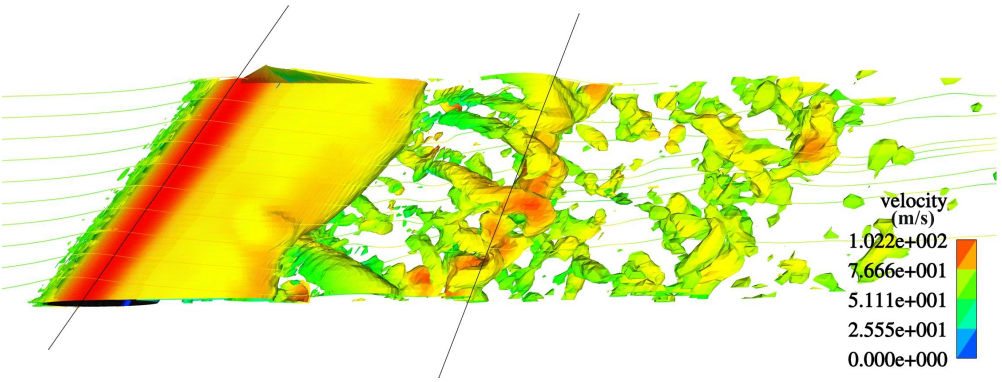

(b) $\Lambda = 45$ deg.

FIGURE 6.2: 3-D DES yawed cylinder flow visualisation: iso-surface of vorticity contours, coloured by velocity magnitude: (a) $\Lambda = 30$ deg, (b) $\Lambda = 45$ deg.

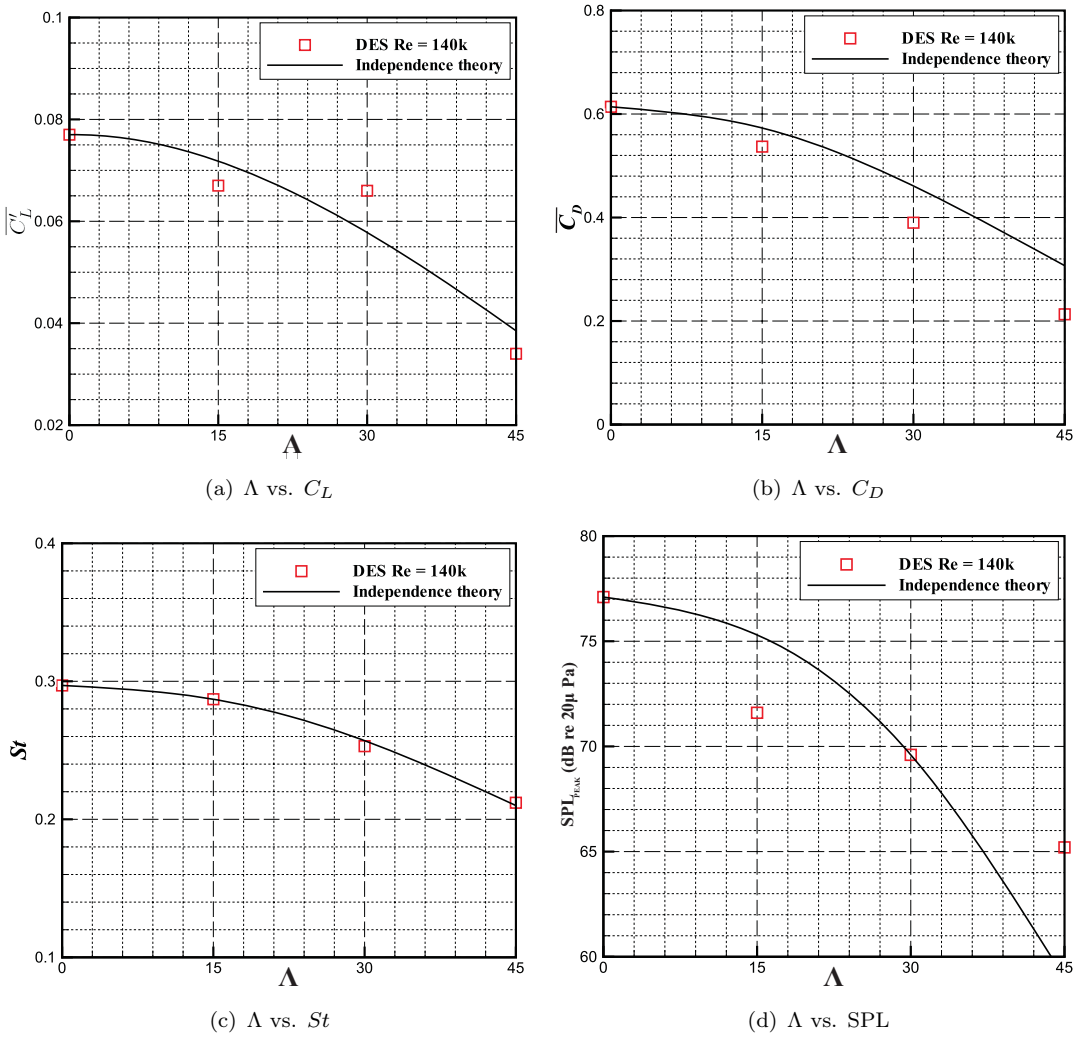

(a) Λ vs. C_L

(b) Λ vs. C_D

(c) Λ vs. St

(d) Λ vs. SPL

FIGURE 6.3: Variation of quantities with yaw angle for yawed cylinder 3-D DES simulations at Re=1.4×10^5: (a) $\overline{C_L}$ vs. Λ, (b) $\overline{C_D}$ vs. Λ, (c) St vs. Λ , (d) peak SPL vs. Λ.

In all cases a fairly irregular vortex shedding was predicted in the cylinder wakes. Figure 6.7 shows a short sample of the force coefficients on the cylinder surface. As the cross-section became more streamlined with increasing Λ the strength of the body force fluctuations significantly reduced due to a much weaker and less coherent vortex shedding. Table 6.2 indicates that the shedding Strouhal number decreased with increasing yaw angle. Figure 6.2 shows how initially the vortex structures are aligned with the cylinder axis, which indicates the influence of V_n on the flow field and on its aerodynamic properties. This alignment feature of the vortex structures is confirmed by experiment [82]. The streamlines in Figure 6.2 illustrate how the freestream vector is distorted in the vicinity of the cylinder due to the reduction of V_n on approach to the cylinder. As the vortex structures propagate downstream, the freestream vector dominates the flow once more and the vortical structures tend to align with it as their convective velocity tends to up..

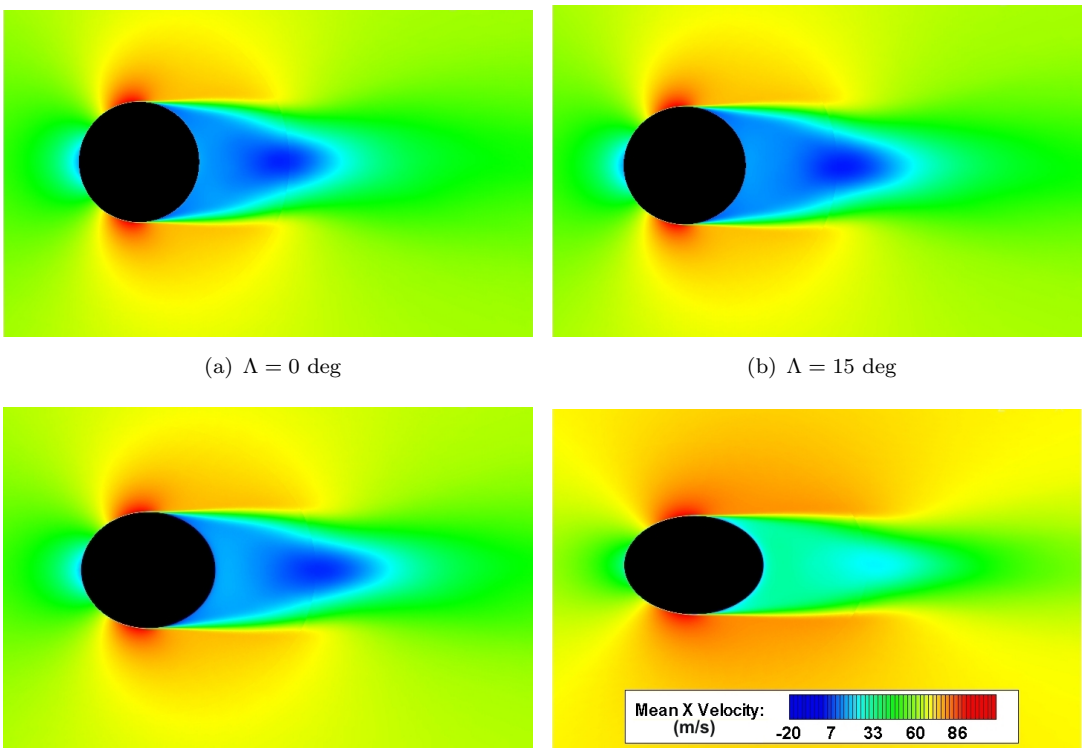

(a) $\Lambda = 0$ deg (b) $\Lambda = 15$ deg

(c) $\Lambda = 30$ deg (d) $\Lambda = 45$ deg

FIGURE 6.4: Mean streamwise velocity contours over yawed cylinders along the $x - y$ plane parallel to the freestream vector.

The results show that the separation angle increased as the yaw angle increased from $\theta_{\text{sep}} = 97.4 - \theta_{\text{sep}} = 107.2$ deg as Λ increased from 0 deg to 45 deg. This is explained by the increasingly elliptical and streamlined effective cross section even though Re_n is decreased due to the reduction in the normal velocity, V_n. The delay of separation had a direct impact on the thickness of the wake which is reflected by the drag coefficient that reduces from $\overline{C_D} = 0.614$ to $\overline{C_D} = 0.213$, accompanied by a rise in $\overline{C_{bp_n}}$. The normal drag coefficient, $\overline{C_{Dn}}$, also decreased with increasing yaw angle, a poor correlation with the Independence Principle.

In Figure 6.3(a), the relationship between $\overline{C'_L}$ and Λ is plotted along with the cosine curve representing results expected from the Independence Principle. The lift coefficient RMS significantly reduced from $C'_L = 0.077$ to $C'_L = 0.034$, however the value measured for $\Lambda = 30$ deg is only a fraction less than that at $\Lambda = 15$ deg. This may be a result of an inadequate sample length.

Chapter 5 revealed that for a cylinder in cross-flow, delayed separation and a reduced $\overline{C_D}$ is normally associated with an increase in the Strouhal number. However, the yawed cylinder results indicate that there is a clear decrease in vortex shedding frequency as these quantities decrease with increasing yaw angle. This is consistent with the literature [83]. However, the Strouhal number based upon the normal velocity components,

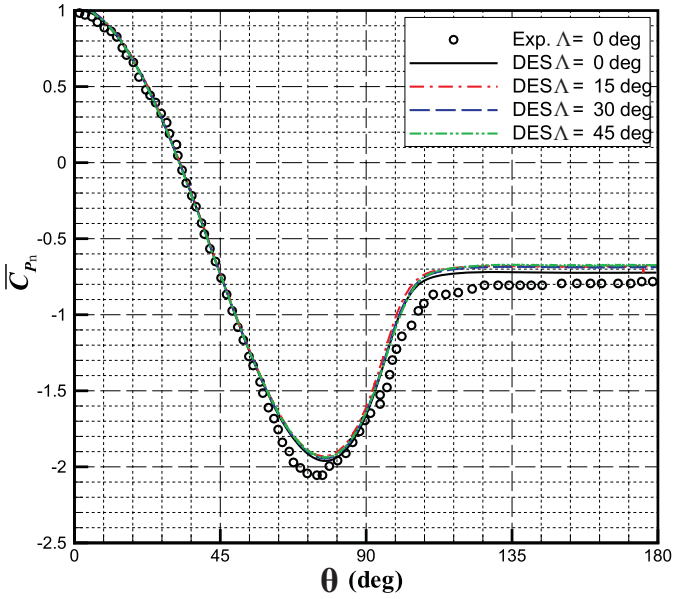

FIGURE 6.5: Yawed cylinder aerodynamic results: $\overline{C_{p_n}}$ distribution comparison.

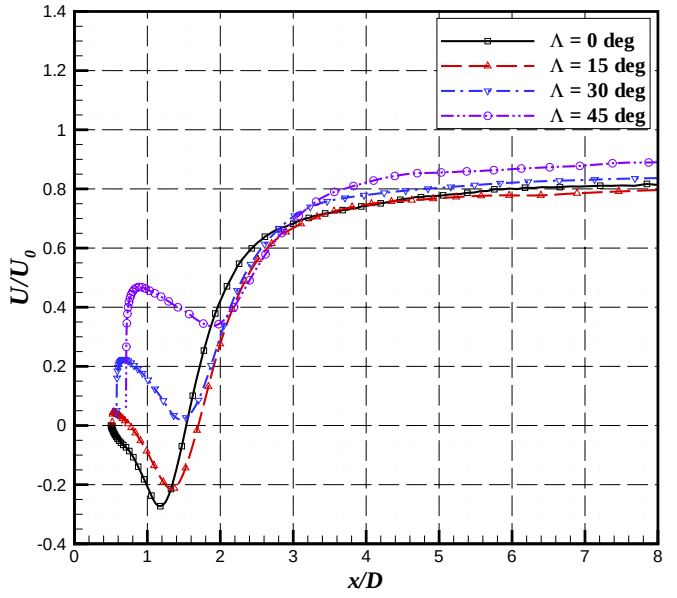

FIGURE 6.6: Centreline velocity, U/U_0, downstream of yawed cylinders.

St_n, remained almost constant with increasing yaw angle. This suggests that the shedding frequency is controlled by the normal velocity, V_n, which is consistent with the Independence Principle. Figure 6.3(c) confirms this by comparing the St predictions with the Independence Principle indicating a very strong correlation.

Figure 6.5 shows the distribution of the normal pressure coefficient C_{p_n}. There is clearly a very strong collapse of C_{p_n} for all angles which shows that the Independence Principle holds for this quantity. Table 6.2 reports the very small change in C_{bp} at different yaw

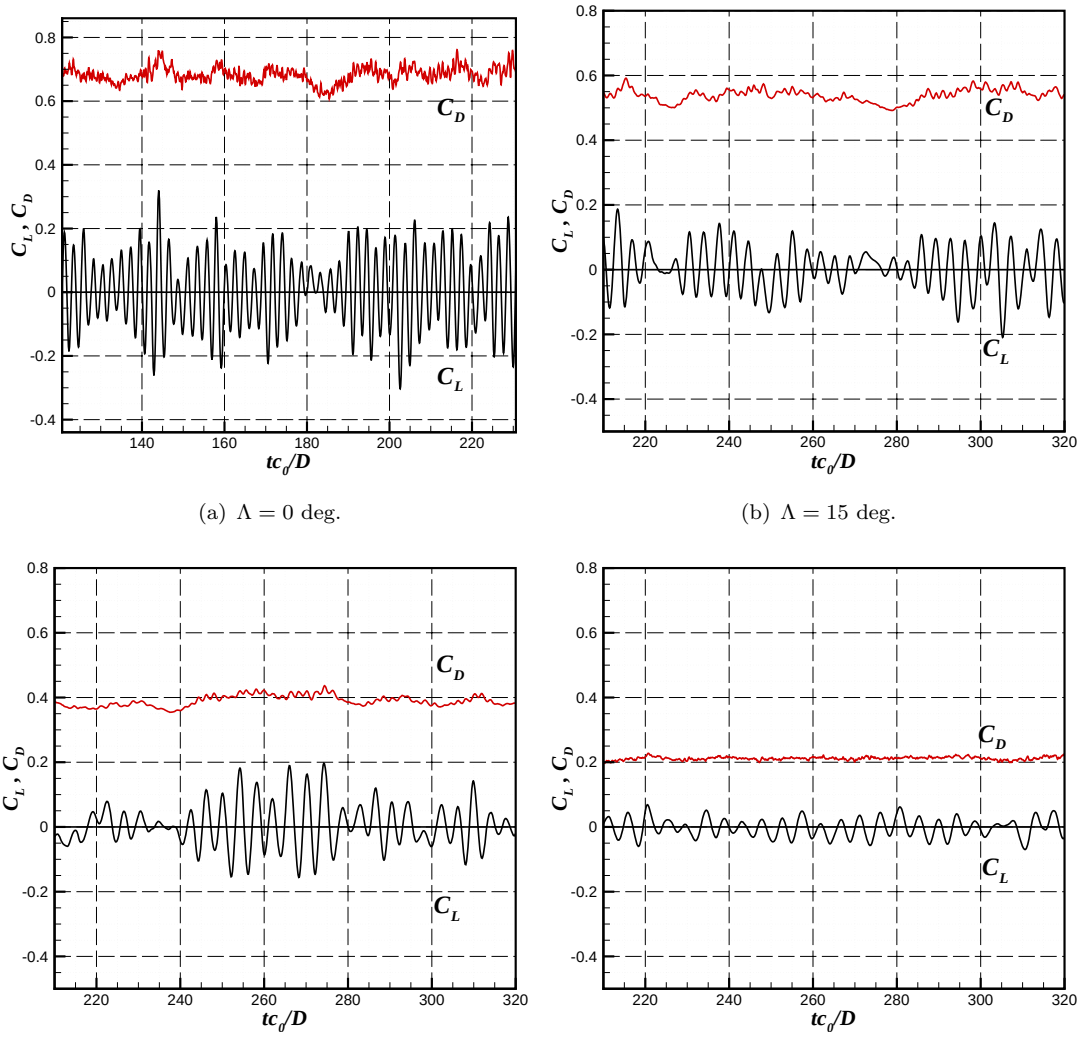

(a) $\Lambda = 0$ deg.

(b) $\Lambda = 15$ deg.

(c) $\Lambda = 30$ deg.

(d) $\Lambda = 45$ deg.

FIGURE 6.7: Comparison between predicted force coefficients on the surface of yawed cylinders. $M = 0.2$, $Re = 1.4 \times 10^5$.

angles. A number of mean-flow parameters could be correlated with the Independence Principle, however the unsteady flow statistics do not tend to correlate well with the Independence Principle.

The wake characteristics are displayed in Figure 6.4 indicating iso-levels of the average velocity in the freestream direction. The two-dimensional slices in the iso-levels plots are $z-$planes (i.e. parallel to the freestream vector) and hence the cylinder profiles appear as ellipses for $\Lambda > 0$. The recirculation bubble increased in length as the cylinders become more elliptic, and the recirculation velocity decreased. The velocity profiles of the normalised streamwise velocity along the cylinder centrelines are plotted in Figure 6.6. The length of the recirculation bubble is clear for $\Lambda = 0$ deg and $\Lambda = 15$ deg, which feature a negative mean streamwise velocity over the range $0 \leq x \leq 1.6D$ of the cylinder at $\Lambda \geq 30$ degrees. The effect of the more streamlined profiles for $\Lambda = 30$ and

45 deg is an always positive mean velocity, therefore there is no time-mean circulation zone downstream.

6.4 Acoustic Results

6.4.1 Spectral Characteristics

Figure 6.8 shows the computed non-dimensional far-field acoustic pressure spectra at the radial distance $R = 100D$ from the cylinder axis at $\theta = 90$ deg and $\theta = 180$ deg, where θ is measured clockwise from the front stagnation point parallel to the $x-$direction. The results from the on-body integration surface are presented here. The analysis of the aerodynamic results suggested that increased yaw should lead to a decrease in SPL and a decrease in the peak frequency due to vortex shedding. In Figure 6.8(a) far-field pressure spectra are compared at an observer located directly overhead the cylinders at $\theta = 90$ deg. It is clear that the introduction of yaw angle leads to a large reduction in both level and frequency of the spectral peak. The basic spectral shape remains similar for all simulations and is dominated by a large tone corresponding to the vortex shedding frequency. The reduction in sound level pressure with increasing yaw is apparent at all frequencies beyond the vorex shedding frequency. The peak SPL at $\theta = 90$ deg is reported in Table 6.2, and shows ΔSPL = 10.1 dB between $\Lambda = 0$ deg and $\Lambda = 45$ deg. Figure 6.8(b) shows far-field pressure spectra predictions at an observer located upstream of the cylinder at $\theta = 180$ deg. A similar reduction in both peak frequency and sound pressure level is seen that can be explained by the weaker fluctuating drag forces on the cylinder reported in Figure 6.7 at increasing Λ.

6.4.2 Directivity Characteristics

The computed OASPL directivity results are presented in Figure 6.9. The directivity plane is parallel to the freestream velocity vector and θ is measured clockwise from the front stagnation point. A dipole directivity pattern similar to that of Figure 5.14 is predicted with a ΔOASPL of 10 to 15 dB between observers at $\theta = 90$ deg and $\theta = 180$ deg. The results show the large level change as the yaw angle increases as a result of the smaller surface pressure forces on the cylinder wall. The largest difference occurs for observers parallel to the freestream at $\theta = 0$ deg and $\theta = 180$ deg, with nearly a 15 dB difference between $\Lambda = 0$ and $\Lambda = 45$ deg. The difference is approximately 12 dB in the overhead direction at $\theta = 90$ deg. The ΔOASPL between $\text{OASPL}_{\text{min}}$ and $\text{OASPL}_{\text{max}}$ is a maximum for $\Lambda = 30$ deg at 15 dB, compared to 12 dB for $\Lambda = 0$ deg.

Figure 6.10 illustrates the three-dimensional directivity field predicted for $\Lambda = 45$ deg, where the cylinder is yawed relative to the z-axis. The three-dimensional plots help to

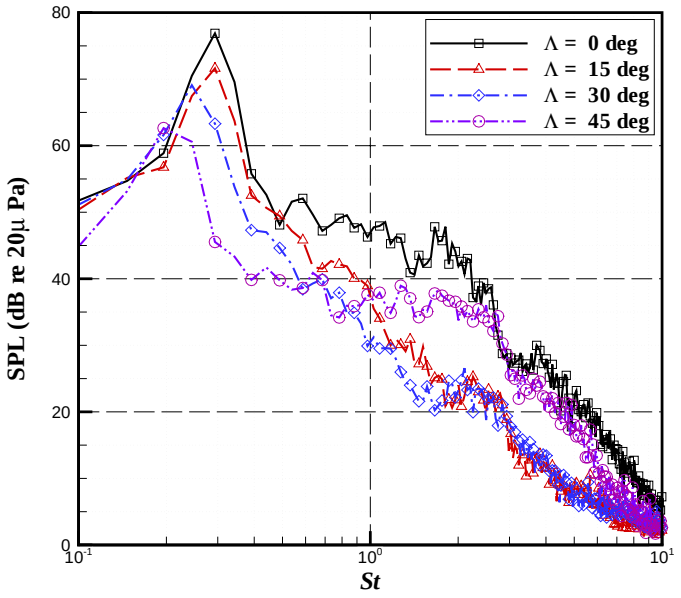

(a) $\theta = 90$ deg.

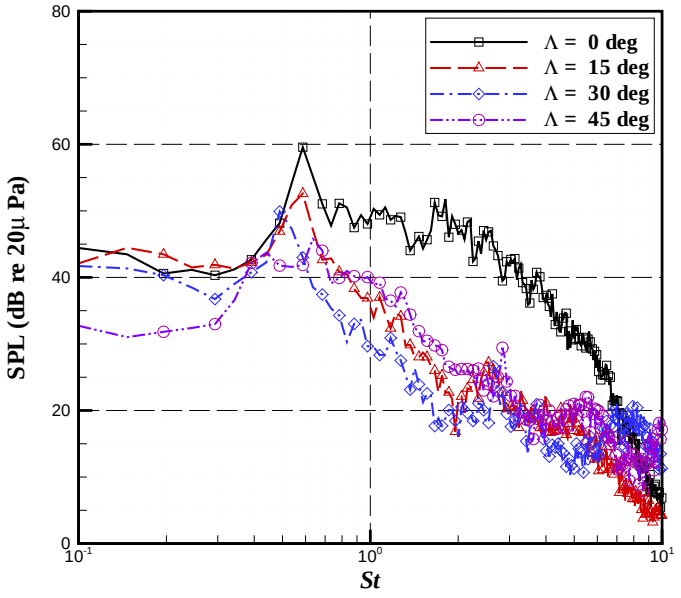

(b) $\theta = 180$ deg.

FIGURE 6.8: Yawed cylinder non-dimensional spectra prediction for $\Lambda = 0 - 45$ deg: (a) $\theta = 90$ deg (b) $\theta = 180$ deg.

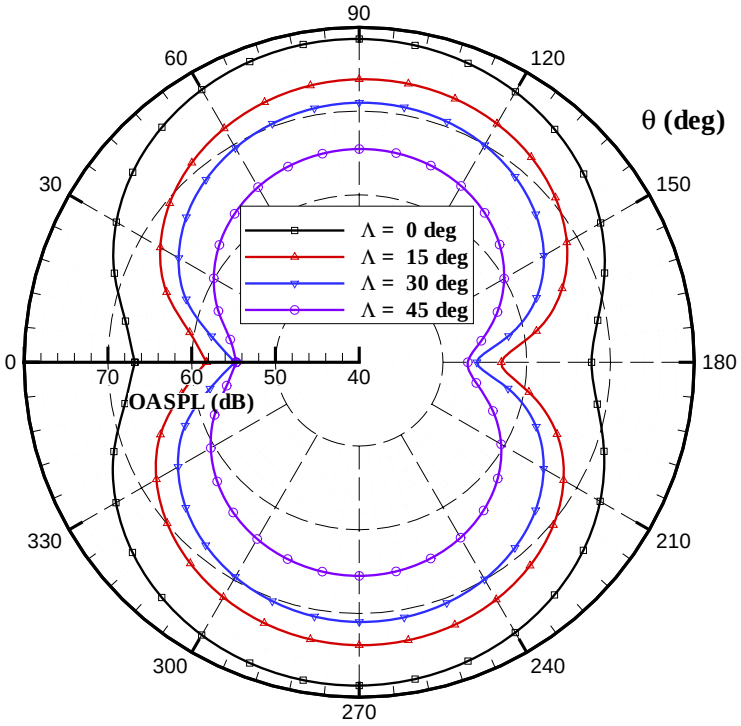

FIGURE 6.9: Yawed cylinder OASPL directivity prediction at a radial distance of $R = 100D$, $\Lambda = 0 - 45$ deg, $M = 0.2$, $Re = 1.4 \times 10^5$.

identify the effect of yaw on the directivity field. The usual overall dipole directivity field is clearly marked in Figure 6.10(a). Comparison with Figure 5.15 shows the attenuation effect of the overall noise level caused by yaw. It is clear that the lift dipole dominates, whereas the drag dipole is far less pronounced. Figures 6.10(b) and 6.10(c) show the directivity of the sound pressure level at the Strouhal numbers of the fluctuating lift and drag forces on the cylinder surface. Figure 6.10(b) shows that the yaw angle does not affect the alignment of the lift dipole, however Figure 6.10(c) shows that the drag dipole is aligned to the cylinder axis, indicating its dependence on the yaw angle and normal velocity, V_n, and not the freestream vector. This is expected since Figure 6.2 indicates how immediately behind the cylinder the streamlines are aligned with V_n.

This acoustic analysis clearly indicates the noise reduction potential of yawed cylinders which reaches a maximum of 15 dB between the $\Lambda = 0$ deg and $\Lambda = 45$ deg predictions. The basic spectral characteristics however do not change significantly with yaw angle. Strut alignment is clearly an important factor and should be considered for an accurate prediction of landing gear component noise.

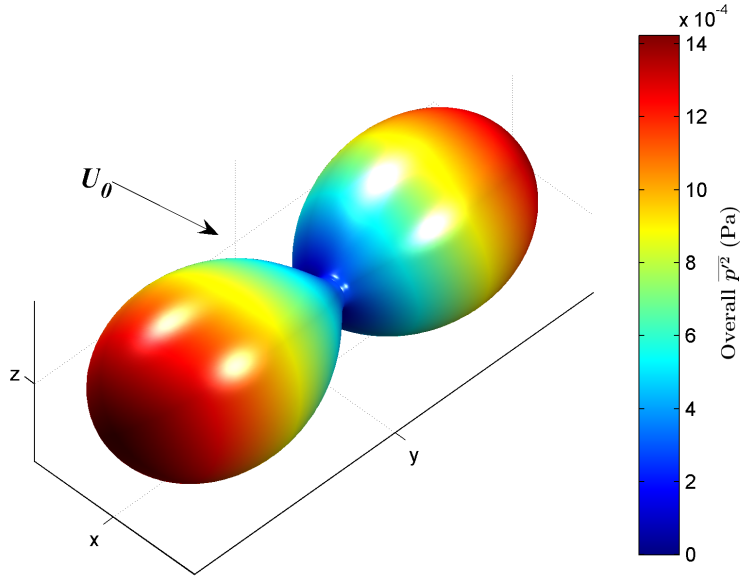

(a) Overall sound pressure.

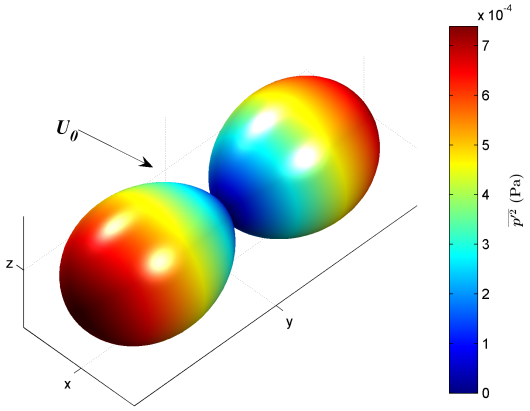

(b) Lift dipole contribution, $St = 0.28$.

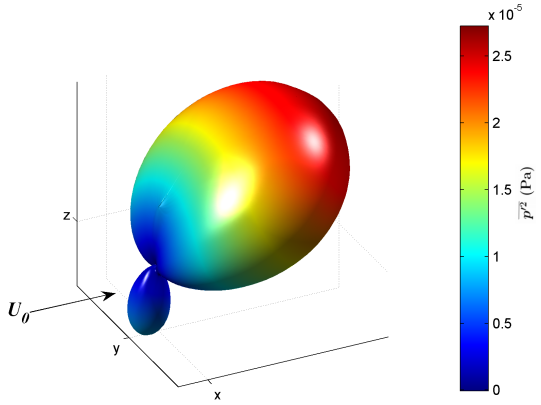

(c) Drag dipole contribution, $St = 0.56$.

FIGURE 6.10: Three-dimensional $\overline{p'^2}$ directivity prediction for a single yawed cylinder, $\Lambda = 45$ deg: (a) overall sound pressure, (b) lift dipole at $St = 0.28$, (c) drag dipole at $St = 0.56$.

6.5 Arbitrary Yaw Angles

6.5.1 The Independence Principle

The Independence Principle suggests that the governing equations of the flow in the normal and spanwise planes are uncoupled and the projected flow in the normal plane is based upon $U_\infty \cos\Lambda$. The mathematical idealisation that the flow is two-dimensional for an infinite span cylinder cannot be realised in practice, however it was investigated whether this theory could be used to estimate the far-field sound levels.

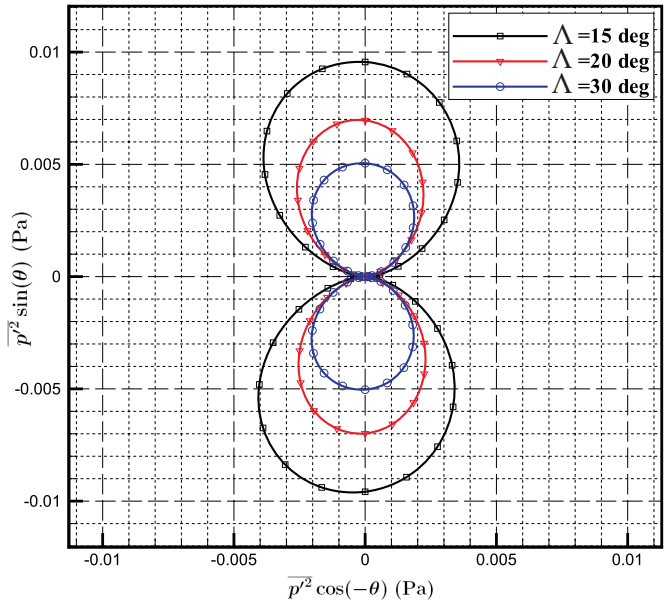

(a) Interpolated directivity

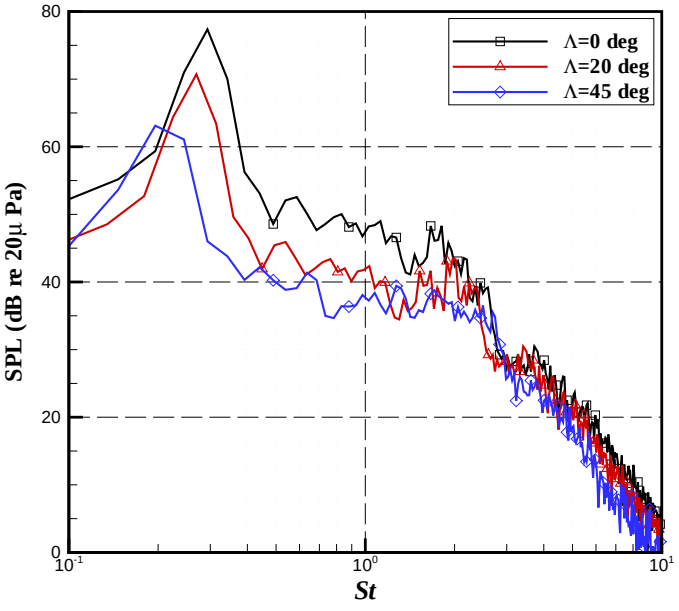

(b) Interpolated spectrum

FIGURE 6.11: Interpolation method results for $\Lambda = 20$ deg: (a) directivity of peak spectral acoustic pressure, (b) spectra comparison.

The theory was tested to see if it could be used to predict the noise generated by struts at arbitrary angles of yaw. The correlation of the Independence Principle with selected aerodynamic quantities has already been discussed and was shown to have partial success. Figure 6.3(c) suggests that the computed shedding frequency could be correlated very well in the range $\Lambda = 0 - 45$ deg. Therefore it was proposed that the Independence Principle could be used to estimate the shedding frequency with sufficient engineering accuracy. The ability to predict noise levels using the Independence Principle was also examined by replacing the freestream Mach number in Equation 3.9 with the normal Mach number, $M_n = \frac{V_n}{c_0}$. The result is shown in Figure 6.3(d) which shows poor correlation, indicating that an alternative method is required for predicting the sound levels for arbitrary yaw angles.

6.5.2 Interpolation

Since the main characteristics of the yawed cylinders far-field spectrum do not change with yaw angle, an alternative approach to the prediction of the far-field SPL for arbitrary yaw angle by way of interpolation was pursued. In this approach, the far-field spectrum at an arbitrary yaw angle can be estimated by interpolation of the results for the $\Lambda = 0$, 15, 30, and 45 deg simulations. It is not ideal to interpolate the actual spectra as this would lead to spurious unphysical peaks due to the noisy nature of the spectra. Instead, the idea was to only interpolate the peak level to determine a scaling factor that could be used to obtain a prediction for an arbitrary yaw angle in the range $\Lambda = 0 - 45$ deg. The scaling factor could then be used to scale the SPL of the results for a cylinder with $\Lambda = 30$ deg. rectangular windowing in the frequency domain was used so that the scaling factor was only applied to Strouhal numbers below $St = 2$, since at higher frequencies the spectra collapse reasonably well. The Independence Principle can then used to shift the frequency scale by the right amount to obtain the final prediction.

The interpolation scheme used the results for $\Lambda = 0$, 15, 30, and 45 deg to compute the scaling factor for $\Lambda = 20$ deg. The scaling factor along with the Independence Principle was then used to scale the non-dimensional spectrum of a cylinder with $\Lambda = 30$ deg to obtain the prediction for $\Lambda = 20$ deg. The result for the predicted spectrum is shown in Figure 6.11(b) and the resulting directivity pattern for $\Lambda = 20$ deg is shown in Figure 6.11(a). The directivity result is obtained by scaling the directivity for the cylinder with $\Lambda = 30$ deg by the same amplitude scaling factor as the spectrum. From both figures it can be concluded that the far-field acoustic characteristics are maintained and a realistic frequency and sound pressure level prediction is achieved.

6.6 Summary

In this chapter, the effect of yaw angle on the far-field acoustic characteristics has been investigated. The aerodynamic features were shown to be strongly influenced by both the introduction of the normal and tangential velocity components, V_n and V_t, and also by the elliptical cross-section of the cylinder in the plane parallel to the freestream. A correlation of the Independence Principle with various aerodynamic quantities was performed with limited success. The force coefficients on the cylinder surface did not correlate well with the theory, although good predictions of the shedding frequency were made. It was shown that, for yawed cylinders, the basic noise characteristics of a single cylinder remain, however increasing the yaw angle leads to a decrease in both the peak SPL in the acoustic spectrum and in the computed OASPL. A decrease in vortex shedding frequency was also predicted. This highlighted the noise reduction potential of yawed cylinders. An interpolation method has been developed so that the results can be used by the model to predict the noise characteristics of arbitrarily aligned struts in the range $\Lambda = 0 - 45$ deg.

Chapter 7

Circular Cylinders in Tandem

7.1 Outline

This chapter reports on the numerical simulation of tandem cylinder noise. The cylinder separation distance, S/D, was varied between 2 and 5 so that various flow regimes could be investigated. The purpose was to assess the effect of the body-wake-body interaction on the far-field noise characteristics of representative struts. The tandem cylinders were of equal diameter and simulated at a Reynolds number of 1.4×10^5, in supercritical flow, using the low-order flow solver.

7.2 Computational Setup

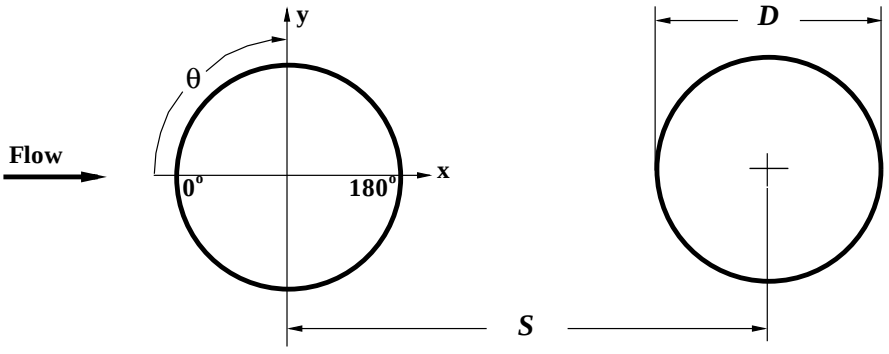

FIGURE 7.1: Definition of the tandem cylinder configuration and nomenclature.

The tandem cylinder geometry and nomenclature are defined in Figure 7.1. The non-dimensional separation distance between cylinders, S/D, was varied between 2 and 5 so that various flow regimes could be simulated. The Reynolds number of the computations

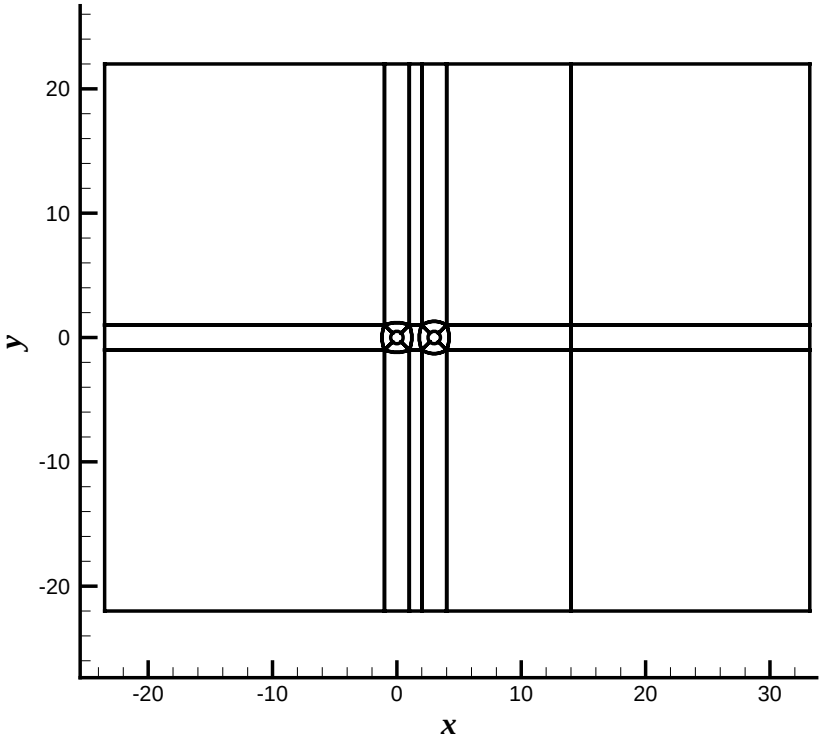

(a) Block Structure

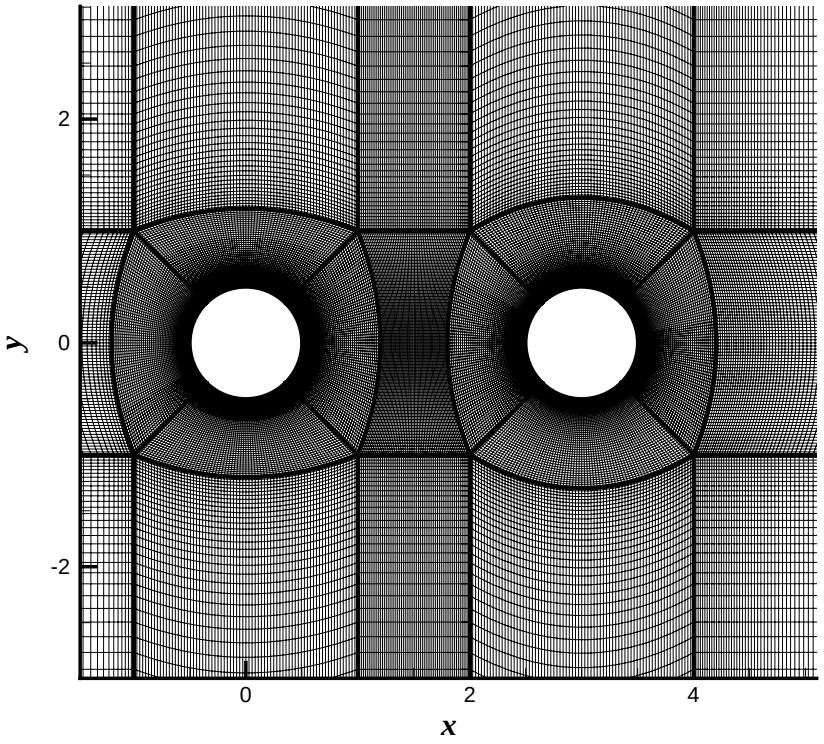

(b)

FIGURE 7.2: Tandem cylinder $S/D = 3$ non-dimensional grid: (a) domain block structure, (b) near-field grid.

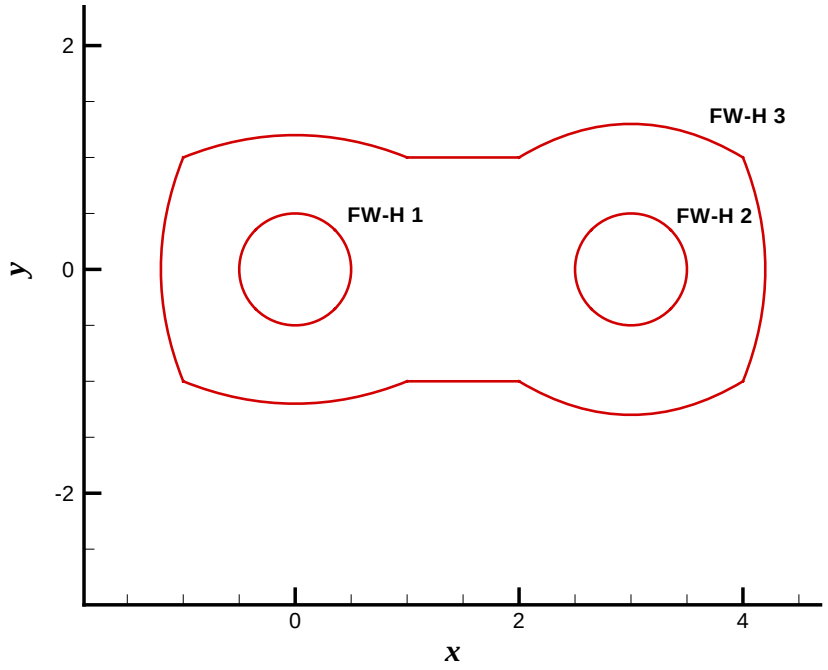

FIGURE 7.3: FW-H surface boundaries: FW-H 1 solid surface on upstream cylinder, FW-H 2 solid surface on downstream cylinder, FW-H 3 permeable surface enclosing both cylinders.

was $Re = 1.4 \times 10^5$, with $M = 0.2$ and $D = 0.0311$ m. The computational parameters were set to simulate supercritical flow as per the single cylinder computations and are reported in Table 7.1.

Structured grids with rectangular domains were generated around the cylinders. The $S/D = 3$ grid is shown in Figure 7.2. Figure 7.2(a) illustrates the block structure of the multi-block grid, whereas Figure 7.2(b) shows the highly resolved near-field region around the cylinders. The cylinder spans were of length $L_s = 2D$ and were resolved by 30 grid points. The number of grid points in the $x - y$ plane was approximately 1×10^5, with 317 points around the circumference of the cylinders. This led to grids of approximately 3 million grid points in total. The grids consisted of 21 blocks for the $S/D = 2$ case and 24 blocks for all other cases. A conscious effort was made to cluster cells in the gap region between the cylinders and in the wake of the downstream cylinder where large levels of flow unsteadiness were expected. A value of $y^+ \approx 1$ was controlled by refining grids so that the boundary layers were adequately resolved.

FW-H integration surfaces were defined on each cylinder surface as well as on a permeable surface enclosing both cylinders. These are indicated in Figure 7.3. This allowed the contribution of each cylinder to be evaluated and compared with the total configuration noise. The noise due to off-body sources was determined by comparing the noise predictions from each integration surface. The solution strategy remained the same

Parameter	**Symbol**	**Value**
Separation distance	S/D	2, 3, 4, 5
Freestream Mach number	M	0.2
Cylinder diameter	D	0.0311 m
Turbulent viscosity ratio	$\frac{\mu_t}{\mu}$	10
Non-dimensional time step	Δt^*	0.02
Reynolds number	Re	1.4×10^5

TABLE 7.1: Parameters used in the tandem cylinder simulations.

as per the single cylinder cases with each simulation lasting approximately 400 non-dimensional times and statistics collected for the last two-thirds of the solution time. Results were compared with the single cylinder cc140k:TS2 simulation so that the effect of the interaction could be determined.

7.3 Gap Region Flow Structures

The results showed that the flow field was highly sensitive to the separation distance between the cylinders. At short distances ($S/D = 2-3$) the downstream cylinder had a large impact on the flow field over the upstream cylinder by "blocking" the development of vortices and restricting the natural wake flow. At larger separation distances ($S/D > 3$), the characteristics of the upstream cylinder tended toward those expected for a single cylinder, however the flow field in the region of the downstream cylinder was significantly modified due to high levels of unsteadiness and turbulence in the approaching flow.

Several contour plots were generated to visualise the flow fields. Figure 7.4 shows instantaneous vorticity iso-surfaces and streamlines for $S/D = 2$, 3, and 5. In Figure 7.5 the mean streamwise velocity contours are plotted and in Figure 7.6 instantaneous turbulent viscosity contours are plotted, each for $S/D = 2$, 3 and 4. The mean streamwise velocity along the cylinders centreline in the gap region was calculated and is plotted in Figure 7.7.

Supercritical flow was simulated to ensure turbulent separation on the surface of the upstream cylinder, however since the downstream cylinder is submerged into the upstream cylinder turbulent wake, the flow around the downstream cylinder was governed by the upstream wake turbulence, rather than the freestream conditions.

At a separation distance of $S/D = 2$, the free shear layers from the upstream cylinder reached the body of the downstream cylinder and the resultant behaviour of the tandem arrangement was similar to that expected from a single elongated body, where the outline of the body is defined by the cylinder surfaces and the boundary of the shear layers. This behaviour has been reported in literature for $S/D \leq 2$ [43, 83]. The separation was just large enough that the shear layers from the upstream cylinder did not completely

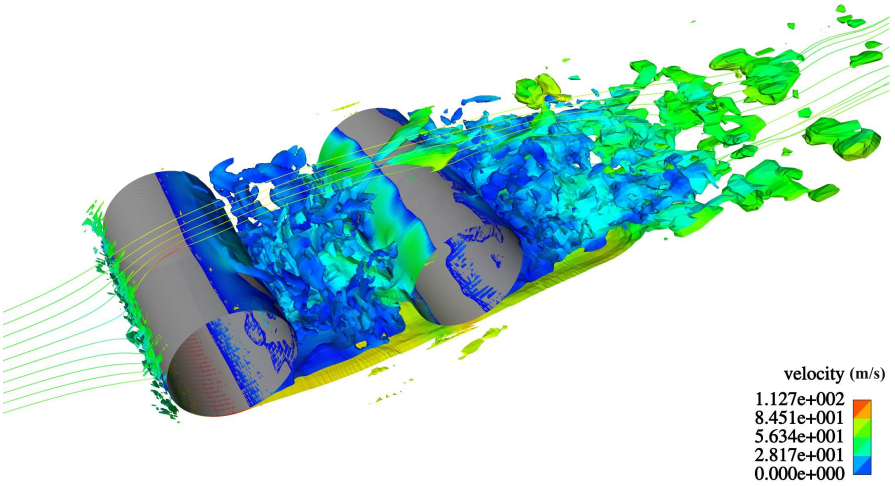

(a) $S/D = 2$.

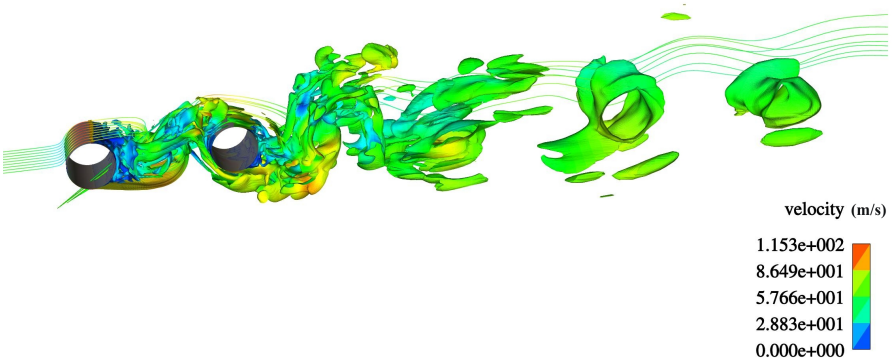

(b) $S/D = 3$.

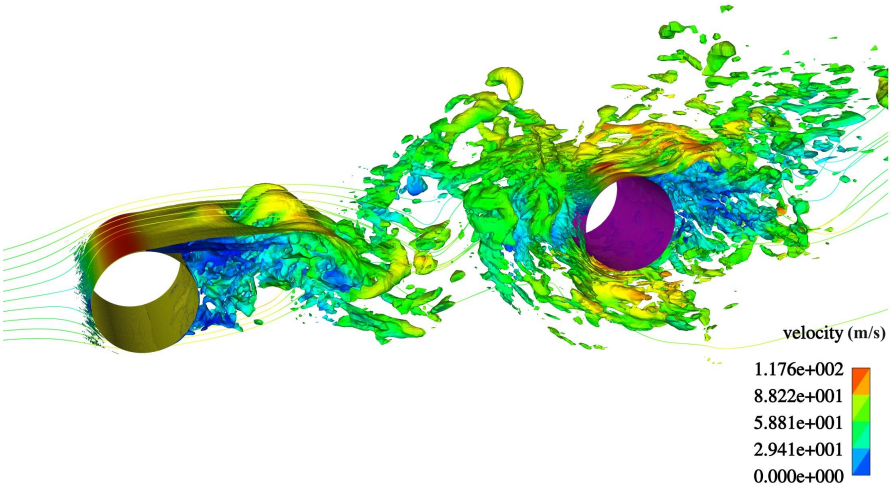

(c) $S/D = 5$.

FIGURE 7.4: 3-D DES tandem cylinder flow visualisation: Iso-surface of instantaneous vorticity contours coloured by velocity magnitude (a) $S/D = 2$, (b) $S/D = 3$, (c) $S/D = 5$. $M = 0.2$, $Re = 1.4 \times 10^5$

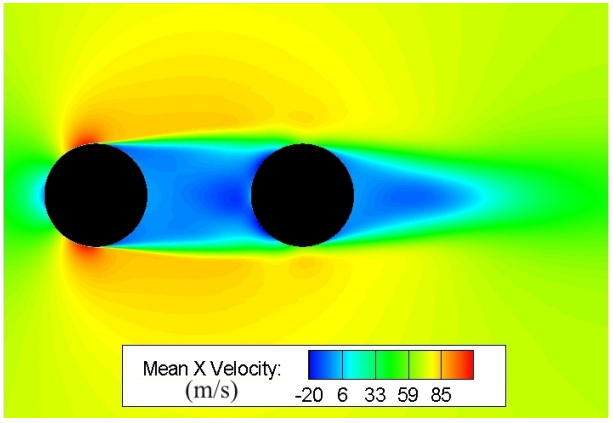

(a) $S/D = 2$.

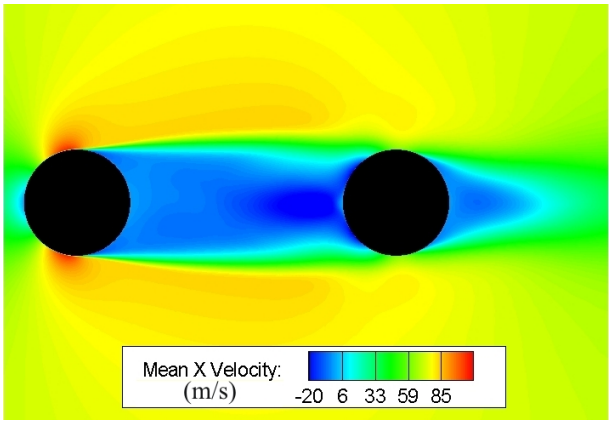

(b) $S/D = 3$.

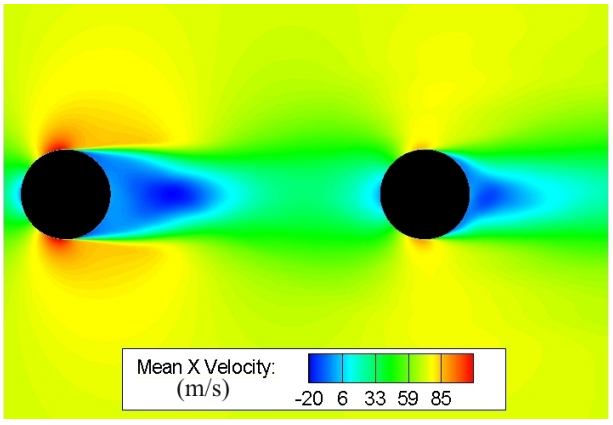

(c) $S/D = 4$.

FIGURE 7.5: 3-D DES tandem cylinder flow visualisation: time-averaged $x-$velocity colour iso-levels (a) $S/D = 2$, (b) $S/D = 3$, (c) $S/D = 4$. $M = 0.2$, $Re = 1.4 \times 10^5$

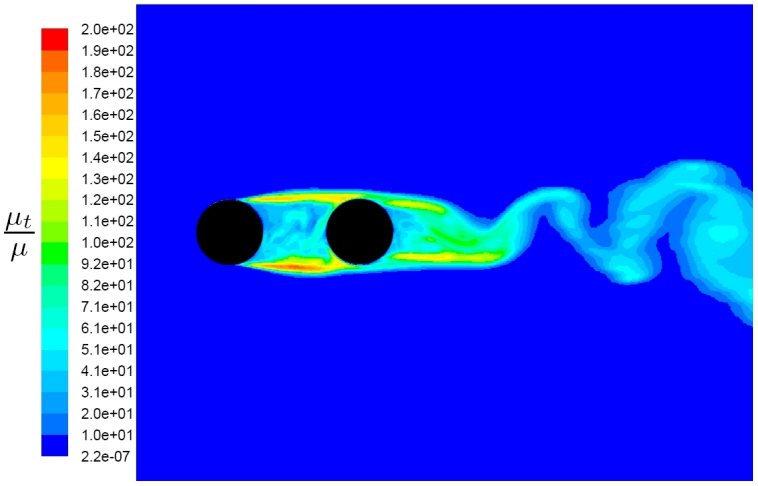

(a) $S/D = 2$.

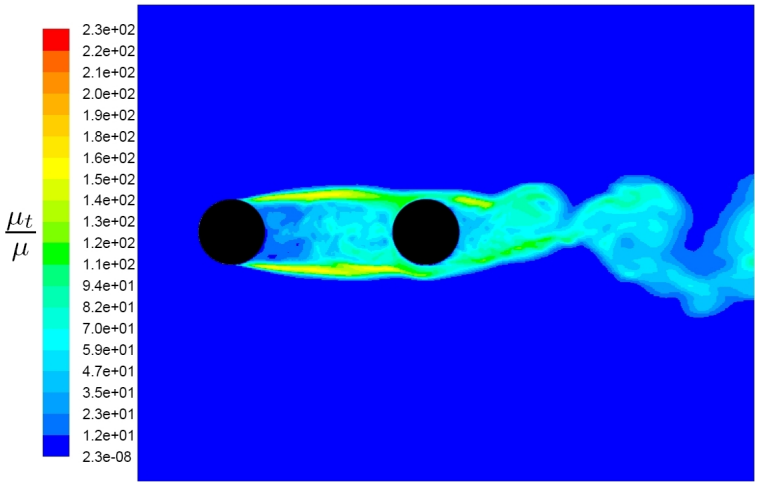

(b) $S/D = 3$.

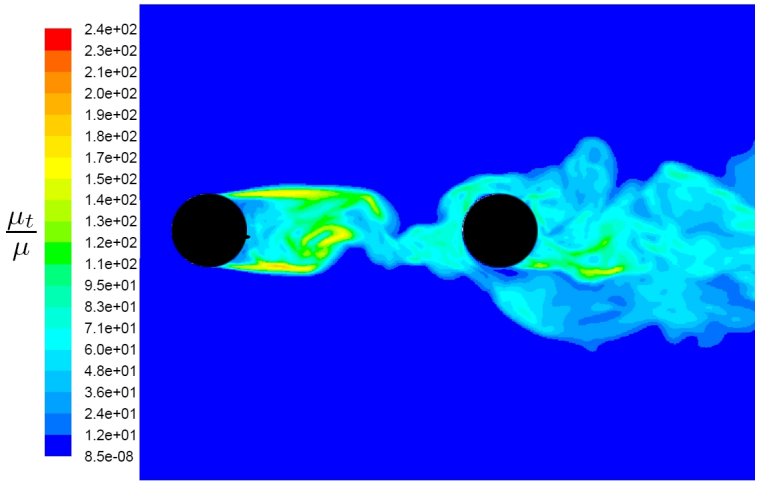

(c) $S/D = 4$.

FIGURE 7.6: 3-D DES tandem cylinder flow visualisation: instantaneous turbulent viscosity ratio, μ_t/μ colour iso-levels: (a) $S/D = 2$, (b) $S/D = 3$, (c) $S/D = 4$. $M = 0.2$, $Re = 1.4 \times 10^5$

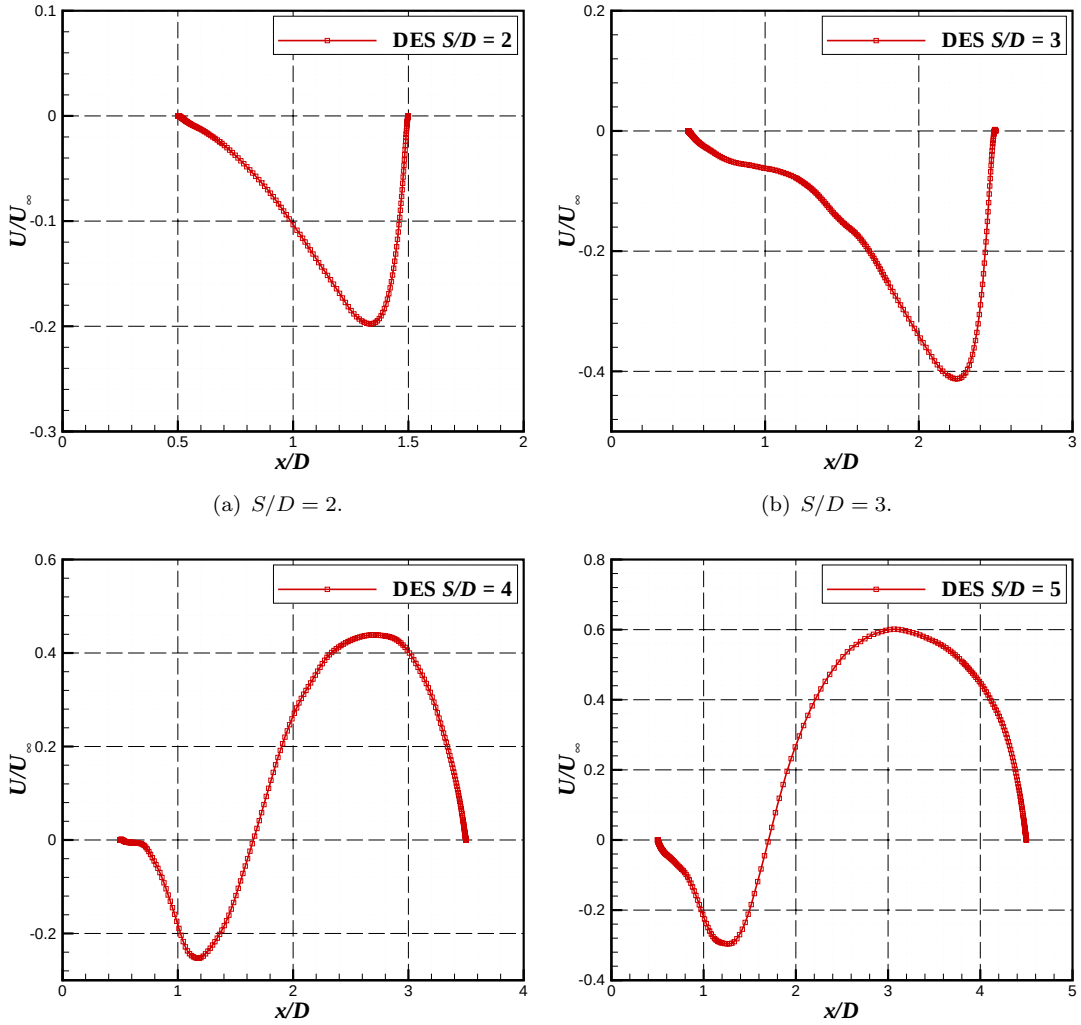

(a) $S/D = 2$. (b) $S/D = 3$.

(c) $S/D = 4$. (d) $S/D = 5$.

FIGURE 7.7: Mean streamwise gap region centreline velocity along $y = 0$ for tandem cylinders: (a) $S/D = 2$, (b) $S/D = 3$, (c) $S/D = 4$, (d) $S/D = 5$. $M = 0.2$, $Re = 1.4 \times 10^5$

enclose the downstream cylinder as can be seen from Figure 7.5(a). The blockage effect of the downstream cylinder meant that the recirculation region behind the upstream cylinder was much longer, but weaker, than expected of a single cylinder. The extent of the recirculation bubble can be seen from the mean centreline velocity plot in Figure 7.7 and this stretches across the full gaps, as shown by $U/U_\infty < 0$ over the range $0.5 \leq x/D \leq 1.5$. Figure 7.4(a) shows that weak shedding occurred behind the cylinder, which is more apparent in Figure 7.6(a).

As the separation distance increased to $S/D = 3$, the presence of the downstream cylinder still caused the blocking of vortices from the upstream cylinder. However, Figure 7.4(b) shows the characteristics of an unsteady wake behind the upstream cylinder that appears to "scrub" the surface of the downstream cylinder. This caused a large variation

Case*	$\overline{C'_L}$	$\overline{C_D}$	St	θ_{sep} (deg)	$-\overline{C_{bp}}$	SPL†
$S/D = 2$: up	0.025	0.502	0.175	93.7	0.521	48.3 dB
$S/D = 2$: dn	0.064	-0.111	0.175	113.9	0.306	64.8 dB
$S/D = 3$: up	0.016	0.466	0.423	92.6	0.438	53.6 dB
$S/D = 3$: dn	0.197	0.042	0.243	115.5	0.296	70.0 dB
$S/D = 4$: up	0.083	0.486	0.250	95.7	0.576	73.4 dB
$S/D = 4$: dn	0.564	0.389	0.250	113.1	0.526	90.6 dB
$S/D = 5$: up	0.094	0.495	0.270	95.9	0.614	74.7 dB
$S/D = 5$: dn	0.506	0.399	0.270	112.7	0.513	89.2 dB
Single cyl.	0.077	0.614	0.297	97.4	0.723	77.2 dB

* Separation distance and upstream (up) or downstream (dn) cylinder
† Peak SPL at observer radius $R = 10$ m, span $L = 1$ m, $\theta = 90$ deg.

TABLE 7.2: Results of 3-D detached-eddy simulation of tandem cylinders at $M = 0.2$, $Re = 1.4 \times 10^5$ with separation $S/D = 2 - 5$.

in the location of the front stagnation point on the downstream cylinder, which in turn meant that the separation angle varied significantly according to the oscillations of the unsteady upstream cylinder wake. Figure 7.5(b) shows that the separated shear layers still reached and affected the flow over the downstream cylinder. The mean centerline velocity profile in Figure 7.7(b) shows the large recirculation region that stretched the full distance between the cylinders giving $U/U_\infty < 0$. Thus the inflow velocity of the downstream cylinder was significantly reduced compared to the freestream velocity. The vorticity iso-surface in Figure 7.4(b) reveals a fairly strong but intermittent and irregular vortex shedding downstream of the downstream cylinder.

At larger separation distances beyond $S/D = 3$, the behaviour of the upstream cylinder was similar to that of a single cylinder. The flow field of the $S/D = 4$ and 5 simulations showed very similar characteristics. However, Figure 7.7 indicates that in the $S/D = 5$ simulation the inflow velocity to the downstream cylinder was higher, reaching 60% of U_∞ compared to 45% of U_∞ for $S/D = 4$, due to the larger separation distance which allowed the wake velocity to recover toward the freestream value. These separation distances allowed enough room for discrete vortices to be shed from the upstream cylinder and the recirculation bubble behind it reduced to a much shorter length, as shown in Figure 7.5(c), compared to Figures 7.5(a) and 7.5(b). The vortices shed from the upstream cylinder had a large impact on the downstream cylinder flow, due to the combination of a highly unsteady turbulent and highly energetic inflow. This can be seen in Figures 7.5(c) and 7.6(c), which show a high level of interaction.

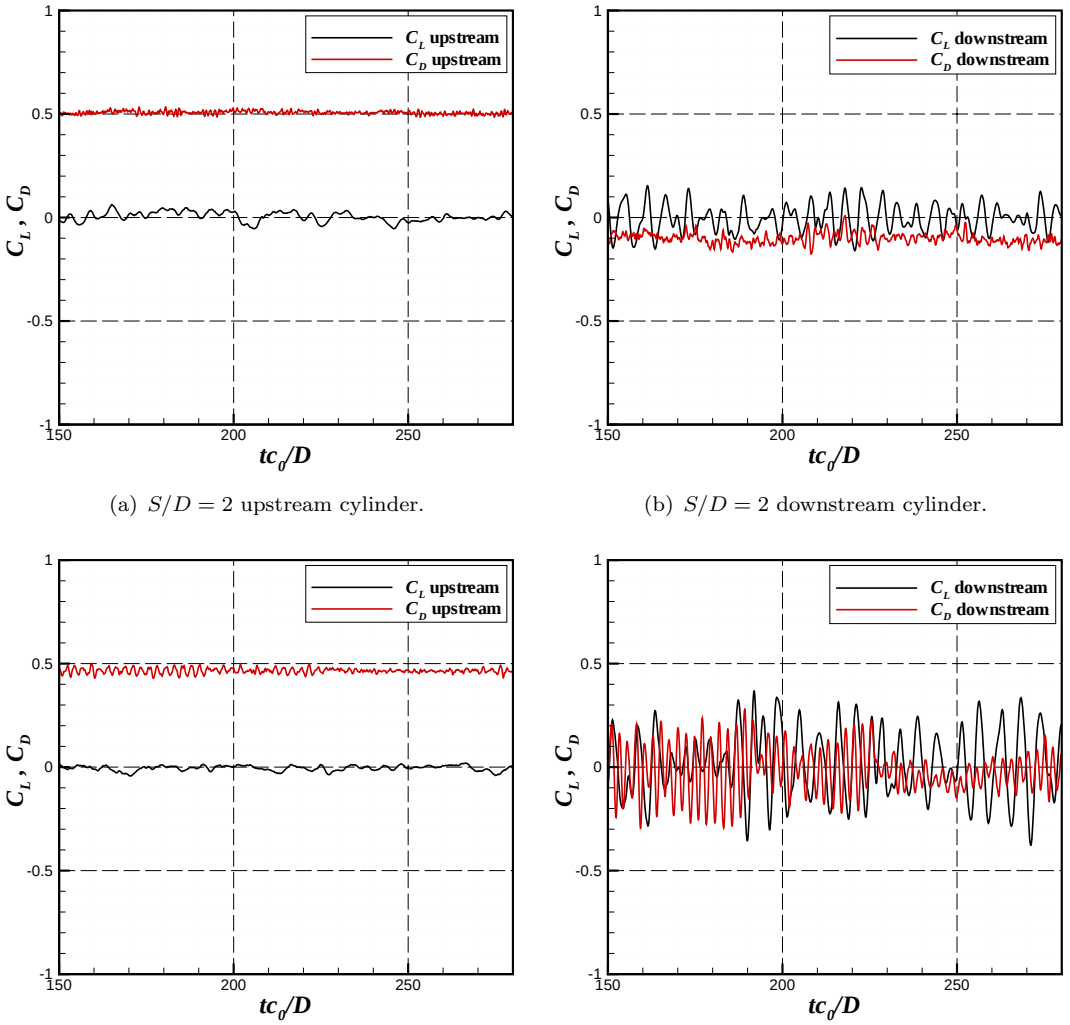

(a) $S/D = 2$ upstream cylinder.

(b) $S/D = 2$ downstream cylinder.

(c) $S/D = 3$ upstream cylinder.

(d) $S/D = 3$ downstream cylinder.

FIGURE 7.8: Comparison between predicted force coefficients on surface of tandem cylinders at $M = 0.2$, $Re = 1.4 \times 10^5$: (a) $S/D = 2$ upstream, (b) $S/D = 2$ downstream, (b) $S/D = 3$ upstream, (b) $S/D = 3$ downstream.

7.4 Aerodynamic Results

Table 7.2 reports the predicted lift coefficient RMS, $\overline{C'_L}$; mean drag coefficient, $\overline{C_D}$; Strouhal number of the primary vortex shedding frequency, St; separation angle, θ_{sep}; back pressure coefficient, $\overline{C_{bp}}$; and the peak SPL for all cylinders.

The Strouhal number of the shedding frequency varied considerably with cylinder separation for both the upstream and downstream cylinders. The nature of the shedding also varied, as indicated by the surface force histories in Figures 7.8 and 7.9. For cylinders that did not shed vortices, the Strouhal number according the frequency of the fluctuating lift is reported. For $S/D = 2$, the Strouhal number of the perturbations was identical for both cylinders, which is consistent with the "single body" analogy. The

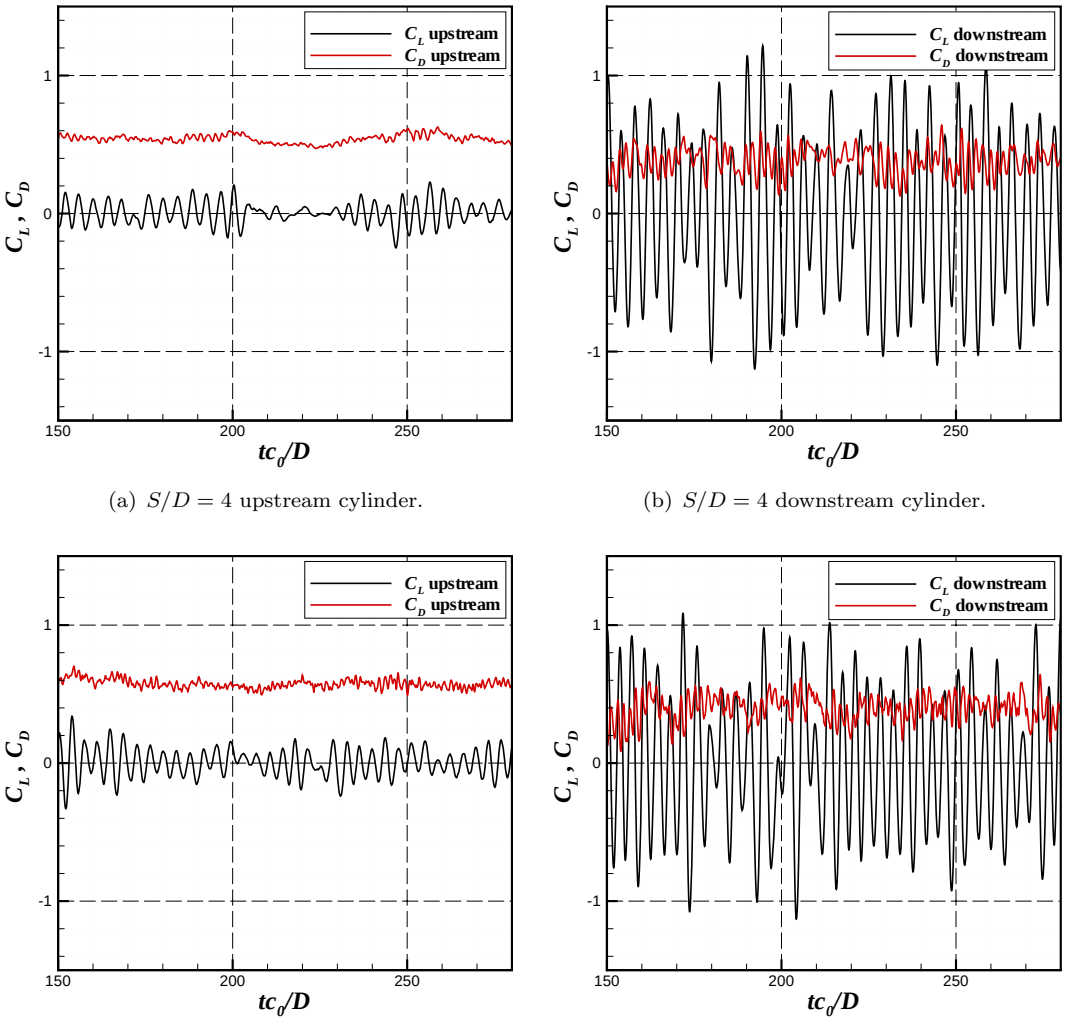

(a) $S/D = 4$ upstream cylinder.

(b) $S/D = 4$ downstream cylinder.

(c) $S/D = 5$ upstream cylinder.

(d) $S/D = 5$ downstream cylinder.

FIGURE 7.9: Comparison between predicted force coefficients on surface of tandem cylinders at $M = 0.2$, $Re = 1.4 \times 10^5$: (a) $S/D = 4$ upstream, (b) $S/D = 4$ downstream, (b) $S/D = 5$ upstream, (b) $S/D = 5$ downstream.

lower Strouhal number of $St = 0.175$ is also consistent with this analogy. At $S/D = 3$ two very different Strouhal numbers were measured. No vortices were shed from the upstream cylinder; however the high Strouhal number of 0.466 for the unsteady wake is likely to be the result of the blockage effect of the downstream cylinder. For a separation of $S/D = 4$ and $S/D = 5$, the shedding frequencies were identical for both cylinders at $St = 0.25$ and $St = 0.27$ respectively indicating that at these separation distances the shedding from the upstream cylinder had a strong influence on the shedding of the downstream cylinder. A similar shedding frequency of $St = 0.242$ was measured for both cylinders by Jenkins *et al.* [43] for $S/D = 3.7$.

At each separation distance there was a strong relationship between the separation angle and the cylinder position. The separation angle for the upstream cylinders ranged

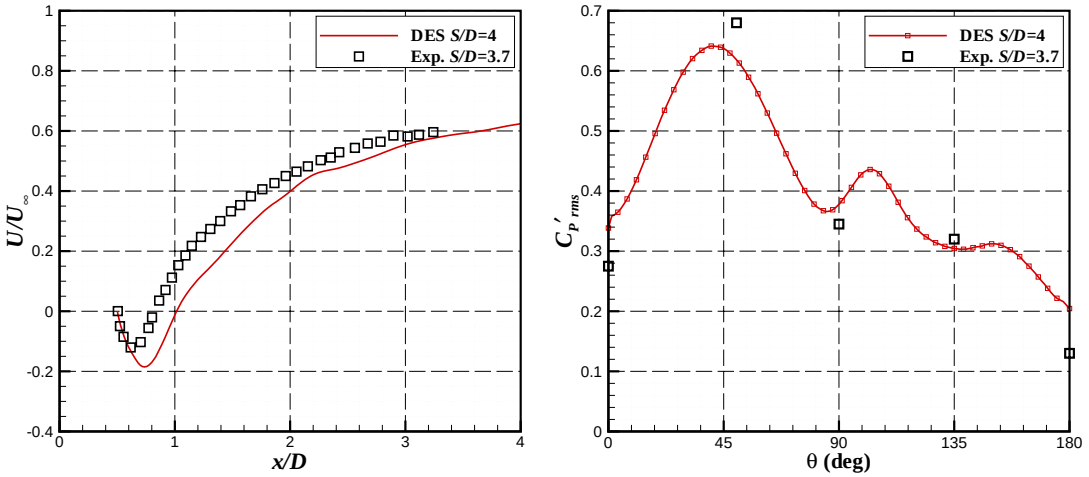

(a) Streamwise velocity.

(b) $C_{p'_{\text{rms}}}$.

FIGURE 7.10: Comparison between DES prediction, $S/D = 4$, and experiment [43] $S/D = 3.7$ at $M = 0.2$, $Re = 1.4 \times 10^5$: (a) normalised mean streamwise centreline velocity the behind rear cylinder, (b) $C'_{p_{\text{rms}}}$ distribution over the downstream cylinder.

between $\theta_{\text{sep}} = 92.6 - 95.9$ deg, compared to $\theta_{\text{sep}} = 97.4$ deg that was measured for a single cylinder. The separation angle measured on the downstream cylinder was significantly larger, predicted between $\theta_{\text{sep}} = 112.7$ to $\theta_{\text{sep}} = 115.5$ deg. This is indicative of the increased turbulent energy of the inflow to the downstream cylinder, leading to higher levels of boundary layer turbulence. The turbulent viscosity in the inflow to the downstream cylinder is visualised from the turbulent viscosity colour iso-levels shown in Figure 7.6. The separation angle quoted was calculated from mean statistics, but it varied considerably with the movement of the front stagnation point due to the unsteadiness of the upstream cylinder wake. This motion of the front stagnation point can be inferred from the snapshot of the vorticity iso-surfaces, particularly for the $S/D = 3$ case in Figure 7.4(b).

The force coefficient histories that were determined on the surface of each individual cylinder are presented in Figures 7.8 and 7.9. The plots show a significant variation dependent on both the separation distance and the cylinder location. The fluctuation amplitude for the C_L and C_D on the cylinders in the $S/D = 2$ simulation were lower than for a single cylinder. There is evidence of weak intermittent shedding behind the downstream cylinder, but clearly no shedding from the upstream cylinder. The predicted combined drag coefficient of $\overline{C_{D\,up}} + \overline{C_{D\,down}} = 0.391$ for both cylinders is less than the C_D for a single cylinder which was measured to be $\overline{C_D} = 0.614$. This lower drag coefficient is consistent with what is expected from a more elongated and less bluff cross-section. For $S/D = 3$, the upstream cylinder C_L and C_D characteristics were very similar to the $S/D = 2$ upstream cylinder, however the downstream cylinder force coefficient history plot reveals an interesting result. Whilst the mean C_D is low, the measured $\overline{C_D}$ perturbations were similar in magnitude to the lift coefficient perturbations. This can be

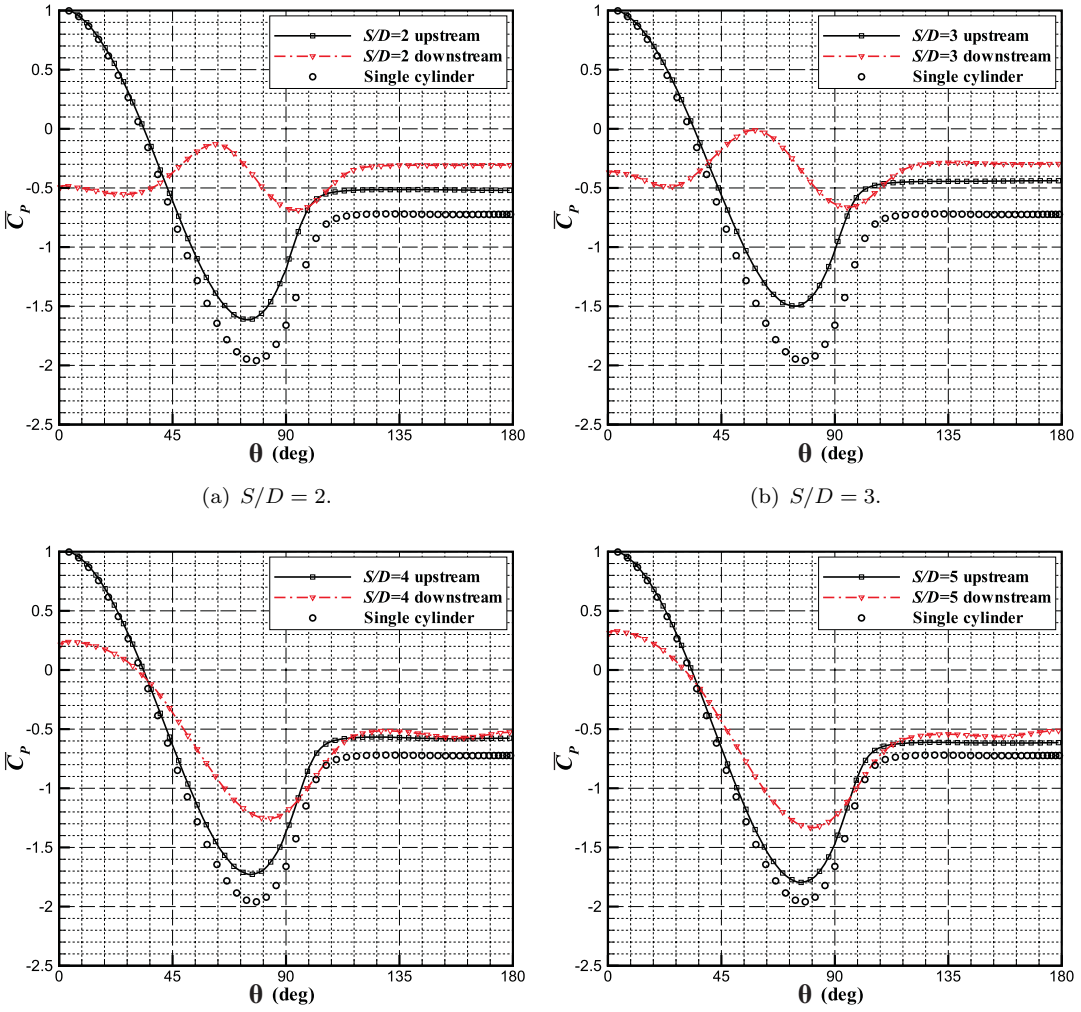

(a) $S/D = 2$. (b) $S/D = 3$.

(c) $S/D = 4$. (d) $S/D = 5$.

FIGURE 7.11: Time-averaged pressure coefficient distribution along upstream and downstream tandem cylinders at $M = 0.2$, $Re = 1.4 \times 10^5$: (a) $S/D = 2$, (b) $S/D = 3$, (c) $S/D = 4$, (d) $S/D = 5$.

explained by the movement of both the front stagnation point and the separation angle: This excursion of the stagnation point from $\theta = 0$ deg would lead to a time-dependent rotation of the lift dipole about the cylinder axis leading to high pressure fluctuations along the length of the cylinder. For $S/D = 4$ and $S/D = 5$, the upstream cylinder force history strongly resembled that of a single cylinder with a similar mean inflow. This again implies that at larger separation distances the upstream cylinder behaves more independently of the downstream cylinder.

The effect of the turbulent and unsteady inflow on the downstream cylinder is strongly reflected by the force history and statistics. The force histories for the downstream cylinder show enhanced force perturbations with respect to the single cylinder prediction, which indicate strong but irregular vortex shedding. The predicted $\overline{C_D}$ is smaller compared to the result for a single cylinder. This can be explained by the drop in drag

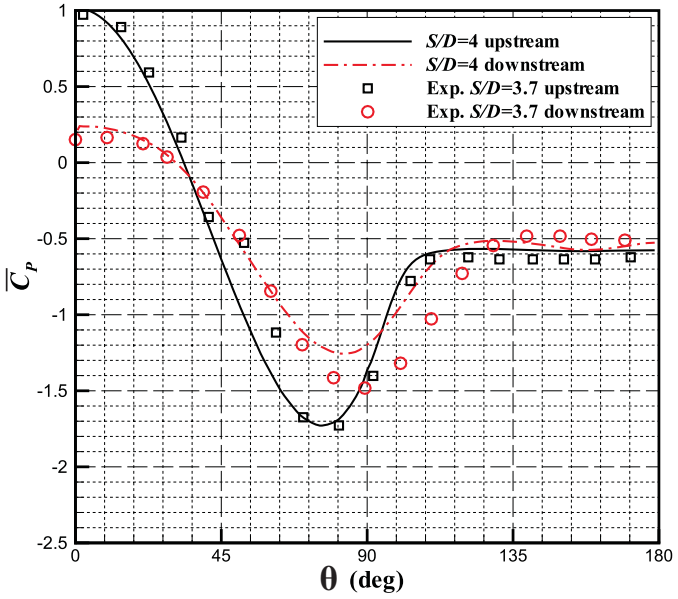

FIGURE 7.12: Time-averaged pressure coefficient comparison between $S/D = 4$ upstream and downstream cylinders at $M = 0.2$, $Re = 1.4 \times 10^5$ and experiment $S/D = 3.7$ [43] at $M = 0.2$, $Re = 1.66 \times 10^5$.

which is expected at higher freestream turbulence levels [82]. The magnitude of the drag force perturbations were much higher than expected for a single cylinder as a result of the higher energy and unsteadiness of the inflow. The RMS lift force coefficient on the downstream cylinder surface is up to tive times higher than measured on a single cylinder. For $S/D = 4$ the mean lift coefficient was measured as $\overline{C'_L} = 0.564$, slightly higher than for $S/D = 5$ at $\overline{C'_L} = 0.506$, compared to the single cylinder prediction of $\overline{C'_L} = 0.077$. This indicates that the $S/D = 4$ and 5 cases could be very noisy configurations compared to a single cylinder, whereas a possible noise reduction potential is seen at shorter separation distances.

A selection of results from the $S/D = 4$ simulation were compared with experimental data [43] for tandem cylinders with a separation distance of $S/D = 3.7$ that were conducted at a Reynolds number of 1.66×10^5. Although the separation distance used in the experiments was slightly lower, it was hoped that the measurements could be used to partially validate the numerical results and confirm any trends. Figure 7.10(a) provides a comparison between the predicted and measured normalised streamwise velocity distribution behind the downstream cylinder, showing reasonable agreement. The recirculation bubble length was slightly over-predicted, however the recovery rate to U_∞ is predicted well. This is consistent with Figure 7.5, which shows that the length of the recirculation bubble decreased between $S/D = 3$ and $S/D = 4$. Figure 7.12 compares the $\overline{C_p}$ distribution over both cylinders and shows excellent agreement for the upstream cylinder. The prediction of the downstream cylinder $\overline{C_p}$ distribution is reasonable with

an excellent agreement for $\overline{C_p}$ at the front stagnation point and the back pressure coefficient, although there is an under prediction of $\overline{C_{p_{\min}}}$. Comparison of the predicted and measured C'_p RMS is provided in Figure 7.10(b) showing agreement and indicating that the FW-H 2 surface should yield an accurate prediction for the far-field sound level and directivity.

The predicted $\overline{C_p}$ distribution over the upper surface of both cylinders for each simulation is provided in Figure 7.11 with the single cylinder result also plotted for comparison. The plots show that the upstream cylinder $\overline{C_p}$ distribution tends toward the single cylinder result as S/D increases, since $\overline{C_{p_{\min}}}$ and $\overline{C_{bp}}$ are lower with increasing S/D. The C_p distribution over the downstream cylinder reflects the large interaction effects due to the the upstream cylinder. Firstly, for $S/D = 4$ and $S/D = 5$, the flow is attached at $\theta = 0$ deg, but there is a disparity between the predicted C_p at this point. This can be attributed to the vortex shedding from the upstream cylinder and its interaction with the downstream cylinder. This also affects the value of $\overline{C_{p_{\min}}}$ which is high compared to the value predicted for the upstream and single cylinders, indicating weaker suction. Secondly, for the $S/D = 2$ and $S/D = 3$ cases, the mean flow is shown in Figure 7.7 to attach near $\theta = 60$ deg, accelerate and then detach around $\theta_{\text{sep}} = 110$ deg, leading to a unique $\overline{C_p}$ curve. The point of attachment and separation is shown by the mean streamwise velocity colour iso-levels shown in Figure 7.5. A similar pressure distribution was measured for $S/D = 1.435$ by Jenkins *et al.* [43].

7.5 Acoustic Results

7.5.1 FW-H Integration Surface Comparison

It is expected that acoustic shielding and scattering due to the adjacent bodies may have an impact on the far-field noise characteristics in tandem cylinder configurations. The off-body permeable surface, FW-H 3, surrounded both cylinders and was selected so that any scattering and shielding effects may be captured. The off-body surface was also expected to capture any off-body noise sources as long as they could be resolved by the grid and sampling frequency.

Figure 7.13 compares the predictions for all three FW-H integration surfaces in the $S/D = 4$ simulation. In Figure 7.13(a) the FW-H 1 and FW-H 2 surfaces are shown to have captured the same spectral characteristics as the FW-H 3 surface at $\theta = 90$ deg. In Figure 7.13(b) the contribution of FW-H 1 and FW-H 2 are combined and compared with the FW-H 3 prediction. The result shows that the FW-H 3 surface predicts a higher peak at the first harmonic ($St \approx 0.5$), which is likely to be due to vortices passing through the integration surface [52]. The FW-H 3 surface also predicts a shallower roll-off in the mid-high frequency range, which indicates either additional off-body sources

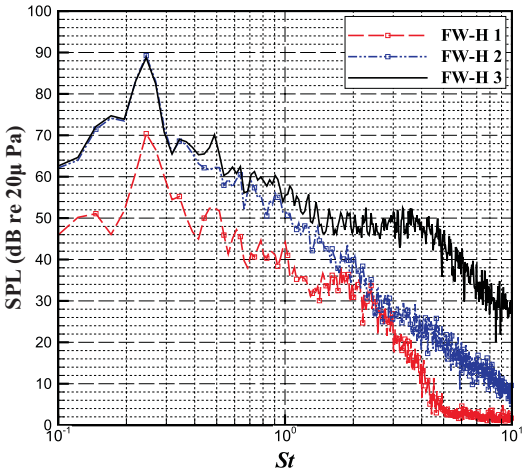

(a) $\theta = 90$ deg, $R = 100D$.

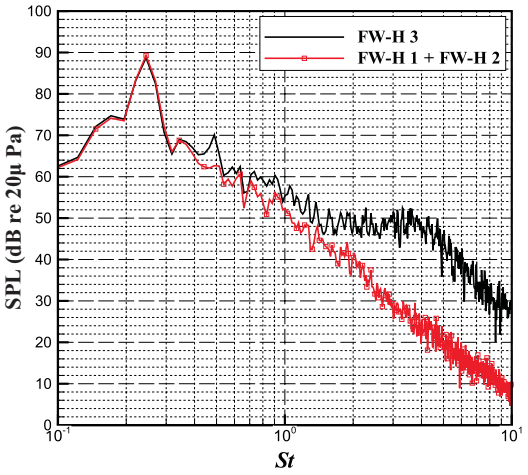

(b) $\theta = 90$ deg, $R = 100D$.

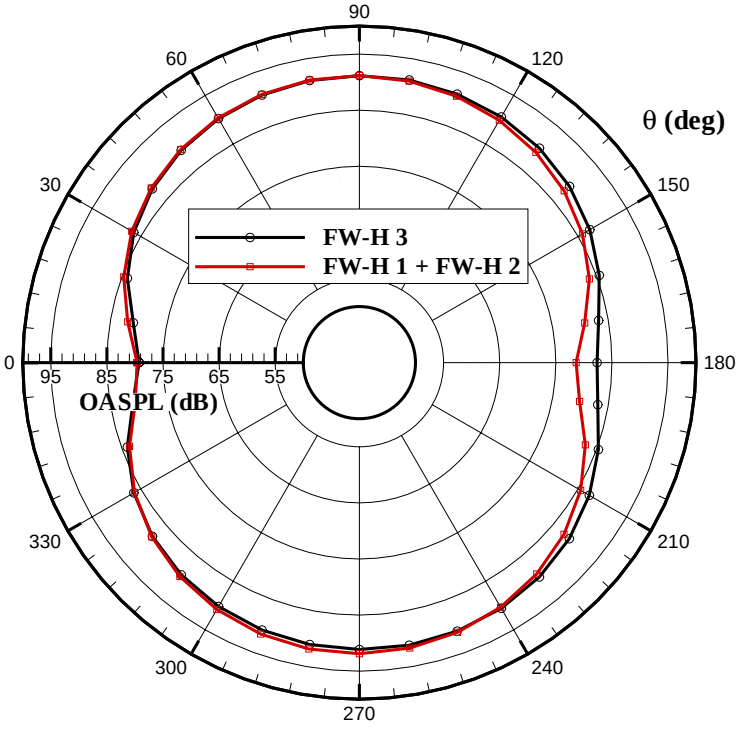

(c) $S/D = 4$ OASPL directivity, $R = 100D$

FIGURE 7.13: Comparison between the far-field directivity predicted from different FW-H surfaces for the $S/D = 4$ simulation at $R = 100D$: (a) spectra prediction at $\theta = 90$ deg, (b) comparison of spectra at $\theta = 90$ deg for on-body and off-body surfaces, (c) OASPL directivity. $M = 0.2$, $Re = 1.4 \times 10^5$.

have been captured or error due to the wake passing through the permeable surface. Figure 7.13(c) shows the directivity predictions of the three FW-H surfaces. Comparison of the combined prediction from FW-H 1 and FW-H 2 and FW-H 3 shows that the on-body and off-body surfaces predict the same dipole trend. The FW-H 3 surface predicted a higher OASPL than the other surfaces between $\theta = 120$ deg and $\theta = 220$ deg. Lockard performed multiple on-body and off-body surface predictions for tandem cylinders separated by $S/D = 3.7$ at $Re = 1.66 \times 10^5$ [55]. The predictions from the various surfaces showed good agreement and it was concluded that any volume sources in the flow field were negligible and that the on-body surfaces were able to capture the noise characteristics. In this case, it appears that scattering and shielding effects are very small and that the difference between off-body and on-body surfaces are due to error associated with the wake passing through the integration surface. Therefore, in the remaining sections, only results from the on-body integration surfaces are considered.

7.5.2 $S/D = 2$ Far-Field Acoustic Characteristics

Figure 7.14 presents the far-field spectrum prediction at $\theta = 90$ deg and $\theta = 0$ deg and also the OASPL directivity prediction. At $\theta = 90$ deg, neither cylinder exhibits the usual strong peak at the vortex shedding frequency that is expected for a single cylinder. Instead, a much broader spectrum was predicted with no distinct peak for the upstream cylinder, and a very broad hump that peaked at $St = 0.19$ for the downstream cylinder. The level of this peak was approximately 14 dB lower that the peak predicted for a single cylinder and the sound pressure level for the upstream cylinder was even lower. Broad spectra were also predicted at $\theta = 0$ deg as shown in Figure 7.14(b), and again the sound pressure level across the spectrum of the upstream cylinder was lower than that of the downstream cylinder. The downstream cylinder generated more low frequency noise than a single cylinder below $St = 0.6$.

The difference in sound pressure level between the cylinders is made clearer in Figure 7.14(c) that shows the OASPL directivity prediction. In both cases the usual dipole directivity pattern is absent and the cylinders exhibit very different directivity patterns indicating a large level of interaction. The upstream cylinder radiates noise predominantly into the rearward arc, with a maximum OASPL of 84.5 dB at $\theta = 180$ deg, corresponding to the direction of the unsteady separated region downstream of it. The directivity of the downstream cylinder shows considerably higher OASPL in all directions ranging from a minimum of 87.5 dB at $\theta = 0$ deg to 92 dB at $\theta = 90$ and $\theta = 270$ deg, and a weak dipole radiation pattern.

The three-dimensional directivity results are presented in Figure 7.15 that shows the overall mean-square pressure, $\overline{p'^2}$, corresponding to each cylinder. The results show depressions at observers located along the line of the cylinder axis, which is expected due to the dipole directivity. For the upstream cylinder, the noise radiation is predominantly

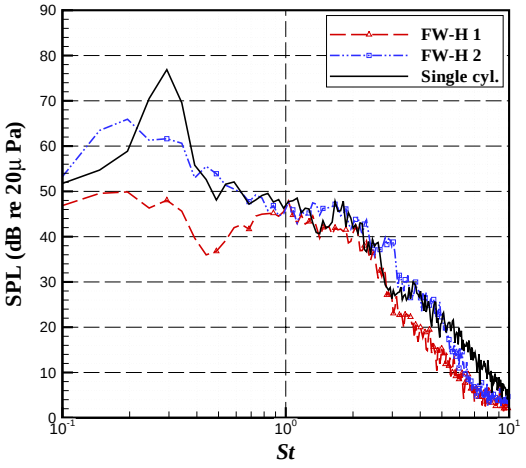

(a) $\theta = 90$ deg, $R = 100D$.

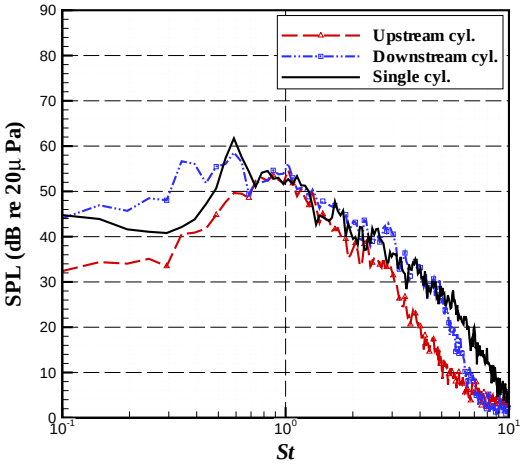

(b) $\theta = 0$ deg, $R = 100D$.

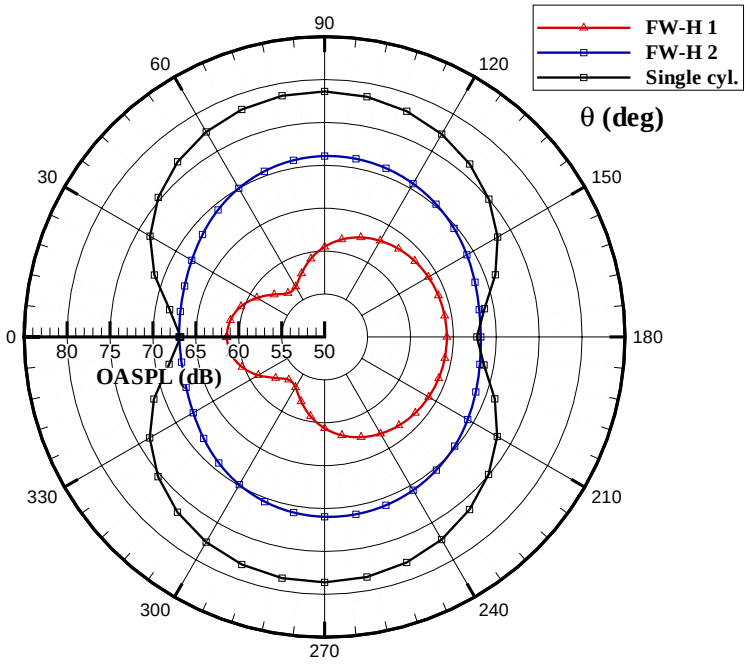

(c) OASPL directivity

FIGURE 7.14: Tandem cylinder far-field acoustic prediction, $S/D = 2$ at $R = 100D$: (a) spectra at $\theta = 90$ deg, (b) spectra at $\theta = 0$ deg, (c) OASPL directivity. $M = 0.2$, $Re = 1.4 \times 10^5$.

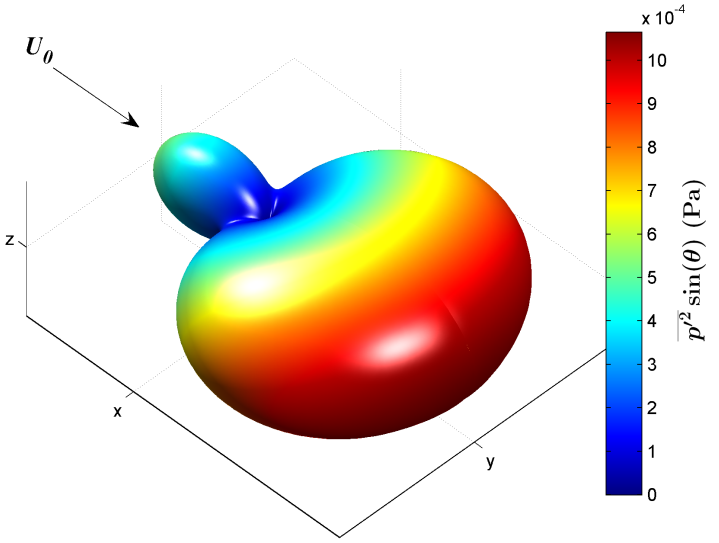

(a) Upstream cylinder.

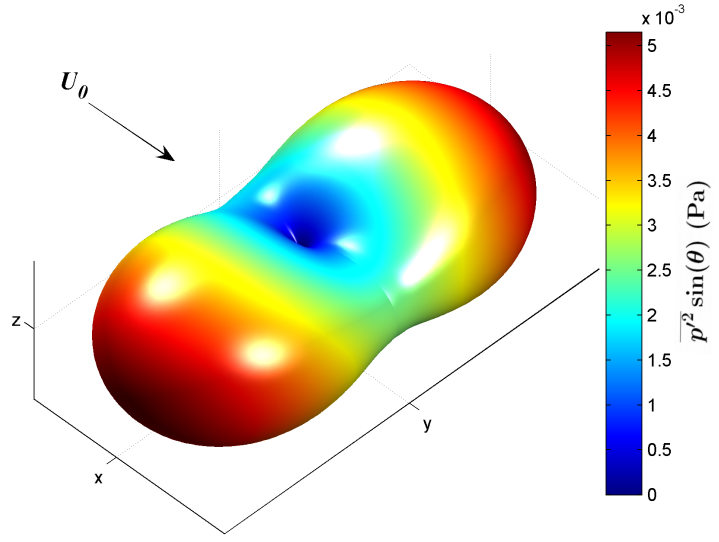

(b) Downstream cylinder.

FIGURE 7.15: Three-dimensional overall $\overline{p'^2}$ directivity prediction for tandem cylinders, $S/D = 2$ $R = 100D$: (a) upstream cylinder, (b) downstream cylinder. $M = 0.2$, $Re = 1.4 \times 10^5$.

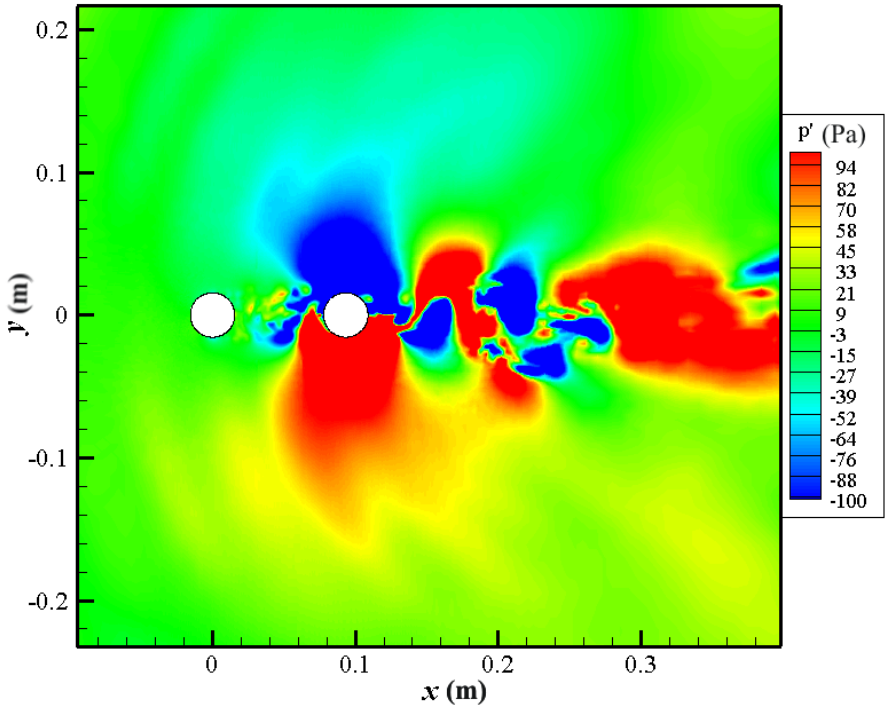

FIGURE 7.16: 3-D DES tandem cylinder $S/D = 3$ flow visualisation of instantaneous pressure perturbation, $p' = p - p_\infty$.

downstream. The directivity pattern of the downstream cylinder clearly shows both the lift and drag dipoles that are aligned perpendicular to each other. The magnitudes of the dipoles are not as disparate compared to the result for a single cylinder.

7.5.3 $S/D = 3$ Far-Field Acoustic Characteristics

The aerodynamic results indicate a highly unsteady flow field in the $S/D = 3$ simulation, especially around the downstream cylinder, due to the movement of the unsteady wake from the upstream cylinder. This unsteadiness meant that the RMS drag pressure forces on the surface of the downstream cylinder were comparable to the lift force fluctuations. The instantaneous pressure perturbation field in Figure 7.16 clearly shows much larger values across the surface of the downstream cylinder. This is also strongly reflected by the OASPL directivity pattern in Figure 7.17(c) that shows a more omni-directional behaviour. The maximum levels were predicted for observers close to $\theta = 0$ deg and $\theta = 180$ deg, where the minimum OASPL is usually expected for a single cylinder. The three-dimensional directivity plot of the downstream cylinder is presented in Figure 7.18(b) and reveals that the directivity resembles a dipole aligned parallel to the freestream and therefore associated with the unsteady drag forces. The directivity of the upstream cylinder closely resembles that of the $S/D = 2$ result in both magnitude and pattern and indicates a significant attenuation relative to a single cylinder.

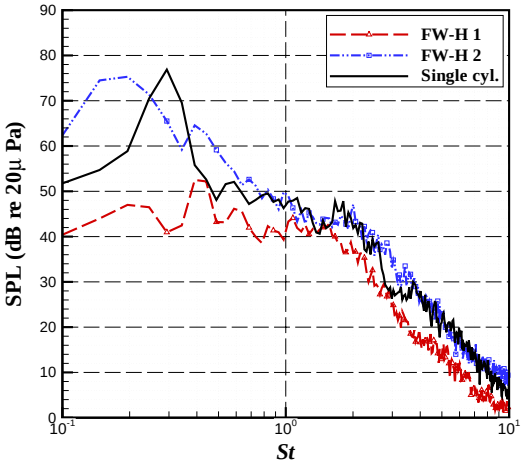

(a) $\theta = 90$ deg, $R = 100D$.

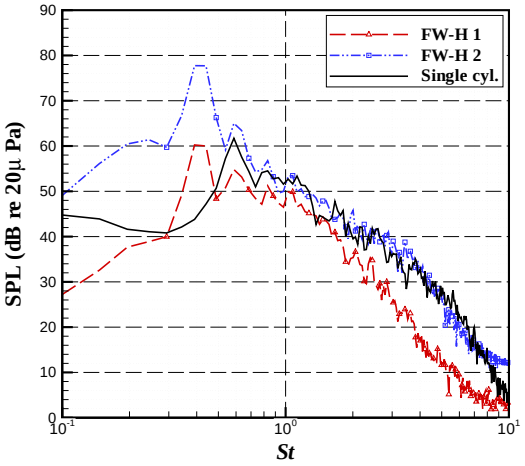

(b) $\theta = 0$ deg, $R = 100D$.

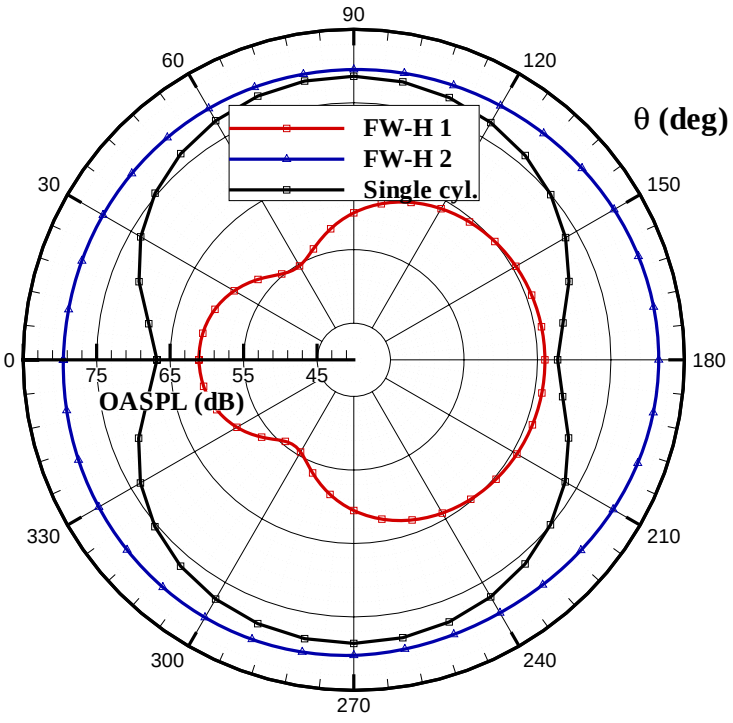

(c) OASPL directivity.

FIGURE 7.17: Tandem cylinder far-field acoustic prediction, $S/D = 3$ at $R = 100D$: (a) spectra at $\theta = 90$ deg, (b) spectra at $\theta = 0$ deg, (c) OASPL directivity. $M = 0.2$, $Re = 1.4 \times 10^5$.

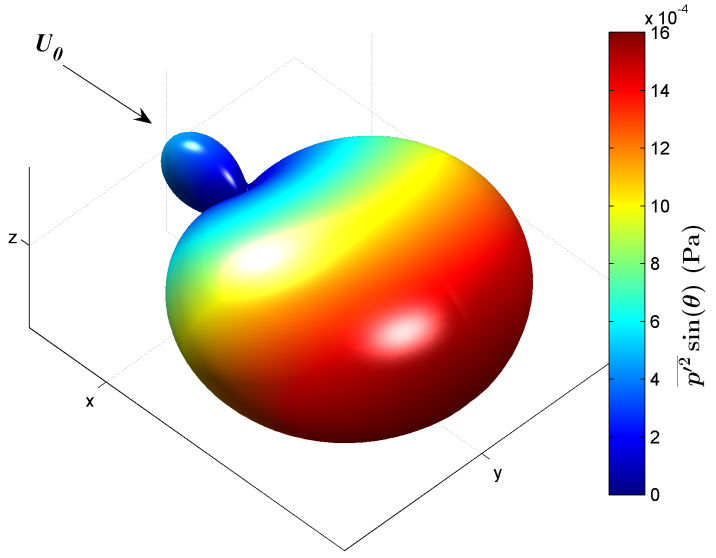

(a) Upstream cylinder.

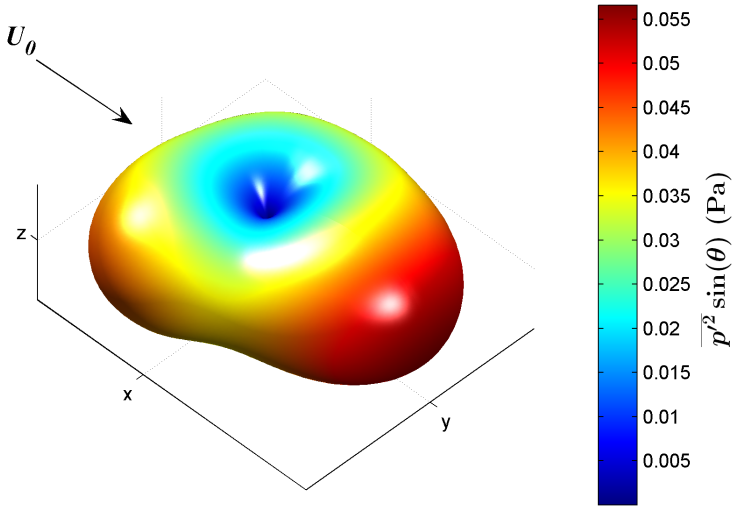

(b) Downstream cylinder.

FIGURE 7.18: Three dimensional overall $\overline{p'^2}$ directivity prediction for tandem cylinders, $S/D = 3$, $R = 100D$: (a) upstream cylinder, (b) downstream cylinder. $M = 0.2$, $Re = 1.4 \times 10^5$.

The highly unsteady flow field is also reflected by the spectral prediction of Figures 7.17. At $\theta = 90$ deg, a broad hump is predicted for the downstream cylinder centred around $St = 0.18$. The broad hump is a result the irregular vortex shedding. A low amplitude tone is predicted for the upstream cylinder that corresponds to the frequency of the measured fluctuating lift force. At $\theta = 0$ deg, a strong tone is predicted for the downstream cylinder at twice the vortex shedding frequency with a level around 2 dB higher than the tone predicted at $\theta = 90$ deg.

At this separation distance, it is clear that the interaction leads to an extremely complex flow field and acoustic far-field. This leads to irregular flow features that give the acoustic prediction a more broadband spectra and an omni-directional directivity field. Thus the usual characteristics expected for a single cylinder are lost due to the interaction.

7.5.4 $S/D = 4$ Far-Field Acoustic Characteristics

The aerodynamic analysis revealed that, for a separation distance of $S/D = 4$, vortices were shed from the upstream cylinder and the "blockage" effect of the downstream cylinder had a less pronounced effect compared to shorter separation distances. As a result, the characteristics of the upstream cylinder are similar to that of a single cylinder. This is also reflected by the far-field acoustic characteristics. The directivity prediction reveals the characteristic dipole directivity pattern and Figure 7.19(a) shows the usual tone at the vortex shedding frequency for an observer at $\theta = 90$ deg. The spectrum is very comparable to the single cylinder spectrum prediction although the shedding frequency was slightly lower at $St = 0.25$ compared to $St = 0.297$ for the single cylinder case, and the SPL is approximately 4 dB lower. Thus it is expected that the downstream cylinder still has a small impact on the upstream cylinder flow field at this separation distance. A similar conclusion can be drawn by comparing predictions at $\theta = 0$ deg in Figure 7.19(b).

The spectra prediction shows a large tone at the vortex shedding frequency. The vortex shedding frequency was the same for both cylinders and was $St = 0.25$. The peak level of the downstream cylinder is some 13 dB higher than that for a single cylinder and 16 dB higher than the upstream cylinder. Therefore the total noise of the tandem cylinders was dominated by the downstream cylinder which is clear from Figure 7.13. At $\theta = 0$ deg a weaker tone was predicted at twice the shedding frequency, 14 dB larger than the result for a single cylinder.

The directivity plot shows that both upstream and downstream cylinders have a dipole OASPL directivity pattern present in Figures 7.19(c) and 7.20. The magnitude of the upstream cylinder dipole is similar to that of a single cylinder, but with a larger ΔSPL between $\theta = 0$ deg and $\theta = 180$, indicating higher perturbations on the rear of the cylinder. The downstream cylinder has a much higher overall level than that of the

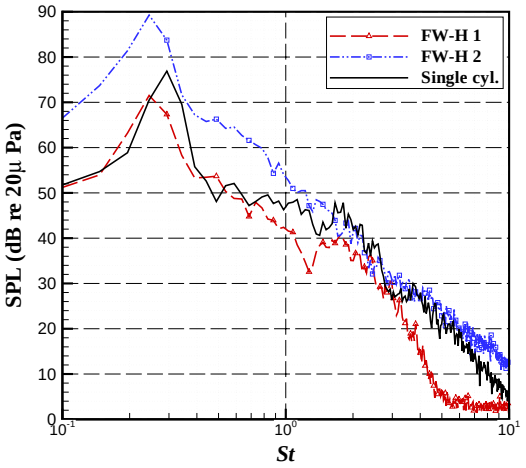

(a) $\theta = 90$ deg, $R = 100D$.

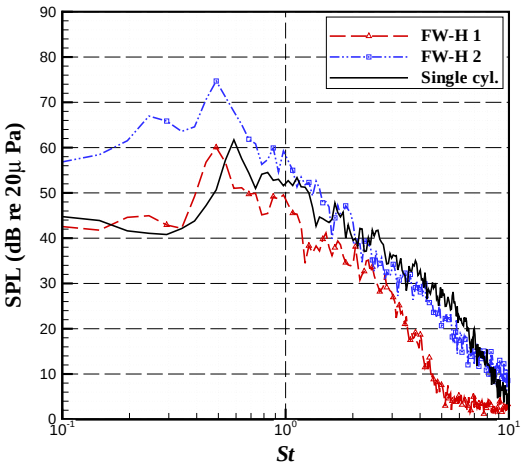

(b) $\theta = 0$ deg, $R = 100D$.

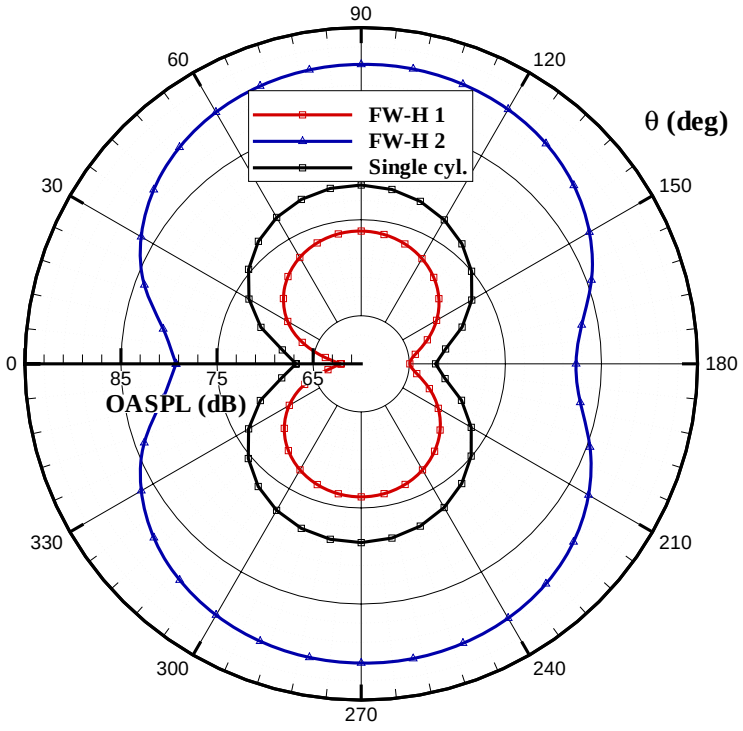

(c) OASPL directivity.

FIGURE 7.19: Tandem cylinder far-field acoustic prediction, $S/D = 4$, $R = 100D$: (a) spectra at $\theta = 90$ deg, (b) spectra at $\theta = 0$ deg, (c) OASPL directivity. $M = 0.2$, $Re = 1.4 \times 10^5$.

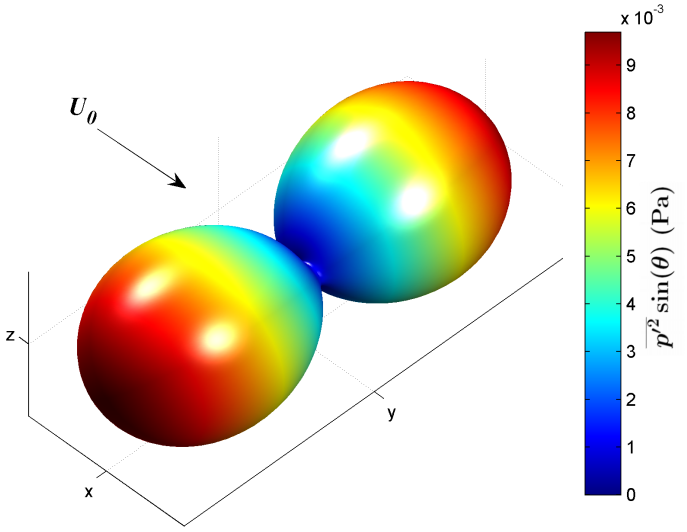

(a) Upstream cylinder.

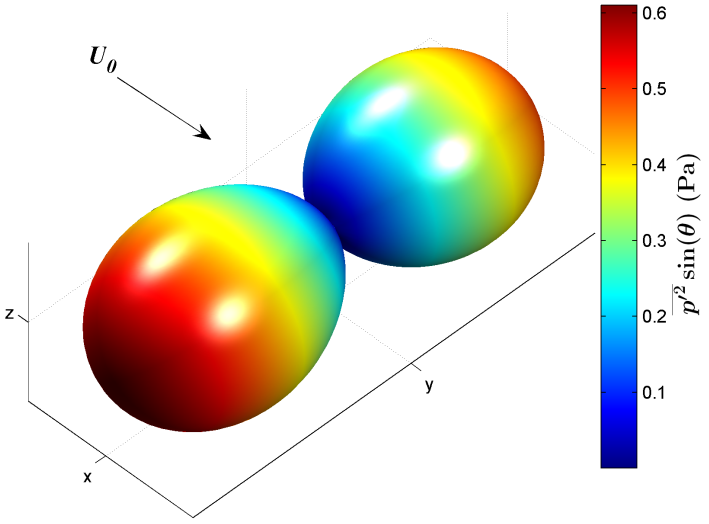

(b) Downstream cylinder.

FIGURE 7.20: Three dimensional overall $\overline{p'^2}$ directivity prediction for tandem cylinders, $S/D = 4$, $R = 100D$: (a) upstream cylinder, (b) downstream cylinder. $M = 0.2$, $Re = 1.4 \times 10^5$.

upstream cylinder, indicative of wake-body interaction. This is consistent with the analysis of Figure 7.9(b). At $\theta = 0$ deg the difference in OASPL between cylinders is close to 18 dB whilst at $\theta = 90$ deg the difference is approximately 14 dB. This is consistent with the levels reported by Lockard *et al.* [55] for simulations performed at $S/D = 3.7$. Figure 7.20 reiterates the dipole directivity patterns and the large disparity between the levels radiated by the cylinders.

7.5.5 $S/D = 5$ Far-Field Acoustic Characteristics

At $S/D = 5$, the predicted acoustic characteristics were very similar to those described for $S/D = 4$, however Figures 7.21(c) and 7.22 show that the overall noise levels were in most cases less, suggesting that the highest level of interaction for tandem cylinders occurs closer to $S/D = 4$. Figure 7.5 indicates that the inflow velocity to the downstream cylinder is higher for $S/D = 5$ compared to $S/D = 4$, and therefore it is suspected that the dissipation of inflow turbulence must be responsible for the lower sound pressure level. It is therefore reasonable to suggest that beyond $S/D = 5$ the interaction effects will become less as the wake turbulence from the upstream cylinder decays. However, at $S/D = 5$, the level of interaction is still very high. The OASPL directivity plot in Figure 7.21(c) indicates a difference of 10-14 dB between the downstream cylinder and the upstream cylinder. The differences between the peak level and frequency at $\theta = 90$ deg for the upstream cylinder and a single cylinder are almost negligible, as shown in Figure 7.21(a), although at $\theta = 0$ deg the spectrum is broader compared to that of a single cylinder. Such small differences indicate that the upstream cylinder does not act completely independently of the downstream cylinder at this separation distance.

7.6 Summary

Tandem cylinder simulations were performed for two equal diameter cylinders at separation distances $S/D = 2$, 3, 4, and 5. The results indicated that the resulting flow structures were sensitive to the separation distance, which in turn impacted the far-field acoustic characteristics considerably. The acoustic predictions indicated that the noise characteristics of tandem cylinders can be significantly different to those of a single cylinder. The results showed that the upstream cylinder and not just the downstream cylinder is affected significantly by the interaction mechanisms. At small separation distances the downstream cylinder created a "blockage" effect that greatly affected the upstream cylinder leading to an attenuation of its noise relative to that from a single cylinder. As the separation distance grew beyond $S/D = 3$, the blockage effect became less and the upstream cylinder behaved similarly to a single cylinder. The downstream cylinder dominated the total configuration noise at $S/D = 4$ and 5, due to the impact of the highly unsteady and turbulent wake on the downstream cylinder. Therefore it can

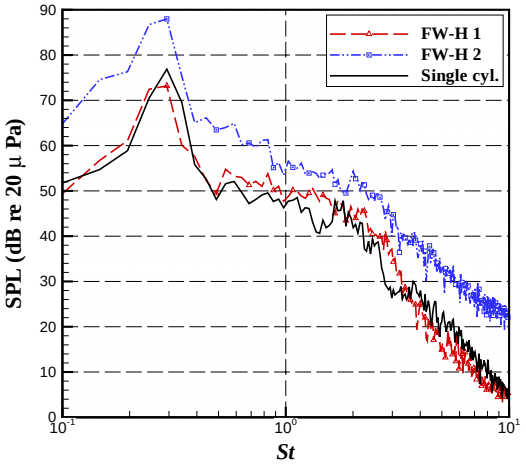

(a) $\theta = 90$ deg, $R = 100D$.

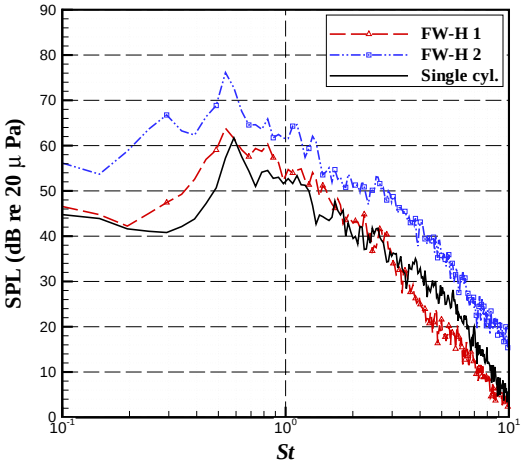

(b) $\theta = 0$ deg, $R = 100D$.

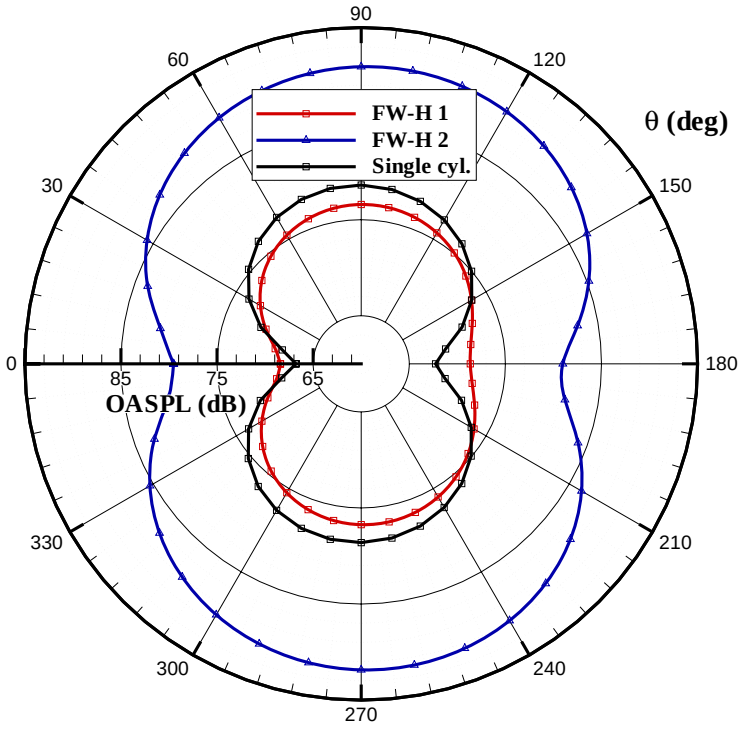

(c) OASPL directivity.

FIGURE 7.21: Tandem cylinder far-field acoustic prediction, $S/D = 5$, $R = 100D$: (a) spectra at $\theta = 90$ deg, (b) spectra at $\theta = 0$ deg, (c) OASPL directivity. $M = 0.2$, $Re = 1.4 \times 10^5$.

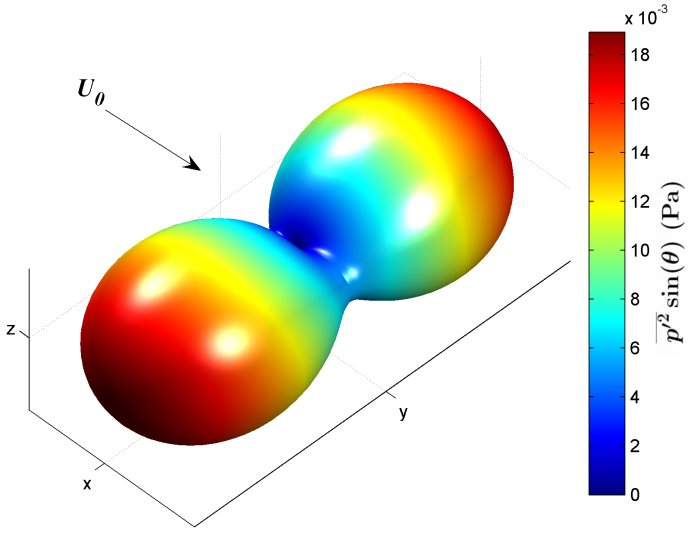

(a) Upstream cylinder.

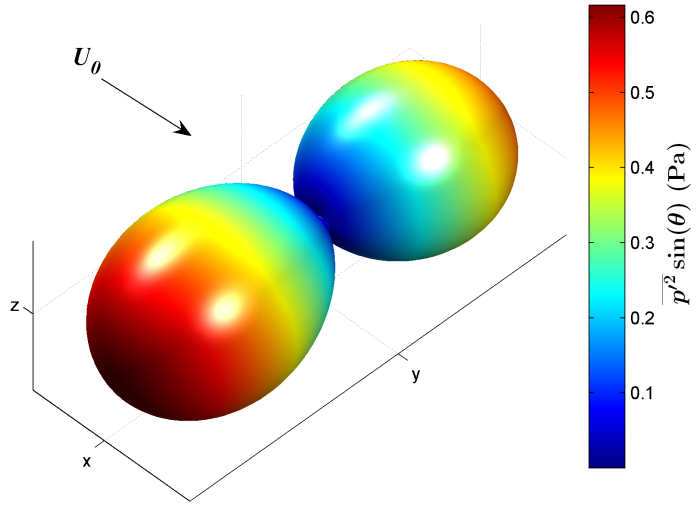

(b) Downstream cylinder.

FIGURE 7.22: Three dimensional overall $\overline{p'^2}$ directivity prediction for tandem cylinders, $S/D = 5$, $R = 100D$: (a) upstream cylinder, (b) downstream cylinder. $M = 0.2$, $Re = 1.4 \times 10^5$.

be concluded that interaction mechanisms can either lead to excessive interaction noise, or attenuation, depending on the separation distance, cylinder location, and observer location.

Chapter 8

High-Order Aeroacoustic Computation of Cylinders in Tandem

8.1 Outline

This chapter focuses on a high-order simulation of tandem cylinders using a high-order CAA solver. Large-eddy simulation was employed to predict the highly non-linear near-field around two cylinders in tandem separated by a distance $S/D = 3$, and a FW-H solver was used to predict the acoustic field at far-field observers.

8.2 Introduction

The high-order finite-difference code SotonCAA was used to solve the three-dimensional flow over two cylinders in tandem at $Re = 1.4 \times 10^5$ and a separation distance of $S/D = 3$. The aim was to further investigate the flow around tandem cylinders and the resulting acoustic field using a high-order CAA code. The work was divided into two parts. First the highly non-linear near-field was computed using a high-order finite differencing scheme and second-order implicit time-stepping scheme. Secondly a FW-H solver was used to determine the acoustic field at far-field observers. Characteristic interface conditions were employed by the CAA code to allow the use of highly skewed grids required by the tandem cylinder geometry. Large-eddy simulation was adopted to resolve the turbulent field and the results are compared to the DES results discussed in Chapter 7. It was hoped that the high-order results may increase the resolution of the source prediction and support the conclusions of Chapter 7.

Parameter	**Symbol**	**Value**
Separation distance	S/D	3
Freestream Mach number	M	0.2
Cylinder diameter	D	0.0321 m
Non-dimensional time step	$\Delta t c^*_\infty / D$	0.00375
Reynolds number	Re	1.4×10^5

TABLE 8.1: Simulation parameters used in the high-order tandem cylinder computation.

8.3 Computational Setup

The geometry consisted of two circular cylinders arranged in tandem and separated by a distance of $S/D = 3$ between cylinder centres. The Reynolds number of the simulation was 1.4×10^5 based on a cylinder diameter of 0.03207 m, and the Mach number was $M = 0.2$. This Reynolds number corresponds to the high sub-critical cylinder regime [82].

The geometry lead to a high degree of grid skew between the block boundaries illustrated in Figure 4.2. Thus it was necessary to employ the characteristic interface conditions [46] to avoid problems associated with grid singularity. The grid consisted of 27 structured blocks which extended 20 diameters upstream, above and below the upstream cylinder, and 30 diameters downstream of the rearward cylinder. The structure of the grid is shown in Figure 7.2. Each cylinder circumference was spit into 317 equally spaced grid points and the first cell distance normal to the wall was chosen to achieve $y^+ \approx 1$. The grid in the $x - y$ plane was extruded along the z direction a distance of two cylinder diameters and was resolved by 30 equally spaced grid points to achieve a total of 3.2 million points. The cell aspect ratios is in the order of 20 in the boundary layers reducing to unity between the two cylinders where $\Delta x \approx \Delta y \approx \Delta z$. Periodic boundary conditions were applied along the spanwise boundary to simulate an infinite span.

Three FW-H integration surfaces were defined: a solid surface on the upstream and downstream cylinder walls, and one off-body permeable surface which enclosed both cylinders. These surfaces are denoted FW-H 1, FW-H 2, and FW-H 3 respectively and are indicated in Figure 7.3.

The high-order CAA code SotonCAA was employed using a sixth-order compact spatial scheme [40] to approximate the spatial derivatives along with a high-order explicit filter. Second-order implicit time-stepping was employed using 5 sub-iterations per time step [61]. The time step size was $t = 0.00375 D/^*_\infty$ yielding a CFL of approximately 8 based on the free stream fasted characteristic $(u^*_\infty + c^*_\infty)$. This time step corresponds to a sampling frequency of 2.89 MHz and one shedding cycle based on a Strouhal number of 0.2 corresponds to 6705 time steps.

The high-order simulation was initiated from a developed low-order solution to increase the convergence time to a quasi-steady solution. Simulation $t = 0$ is refers to the start of the high-order simulation. Mean statistics were taken after 300 non-dimensional times tU_∞/L^*, where the characteristic length L^* is taken to be the cylinder diameter D, and flow variables were then sampled on the FW-H integration surfaces for a duration of 500 non-dimensional times and were sampled every 10 time steps, yielding a sampling frequency of 288 kHz. The simulation was performed on between 16 and 27 processors utilising Quad-Core Intel nodes on the Microsoft High-Performance Computing Cluster at the University of Southampton. The nodes consist of 2.4Ghz AMD Opteron processors with 4GB or 8GB of RAM and a Myranet inter-communication network. The 27 processor configuration has a theoretical top performance of 0.1TFLOPS and the computational time was approximately 6000 CPU hours.

8.4 Aerodynamic results

Due to the relatively cell high aspect ratios close to the cylinder wall the simulation can be considered a very large-eddy simulation (VLES). The subgrid model turbulent viscosity, μ_t, controls the kinetic energy of the vortex shedding process so that the large-scale eddies that dictate the shedding mechanism are resolved and their growth is managed by the subgrid model.

In the VLES computation, the expected flow unsteadiness and non-linearity was captured in the gap region and in the wake of both cylinders. Large interaction between the upstream cylinder wake and the downstream cylinder was also captured. Figure 8.1 indicates the three-dimensional vortical structures behind the cylinder by displaying iso-surfaces of $z-$ vorticity coloured by the $x-$component of the velocity vector. Weak vortex shedding was captured behind both cylinders at a Strouhal number of $St = 0.192$ which is in general agreement with experimental results [42]. The downstream cylinder was subjected to higher unsteadiness due to the turbulent inflow due to the wake/body interaction mechanism. In this section the results presented focus on the instantaneous and the time-averaged flow field around each cylinder.

Unless stated otherwise, all values in the following sections have been non-dimensionalised. The length scales are non-dimensionalised by $L_0 = 0.03207$ m, the velocities by $c^*_\infty = 340$ m/s, density by $\rho^*_\infty = 1.225$ kg/m^3, and pressures by $\rho^*_\infty c^{*2}_\infty$.

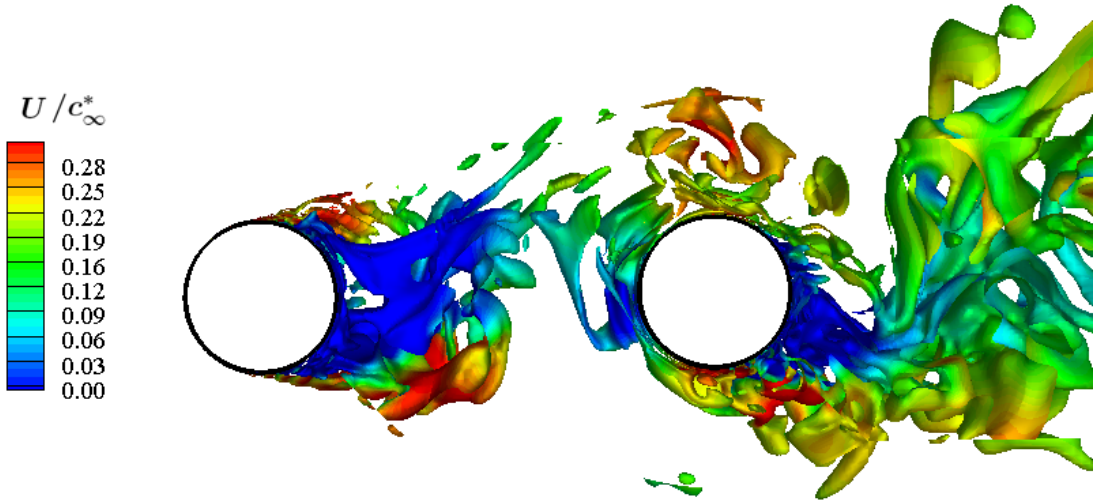

FIGURE 8.1: High-order tandem cylinder computation: iso-surface of instantaneous z-vorticity magnitude coloured by $x-$component of velocity.

8.4.1 Instantaneous Flow Features

The Q-criterion [13] is useful for visualising the vortical content in the instantaneous solution and is defined by

$$Q = \frac{1}{2}\left(\Omega_{ij}\Omega_{ij} - S_{ij}S_{ij}\right) = \frac{\partial u_i}{\partial x_j}\frac{\partial u_j}{\partial x_i} > 0, \tag{8.1}$$

where S_{ij} and Ω_{ij} are the strain rate tensor of Equation B.8 and the mean vorticity tensor of Equation B.9.

Figures 8.2 and 8.3 display instantaneous iso-Q surfaces coloured by z-vorticity magnitude. The two figures reveal the resolution of the simulation indicating that the grid, time step, and numerical schemes are capable of capturing a range of turbulent structures. The larger structures indicate weak but coherent vortex shedding behind both cylinders. The downstream cylinder is clearly affected by the upstream disturbance which is most clearly shown in Figure 8.3. The streamtraces show how the front stagnation point and the upper and lower separation points deviate from the locations expected for an isolated cylinder.

Figure 8.4 displays instantaneous pressure perturbation contours $p' = (p - p_0)/\rho^*_\infty c^{*2}_\infty$ on an $x - y$ slice along the cylinder span, and the location of pressure monitors. The pressure was monitored at a number of locations both on the cylinder and in the flow field. Monitors A-E are located on the cylinder surface and monitor F is located in the wake of the downstream cylinder. Figure 8.5 displays the spectral content of the pressure signal at these monitors.

Large pressure perturbations were captured in the separated regions induced by the upstream cylinder, in the gap region, and on the surface and in the wake of the downstream

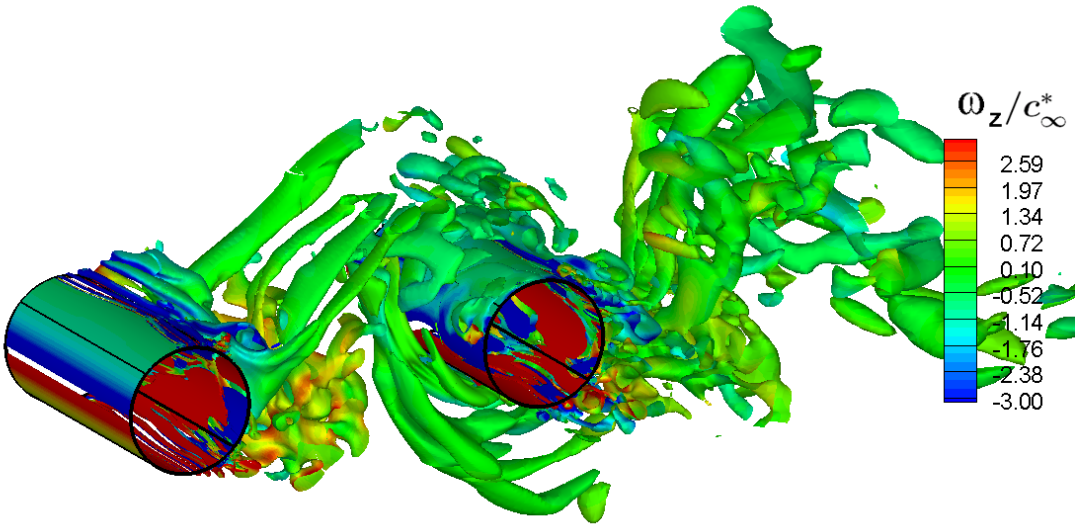

FIGURE 8.2: High-order tandem cylinder computation: iso-surface of instantaneous Q-criterion coloured by $z-$vorticity. ($Q = 0.1$, ω_z = -3 to 3).

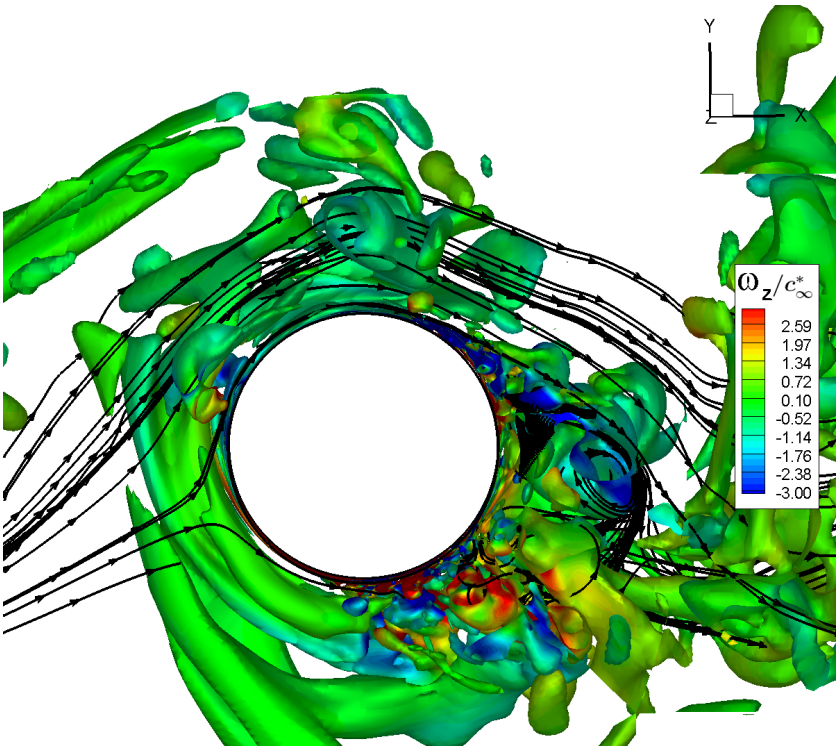

FIGURE 8.3: High-order tandem cylinder computation: iso-surface of instantaneous Q-criterion coloured by $z-$vorticity. ($Q = 0.1$, ω_z = -3 to 3).

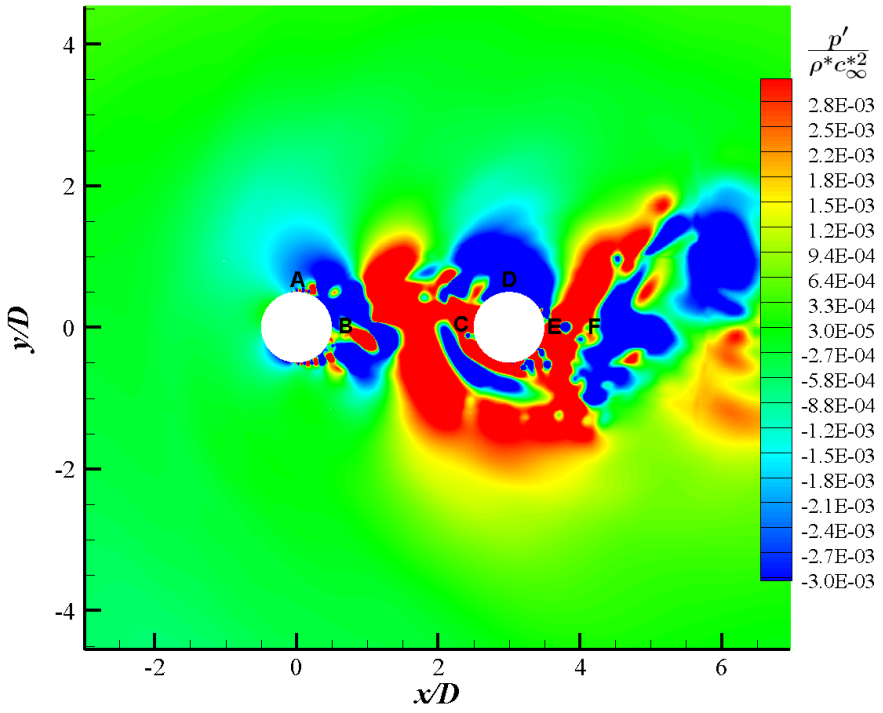

FIGURE 8.4: High-order tandem cylinder computation: non-dimensional instantaneous p' pressure perturbation contours and pressure monitor locations.

cylinder. Small coherent vortex structures were captured along the separated shear layers of the upstream cylinder. These higher frequency structures were not captured in the low-order DES simulation. Monitor A was able to capture these structures. Figure 8.5(a) displays the spectral content revealing a large peak at approximately 2.5 kHz.

8.4.2 Time-Averaged Flow Features

The mean variables were averaged over the last 120,000 steps of the simulation which corresponds to 450 non-dimensional times. Figure 8.6 displays the mean $x-$velocity colour iso-levels around the cylinders and Figure 8.7 displays the mean velocity along the line $y = 0$ between the two cylinders. It is clear from comparison between Figure 8.6 and Figure 7.5(b) that the DES result predicted a larger recirculation region behind the upstream cylinder. This is due to the absence of coherent shedding in the DES results as shown by Figure 7.6, whereas in the LES simulation vortices were captured in the wake of the upstream cylinder. Figure 8.7 indicates that the velocity reached 28% of the freestream value, and is more comparable with the trend predicted for $S/D = 4$ by DES shown in Figure 7.7(c). Examination of the results in Figure 8.6 indicates a time-averaged separation angle on the upstream cylinder of $\theta_{\text{sep}} = 88$ deg for the LES simulation compared to $\theta_{\text{sep}} = 92$ deg in the DES. Both shedding frequency and separation angle predicted by the LES are consistent with a cylinder in the sub-critical regime [82].

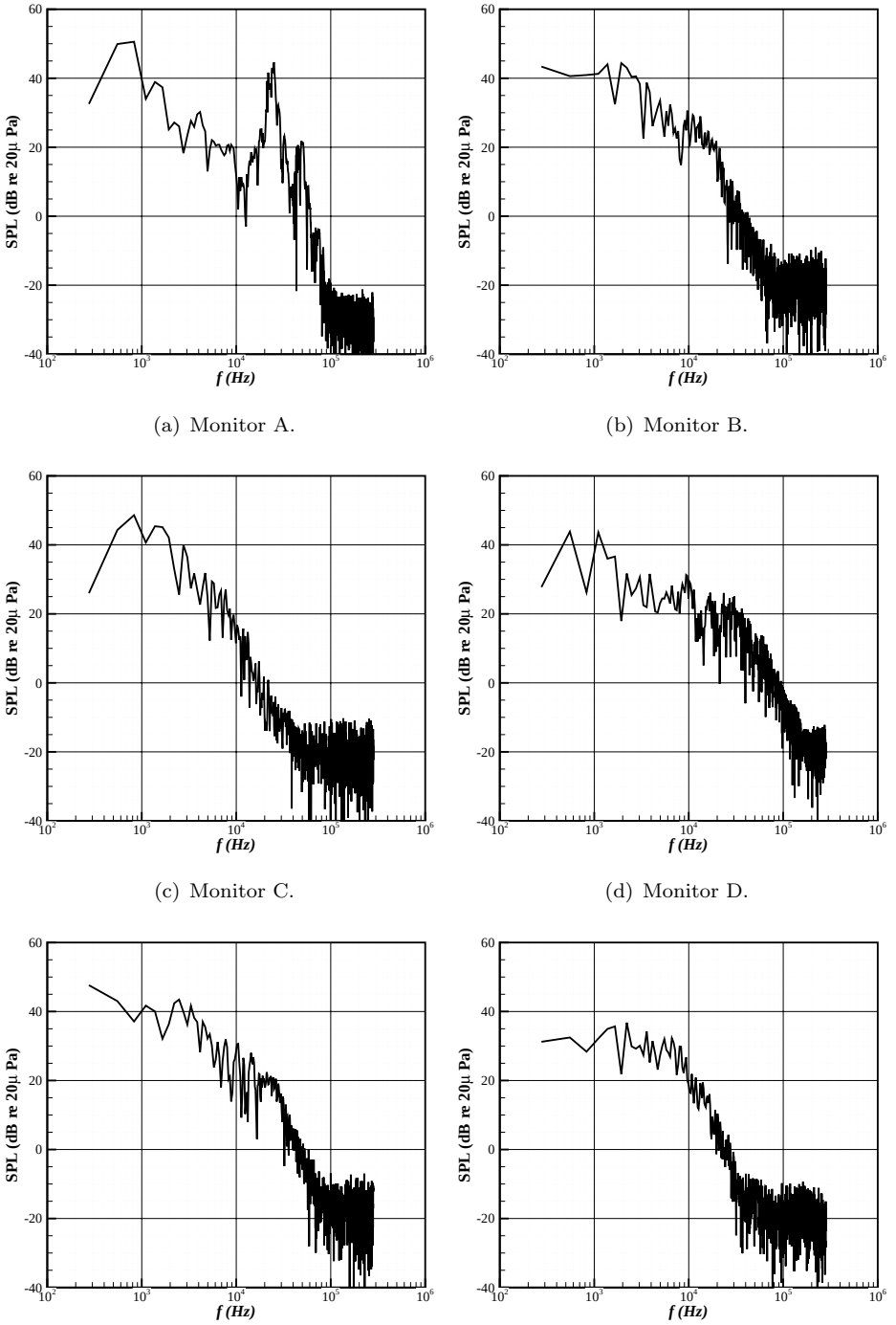

(a) Monitor A.

(b) Monitor B.

(c) Monitor C.

(d) Monitor D.

(e) Monitor E.

(f) Monitor F.

FIGURE 8.5: High-order tandem cylinder computation: pressure monitor SPL results.

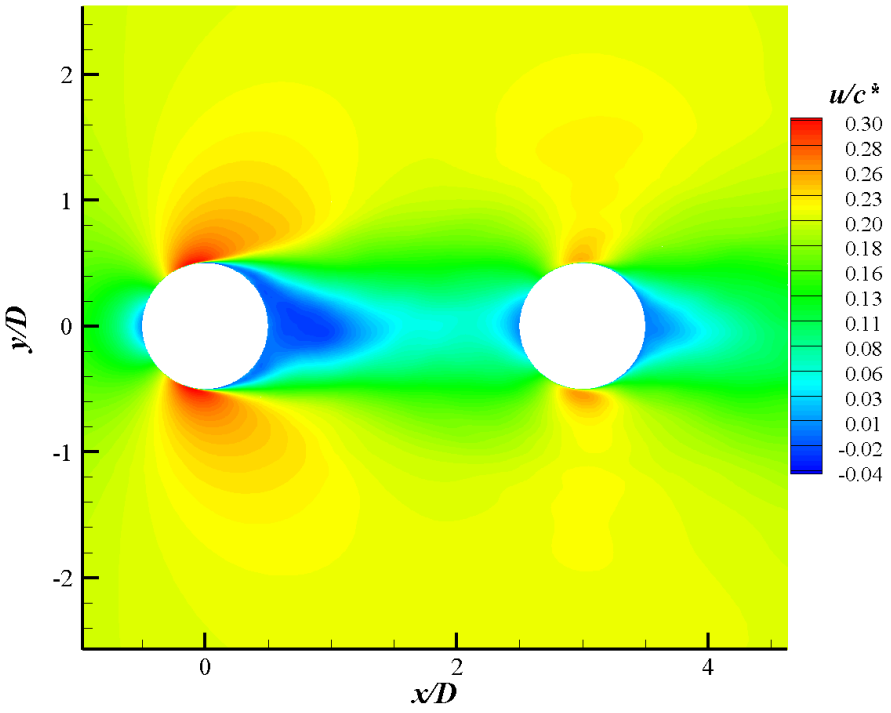

FIGURE 8.6: High-order tandem cylinder computation: time-averaged x-velocity contours.

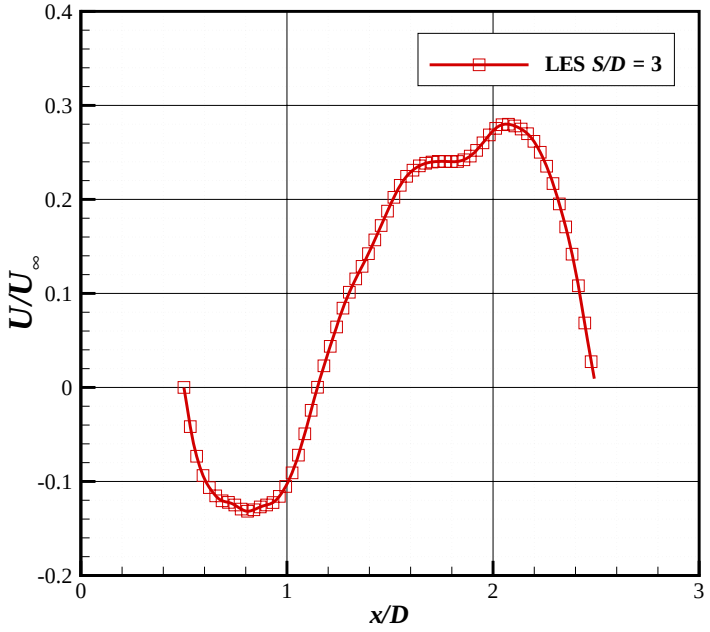

FIGURE 8.7: High-order tandem cylinder computation: time-averaged streamwise gap region centreline velocity along $y = 0$ between tandem cylinders, $S/D = 3$.

In the DES, the freestream turbulent viscosity ratio was set at a high value $\mu_t/\mu = 10$ to simulate the supercritical Reynolds number cylinder regimes [79], even though the simulation Reynolds number was sub-critical. In the LES, the boundary layer was left

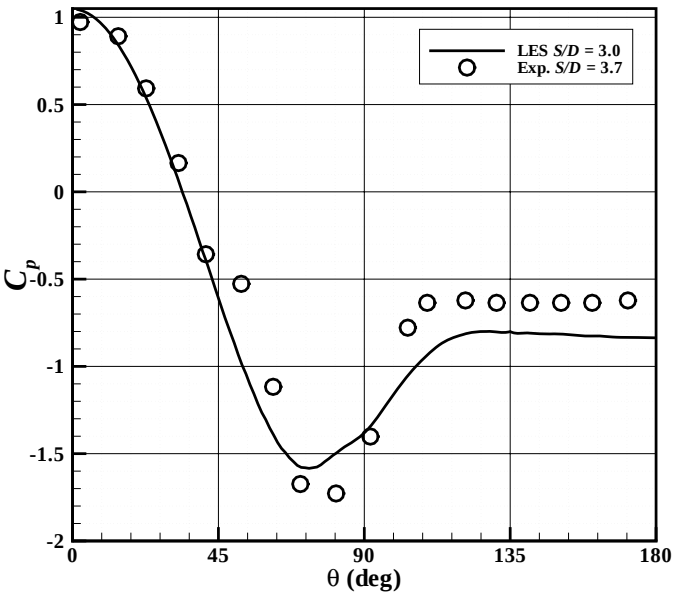

(a) Upstream cylinder.

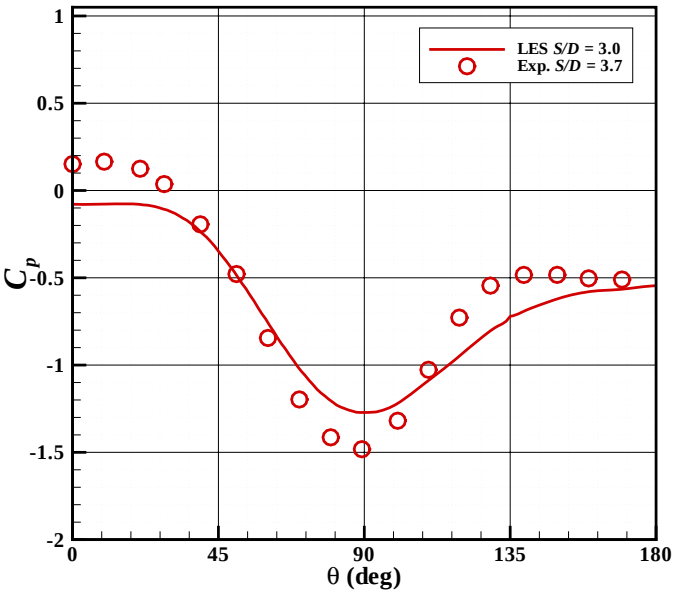

(b) Downstrea cylinder.

FIGURE 8.8: High-order tandem cylinder computation: mean C_p on upper surface of tandem cylinders - comparison between LES results with $S/D = 3$, $Re = 1.4 \times 10^5$, $M = 0.2$ and experimental results at $S/D = 3.7$, $Re = 1.66 \times 10^5$, $M = 0.2$.

to develop naturally and the transition location, and thus cylinder regime obtained in the solution was largely dependent on the Reynolds number, which was sub-critical at $Re = 1.4 \times 10^5$ [82]. This explains the difference between the DES and the LES results. This suggests that the tandem cylinder regimes outlined in Table 2.1 are dependent not only on the separation distance, but also on the cylinder regime associated with the upstream cylinder. This is supported by experiment [50] as it was observed that at the critical separation distance no vortices developed in the gap region and this distance was shown to be a function of the Reynolds number, which determined the regime of the upstream cylinder.

The mean pressure coefficient on the upper surface of the cylinders is displayed in Figure 8.8. The results are compared with experiments [43] for tandem cylinders with a separation distance of $S/D = 3.7$, conducted at a Reynolds number of 1.66×10^5 and a Mach number of 0.2. In the experiments, vortex shedding was observed behind the upstream cylinder. The results show acceptable agreement for both cylinders, given the difference in Mach number and separation distance. The difference in separation points between the results for the upstream cylinder is clear with the LES indicating laminar separation just before the point of maximum thickness indicated by the kink along the pressure recovery region at $\theta = 88$ deg. The lower $-C_{p_{\text{base}}}$ at $\theta = 180$ deg and smaller favourable pressure gradient region predicted by LES is an indication of the sub-critical flow. The computed mean drag coefficient is C_D=0.824, which is slightly higher than that predicted by the DES, due to the earlier separation and the resulting larger wake thickness, but is in the range expected at this Reynolds number [82]. The C_p distribution of the downstream cylinder is indicative of the large unsteadiness and the fluctuation of the front stagnation point and separation points. The predicted trend follows the features of experimental result. The predicted mean separation angle is $\theta_{\text{sep}} = 105$ degrees leading to a drop in the drag coefficient to $C_D = 0.370$. This is consistent with the interaction effects found in Chapter 7.

8.5 Acoustic results

The acoustic results were sampled on the three integration surfaces at a frequency of 282.7 kHz for the last 500 non-dimensional times of the simulation. The location of the far-field observers was defined by $x = R\sin\phi\cos\theta$, $y = R\sin\phi\sin\theta$, $z = R\cos\phi$, where $R = 100D$, $0 \leq \theta \leq 2\pi$, and $0 \leq \phi \leq \pi$. This generated a spherical observer surface with a resolution of $\Delta\theta = \Delta\phi = \pi/18$, with the origin at (0,0,0). The FW-H solver was then used to compute the far-field acoustic pressure histories at each observer. Fast Fourier Transforms were applied to the time histories to yield the far-field acoustic spectra. In this section, the spectra and directivity are presented.

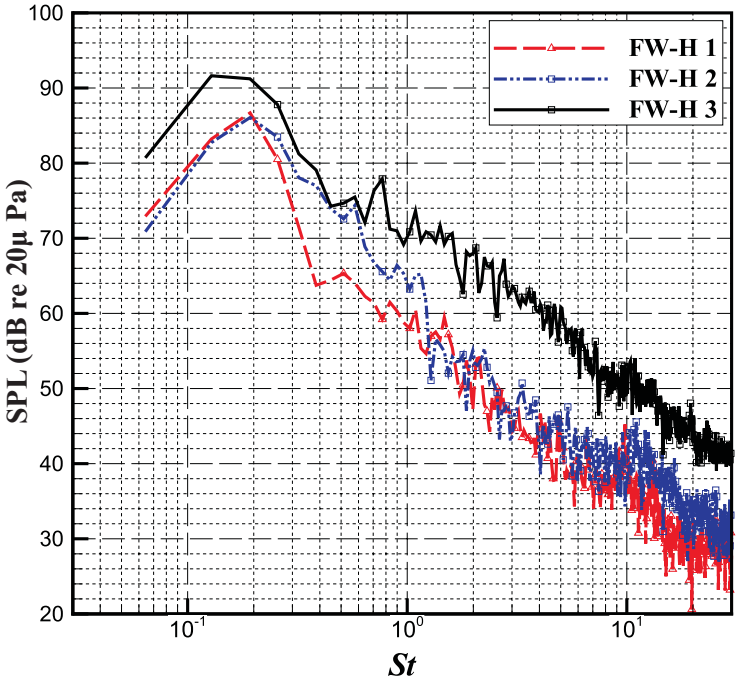

(a) $\theta = 90$ deg.

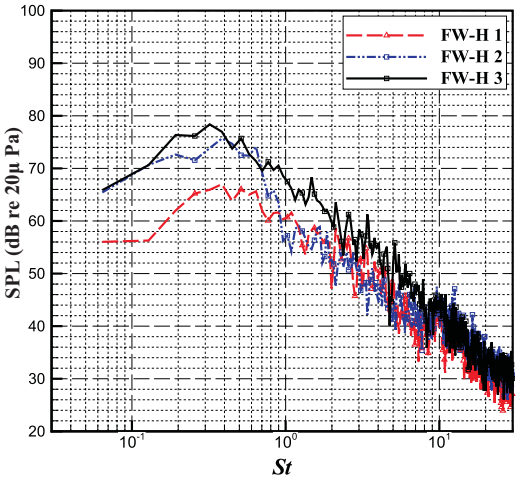

(b) $\theta = 0$ deg.

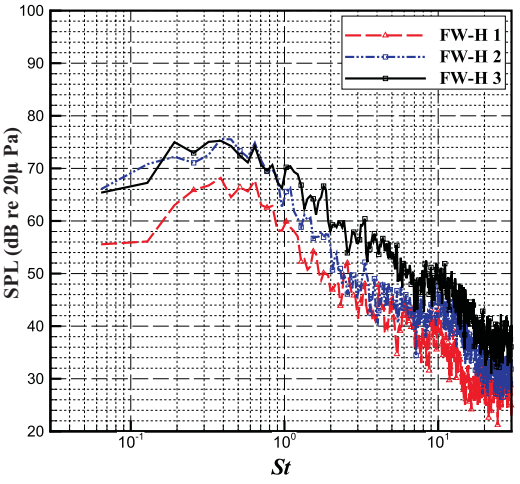

(c) $\theta = 180$ deg.

FIGURE 8.9: High-order tandem cylinder computation: LES spectra prediction for tandem cylinders $S/D = 3$ at observers: (a) $(0, 100D, 0)$, (b) $(-100D, 0, 0)$, (c) $(100D, 0, 0)$.

8.5.1 Far-Field Pressure Spectra

The predicted spectra for each cylinder at selected observer positions are plotted in Figure 8.9. In Figure 8.9(a), the observer is located directly above the upstream cylinder at $(0, 100D, 0)$ and the predictions from each integration surface are presented. At this location the noise due to vortex shedding is captured by a broad spectral peak centred at $St = 0.192$. The coincidence of the shedding frequency of both cylinders suggests that the vortex shedding is coupled, which has been noted in experiment [83]. The peak

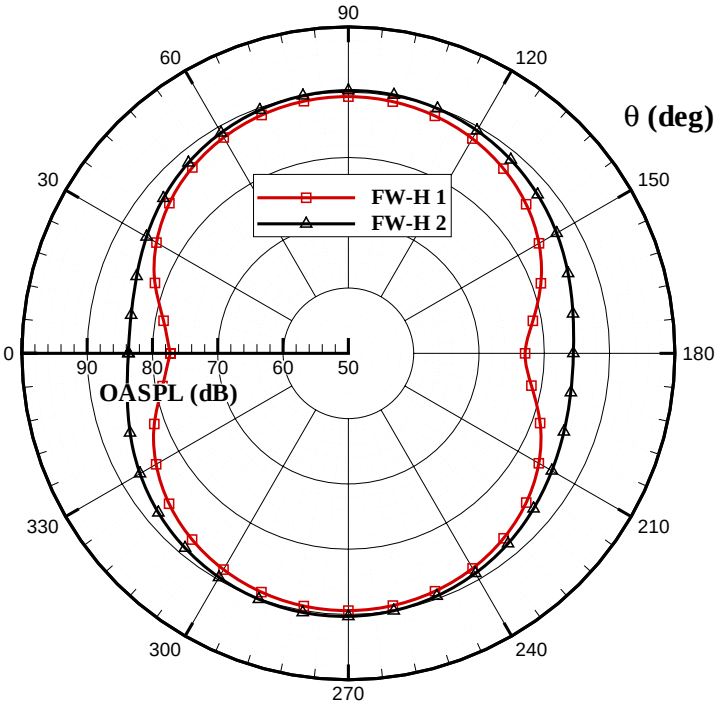

(a)

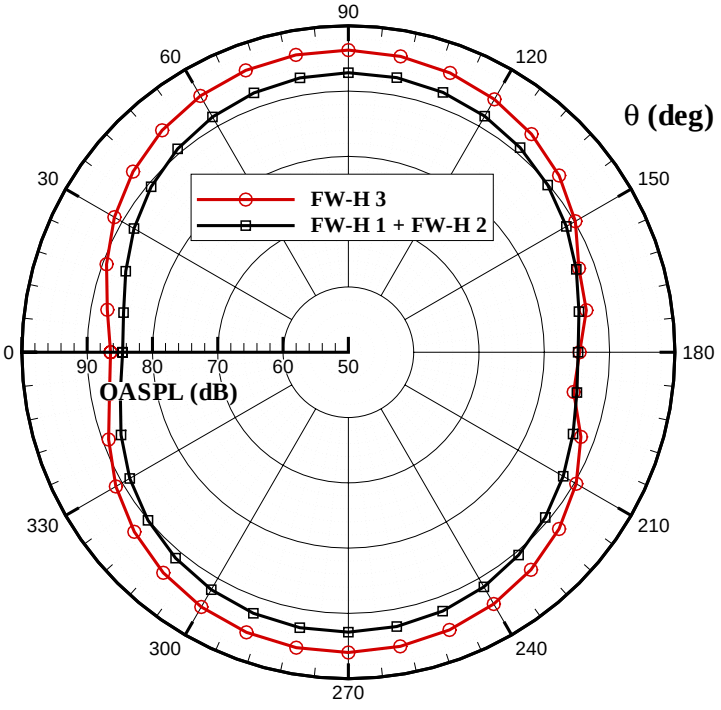

(b)

FIGURE 8.10: High-order tandem cylinder computation: LES OASPL directivity prediction for tandem cylinders $S/D = 3$, $R_o = 100D$, where θ is measured clockwise from the negative $x-$axis as shown in Figure 7.1.

SPL prediction for both cylinders is approximately 85 dB. Higher levels were predicted for the downstream cylinder between the peak frequency and $St \approx 10$, which can be attributed to the increased unsteadiness due to the wake interaction. The off-body surface predicted a mild peak at twice the shedding frequency corresponding to the passage of vortices through the integration surface and also higher levels at $St > 0.5$. This is likely to be due to error due to the wake passing through the integration surface. The the high sound pressure level corresponding to the vortex shedding frequency is due to the off-body surface capturing the contribution of both cylinders.

In Figure 8.9(c) the observer is located directly downstream of the cylinders at $(100D, 0, 0)$. At this observer location, the noise is largely generated by the drag dipoles on the cylinder surfaces. For each surface, a broader spectrum was predicted centred at a Strouhal number of twice the vortex shedding frequency. Lower levels were predicted from the surface of the upstream cylinder with the contribution from the downstream cylinder between $4 - 10$ dB at $St < 1.0$. Since in the off-body solution the downstream cylinder shields much of the contribution from the upstream cylinder, the FW-H 2 and FW-H 3 predictions agree well at low frequencies. In the mid-frequency region between $St = 1 - 10$ the off-body surface predicted higher levels, again likely to be due to error, as the unsteady wake passes through the integration surface. Despite this apparent error it can be concluded that the on-body surfaces captured the noise characteristics of each cylinder.

The difference between the predicted flow regime for the DES and VLES simulations is manifested in the far-field acoustic results shown in Figures 7.17 and 8.9. In the VLES, the spectra of both cylinders are more broadband, due to less coherent vortex shedding, and there is less disparity between the characteristics and the sound pressure level predicted for each cylinder. The VLES predicts higher sound pressure levels due to higher pressure fluctuations on the cylinder surfaces characteristic of earlier separation.

8.5.2 Directivity Prediction

The OASPL predictions were calculated by integrating the pressure at each observer location across the resolved frequency range using Equations D.5 and D.6. The directivity in the 2-D $x - y$ plane is presented in Figure 8.10 in polar form where the flow is from left to right. In Figure 8.10(a) the predictions for the two on-body integration surfaces are presented. Dipole directivity patterns were predicted for both cylinders. The levels are comparable at the overhead position at $\theta = 90$ deg; however the contribution of the drag dipole is clearly less for the upstream cylinder along the upstream and downstream directions by ≈ 6 OASPL dB. This is attributed to the interaction effects and is consistent with the results presented in Chapter 7.

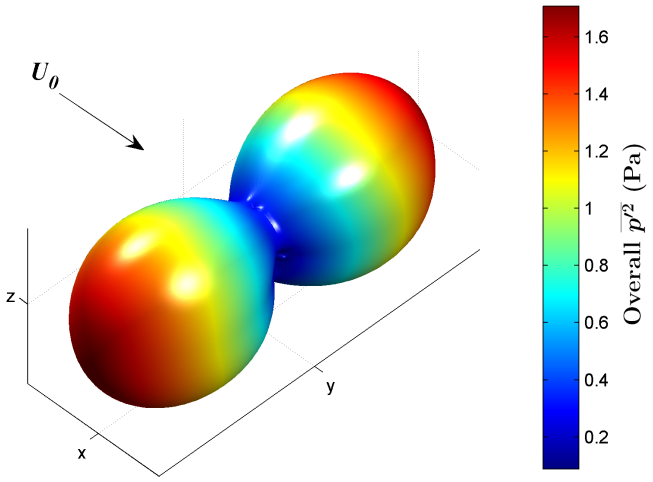

(a) Off-body surface.

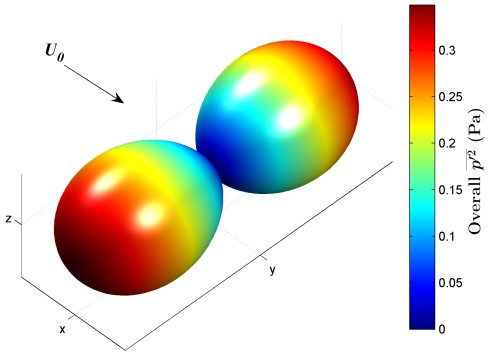

(b) Upstream cylinder.

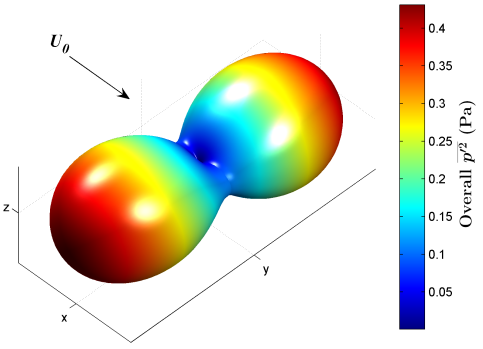

(c) Downstream cylinder.

FIGURE 8.11: High-order tandem cylinder computation: 3-D overall $\overline{p'^2}$ directivity prediction for tandem cylinders $S/D = 3$.

In Figure 8.10(b) the combined level of the on-body surfaces is compared with the result for the off-body surface. The off-body surface consistently predicted higher levels in all directions and the difference reaches 3 dB this is likely to be due to the aforementioned error as the wake passes through the integration surface.

The three-dimensional directivity was calculated and is presented in Figure 8.11. The results are presented in terms of the mean-square pressure, $\overline{p'^2}$, integrated over the resolved frequency range. In Figure 8.11(b) the directivity of the upstream cylinder is plotted and clearly indicates a marked dipole radiation pattern. The magnitude of the drag dipole is negligible compared to that of the lift dipole. Figure 8.11(c) displays the directivity pattern of the downstream cylinder and shows that the drag dipole is stronger and is clearly visible. For both cylinders, the minimum radiation was in the spanwise

direction. Figure 8.11(a) indicates the dipole directivity of the complete tandem cylinder configuration.

8.6 Summary

In this chapter, the high-order CAA code SotonCAA was employed to investigate the aerodynamic and noise generating characteristics of the tandem cylinder arrangement. The aerodynamic results for the upstream cylinder are indicative of a single cylinder in the sub-critical regime. Vortex shedding at a frequency of $St = 0.192$ were captured behind both cylinders. Comparison with the DES results indicated that the regime of the upstream cylinder and the separation distance are key factors in determining the nature of the flow in the gap region. The interaction effects in the form of a highly non-linear inflow subjected to the downstream cylinder leads to high unsteadiness on the cylinder surface. This leads to high noise levels radiated by the downstream cylinder, which was largely due to higher fluctuations of the drag dipole. Dipole directivity patterns were predicted by all three integration surfaces and a broad peak centred around the shedding frequency was captured in the spectral results at the overhead position of $theta = 90$ deg.

Chapter 9

Model Validation

9.1 Outline

In this chapter, the prediction model was validated by comparing predictions with theory and measured data for the noise radiated by a simple landing gear model. The geometry consisted of three circular struts and two-wheels. It was decomposed so that each component could be modelled individually using results from the previous chapters and the model scaling law. The results are compared at a range of observer locations to test both the directivity and spectral prediction capabilities.

9.2 Validation of the Model Scaling Law

Validation of the scaling law in Equation 3.9 was required on a component basis before the prediction of the noise radiated by a landing gear geometry could be attempted. This included the validation of the relationships

$$\overline{p'^2} \propto M^6, \quad \overline{p'^2} \propto L_c^2, \quad \text{and} \quad \overline{p'^2} \propto 1/R_o^2.$$

To test the M^6 power law, a set of 2-D URANS simulations were performed at $Re = 1.4 \times 10^5$ at Mach numbers ranging from $M = 0.1 - 0.5$. An example of these simple test cases is outline in Section A.3, where the turbulent flow at $M = 0.2$ is computed. The sound pressure level at an observer located at a distance of $R_o = 100D$ at an angle $\theta = 90$ degrees was predicted for each Mach number and the results are presented in Figure 9.1(a). The slope corresponding to the theoretical sixth-power law is plotted for comparison. The result shows good agreement between the theoretical slope and CFD results indicating that the dipole noise measured in the computations matches the $\overline{p'^2} \propto M^6$ theory of Curle [11]. Next the relationship $\overline{p'^2} \propto L_c^2$ was tested by evaluating the SPL at the same observer location. This time results from the 3-D single cylinder

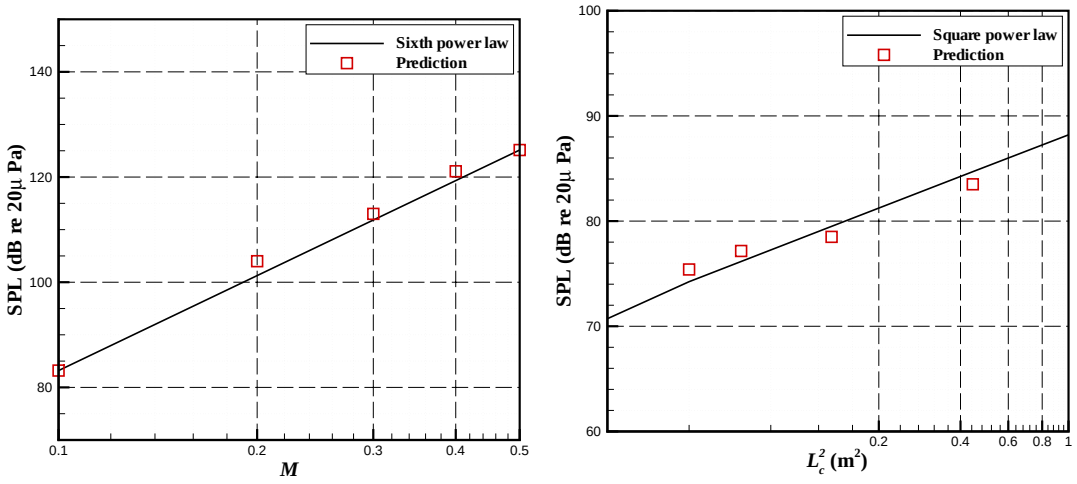

(a) SPL vs M^6, $L_c = 1$m, $R_o = 10$m.

(b) SPL vs. L^2.

FIGURE 9.1: Comparison between predictions of peak SPL and theoretical scalings laws: (a) sixth-power law for Mach number, (b) square-power law for length scale, L^2.

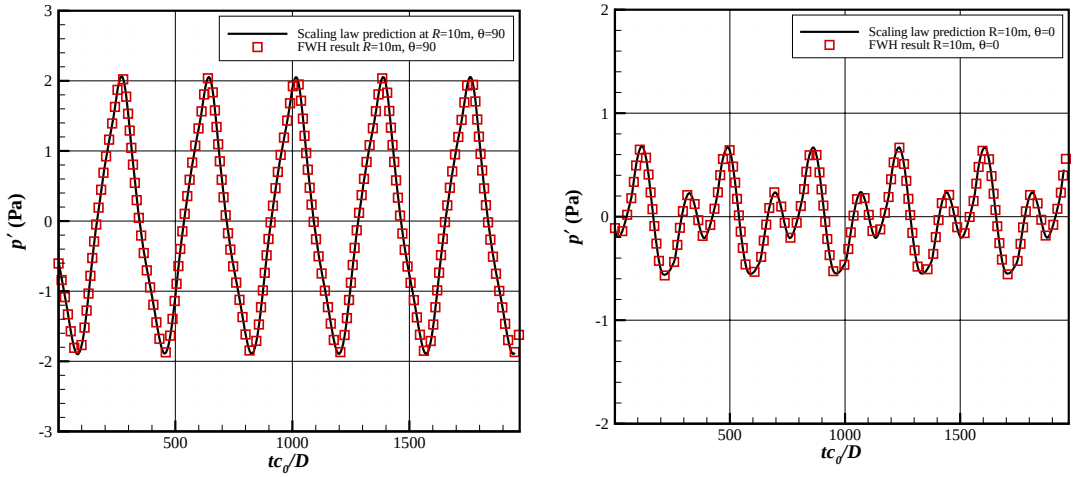

(a) p' vs. tc_0/D

(b) p' vs. tc_0/D

FIGURE 9.2: Comparison between FW-H result and scaling law prediction for the acoustic signal generated by the viscous flow over a 2-D cylinder.

simulations presented in Chapter 5 were used and L_c was taken to be the cylinder span. The results are presented in Figure 9.1(b) accompanied by the theoretical slope. Again the result indicates a strong correlation between the predicted levels and theory. Finally, the relationship $\overline{p'^2} \propto 1/R_o^2$ was tested. The validation case used to obtain the FW-H at an observer distance of $R_o = 100D = 3.11$ m at $\theta = 0$ deg and $\theta = 90$ deg prediction is presented in Section A.3. The prediction was scaled by Equation 3.9 to predict the acoustic pressure at an observer located at an observer radius of $R_o = 10$m. An additional FW-H calculation was performed for $R = 10$m and is compared to the scaling law prediction in Figure 9.2. The result shows excellent agreement between the

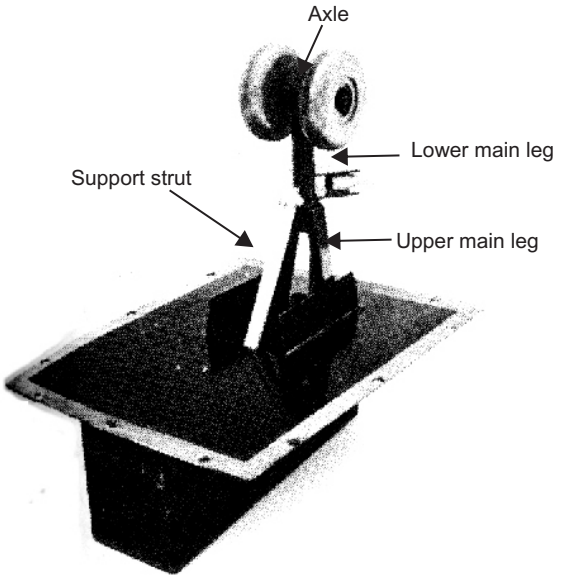

FIGURE 9.3: Photograph of scale model nose landing gear tested by Heller and Dobrzynski [39].

FW-H prediction and the scaling law.

These results provided confidence that Equation 3.9 could be used to scale the computational results on a component basis. The next step was to validate the model for a complete landing gear prediction.

9.3 Experimental Data

In 1977 Heller and Dobrzynski published work on their experimental program which aimed to determine the radiation from landing gear/wheel well configurations of large commercial aircraft [39]. They exposed scale models of synthesized, representative landing gears to an outdoor wall-jet facility at flow velocities of up to 65 m/s. Their nose gear model consisted of a circular cross-section main leg, support strut, and axle, and two-wheels of diameter $D_w = 0.075$ m. The model is shown in Figure 9.3. Far-field microphone measurements were taken at three observer locations to investigate the directivity of the model. The measured spectra are presented in Figure 9.4 along with an illustration indicating the location of the far-field microphones. The measured noise spectrum was normalised by the wheel diameter of $D_w = 0.075$ m and a reference velocity $U_0 = 100$ m/s, and is plotted against the Strouhal number defined by $St_w = fD_w/U_0$. Due to the lack of small-scale features, it is reasonable to suggest that the noise was dominated by the fluctuating forces on the surface of the individual components and

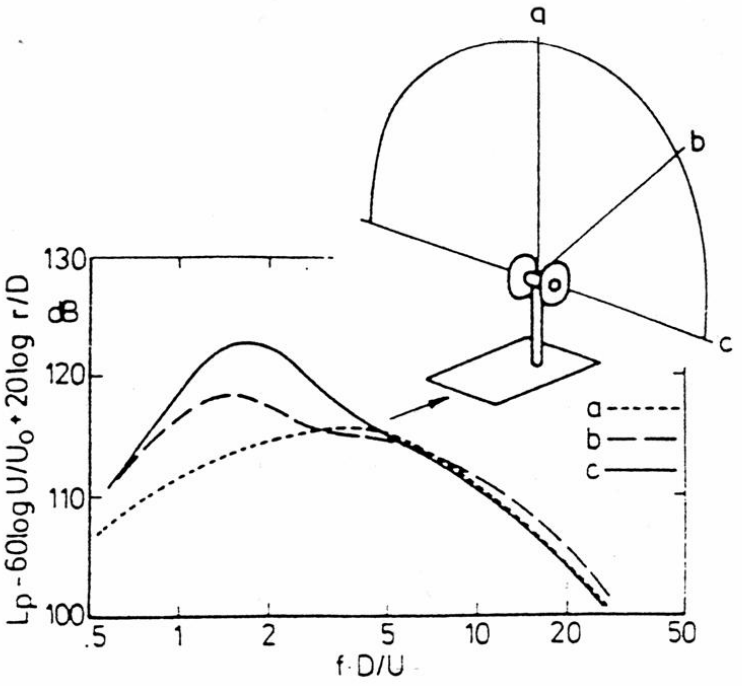

FIGURE 9.4: Location of observers and measured spectrum for validation case extracted from reference [39].

therefore the current database of representative components was thought to be suitable to model the test gear. Heller and Dobrzynski's experiment thus provided an ideal validation case for the new prediction model that would test its ability to predict correct sound pressure levels, spectral characteristics, and directivity.

Figure 9.4 reveals that the highest noise level was measured at observer "c". The measured spectrum at this location consisted of a low frequency hump at a Strouhal number of $St_w \approx 1.5$. Observer "c" relates to a sideline position which was perpendicular to the main leg axis and the freestream velocity vector, i.e. at $\theta_o = 90$ deg, $\phi_o = 90$ deg. Therefore it is likely that this low frequency hump was due to the vortex shedding from the main leg and support strut, since at this location the expected dipole directivity of these struts is expected reach a maximum. However, the spectrum is broad rather than tonal, suggesting that the interaction between the struts is non-negligible.

At observer "b" ($\theta_o = 90$, $\phi_o = 45$), the hump is lower by approximately 6 dB. This can be explained by the effect of the dipole directivity of the struts which would mean a lower level compared to observer "c" ($\theta_o = 90$, $\phi_o = 90$), but a similar peak frequency.

Location "a" refers to an observer that was located directly above the landing gear. The measured spectrum at this location consists of a broadened hump that peaks at a Strouhal number of approximately $St_w = 5$. The low frequency hump predicted at observers "b" and "c" is absent from the spectrum. This is consistent with the expected

directivity characteristics of the struts which would mean the spectral peak due to vortex shedding is a minimum at this location. Since it was not directly affected by the shedding from the struts, observer "a" had the lowest peak sound pressure level, with the peak level some 10 dB less than the sound pressure level measured at observer "c". It is likely that the noise was dominated by the wheels at observer "a" since "a" is located both perpendicular to the freestream and to the axis of the wheels.

The measurements at all observers collapsed well at higher frequencies beyond $St_w = 5$. Therefore it is likely that the higher frequency noise source radiated omnidirectionally. This is consistent with the theory that at high frequencies the sources usually are not compact [31].

9.4 Geometry Decomposition and Modelling Database

Given that the wheel diameter of the model tested by Heller and Dobrzynski was 0.075 m, the dimensions and orientation of the other components were determined from Reference [39]. The measured geometrical parameters that were used in the prediction are presented in Table 9.1. The main leg was decomposed into upper and lower sections so that the tandem arrangement between the upper leg and the support strut could be modelled. The S/D range of the support strut relative to the upper main leg is $S/D = 0$, at the junction of the struts, to $S/D = 5$ at the junction with the tunnel floor. Since a model of the orthogonal-yaw tandem configuration was not available, a tandem cylinder simulation was chosen to model the interaction. Initially, predictions were made using the various tandem cylinder regime. Predictions for the $S/D = 3$ DES case was shown to fall in line with experiment, whereas lower S/D led to an under-prediction, and higher S/D led to an over-prediction. This result can be explained since $S/D = 3$ represents the intermediate separation distance, which is likely to dominate the flow regime of the geometry. Therefore, the $S/D = 3$ simulation was used to model the interaction between the support strut and upper leg.

In Table 9.1 the "type" column indicates the database component that was used to model the component. Details of the modelling database resulting from the work presented in Chapters 5, 6, and 7 are listed in Appendix C. The UTDM3 and DTDM3 entries indicate that the upstream and downstream cylinder results from the $S/D = 3$ tandem cylinder case were used to model the upper leg and support strut respectively. The SCC90K entry indicates that the single cylinder case performed at $Re = 9 \times 10^4$ was used, which represents the Reynolds number that best matches that of the strut. The alignment of each strut is defined by θ_c and ϕ_c that indicate the polar and azimuth angles of the strut axis with respect to the model coordinates (see Figures 3.3) and 3.4). θ_c and ϕ_c are also the rotation by which the component coordinates stand with respect to the model

Component	Type*	D (m)	L (m)	$(\theta_c, \phi_c)_a$	$(\theta_c, \phi_c)_b$	$(\theta_c, \phi_c)_c$
Upper main leg	UTDM3	0.013	0.0825	0,0	45,90	90,90
Lower main leg	SCC90K	0.013	0.0675	0,0	45,90	90,90
Support strut	DTDM3	0.013	0.108	45,0	45,45	90,90
Axle	SCC90K	0.0065	0.0225	90,90	45,90	0,90

* Modelling database component: UTDM3/DTDM3 = upstream/downstream tandem cylinder $S/D = 3$, SCC90K = single circular cylinder $Re = 9.0 \times 10^4$

TABLE 9.1: Component modelling parameters for the validation case.

coordinates. The wheel noise was predicted using the semi-empirical approach adopted by Smith [71] as outlined in Chapter 3.

9.5 Results

9.5.1 Spectral Prediction

Predictions were made for each of the three observer locations using the parameters defined in Table 9.1. For each observer location two figures were generated; one presenting the total noise spectrum and its breakdown into the individual contributions, and the other comparing the total predicted spectrum with the experimental measurements and the prediction made by the semi-empirical model of Smith *et al.* [71]. In Figures 9.5-9.7, the frequency scale has been normalised by St_w whereas the noise level is represented by $\mathrm{SPL_n} = \mathrm{SPL} - 60\log(\mathrm{U/U_0}) + 20\log(\mathrm{R/D_w})$.

The prediction for observer "a" is presented in Figure 9.5. Figure 9.5(a) displays the total spectrum and the component breakdown. The noise in the low and high frequency range is dominated by the wheel spectrum, whereas in the mid frequency range the strut noise dominates. The breakdown of the total spectrum into individual component spectra reveals that the lower leg is the main contributor to the overall noise. A tone was predicted at $St_w = 3.2$ due to vortex shedding from the axle that is above the broadband noise. The modelling of axle noise was tricky since the level of interaction caused by flow acceleration from the wheels was not established in the tests. The contribution from other struts was fairly negligible at this observer angle. The noise radiated by the upper leg was predicted to be attenuated due to the blockage effect that was measured for the upstream cylinder in the $S/D = 3$ configuration. The combined spectral shape can be described as a shallow hump and Figure 9.5(b) reveals that it follows the measured spectral characteristics very well. This indicates that the model is capable of capturing the physical noise mechanisms at this observer location.

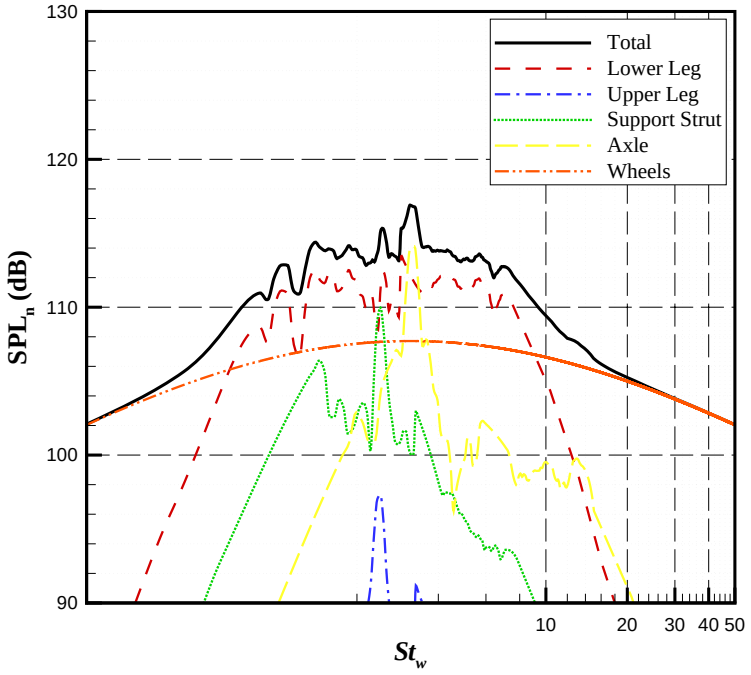

(a) $\theta_o = 0$ deg, $\phi_o = 90$ deg.

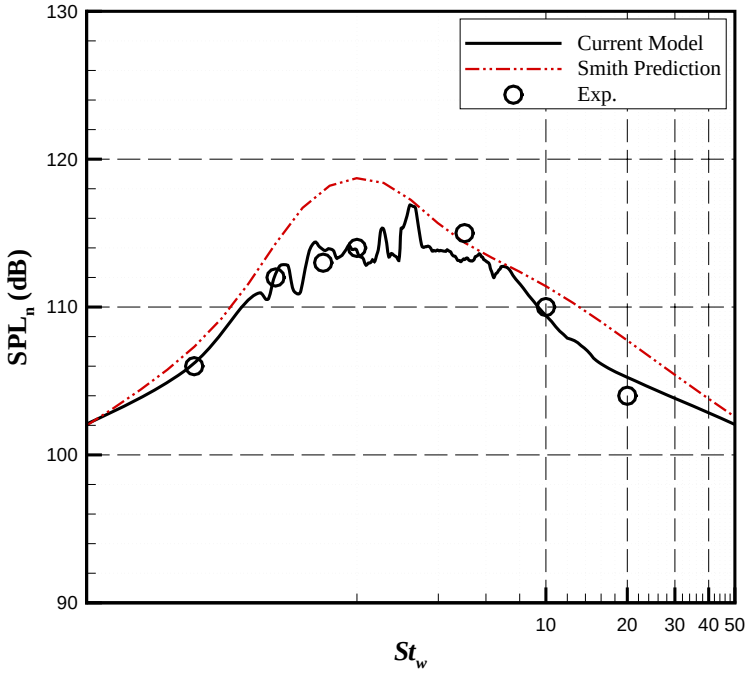

(b) $\theta_o = 0$ deg, $\phi_o = 90$ deg.

FIGURE 9.5: Comparison between measured and predicted spectra at observer "a". The frequency scale is normalised by $St_w = fD_w/U_0$, and the level is defined by $\mathrm{SPL_n} = \mathrm{SPL} - 60\log(\mathrm{U/U_0}) + 20\log(\mathrm{R/D_w})$.

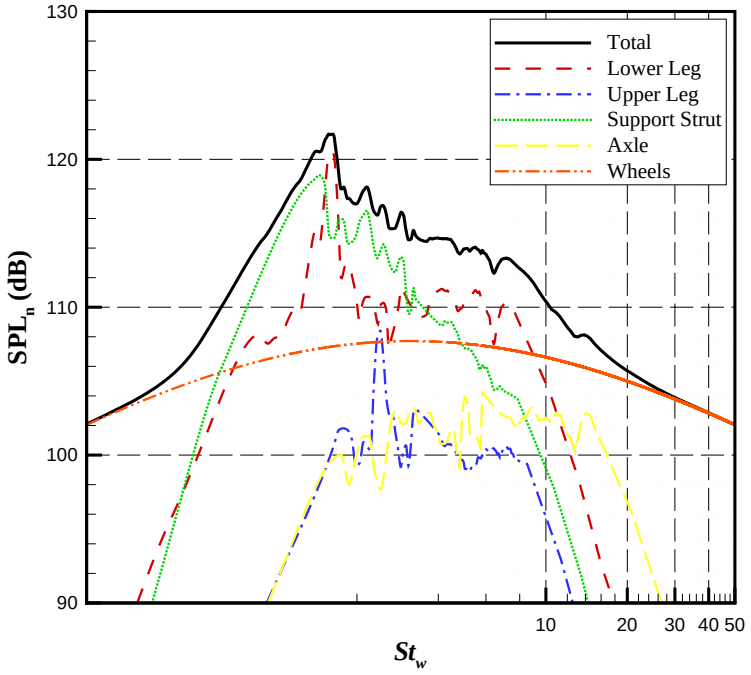

(a) $\theta_o = 45$ deg, $\phi_o = 90$ deg.

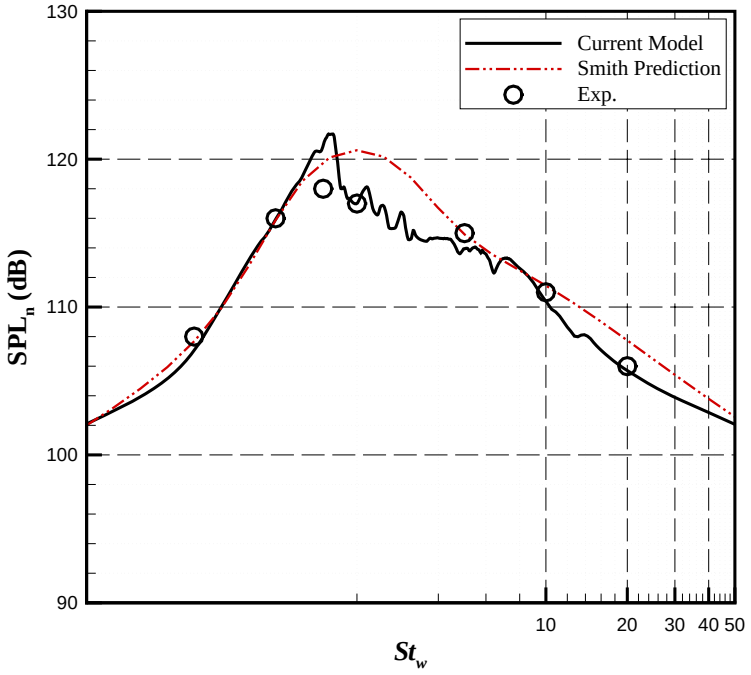

(b) $\theta_o = 45$ deg, $\phi_o = 90$ deg.

FIGURE 9.6: Comparison between measured and predicted spectra at observer "b". The frequency scale is normalised by $St_w = fD_w/U_0$, and the level is defined by $\mathrm{SPL_n} = \mathrm{SPL} - 60\log(\mathrm{U/U_0}) + 20\log(\mathrm{R/D_w})$.

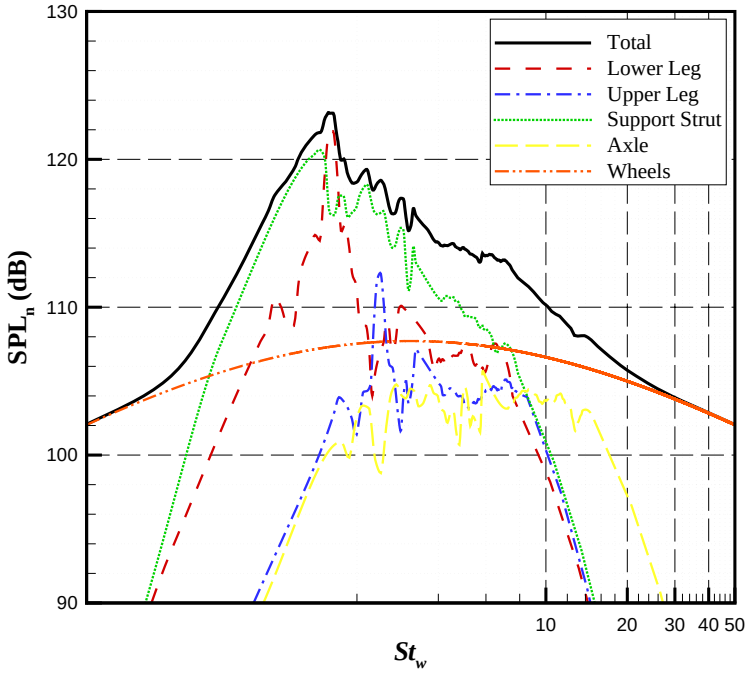

(a) $\theta_o = 90$ deg, $\phi_o = 90$ deg.

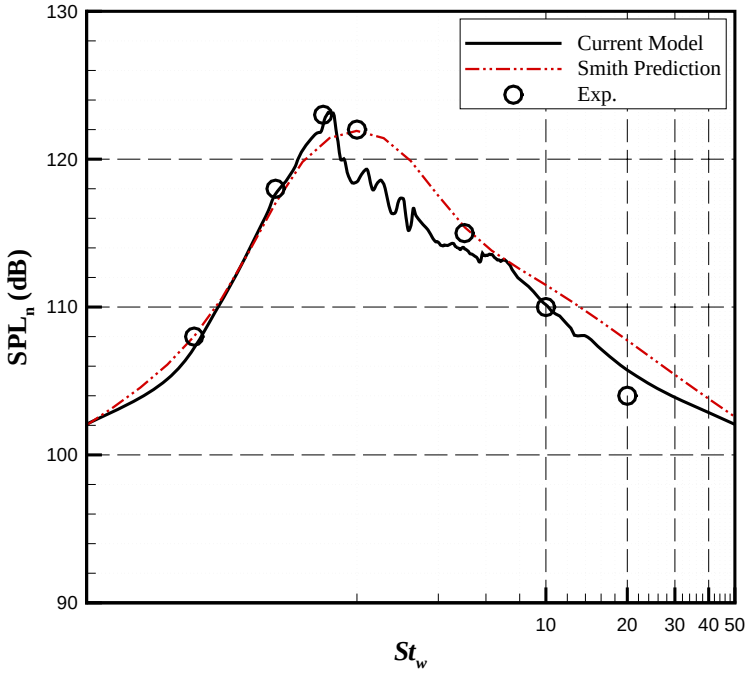

(b) $\theta_o = 90$ deg, $\phi_o = 90$ deg.

FIGURE 9.7: Comparison between measured and predicted spectra at observer "c". The frequency scale is normalised by $St_w = fD_w/U_0$, and the level is defined by $\mathrm{SPL_n} = \mathrm{SPL} - 60\log(\mathrm{U/U_0}) + 20\log(\mathrm{R/D_w})$.

At observer "b" Figure 9.6 reveals that the prediction model predicted a spectrum with a fairly strong peak at $St = 1.8$. The peak is due to the vortex shedding noise expected to be generated by the lower leg and support strut. The noise of the upper leg remains negligible due to the attenuation effect caused by the interaction with the support strut. Noise from the axle and wheels were also fairly insignificant at this observer position. Comparison with the measured results in Figure 9.6(b) shows that model over-predicted the spectral peak by approximately 3 dB. However, the predicted St_w of the peak agrees well with the measured data. At other frequencies, there is a very strong correlation between the predicted and measured results. At this observer location it is expected that the wheels may shield the noise radiated by part of the lower leg, leading to a lower sound pressure level. This acoustic shielding effect was not captured by the model and therefore may explain the over-prediction of the peak sound pressure level.

Figure 9.7 reveals that the overall spectral characteristics at observer "c" remain very similar to those at observer "b". The model again predicted a broad tone at $St_w = 1.8$ due to the shedding from the lower main leg and the support strut, but this time at a slightly higher sound pressure level due to the change in observer location. The contribution from the upper main leg and axle is still negligible at this observer location. At this sideline location, the effect of acoustic shielding should be less than at observer "b" and as a result the predicted spectrum agrees very strongly with the measured spectrum in terms of both frequency and sound pressure level. The peak in the predicted spectrum was slightly less broad than that observed in experiment leading to a small $\Delta\mathrm{SPL_n}$ between measurement and prediction just above the peak frequency. There was a slight over-prediction in the high frequency range, but it appears this is due to the semi-empirical wheel prediction.

9.5.2 Directivity Prediction

Directivity predictions were made for two observer planes: the first in the flyover plane, defined by polar angles $0 \ll \theta_o \ll 180$ deg and constant azimuth of $\phi = 0$ deg, and the second in the sideline plane, defined by $-90 \ll \phi_o \ll 90$ deg at constant polar angle $\theta_o = 90$, where $\phi_o = 0$ deg is directly below the landing gear. These directivity predictions are shown in Figure 9.8(a) and 9.8(b) respectively. The directivity of the overall normalised sound pressure level, $\mathrm{OASPL_n} = \mathrm{OASPL} - 60\log(\mathrm{U/U_0}) + 20\log(\mathrm{R/D_w})$, was calculated for each individual component from which the total configuration was determined.

The directivity pattern in the flyover plane indicates a weak dipole field and is dominated by the contributions of the lower main leg, support strut, and the wheels. The minimum $\mathrm{OASPL_n}$ was predicted at $\theta_o = 0$ deg due to the dipole directivity and alignment of the struts. Marginally higher noise levels were predicted in the rearward arc due to the alignment of the dipole corresponding to the support strut. The difference between the OASPL at $\theta_o = 0$ deg and $\theta_o = 180$ deg is approximately 0.5 dB.

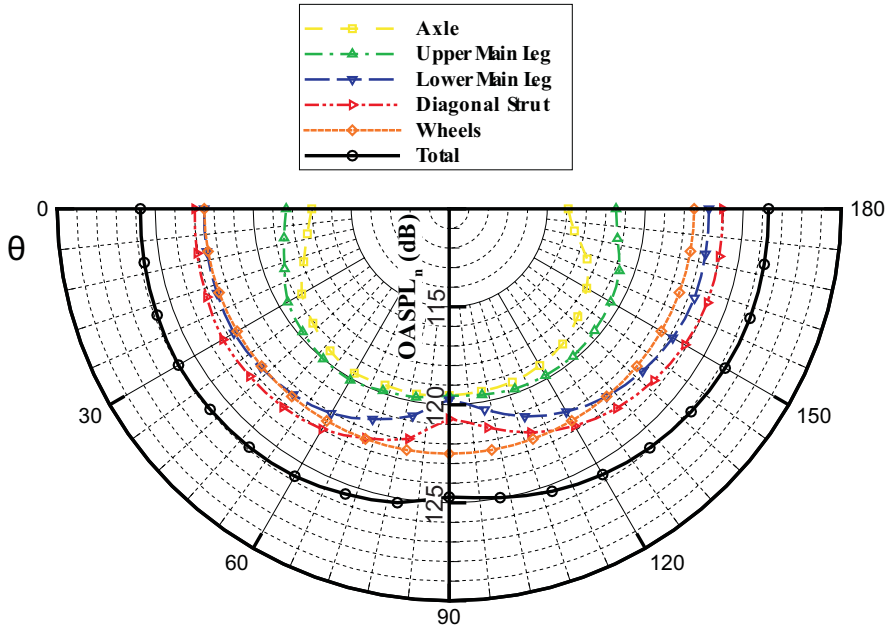

(a) Polar directivity (flyover plane).

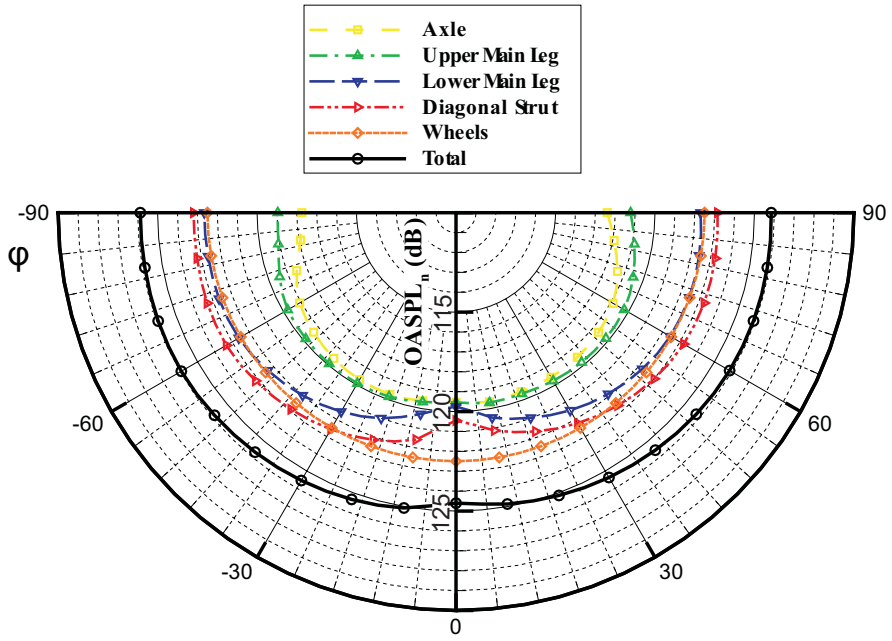

(b) Azimuth directivity (sideline plane).

FIGURE 9.8: Predicted $OASPL_n$ directivity for model geometry: $OASPL_n = OASPL - 60\log(U/U_0) + 20\log(R/D_w)$.

Figure 9.8(b) shows that a high degree of symmetry was predicted along the sideline plane. This was expected due to the symmetry of the model geometry. The minimum OASPL_n was predicted at $\phi_o = 0$ deg due to the dipole directivity and alignment of the struts. Conversely the maximum level was predicted for the sideline observers at $\phi_o = 90$ deg and $\phi_o = -90$ deg where the maximum is expected for the vertically aligned struts. The difference between the maximum and minimum OASPL_n is $\Delta\text{OASPL}_\text{n} \approx 1.5$ dB. The diagonal strut and lower main leg are predominately responsible for the overall directivity pattern, whereas the axle and upper main leg contribute very little. The prediction at $\phi_o = 0$ deg is equal to that at $\theta = 0$ deg in Figure 9.8(a).

The directivity results are consistent with what has been reported in literature for full size landing gear [9, 14, 16]. The minimum noise level is usually measured directly below the gear, where the dipole noise from vertically aligned components is a minimum. The maximum level usually occurs at sideline observers that are directly affected by the vortex shedding noise, and in the forward and rearward arcs. This indicates a dipole directivity field largely dictated by the alignment of the main contributing struts. However the ΔOASPL was small due to the alignments of the individual components and their resulting directivity.

9.6 Summary

Comparison between the predicted noise and the measured data for a simple two-wheel landing gear has successfully demonstrated the capability of the new prediction model. Predictions of the spectra at selected observers showed very good agreement with measured results.

The results demonstrated the sensitivity of the model to observer location. The results also showed the need to model interaction noise as the accurate prediction for the geometry was largely due to the modelling of the upper leg and support strut which were configured in a tandem arrangement. The tandem cylinder modelling provided the correct spectral characteristics and correct levels. Modelling the upper main leg and support strut as single cylinders would have lead to an over-prediction in terms of the peak noise level and also a more tonal and incorrect spectral shape. The results also showed that the expected directivity characteristics of landing gear noise can be predicted well.

Chapter 10

Conclusions and Suggestions for Future Work

10.1 Outline

In this final chapter the major conclusions of the research are summarised with reference to the aims and objectives laid out at the start of the thesis. The chapter will also discuss areas of research that might be considered for future work.

10.1.1 Bluff-Body Noise Modelling

The noise radiated by circular cylinders has been studied in the past, but no database was available that could be used for the noise modelling of landing gear struts. In this work, supercritical cylinder flows were simulated at various Reynolds numbers between $Re = 9 \times 10^4 - 1 \times 10^6$ in cross-flow to represent basic landing gear struts. The predicted cylinder noise characteristics was a strong tone corresponding to either the fluctuating lift or drag forces on the cylinder surface, and a dipole directivity pattern with maximum noise radiated perpendicularly to both the freestream vector and cylinder axis. The importance of observer location to the noise characteristics was demonstrated by comparing the predicted far-field spectra at various observer locations. The overall spectral shape was shown to be a strong function of observer angle, with both the frequency and magnitude sensitive to the observer location.

This work was extended to investigate the effect of the arbitrary alignment of struts to the inflow velocity vector by investigating cylinder flows at yaw angles of $\Lambda = 0$, 15, 30, and 45 deg at a Reynolds number of 1.4×10^5. The results showed a strong correlation between the far-field noise and the yaw angle. It was found that:

- As the yaw angle increased, the peak sound pressure level decreased

- As the yaw angle increased, the frequency of the spectral peak decreased

These features were associated with the reduction in the shedding frequency and the magnitude of fluctuating forces on the cylinder surface. The Independence Principle was correlated to various aerodynamic quantities with partial success. An interpolation method for predicting the spectra for arbitrary yaw angles between $\Lambda = 0^\circ - 45^\circ$ was developed for the prediction model.

Finally, the effect of component body-wake-body interactions due to the close proximity between landing gear struts was investigated. This was achieved by investigating circular cylinders in a tandem arrangement. The distance between the cylinders was varied between 2 and 5 cylinder diameters. The characteristics and influence of the interaction effects varied considerably with the separation distance. At short separation distances, less than three cylinder diameters, the downstream cylinder created a "blockage" effect that restricted the shedding of vortices from the rear of the upstream cylinder. This meant that the surface pressure perturbations and the far-field noise levels were reduced for the upstream cylinder compared to a single cylinder. The noise spectra and directivity were also shown to be heavily modified by the interaction. The nature of the flow field around the downstream cylinder was largely determined by the characteristics of the inflow, which was controlled by the upstream cylinder. At short separation distances, the inflow velocity was low, but the flow field was highly unsteady. This led to broadened far-field acoustic spectra and a more omnidirectional directivity. At larger separation distances, the aerodynamic and acoustic characteristics of the upstream cylinder resembled those of a single cylinder. However, the highly turbulent and unsteady wake that impinged on the surface of the downstream cylinder lead to much higher surface pressure fluctuations and therefore a higher far-field noise. The difference in sound pressure level between the two cylinders was predicted to be as much as 17 dB. The noise characteristics were thus shown to be highly sensitive to the separation distance and cylinder location, and the inclusion of interaction effects was shown to be an important part of the modelling database.

10.1.2 Low Noise Guidelines

The aeroacoustic analysis of bluff-body flows revealed ways in which the far-field noise could potentially be reduced. These are presented as suggested low noise guidelines:

- **Flow regime control**. The literature review revealed a strong relationship between the flow regimes of a circular cylinder and its noise potential. The characteristic of subcritical flows is strong vortex shedding leading to a very strong tone at the vortex shedding frequency. In the supercritical regime, this shedding

weakens and is more irregular, leading to a noise reduction compared to the subcritical regime. Therefore, where the flow over a landing gear component may be subcritical, forcing turbulent flow by tripping boundary layers can lead to more reduction.

- **Component alignment control**. A clear noise reduction potential was seen for a basic strut that is yawed to the incoming flow field. Since landing gear designs are driven from a structural standpoint, in most cases structural constraints determine the strut alignment. Nevertheless, it is useful to understand the noise reduction potential of a strut yawed to the inflow velocity.
- **Component separation control**. The tandem cylinder investigations indicated that there is a noise reduction potential for struts that are separated by very short distances. Conversely, the interaction mechanisms can lead to increased noise at medium separation distances. Therefore, wherever possible, the distance between components should be controlled to achieve minimum noise, and potentially noisy component configurations should be avoided.

10.1.3 Landing Gear Noise Prediction

The new model was validated by comparing noise predictions with measurements for a simple nose landing gear model that consisted of two wheels and three circular struts. The model geometry was decomposed and modelled by representative components in the modelling database. The wheel noise prediction was provided by an existing semi-empirical model. The results showed that the model was capable of predicting the spectral characteristics and correct levels at three different observer locations. The model was also used to predict the overall sound pressure level directivity. Results were also compared to an existing semi-empirical prediction model. The physics-based model was able to include more physics and higher levels of detail in the prediction.

The results validated the model methodology and demonstrated its potential as a low-noise design tool. They also suggested that through further development it could be used to predict the noise of a more complex landing gear. Suggestions for future work that could extend the model are presented in the next section.

10.2 Suggestions for Future Work

The results demonstrated the capability of the new model to predict the noise of a simple landing gear resulting from unsteady pressures on the component surfaces. For a more complex landing gear, additional noise generating mechanisms and also more complex components would need to be considered. This means that the prediction of

more complex landing gear will require extension of the modelling database. Suggested ways in which the model could be extended are described below:

- **Alternative cross-sections**. Since not all struts are circular in cross-section, and that the cross-section is likely to have a large impact on the struts noise characteristics, it is recommended that the investigation of non-circular strut noise is performed. Perhaps the next most common strut cross-section is the "H" beam, which is potentially very noisy due to cavities and sharp edges and this would be a natural progression from the circular cylinder.

- **Component interaction parameters**. The modelling of tandem cylinders in this work only investigated the separation distance between struts. There are many other parameters that affect the interaction mechanisms, such as non-equal component diameters, offset separation, and component alignment.

- **Other component groups**. So far only strut noise has been included in the model and in the future the database should be enhanced to include more components and configurations. For example, different strut cross-sections are likely to modify the noise characteristics. The impact of landing gear bay doors that are usually an integral part of the structure should be considered. The wheel noise was obtained from a semi-empirical prediction, and this could be improved through a physics-based prediction.

- **Acoustic scattering, shielding, and installation effects**. At present, the effect of acoustic scattering and shielding has not been considered and this is likely to be very important for complex geometries. Installation effects and the interaction with other airframe components should also be considered for comprehensive landing gear noise prediction.

- **Validation**. Validation is a key part of future progress and should be performed as the model is extended. Such validation should be performed with fly-over data as well as wind tunnel data as these can compliment each other effectively.

10.3 Summary

The landing gear noise problem presents issues and topics for future investigation, and the advancement of computational techniques and computational resource can lead to improved modelling results, and thus prediction tools. The industry goal is to perform accurate and reliable noise predictions very quickly, allowing the optimisation of landing gear designs, leading to quieter aircraft and an improved environment for those affected by aircraft noise.

Appendix A

Validation of Computational Aeroacoustics Code

In this appendix various parts of the CAA code were validated including boundary conditions and numerical schemes. Simple test cases were used for this purpose.

A.1 Gaussian Pulse Propagation

The test case of two-dimensional Gaussian pulse propagation was used to validate the time-stepping scheme, filtering schemes, and the characteristic interface condition. The Euler equations were used to solve the initial value problem at $t = 0$ given by

$$p' = p - p_0 = A\exp\left[-\ln 2\left(\frac{x^2+y^2}{9}\right)\right],$$

$$u' = 0, \quad v' = 0, \quad \rho' = p' \tag{A.1}$$

where u' and v' are the velocity perturbations in the x and y directions, and A is the pulse amplitude. The freestream Mach number was $M_x = 0.5$, and a small initial pulse amplitude of $A = 0.001$ was specified so that the solution could be directly compared to the linearized solution. The analytical solution of the linearized Euler equations (LEE) corresponding to this this problem is given in [36] as

$$p = \frac{A}{2\alpha_1}\int_0^\infty e^{\frac{-\xi^2}{4\alpha_1}}\cos(\xi t)J_0(\xi\eta)\xi d\xi, \tag{A.2}$$

where $\alpha_1 = \frac{(\ln 2)}{9}$, $M = 0.5$, $\eta = [(x - Mt)^2 + y^2]^{\frac{1}{2}}$, and J_0 is the Bessel function of order 0 of the first kind. In the calculation the length scales are non-dimensionalised by $L^* = 1$m, the velocities by $c^* = 340$ m/s, the density by $\rho^* = 1.225$ kg/m^3 and the

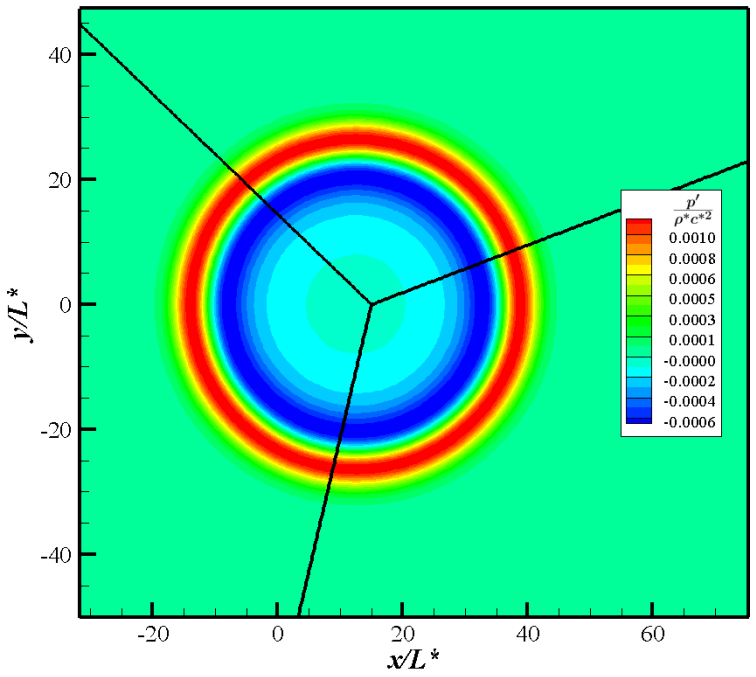

FIGURE A.1: Solution of non-dimensional Gaussian pressure distribution, $\frac{\overline{p^{*2}}}{\rho^* c^{*2}}$, at $tc^*/L^* = 28.45$ obtained using implicit time-stepping with the characteristic boundary condition along the interior block boundaries.

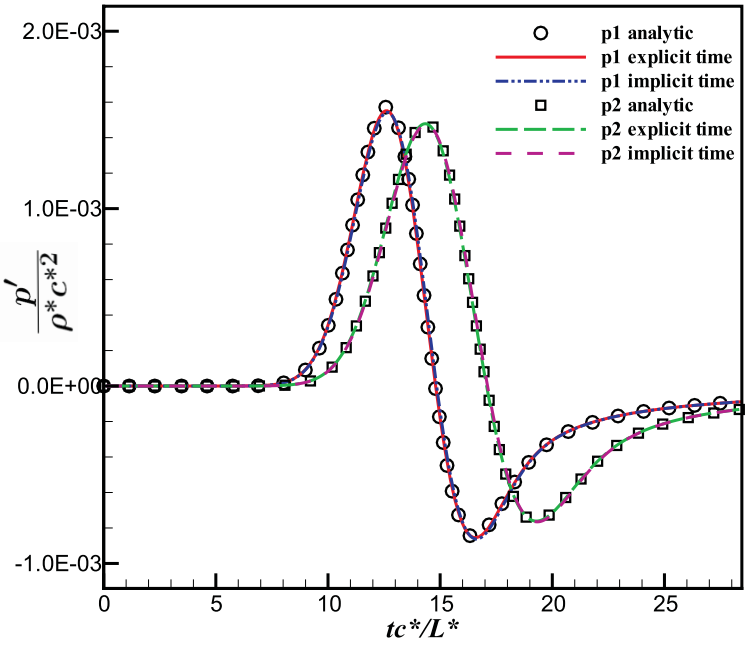

FIGURE A.2: Solution of non-dimensional Gaussian pressure distribution: comparison between explicit and implicit time stepping and analytical solution at two locations, p1 at (20.326,-0.067), and p2 at (14.315,14.070).

pressure by $\rho^* c^{*2}$. The time step of $\Delta t = 0.0569 L^*/c^*$ was adopted leading to a CFL number of approximately 0.2.

The pressure distribution was solved on a highly skewed three-block grid to demonstrate the capability of the characteristic interface condition applied to along the skewed grid interfaces. Each block featured 200×200 cells and the grid spacing was in the order 0.05. The case was also used to provide a comparison between the second-order implicit and the fourth-order explicit time stepping algorithms. The buffer zone boundary condition was adopted along the external boundaries and the solution was filtered by the sixth-order explicit filter. The simulation was run for 500 iterations were performed to reach a non-dimensional time of 28.45.

The non-dimensional pressure field after time $t = 28.45$ is shown in Figure A.1. The pulse was initiated at (0,0) and convected downstream in the positive $x-$direction according to the freestream Mach number, $M_x = 0.5$. The distribution shows correct propagation across the skewed grid lines. The pressure was monitored at two locations, namely p1 at (20.326,-0.067) and p2 at (14.315,14.070) corresponding to nodal values on the grid. The result at these locations is shown in Figure A.2. Excellent agreement between implicit/explicit time stepping and the analytical solution in both time and amplitude can be concluded.

A.2 Monopole Radiation

The acoustic field radiated by a monopole source was used to validate the FW-H solver. The complex potential for the monopole is given in [18] as

$$\phi(x, y, z, t) = A \frac{1}{4\pi r} \exp^{i(\omega t - \frac{\omega r}{c_0})} \tag{A.3}$$

where r is the distance to the far-field observer, $\omega = 4\pi/46$ is the non-dimensional circular frequency, c_0 defines the speed of sound, and $A = 0.1$ is the normalised amplitude. In the calculation the length scales are non-dimensionalised by $L^* = 1$m, the velocities by $c^* = 340$ m/s, the density by $\rho^* = 1.225$ kg/m^3 and the pressure by $\rho^* c^{*2}$. The real parts of $p' = -\rho_0 \partial\phi/\partial t$, $u' = \partial\phi/\partial x$, $v' = \partial\phi/\partial y$, $w' = \partial\phi/\partial z$, and $\rho' = p'/c_0^2$ were used as the variables in the FW-H equation. The flow variables were evaluated over four periods on the integration surface and were used as the sources terms in the FW-H equation. The integration surface was defined as a cube that extends from -5L to -5L in each direction and each face consisted of $50L \times 50L$ evenly spaced integration panels. The predicted pressure and analytic solution for an observer located at (50L,0,0) is displayed in Figure A.3 which shows very good agreement.

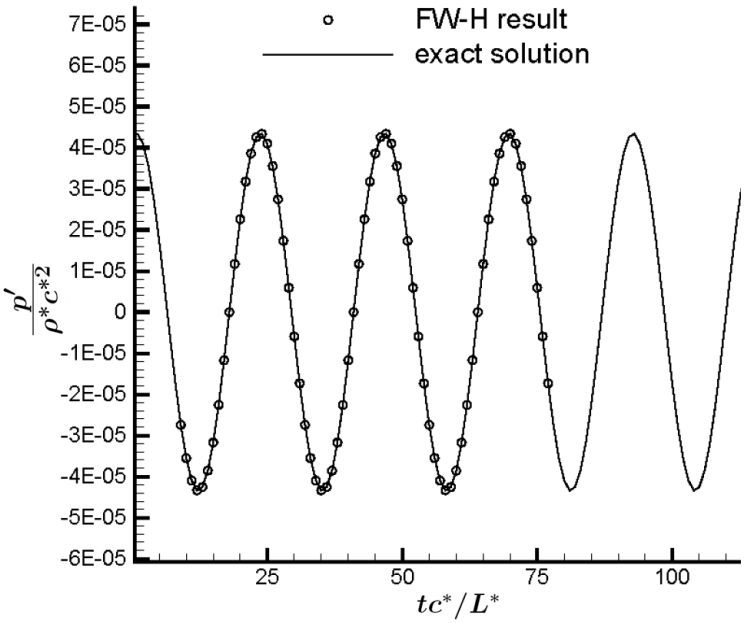

FIGURE A.3: Comparison between predicted non-dimensional pressure history and analytic solution for a monopole source.

A.3 2-D Circular Cylinder in Turbulent Flow

In this validation case the high-order SotonCAA code was deployed to solve the turbulent flow around a two-dimensional cylinder. The CAA solver was used to predict the near-field flow and the FW-H solver was used to predict the acoustic field at far-field observers. The Spalart-Almaras RANS model was used to model the turbulent solution with a freestream turbulence viscosity ratio of $\frac{\mu_t}{\mu} = 10$. The 6th-order compact scheme and the 2nd-order implicit time stepping scheme were used to obtain the highly nonlinear flow field. A non-slip boundary condition was used on the cylinder surface and the buffer zone boundary condition was imposed along the far-field domain. The characteristic interface was used along all of the internal block boundaries. The freestream Mach number was 0.2, and the Reynolds number was 140,000 based on the cylinder diameter, $D = 0.0311m$. The O-grid extended to $30D$ around the cylinder with one grid point per degree around the cylinder circumference. The total number of grid points is approximately 100,000. In the calculation the length scales are non-dimensionalised by D, the velocities by $c^* = 340$ m/s, the density by $\rho^* = 1.225$ kg/m^3 and the pressure by $\rho^* c^{*2}$. The non-dimensional time step is $t = 0.0025$ leading to a CFL number of approximately 8 and the first grid size off the wall was 3.0×10^{-4}. The solution was run for 300,000 time steps and data was sampled for the FW-H prediction during the last 100,000 steps.

Strong shedding was predicted behind the cylinder at a Strouhal number of approximately 0.26, which is in agreement with other studies and experiments [10, 82]. Figure A.4 displays the density contours which clearly indicate the coherent shedding in

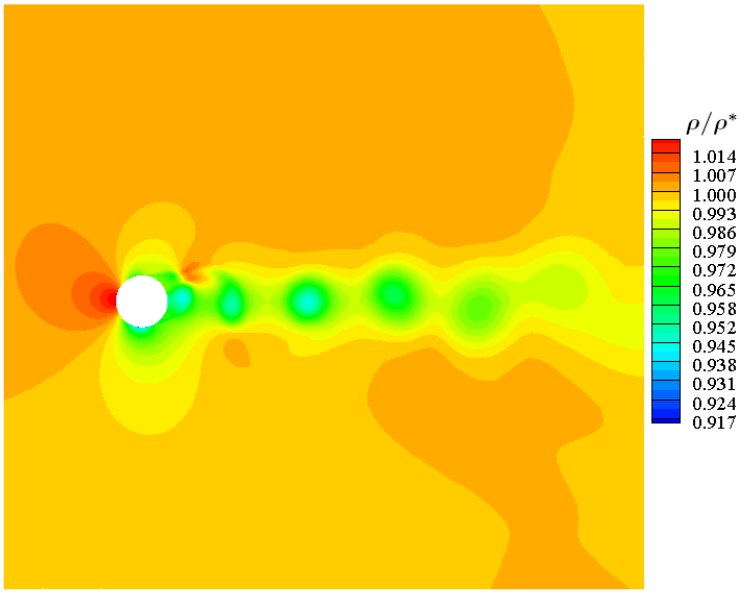

FIGURE A.4: Two-dimensional high-order CAA prediction: computed 2-D cylinder density contours.

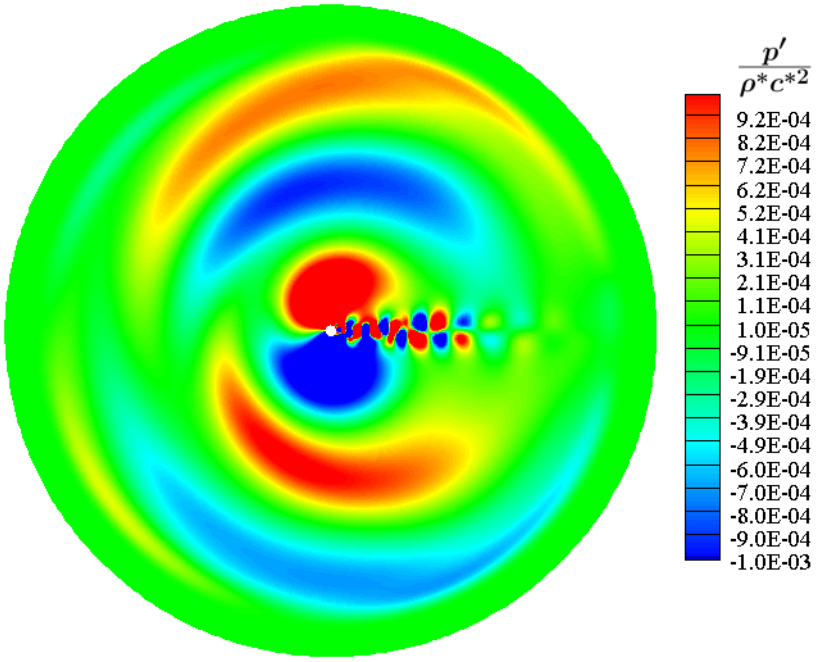

FIGURE A.5: Two-dimensional high-order CAA prediction: contours of computed instantaneous non-dimensional pressure perturbation for 2-D viscous cylinder flow.

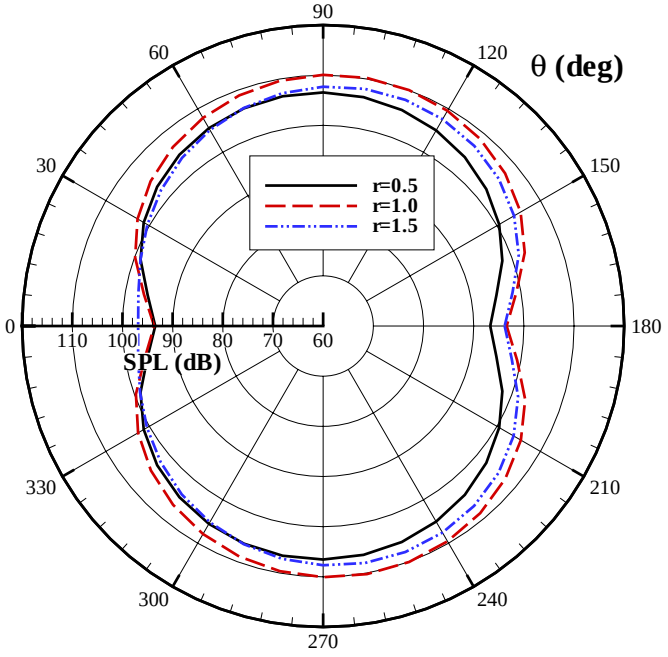

FIGURE A.6: Two-dimensional high-order CAA prediction: computed 2-D cylinder SPL directivity at observers located a distance $R = 100D$, θ is measured from the positive $x-$axis.

the cylinder wake. Figure A.5 displays the instantaneous pressure perturbation field throughout the computational domain. The large wave fronts associated with the vortex shedding are clearly marked and indicate a slight downstream convection direction.

The far-field observers were defined along a circular arc of radius $100D$ in the $z-$plane with the origin located at (0,0,0). The $2D$ solution was extruded in the $z-$direction to generate the necessary three-dimensional integration surface for the FW-H solver. Various integration surfaces were defined in order to test the sensitivity of the acoustic solution on its placement. The far-field directivity is displayed in Figure A.6 which indicate the expected dipole pattern. The three integration surfaces tested show that the solution is sensitive to their placement within the range of $r = 0.5 - 1.5$. Due to the low Mach number, it is assumed that the difference is due to vortices passing through the integration surface [52].

Appendix B

Details of the Numerical Method

In this appendix some important details concerning the numerical method are outlined. Details of the transformation matrices used for the characteristic interface boundary condition are provided, followed by details of the Spalart-Almaras turbulence model.

B.1 Characteristic Transformation Matrices

The matrix $\bar{\mathbf{P}}^{-1}$ transforms the conservative variables to characteristic variables, whilst its inverse $\bar{\mathbf{P}}$ diagonalises the flux-Jacobian matrices in the direction normal to the interface. These transformation matrices are given as:

$$\bar{\mathbf{P}}^{-1} =$$

$$\begin{bmatrix}
\mathbf{B_o}\cdot\mathbf{l}_x & (\gamma-1)\frac{u}{c^2}\tilde{\xi}_x & (\gamma-1)\frac{v}{c^2}\tilde{\xi}_x+\frac{\tilde{\xi}_z}{\rho} & (\gamma-1)\frac{w}{c^2}\tilde{\xi}_x-\frac{\tilde{\xi}_y}{\rho} & -\frac{\gamma-1}{c^2}\tilde{\xi}_x \\
\mathbf{B_o}\cdot\mathbf{l}_y & (\gamma-1)\frac{u}{c^2}\tilde{\xi}_y-\frac{\tilde{\xi}_z}{\rho} & (\gamma-1)\frac{v}{c^2}\tilde{\xi}_y & (\gamma-1)\frac{w}{c^2}\tilde{\xi}_y-\frac{\tilde{\xi}_x}{\rho} & \frac{\gamma-1}{c^2}\tilde{\xi}_y \\
\mathbf{B_o}\cdot\mathbf{l}_z & (\gamma-1)\frac{u}{c^2}\tilde{\xi}_z+\frac{\tilde{\xi}_y}{\rho} & (\gamma-1)\frac{v}{c^2}\tilde{\xi}_z-\frac{\tilde{\xi}_x}{\rho} & (\gamma-1)\frac{w}{c^2}\tilde{\xi}_z & \frac{\gamma-1}{c^2}\tilde{\xi}_y \\
\frac{c}{\rho}\left(\frac{\gamma-1}{2}M^2-\frac{\mathbf{v}\cdot\mathbf{l}_\xi}{c}\right) & \mathbf{C}_+\cdot\mathbf{l}_x & \mathbf{C}_+\cdot\mathbf{l}_y & \mathbf{C}_+\cdot\mathbf{l}_z & \frac{\gamma-1}{\rho c} \\
\frac{c}{\rho}\left(\frac{\gamma-1}{2}M^2-\frac{\mathbf{v}\cdot\mathbf{l}_\xi}{c}\right) & \mathbf{C}_-\cdot\mathbf{l}_x & \mathbf{C}_-\cdot\mathbf{l}_y & \mathbf{C}_-\cdot\mathbf{l}_z & \frac{\gamma-1}{\rho c}
\end{bmatrix}$$

$$\bar{\mathbf{P}} =$$

$$\begin{bmatrix}
\tilde{\xi}_x & \tilde{\xi}_y & \tilde{\xi}_z & \frac{\rho}{2c} & \frac{\rho}{2c} \\
u\tilde{\xi}_x & u\tilde{\xi}_y-\rho\tilde{\xi}_z & u\tilde{\xi}_z+\rho\tilde{\xi}_y & \frac{\rho}{2c}(u+\tilde{\xi}_x c) & \frac{\rho}{2c}(u+\tilde{\xi}_x c) \\
v\tilde{\xi}_x+\rho\tilde{\xi}_z & v\tilde{\xi}_y & v\tilde{\xi}_z-\rho\tilde{\xi}_x & \frac{\rho}{2c}(v+\tilde{\xi}_y c) & \frac{\rho}{2c}(v+\tilde{\xi}_y c) \\
w\tilde{\xi}_x+\rho\tilde{\xi}_y & w\tilde{\xi}_y+\rho\tilde{\xi}_x & w\tilde{\xi}_z & \frac{\rho}{2c}(w+\tilde{\xi}_z c) & \frac{\rho}{2c}(w+\tilde{\xi}_z c) \\
\mathbf{b}\cdot\mathbf{l}_x & \mathbf{b}\cdot\mathbf{l}_y & \mathbf{b}\cdot\mathbf{l}_z & \frac{\rho}{2c}(\mathbf{H}+c\mathbf{v}\cdot\mathbf{l}_\xi) & \frac{\rho}{2c}(\mathbf{H}-c\mathbf{v}\cdot\mathbf{l}_\xi)
\end{bmatrix}$$

The vectors in $\bar{\mathbf{P}}^{-1}$ and $\bar{\mathbf{P}}$ are defined as follows:

$$\mathbf{B_o} = \left(1 - \frac{\gamma-1}{2}M^2\right)\mathbf{l}_x - \frac{1}{\rho}(\mathbf{v}\times\mathbf{l}_\xi), \qquad \mathbf{C}_\pm = \pm\frac{\mathbf{l}_\xi}{\rho} - \frac{\gamma-1}{\rho c}\mathbf{v}, \qquad \mathbf{v} = (u,v,w)^T$$

$$\mathbf{b} = \frac{|\mathbf{v}|^2}{2}\mathbf{l}_\xi + \rho(\mathbf{v}\times\mathbf{l}_\xi), \qquad \mathbf{H} = \frac{|\mathbf{v}|^2}{2} + \frac{c^2}{\gamma-1}$$

where $\mathbf{l}_x$, $\mathbf{l}_y$, and $\mathbf{l}_z$ are unit vectors in the x, y, and z directions respectively, and:

$$\mathbf{l}_\xi = \nabla\xi/|\nabla\xi|.$$

B.2 Spalart-Almaras Model Constants

In this section the functions and constants used by the Spalart-Allmaras turbulence model are described. The transport equation is defined in Chapter 4, in Equation 4.10, and the modified turbulent viscosity, $\tilde{\nu}$ is defined in Equation 4.9.

The viscous damping function in Equation 4.9 is given by:

$$f_{v1} = \frac{\chi^3}{\chi^3 + C_{v1}^3} \tag{B.1}$$

where

$$\chi \equiv \frac{\tilde{\nu}}{\nu} \tag{B.2}$$

The production term, G_ν, in Equation 4.10, is modelled as

$$G_\nu = C_{b1}\rho\tilde{S}\tilde{\nu} \tag{B.3}$$

where

$$\tilde{S} \equiv S + \frac{\tilde{\nu}}{\kappa^2 d^2} f_{v2} \tag{B.4}$$

and

$$f_{v2} = 1 - \frac{\chi}{1+\chi f_{v1}} \tag{B.5}$$

where S is a scalar measure of the deformation tensor and d is from Equation 4.11. The modified strain/vorticity relationship used to model G_ν comes in the way of the definition of S as follows:

$$S \equiv |\Omega_{ij}| + C_{\mathrm{prod}}\min(0, |\mathrm{S_{ij}}| - |\Omega_{\mathrm{ij}}|) \tag{B.6}$$

where

$$C_{\mathrm{prod}} = 2.0, |\Omega_{ij}| \equiv \sqrt{2\Omega_{ij}\Omega_{ij}}, |S_{ij}| \equiv \sqrt{2S_{ij}S_{ij}} \tag{B.7}$$

where the mean strain rate tensor, S_{ij}, is defined as

$$S_{ij} = \frac{1}{2}\left(\frac{\partial u_j}{\partial x_i} + \frac{\partial u_i}{\partial x_j}\right) \tag{B.8}$$

and the mean vorticity tensor, Ω_{ij}, is defined as

$$\Omega_{ij} = \frac{1}{2}\left(\frac{\partial u_i}{\partial x_j} - \frac{\partial u_j}{\partial x_i}\right). \tag{B.9}$$

The destruction term in Equation 4.10, Y_ν, is modelled as

$$Y_\nu = C_{w1}\rho g\left[\frac{1+C_{w3}^6}{g^6+C_{w3}^6}\right]^{\frac{1}{6}}\left(\frac{\tilde{\nu}}{d}\right)^2 \tag{B.10}$$

where

$$g = \frac{\tilde{\nu}}{\tilde{S}\kappa^2 d^2} + C_{w2}\left(r^6 - r\right), \qquad r \equiv \frac{\tilde{\nu}}{\tilde{S}\kappa^2 d^2}. \tag{B.11}$$

The various constants in the above equations are:

$$C_{b1} = 0.1355, \quad C_{b2} = 0.622, \quad \sigma_{\tilde{\nu}} = \frac{2}{3}, \quad C_{v1} = 7.1$$

$$C_{w1} = \frac{C_{b1}}{\kappa^2} + \frac{(1+C_{b2})}{\sigma_{\tilde{\nu}}}, \quad C_{w2} = 0.3, \quad C_{w3} = 2.0, \quad \kappa = 0.4187$$

Appendix C

The Modelling Database

In this appendix details of the modelling database are provided. The database comprises of non-dimensional far-field acoustic spectra resulting of the numerical modelling of circular cylinders. Three categories are defined as single cylinders in cross flow, single cylinders with yaw, and tandem cylinders, corresponding to results from Chapters 5, 6, and 7 respectively.

C.1 Definition of Database

In Table C.1 the database entry name is listed followed by the component group, the Reynolds number of the simulation, and the details of the simulation.

Name	**Group**	**Re**	**Details**
SCC90K	Single	9.0×10^4	Cross-flow, TS
SCC140K	Single	1.4×10^5	Cross-flow, TS
SCC300K	Single	3.0×10^5	Cross-flow, TS
SCC1M	Single	1.0×10^6	Cross-flow, TS
YCC15	Yawed	1.4×10^5	$\Lambda = 15°$
YCC30	Yawed	1.4×10^5	$\Lambda = 30°$
YCC45	Yawed	1.4×10^5	$\Lambda = 45°$
UTDM2	Tandem	1.4×10^5	Upstream cyl. $S/D = 2$
DTDM2	Tandem	1.4×10^5	Downstream cyl. $S/D = 2$
UTDM3	Tandem	1.4×10^5	Upstream cyl. $S/D = 3$
DTDM3	Tandem	1.4×10^5	Downstream cyl. $S/D = 2$
UTDM4	Tandem	1.4×10^5	Upstream cyl. $S/D = 4$
DTDM4	Tandem	1.4×10^5	Downstream cyl. $S/D = 2$
UTDM5	Tandem	1.4×10^5	Upstream cyl. $S/D = 5$
DTDM5	Tandem	1.4×10^5	Downstream cyl. $S/D = 2$

Table C.1

Appendix D

Glossary of Aeroacoustic Terms

A-weighted Decibel, dB(A) - The A-weighted decibel scale denoted by dB(A) is regularly adopted for environmental sound measurement. The A-weighting emphasises frequencies around 1-6 kHz where the human ear is most sensitive, while attenuating very high and very low frequencies to which the ear is insensitive. The aim is to ensure that measured loudness corresponds well with subjectively perceived loudness. The weighting curve is shown in Figure D.1. The peak of the dB(A) spectrum gives an overall assessment of perceived noise

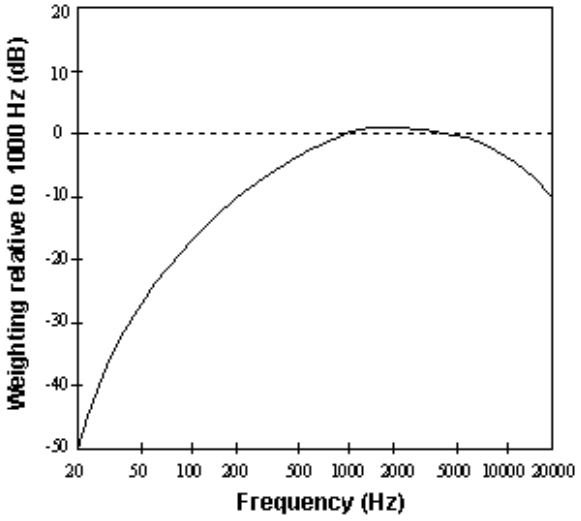

FIGURE D.1: A-weighting curve.

Acoustic Intensity - A fundamental acoustic quantity which describes the rate of flow of acoustic energy through a unit of area perpendicular to the flow direction defined by:

$$I = \frac{P_{ac}}{A} \tag{D.1}$$

where P_{ac} is the acoustic power and A is the area.

Acoustic Power - The total sound energy radiated by a source per unit time:

$$P_{ac} = IA \tag{D.2}$$

Acoustic Pressure - A dynamic variation in the atmospheric pressure denoted by p' or $\overline{p'^2}$ if the root mean square pressure is used. The total pressure is given by:

$$p_{total} = p_0 + p' \tag{D.3}$$

where p_0 is the local ambient pressure.

Acoustic scattering - Irregular and diffuse reflection of sound waves in various directions.

Airframe noise - The non-propulsive noise generated by an aircraft in flight.

Broadband noise - Noise produced by sources that are both random in time and space and distributed continuously in frequency.

Compact source - A source for which the differences between emission times of points on the source can be regarded negligible compared to the period of the fluctuations.

Decibel (dB) - A dimensionless unit with denotes the ratio between the acoustic pressure and the reference pressure. The decibel or dB scale is a logarithmic scale and uses the hearing threshold of 20μPa as the reference level.

Dipole source - A source that is represented by two equal monopole sources that are a small distance apart and pulsate 180 deg out of phase. The resulting radiation pattern is a directional "figure of eight".

Doppler effect - The changing of the observed frequency of a sound source that is moving with respect to an observer. The frequency is observed to increase if the source is moving toward the observer, or decrease if the source is moving away. The Doppler factor is expressed as:

$$(1 - M\cos\theta)^{-1} \tag{D.4}$$

where M is the Mach number of the source and θ is the radiation angle between the source direction vector and the observer. In radiation equations it is often raised to various powers to account for convective amplification effects of the sound level for a particular source type.

Effective Perceived Noise Level (EPNL) - A measure of human annoyance to aircraft which has spectral characteristics and persistence of sounds and is commonly used for aircraft noise certification. it accounts for human response to spectral shape, intensity, tonal content and duration of noise from an aircraft.

Far-field - The region far from the acoustic source where the sound waves spread spherically and where the sound pressure is reduced by a factor R^{-2} where R is the distance from the source.

Fundamental frequency - The reciprocal of the shortest period during which a periodic sound is reproduced.

Harmonic - A sinusoidal component whose frequency is an integral multiple of the fundamental frequency of a periodic source. The fundamental (lowest) frequency of the sound is sometimes refered to as the "first harmonic".

Karmen vortex shedding - Geometric arrangement of eddies in the wake of a bluff body resulting from periodic shedding which results in a tone at the vortex shedding frequency.

Loading noise - Noise resulting from forces acting on a body.

Monopole source - Source that can be represented by a pulsating sphere whose dimension is small compared to the wavelength of the sound radiation. If it is assumed that all parts of the sphere are moving in phase then an omni-directional radiation pattern results.

Near-field - The part of the sound field close to the source in which the sound radiates in a non-linear fashion.

Octave band - A frequency interval whose upper limiting frequency is two times its lowest frequency.

Overall sound pressure level (OASPL) - The overall sound pressure level (OASPL) in decibels is a measure of the overall noise of a source and is defined as:

$$\mathrm{OASPL} = 10 \log_{10} (E) \,. \tag{D.5}$$

where E is the total energy contained in the spectrum and is defined as:

$$E(f) = \int \overline{p'^2(f)} \mathrm{d}f, \tag{D.6}$$

where the integral is over all resolved frequencies.

Point source - A source that can be represented by sound radiation from a single point.

Quadrupole source - Noise produced by fluid flow in a volume in which no sources of mass or momentum are present. It is the main component of aerodynamic noise resulting from turbulent flow in the absence of solid boundaries and can be modelled by the superposition of four equal monopole sources that oppose each other in pairs.

Retarded time - The time at which a sound wave traveling at the local speed of sound would have to leave the source to arrive at an observer location at the present time.

Reynolds Number (Re) - The Reynolds number is a dimensionless number that expresses the ratio of inertial forces to viscous forces and is defined by $Re\frac{\ell U}{\nu}$ where ℓ and U are the characteristic length and velocity respectively and ν is the kinematic viscosity of the fluid.

Sound field - A region where sound waves are present.

Sound pressure level (SPL) - The sound pressure expressed in decibels (dB). The SPL spectrum is defined as:

$$\mathrm{SPL}(f) = 10\log_{10}\left(\frac{\overline{p'^2(f)}}{p_{\mathrm{ref}}^2}\right) \tag{D.7}$$

where $\overline{p'^2(f)}$ is the mean-square acoustic pressure and p_{ref} is the reference pressure equal to 20 μPa.

Strouhal number (St) - A dimensionless number $St = \frac{fU}{\ell}$ where f is the frequency, U is the reference velocity and ℓ is the reference length.

Thickness noise - Noise resulting from the periodic displacement of air due to flow around a solid body which can be represented as a monopole source distribution.

Wave number - The ratio of circular frequency of a periodic sound signal to the speed of sound, $k = \frac{2\pi}{\lambda}$.

Bibliography

[1] ACARE. Strategic research agenda. *International Journal of Fluid Mechanics 1 and 2* (2002).

[2] Achenbach, E. Distribution of local pressure and skin friction around a circular cylinder in cross-flow up to re= 5×10^6. *Journal of Fluid Mechanics 34*, 4 (1968), 625–639.

[3] Blevins, R. *Flow Induced Vibration*. Rheinhold, 1990.

[4] Block, P. An experimental investigation of airframe component interference noise. AIAA Conference, Los Angeles, CA, AIAA Paper 77-56.

[5] Blumenthal, V., and Streckenbach, J. Aircraft environmental problems. AIAA Conference, AIAA Paper No. 73-5.

[6] Brentner, K., and Farassat, F. Analytical comparison of the acoustics analogy and kirchhoff formulation for moving surfaces. *AIAA Journal 36*, 8 (1998).

[7] Cantwell, B., and Coles, D. An experimental study on entrainment and transport in the turbulent near wake of a circular cylinder. *Journal of Fluid Mechanics 136* (1983), 321–374.

[8] Choi, J.-S., and Hong, H.-B. Experimental study on the vortex-shedding sound from a yawed circular cylinder. *The Journal of the Acoustical Society of America 103*, 5 (1998), 2972.

[9] Chow, L., Mau, K., and Remy, H. Landing gears and high lift devices airframe noise research. 8th AIAA/CEAS Aeroacoustics Conference and Exhibit, Breckenridge, Colorado, AIAA Paper 2002-2408.

[10] Cox, J. Computation of vortex shedding and radiated sound for a circular cylinder: Subcritical to transcritical reynolds numbers. *Theoretical and Computational Fluid Dynamics 12*, 4 (1998), 233–253.

[11] Curle, N. The influence of solid boundaries upon aerodynamic sound. *Proceedings of the Royal Society* (1955), 505–514.

[12] Dacles-Mariani, J., Zilliac, G., Chow, J., and Bradshaw, P. Numerical/experimental study of a wingtip vortex in the near field. *AIAA Journal 33*, 9 (1995), 1561–1568.

[13] Delcayre, F., and Dubief, Y. On coherent-vortex identification in turbulence. *Journal of Turbulence 1*, 11 (2000), 1–22.

[14] Dobryznski, W., and Buchholz, H. Full-scale noise testing on airbus landing gears in the german dutch wind tunnel. 3rd AIAA/CEAS Aeroacoustics Conference, Atlanta, GA, AIAA Paper 97-1597-CP.

[15] Dobryznski, W., Chow, L., Guion, P., and Shiells, D. A european study on landing gear airframe noise sources. AIAA/CEAS Aeroacoustics Conference and Exhibit, Lahaina, Hawaii, AIAA Paper 2000-1971.

[16] Dobrzynski, W., Chow, L., Guion, P., and Shiells, D. Research into landing gear airframe noise reduction. 8th AIAA/CEAS Aeroacoustics Conference and Exhibit, Breckenridge, Colarado, AIAA Paper 2002-2409.

[17] Dobrzynski, W., Pott-Pollenske, M., Foot, D., and Goodwin, M. Landing gears aerodynamic interaction noise. ECCOMAS Conference 2004.

[18] Dowling, A., and Ffwocs Williams, J. *Sound and Sources of Sound.* Ellis Horwood, 1983.

[19] Dyke, M. *An Album of Fluid Motion.* The Parabolic Press, 1982.

[20] Ewert, R., and Schroder, W. Acoustic perturbation equations based on flow decomposition via source filtering. *Journal of Computational Physics 188*, 2 (2003), 365–398.

[21] Fage, A., and Faulkner, V. Aspect ratio and end plate effects on vortex shedding from a circular cylinder. *Aero. Res. Counc. RM 1369* (1931).

[22] Farassat, F. Theory of noise generation from moving bodies with an application to helicopter rotors. Tech. rep., 1975.

[23] Farassat, F., and Succi, G. The prediction of helicopter rotor discrete frequency noise. *Vertica 7*, 4 (1983), 309–320.

[24] Ffowcs Williams, J., and Hawkings, D. Sound generation by turbulence and surfaces in arbitrary motion. *Philosophical Transactions of the Royal Society of London A 342* (1969), 264–321.

[25] Fink, M. Airframe noise prediction method. Tech. rep., FAA-RD-77-29, 1979.

[26] Fink, M. Noise component method for airframe noise. *Journal of Aircraft 16*, 10 (1979), 659–665.

[27] Fink, M., and Schlinker, R. Airframe noise component interaction studies. *Journal of Aircraft 17*, 2 (1980), 99–105.

[28] Fujita, H., and Suzuki, H. The aeolian tone characteristics of a circular cylinder in high reynolds number flow. AIAA Paper 99-1849.

[29] Gibson, J. S. Non-engine aerodynamic noise investigation of a large aircraft. Tech. rep., 1974.

[30] Grosche, F.-R., Schneider, G., and Stiewitt, H. Wind tunnel experiments on airframe noise sources of transport aircraft. 3rd AIAA/CEAS Aeroacoustics Conference, Atlanta, GA, AIAA Paper 97-1642-CP.

[31] Guo, Y. A statistical model for landing gear noise prediction. 9th AIAA/CEAS Aeroacoustics Conference and Exhibit, Hilton Head, South Carolina, AIAA Paper 2003-3227.

[32] Guo, Y., and Yamamoto, K. An empirical model for landing gear noise prediction. 10th AIAA/CEAS Aeroacoustics Conference, AIAA Paper 2004-2888.

[33] Haramoto, Y., Yasuda, S., Matsuzaki, K., and Ohba, H. Analysis of aerodynamic noise generated from inclined circular cylinder. *Journal of Thermal Science 9*, 2 (2000), 122–128.

[34] Hardin, J. Toward a compressive analysis of landing approach noise sources. 3rd AIAA/CEAS Aeroacoustics Conference, Atlanta, GA, AIAA Paper 97-1593-CP.

[35] Hardin, J., Fratello, D., Haydeb, R., Kadman, Y., and Africk, S. Prediction of airframe noise. Tech. rep., 1975.

[36] Hardin, J., Ristorcelli, J., and Tam, C. Icase/larc workshop on benchmark problems in computational aeroacoustics. NASA Conference Publication 3300, Washington, DC.

[37] Hayes, J., Horne, W., and Soderman, P. Airframe noise characteristics of a 4.7% scale dc-10 model. 3rd AIAA/CEAS Aeroacoustics Conference, Atlanta, GA, AIAA Paper 97-1594-CP.

[38] Hedges, L., Travin, A., and Spalart, P. Detached-eddy simulations over a simplified landing gear. *Journal of Fluids Engineering 123* (2002), 413–423.

[39] Heller, H., and Dobryznski, W. Sound radiation from aircraft wheel-well/landing-gear configurations. *Journal of Aircraft 14*, 8 (1977), 768–774.

[40] Hixon, R. Prefactored small-stencil compact schemes. *Journal of Computational Physics 165* (2000), 522–541.

[41] Holbeche, T., Hopkins, P., Phillipson, P., Riordan, D., and Woodrow, R. Airframe noise prediction. Tech. rep., ESDU Data Item 90023, June 2003.

[42] Hutcheson, F., and Brooks, T. Noise radiation from single and multiple rod configurations. 12th AIAA/CEAS Aeroacoustics Conference, Cambridge, UK, AIAA Paper 2006-2629.

[43] Jenkins, L., Khorarami, M., Choudhari, M., and McGinley, C. Characterization of unsteady flow structures around tandem cylinders for component interaction studies in airframe noise. 11th AIAA/CEAS Aeroacoustics Conference, AIAA 2005-2812.

[44] Khorrami, M., Choudhari, M., Jenkins, L., and McGinley, C. Unsteady flowfield around tandem cylinders as prototype for component interaction of airframe noise. *AIAA journal 45*, 8 (2007).

[45] Khorrami, M., Lockard, D., Choudhari, M., Jenkins, L., Neuhart, D., and McGinley, C. Simulations of bluff body flow interaction for noise source modeling. 36th AIAA Fluid Dynamics Conference and Exhibit, AIAA 2006-3203.

[46] Kim, J. W., and Lee, D. J. Characteristic interface conditions for multiblock high-order computation on singular structured grid. *AIAA Journal 41*, 5 (2003), 2341–2348.

[47] Lazos, B. Mean flow features around the inline wheels of four-wheel landing gear. *AIAA Journal 40*, 2 (2002), 193–198.

[48] Li, F., Khorrami, M., and Malik, M. Unsteady simulation of a landing-gear flow field. 8th AIAA/CEAS Aeroacoustics Conference Breckenridge, Colorado, AIAA Paper 2002-2411.

[49] Lighthill, M. On sound generated aerodynamically. *Proceedings of the Royal Society* (1952), 564–587.

[50] Lin, J.-C., Yang, Y., and Rockwell, D. Flow past two cylinders in tandem: Instantaneous and averaged flow structure. *Journal of Fluids and Structures 16*, 8 (2002), 1059–1071.

[51] Lockard, D. A comparison of ffowcs williams-hawkings solvers for airframe noise applications. 8th AIAA/CEAS Aeroacoustics Conference and Exhibit, Breckenridge, Colorado, AIAA Paper 2002-2580.

[52] Lockard, D., and Casper, J. Permeable surface corrections for ffowcs williams and hawkings integrals. 11th AIAA/CEAS Aeroacoustics Conference, Monterey, California, AIAA Paper 2005-2995.

[53] Lockard, D., and Khorrami, M. Aeroacoustic analysis of a simplified landing gear. 9th AIAA/CEAS Aeroacoustics Conference and Exhibit, Hilton Head, South Carolina, AIAA Paper 2003-3111.

[54] Lockard, D., and Khorrami, M. High resolution calculation of a simplified landing gear. 10th AIAA/CEAS Aeroacoustics Conference, Manchester, UK, AIAA Paper 2004-2887.

[55] Lockard, D., Khorrami, M., and Choudhari, M. Tandem cylinder noise predictions. 13th AIAA/CEAS Aeroacoustics Conference, Rome, Italy, AIAA Paper 2007-3450.

[56] Lopes, L., Brentner, K., Morris, P., Lilley, G., and Lockard, D. Complex landing gear noise prediction using a simple toolkit. AIAA Paper 2005-1202.

[57] Lyrintzis, S. Review: The use of kirchhoff's method in computational aeroacoustics. *Journal of Fluids Engineering 116* (1994), 665–676.

[58] Ramberg, S. The influence of yaw angle upon the vortex wakes of stationary and vibrating cylinders. Tech. rep., Navel Res. Lab. Mem Report 3822, 1978.

[59] Ravetta, P. A., Burdisso, R. A., and Ng, W. F. Wind tunnel aeroacoustic measurements of a 26%-scale 777 main landing gear model. 10th AIAA/CEAS Aeroacoustics Conference, AIAA Paper 2004-2885.

[60] Revell, J., and Healy, G. Methods for the prediction of airframe noise. 2nd AIAA Aeroacoustics Conference, AIAA Paper 75-539.

[61] Rizzetta, D., Visbal, M., and Blaisdell, G. A time-implicit high-order compact differencing and filtering scheme for large-eddy simulation. *International Journal of Numerical Methods in Fluids 42* (2003), 665–693.

[62] Roe, P. Technical prospects for computational aeroacoustics. AIAA Aerospace Sciences Conference, AIAA Paper 92-02-032.

[63] Roshko, A. Experiments on the flow past a circular cylinder at very high reynolds number. *Journal of Fluid Mechanics 10* (1961), 345–356.

[64] Schewe, G. Reynolds-number effects in flow around more-or-less bluff bodies. *Journal of Wind Engineering and Industrial Aerodynamics*, 89 (2001), 1267–1289.

[65] Schlinker, R., Fink, M., and Amiet, R. Vortex noise from nonrotating cylinders and aerofoils. 3rd AIAA/CEAS Aeroacoustics Conference, Atlanta, GA, AIAA Paper 1976-81.

[66] Sen, R., Hardy, B., Yamamoto, K., Guo, Y., and Miller, G. Airframe noise sub-component definition and model. Tech. rep., 2004.

[67] Seo, J. H., Chang, K. W., and Moon, Y. J. Aerodynamic noise prediction for long-span bodies. 12th AIAA/CEAS Aeroacoustics Conference and Exhibit, Cambridge, UK, AIAA Paper 2006-2573.

[68] Seror, C., Sagaut, P., and Belanger, A. A numerical aeroacoustics analysis of a detailed landing gear. 10th AIAA/CEAS Aeroacoustics Conference, Manchester, UK, AIAA Paper 2004-2884.

[69] Shur, M., Spalart, P., Strelets, M., and Travin, A. Detached-eddy simulation of an airfoil at high angle of attack. 4th Intl. Symposium on Eng. Turb. Modelling and Experiments, 2426 May, Elsevier, Amsterdam, pp. 669678.

[70] Smagorinsky, J. General circulation experiments with the primative equations. *Monthly Weather Review 91*, 3 (1963), 99–165.

[71] Smith, M., and Chow, L. Prediction method for aerodynamic noise from aircraft landing gear. AIAA Aeroacoustics Conference, AIAA Paper 98-2228.

[72] Smith, M., and Chow, L. Validation of a prediction model for aerodynamic noise from aircraft landing gear. 8th AIAA/CEAS Aeroacoustics Conference and Exhibit, Breckenridge, Colorado, AIAA Paper 2002-2581.

[73] Souliez, F., Long, L., Morris, P., and Sharma, A. Landing gear aerodynamic noise prediction using unstructured grids. *International Journal of Aeroacoustics 1*, 2 (2002), 115–135.

[74] Spalart, P. Young-person's guide to detached-eddy simulation grids. Tech. rep., NASA CR-2001-211032, 2001.

[75] Spalart, P., and Almaras, S. A one-equation turbulence model for aerodynamic flows. AIAAs Conference, AIAA Paper 92-0439.

[76] Stoker, R., and Guo, Y. Airframe, noise source locations of a 777 aircraft in flight and comparisons with past model scale tests. 9th AIAA/CEAS Aeroacoustics Conference and Exhibit, Hilton Head, South Carolina, AIAA Paper 2003-3232.

[77] Stowell, E., and Deming, A. Vortex noise from rotating cylindrical rods. Tech. rep., NASA Techinical Paper 519, 1935.

[78] Tam, C. Computational aeroacoustics: Issues and methods. *AIAA Journal 33*, 10 (1995), 1788–1796.

[79] Travin, A., Shur, M., Strelets, M., and Spalart, P. Detached-eddy simulations past a circular cylinder. *Flow Turbulence and Combustion 63*, 1-4 (1999), 293–313.

[80] Vasta, V., and Singer, B. Evaluation of a second-order accurate navier-stokes code for detached eddy simulation past a cylinder. 9th AIAA/CEAS Aeroacoustics Conference and Exhibit, Hilton Head, South Carolina, AIAA Paper 2003-4085.

[81] Wilcox, D. *Turbulence Modelling for CFD*. Griffin Printing, CA, 1994.

[82] Zdravkovich, M. *Flow Around Circular Cylinders, Vol 1: Fundamentals*. Oxford University Press, 1997.

[83] Zdravkovich, M. *Flow Around Circular Cylinders, Vol 2: Applications*. Oxford University Press, 2003.